Doctoral Dissertation

# Study on the interfacial structure between Cu and AlN using Ag-free bonding materials for high-voltage applications

# 高耐圧用途向け Ag-free 接合材を用いた Cu/AlN 接合界面構造に関する研究

Nobuyuki Terasaki

June 2023

Division of Materials and Manufacturing Science

Graduate School of Engineering,

Osaka University

**Supervisor**

Prof. Tohru Sekino, Ph.D.

*SANKEN, The Institute of Scientific and Industrial Research*

*Osaka University*

**Doctoral Committee**

Prof. Yuichiro Koizumi, Ph.D.

*Division of Materials and Manufacturing Science*

*Osaka University*

Prof. Hidetoshi Fujii, Ph.D.

*Joining and Welding Research Institute*

*Osaka University*

Assoc. Prof. Tomoyo Goto, Ph.D.

*SANKEN, The Institute of Scientific and Industrial Research*

*Osaka University*

# Contents

# List of abbreviations

**ABF**: annular bright-field

**AC**: alternating current

**AES**: auger electron spectroscopy

**AMB**: active metal brazing

**BF**: bright-field

**BSE**: backscattered electron

**CTE**: coefficient of thermal expansion

**DBA**: direct bonded aluminum

**DBC**: direct bonded copper

**DC**: direct current

**DF**: dark-field

**DFT**: density functional theory

**ECM**: electrochemical migration

**EDS**: energy-dispersive X-ray spectroscopy

**EM**: electromigration

**EPMA**: electron probe micro analyzer

**EsB**: energy-selective backscattered electron

**FIB**: focused ion beam

**HAADF**: high-angle annular dark-field

**HVDC**: high-voltage direct current

**ICP-OES**: inductively coupled plasma optical emission spectrometry

**IEEE**: Institute of Electrical and Electronics Engineers

**IGBT**: insulated gate bipolar transistor

**IMC**: intermetallic compound

**JFCA**: Japan Fine Ceramics Association

**JIEP**: The Japan Institute of Electronics Packaging

**JIS**: Japan Industrial Standards

**MOSFET**: metal-oxide-semiconductor field-effect transistor

**NBD**: nano-beam electron diffraction

**OFC**: oxygen-free copper

**PVD**: physical vapor deposition

**SAED**: selected area electron diffraction

**SAICAS**: surface and interfacial cutting analysis system

**SAT**: scanning acoustic tomography

**SE**: secondary electron

**SEM**: scanning electron microscopy

**SPS**: Smart Processing Society for Materials, Environment & Energy

**TEM**: transmission electron microscopy

**TLP**: transient liquid phase

# Chapter 1: General introduction

## 1.1 Metal-bonded ceramic substrates for power modules

To meet the targets set out in the Paris Agreement, adopted in 2015, countries around the world have been actively developing technologies to improve energy efficiency and utilize renewable energy toward the common global goal of carbon neutrality, meaning net zero greenhouse gas emissions, by the second half of the 21st century [1–3]. With the development of technology necessary for countries to realize the societal changes required, progress is being made in power equipment for industrial applications. One example is the replacement of conventional power modules equipped with Si–IGBT (silicon–insulated gate bipolar transistor) chips with power modules equipped with SiC–MOSFET (silicon carbide–metal-oxide-semiconductor field-effect transistor) chips, which have both high voltage and low resistance [4–8]. An insulating substrate for power modules is composed of a thermally conductive metal layer such as aluminum (Al) or copper (Cu), and an insulating ceramic layer such as aluminum nitride (AlN), silicon nitride ($Si_3N_4$), or aluminum oxide ($Al_2O_3$). These metal-bonded ceramic substrates are grouped into one type of aluminum circuit substrate, namely, direct bonded aluminum (DBA) substrates [4, 9–11], and two types of copper circuit substrates, namely, direct bonded copper (DBC) substrates [12–14] and active metal brazing (AMB) substrates [15–17].

A cross-sectional view of a typical power module structure is shown in Fig. 1.1 [18]. The power module consists of a Si–IGBT chip, a ceramic substrate to which metal circuit such as Cu and Al are bonded, a heat spreader, and a heat sink. The metal-bonded ceramic

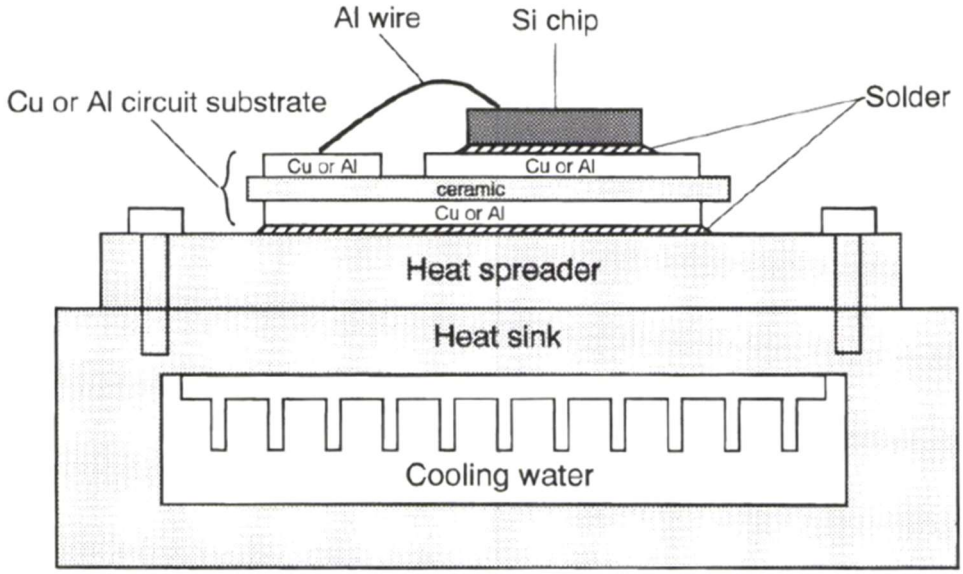


**Fig. 1.1 Cross-sectional view of a typical power module structure [18], © 2000 by JIEP, reproduced with permission.**

substrate is responsible for ensuring insulation between the Si–IGBT chip and the heat spreader and for the rapid transport of the heat generated by the Si–IGBT chip to the heat sink, and long-term use can be ensured by increasing the reliability of the metal/ceramic bonding interface.

## 1.2 Manufacturing process for insulating substrates and their interfacial structure

### 1.2.1 DBA substrates

DBA substrates consist of Al bonded as a circuit layer to both sides of a ceramic substrate such as AlN, $Si_3N_4$, or $Al_2O_3$. Industrially, two methods have been established for bonding Al onto ceramic substrates: the casting method [9] and the brazing method [4]. In the casting method, the elemental distribution in the Al layer is uniform. In the

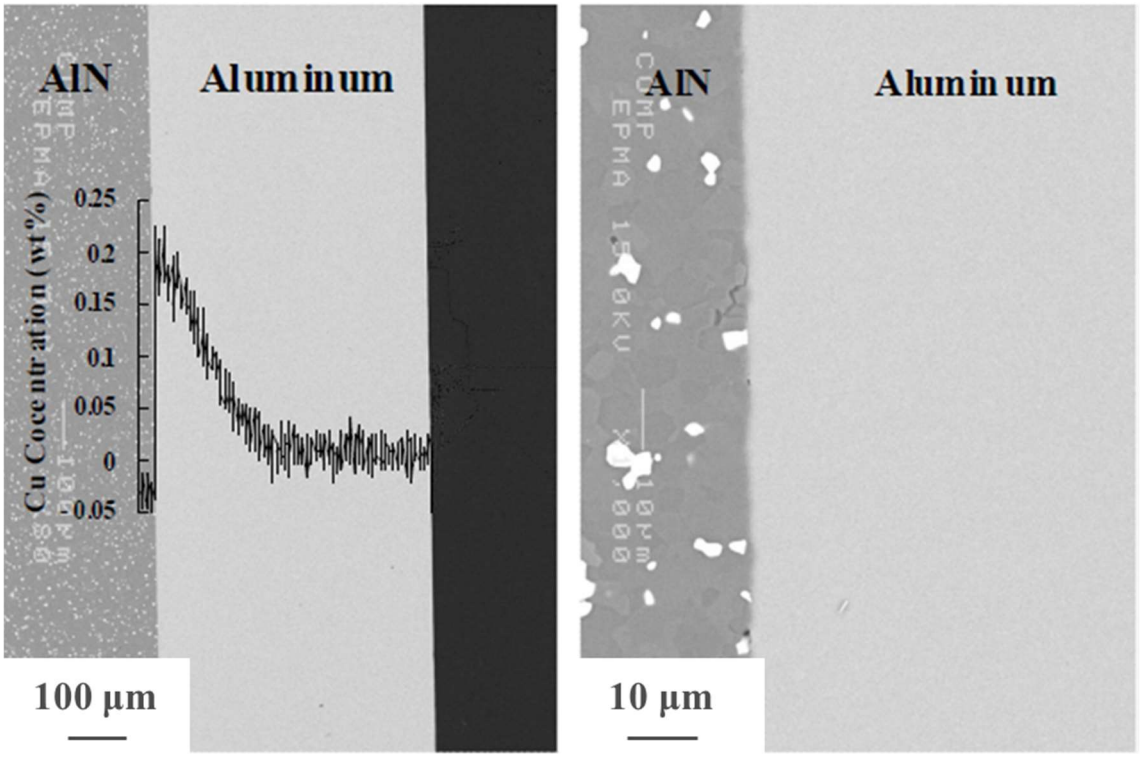


**Fig. 1.2 Cross-sectional BSE images of an Al/AlN bonding interface with quantitative line profile [10], © 2010 by IEEE, reproduced with permission.**

brazing method, on the other hand, when using an Al–*X* eutectic base brazing material, the Al/ceramic bonding interface has a structure in which the concentration of *X* decreases from the Al/ceramic bonding interface toward the Al layer surface as shown in Fig. 1.2 [10]. In addition, no obvious interfacial reaction layer can be observed at the Al/ceramic bonding interface by scanning electron microscopy (SEM) observations (Fig. 1.2), and this lack of reaction layer is independent of the bonding method.

The dependence of the bonding area ratio at the Al/AlN bonding interface on the number of thermal cycles is shown in Fig. 1.3 [19]. The thermal cycling tests were performed in an inert liquid between -40 °C and 150 °C. The reliability of the Al/AlN interface bonded using Al–7.5 wt% Si–0.1 wt% Mg brazing alloy with the intentional addition of Mg at the lowest bonding temperature of 600 °C is equivalent to that bonded

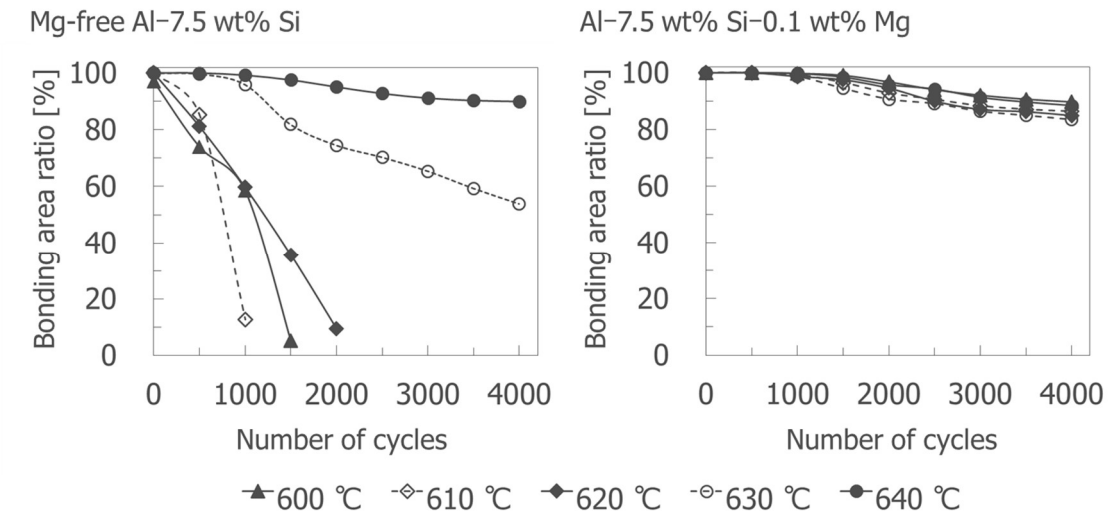


**Fig. 1.3 Bonding area ratio at the Al/AlN bonding interface after thermal cycling tests [19], © 2017 by JFCA, reproduced with permission.**

using Mg-free Al–7.5 wt% Si brazing alloy at 640 °C, which shows the greatest improvement. Segregation of Si, Mg, and O is observed at the Al/AlN bonding interface when using an Al–7.5 wt% Si–0.1 wt% Mg brazing alloy, which achieves high bonding reliability, as shown in Fig. 1.4 [19]. The O is derived from the thin amorphous Al–O phase, which is present as a natural oxide film on the surfaces of Al, Al–Si–Mg brazing alloy and AlN.

Kumamoto et al. [20] evaluated model specimens in which an A6063 alloy containing Si and Mg was bonded onto single-crystal AlN to clarify the effects of these elements at the Al/AlN bonding interface. The Mg- and O-containing segregation structure is formed just above AlN, but Si is shifted to the Al alloy side as shown in Fig. 1.5 [20]. This segregation structure is crystalline MgO, which has a configuration of (111) MgO//(0001) AlN, $[1\bar{1}0]$ MgO//$[11\bar{2}0]$ AlN. In addition, calculations shown in Table. 1.1 based on density functional theory (DFT) for a heterointerface model with supercells containing vacuum layer(s) of different polarities suggest that the AlN/MgO

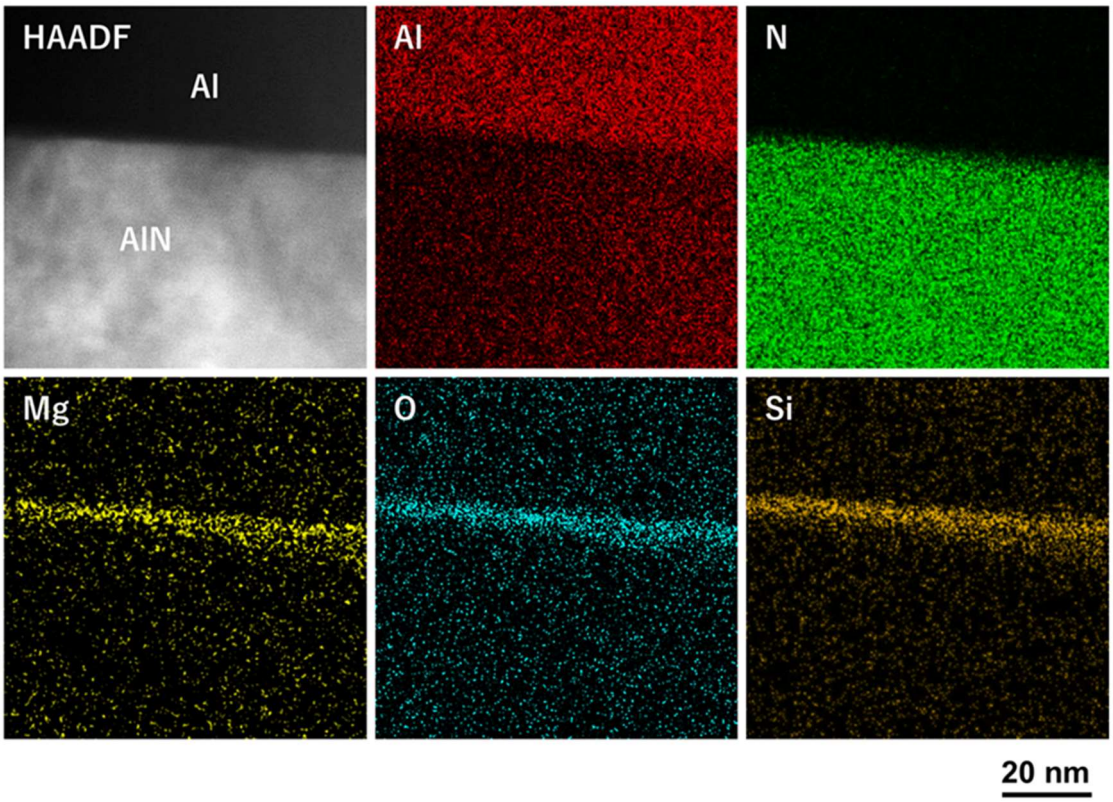


**Fig. 1.4 Cross-sectional HAADF image of an Al/AlN bonding interface after bonding at 630 °C using Al–7.5 wt% Si–0.1 wt% Mg, together with elemental distributions [19], © 2017 by JFCA, reproduced with permission.**

interface favors the Al-polar AlN with the O-polar MgO, as shown in Fig. 1.6(c). Furthermore, if the amorphous Al–O phase is considered as $Al_2O_3$, which acts as an oxidant for Mg, a spinel structure is formed according to Equation (1.1) [21].

$$3Mg + 4Al_2O_3 \rightarrow 3MgAl_2O_4 + 2Al \quad (1.1)$$

When metallic Mg is continuously supplied, the subsequent reaction between Mg and $MgAl_2O_4$ makes MgO thermodynamically more stable, as shown in Equation (1.2).

$$MgAl_2O_4 + 3Mg \rightarrow 2Al + 4MgO \quad (1.2)$$

The change in the standard free energy of formation is -54 kJ/mol and -119 kJ/mol for Equations (1.1) and (1.2), respectively, at 650 °C [22]. The reliability of the Al/AlN bonding interface has been achieved by forming this atomic-scale interfacial reaction layer.

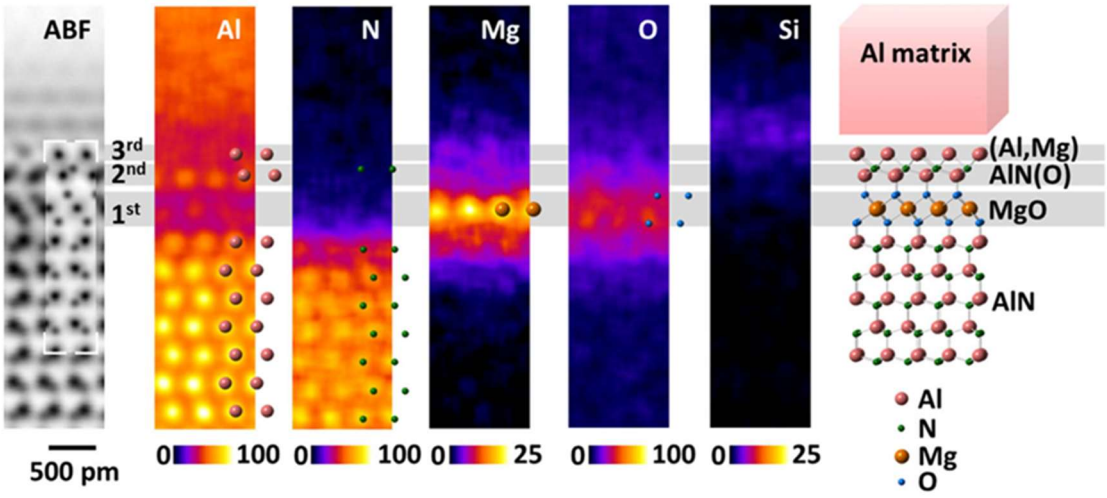


**Fig. 1.5 Atomic-scale structural determination of the Al alloy/AlN interface [20], © 2016 by authors, reproduced with license.**

**Table 1.1 Calculated adhesion energies ($E_{ad}$) shown in Fig. 1.6 [20], © 2016 by authors, reproduced with license.**

| | Interface | | $E_{ad}$ |
|---|---|---|---|
| | Materials | Terminations | [J/m²] |
| a | Al/AlN | Al–N | 4.45 |
| b | Al/AlN | Al–Al | 2.46 |
| c | MgO/AlN | O–Al | 8.87 |
| d | MgO/AlN | Mg–N | 4.81 |

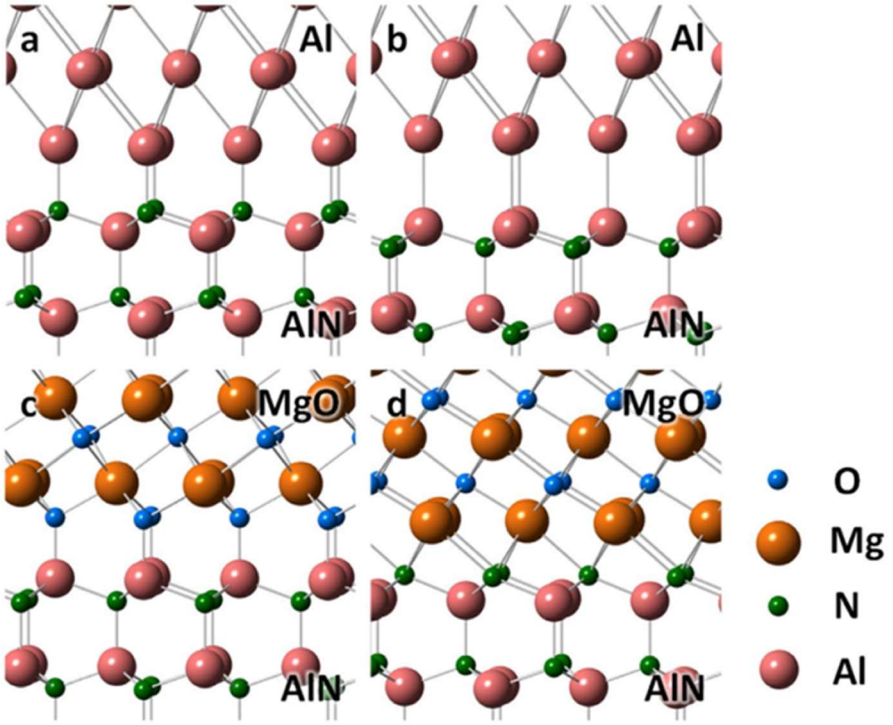


**Fig. 1.6 The energetically stable DFT models for heterointerfaces of different polarity. (a) Al/AlN and (c) MgO/AlN compared with those with inversion polar (b,d), © 2016 by authors, reproduced with license.**

### 1.2.2 DBC substrates

DBC substrates consist of Cu as a circuit layer bonded to both sides of a ceramic substrate such as $Al_2O_3$ [12, 13] or AlN with an oxidized surface [14]. An interfacial reaction layer consisting of complex oxides such as $CuAlO_2$ and $CuAl_2O_4$ is formed at the $Cu/Al_2O_3$ bonding interface by the interfacial reaction between the $Cu–Cu_2O$ eutectic liquid phases and $Al_2O_3$ [12–14]. In the DBC method, precise control of the oxidizing atmosphere is required to form a good $Cu/Al_2O_3$ bonding interface. Industrially, nitrogen flow furnaces using pure $N_2$ gas (purity > 99.999%) are used to achieve a low oxygen atmosphere of 5 ppmv $O_2$ or less. However, the use of nitrogen flow furnaces increases the risk of electrical discharges during voltage application due to the sealing of the $N_2$ gas in voids at the $Cu/Al_2O_3$ bonding interface, which is more pronounced in high-voltage

applications.

### 1.2.3 AMB substrates

As with DBC substrates, AMB substrates consist of Cu as the circuit layer bonded to both sides of a ceramic with an active metal braze filler, and not only AlN and $Al_2O_3$, but also $Si_3N_4$ can be used as the ceramic. AMB fillers used in industry are Ag–Cu eutectic-based fillers, such as the Ag–Cu system, Ag–Cu–In system, and Ag–Cu–Sn system, to which highly reactive elements called active metals, such as Ti, Zr, and Hf, have been added. When bonding Cu onto ceramic, the use of Ag–Cu-based systems, which have lower eutectic temperatures compared to Ag-free Cu–active metal systems, is very effective in reducing the ceramic fractures due to thermal and residual stress caused by the coefficient of thermal expansion (CTE) difference between Cu and ceramic. In addition, this brazing material can wet a chemically inert ceramic surface by forming a layer of active metal compound on it [15, 23–25]. An active metal compound layer containing ceramic components is formed at the bonding interface. For example, use of Ti as the active metal results in the formation of TiN for nitride ceramics [15–17, 23, 24, 26–28], $TiO_x$ for oxide ceramics [29–32], and TiC for carbide ceramics [33–37]. In cross-sectional SEM images of the Cu/AlN bonding interface (Fig. 1.7), a TiN layer is formed at the Cu/AlN interface [38]. Ag and Cu inclusions were detected in the TiN layer at the Cu/AlN part of the substrate/braze interface in work on the wettability of AlN–based ceramics using Ag–Cu–Ti AMB alloys reported by Taranets et al. [15] and on their heat transfer characteristics reported by Sivaprahasam et al. [39]. In addition, a Ag–Cu alloy layer consisting of Ag-rich and Cu-rich phases is formed between the Cu and TiN layers, where a large amount of Ag is present.

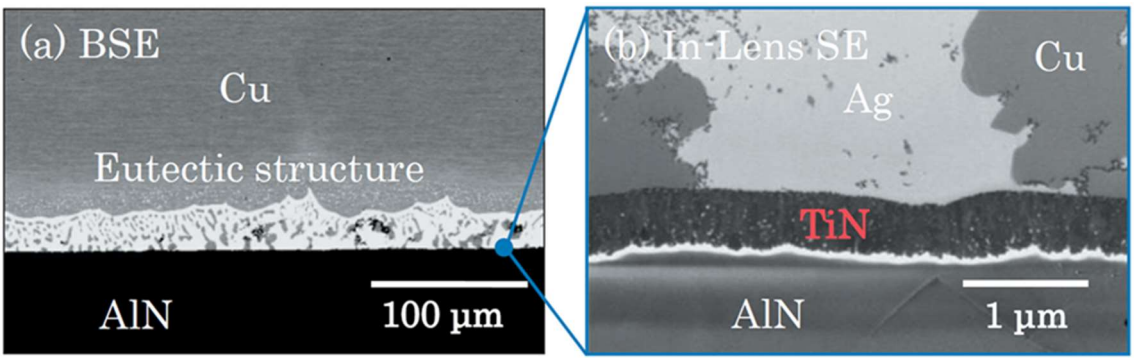


**Fig. 1.7 Cross-sectional SEM images of a Cu/AlN interface formed by the AMB method [38], © 2018 by SPS, reproduced with permission.**

## 1.3 AMB method based on interdiffusion process

Interdiffusion between Cu and a Cu-free Ag–Ti-based bonding material is a process essentially equivalent to bonding Cu onto ceramics using a Ag–Cu–Ti-based active brazing material. The dissolution of Ti into the Ag–Cu eutectic liquid phase generated by the interdiffusion of Ag in the Cu-free Ag–Ti bonding material and the Cu to be bonded produces the Ag–Cu–Ti liquid phase, which can achieve the same interfacial reaction as when a Ag–Cu–Ti bonding material is used. Microstructural classification results for the Cu/AlN bonding interface after bonding at 850 °C for 0.5 h under 0.1 MPa using Ag–Ti pastes with 42 different Ag/Ti ratios are shown in Fig. 1.8 [16]. When using Ti-free Ag pastes, no Cu/AlN bonding is obtained in the range of Ag amounts from 2.1 mg/cm$^2$ to 25.2 mg/cm$^2$. On the other hand, when Ti-containing Ag paste is used, the microstructure of the Cu/AlN bonding interface can be classified into four categories according to the amount of Ag and Ti. Cross-sectional secondary electron (SE) images and corresponding scanning acoustic tomography (SAT) images of the five Cu/AlN bond samples marked in Fig. 1.8 [16] are shown in Fig. 1.9 [16]. The SAT images of the Type B, Type C, and Type D Cu/AlN bonding interfaces show the following defects corresponding to the bright

contrasts: formation of large voids in the Ag–Cu alloy layer for Type B, discontinuous formation of the TiN layer for Type C, and no formation of a TiN layer for Type D. To successfully form the Cu/AlN bonding interface by the AMB method, the most important aspect is to form a continuous defect-free TiN layer, which is the interfacial reaction layer. In addition, Zhang et al. [17] reported that large voids in the Ag–Cu alloy layer can be reduced by increasing the bonding pressure.

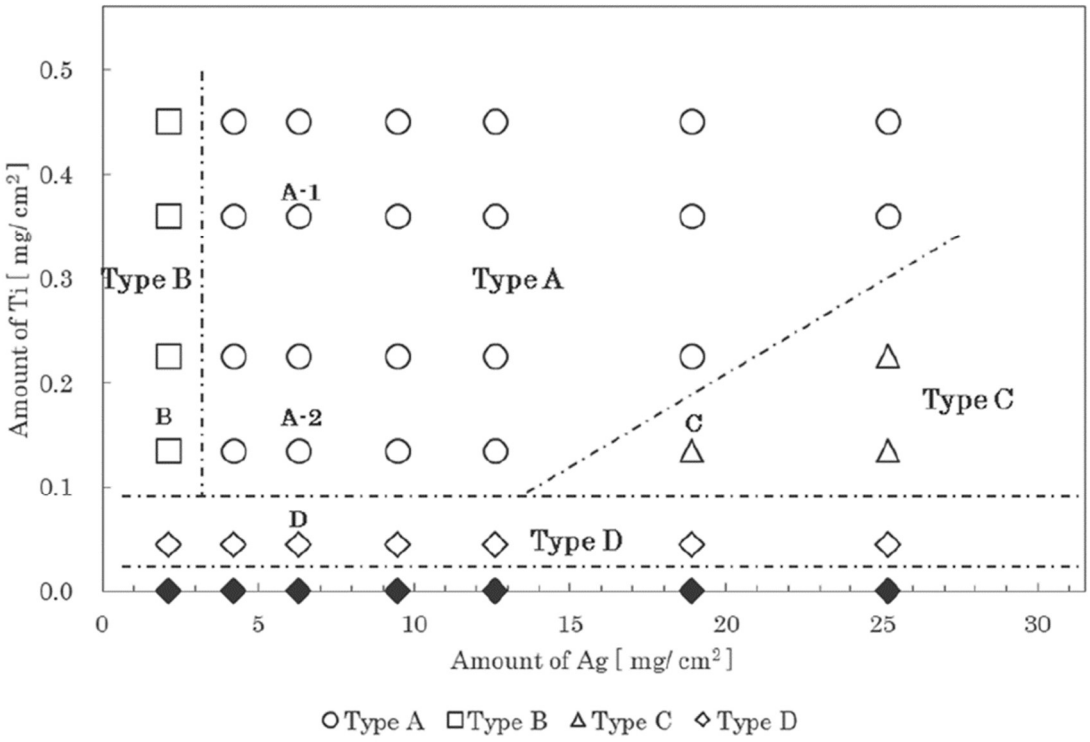


**Fig. 1.8 Microstructural classification of the Cu/AlN bonding interface after bonding at 850 °C for 0.5 h using Ag–Ti pastes with 42 different Ag/Ti ratios [16], © 2019 by Springer Science Business Media, reproduced with license.**

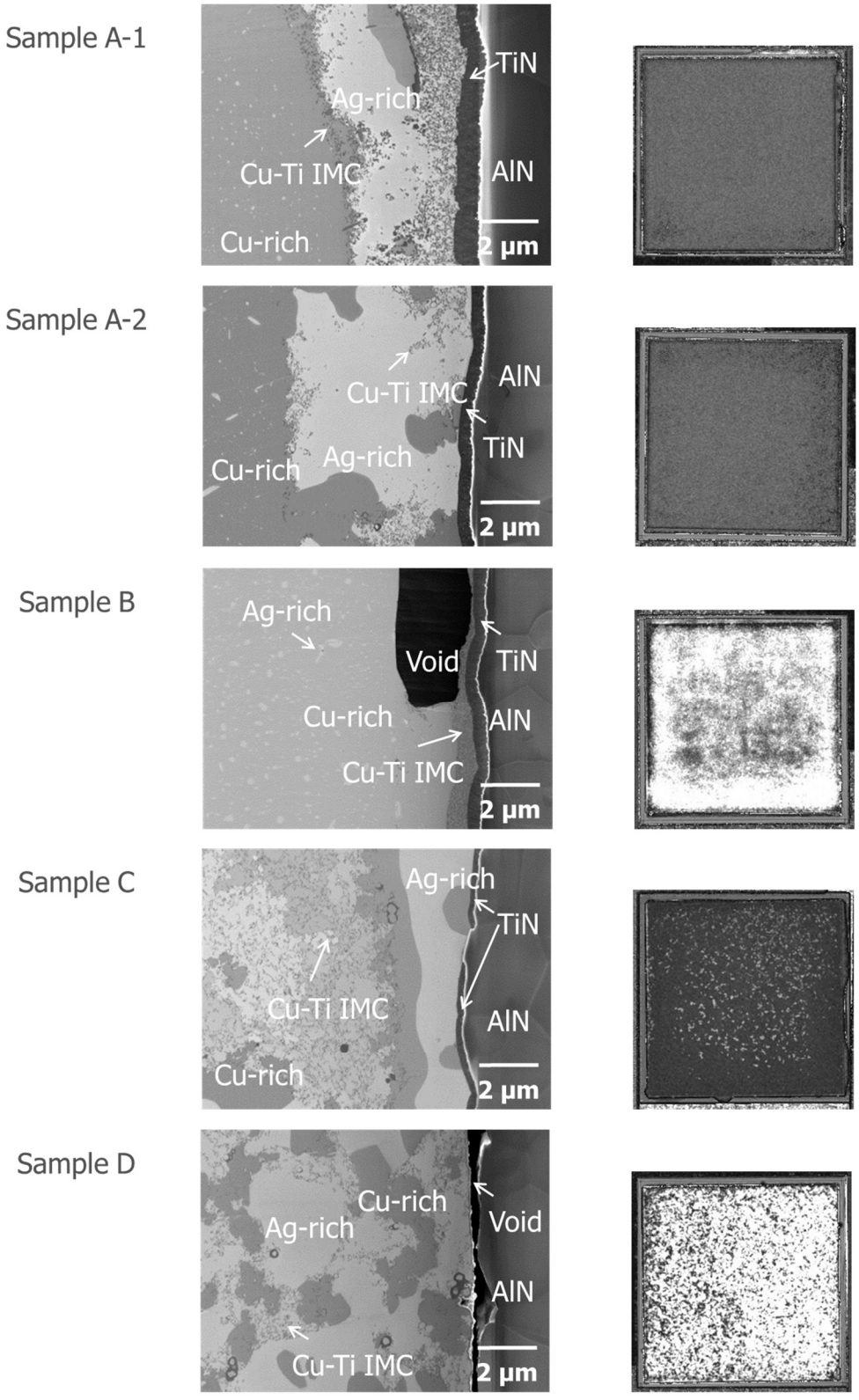


**Fig. 1.9 Cross-sectional SE images and corresponding SAT images of five selected Cu/AlN bonded samples (marked in Fig. 1.8) [16], © 2019 by Springer Science Business Media, reproduced with license.**

## 1.4 Potential risks of AMB substrates in high-voltage applications

### 1.4.1 High-voltage applications

Power module applications are shown as a function of operating voltage in Fig. 1.10 [40]. Applications with operating voltages below 200 V, such as household appliances, are defined as low-voltage applications. Applications with operating voltages between 600 V and 1.2 kV, such as industrial equipment and automotive, are defined as medium-voltage applications. Applications with operating voltages above 1.7 kV, such as electric railways and high-voltage direct current (HVDC) transmission, are defined as high-voltage applications. Generally, a breakdown voltage of 2 to 3 times the operating voltage is required to ensure reliability of the power module during operation. In recent years, power modules with an operating voltage of 6.5 kV using SiC have been developed, which can operate at temperatures above 200 °C [7, 41–45]. These high-voltage modules are compatible with the expanding use of renewable energy sources such as wind, hydropower, geothermal power, and solar power, which do not emit the greenhouse gas carbon dioxide, and are expected to become increasingly important for realizing a carbon-free society in the future [46–50]. Renewable energy can be easily connected to grids of different frequencies through HVDC lines, which can transmit large amounts of power over long distances with little transmission loss and are more efficient than conventional alternating current (AC) power transmission [51, 52]. An AC/DC conversion module is required to connect HVDC power transmission to power grids where AC power is consumed. For AC/DC conversion modules, AlN substrates with high thermal conductivity prepared by AMB are considered suitable since thick ceramics can be

applied due to their favorable insulation characteristics, such as their high breakdown voltage and high partial discharge voltage.

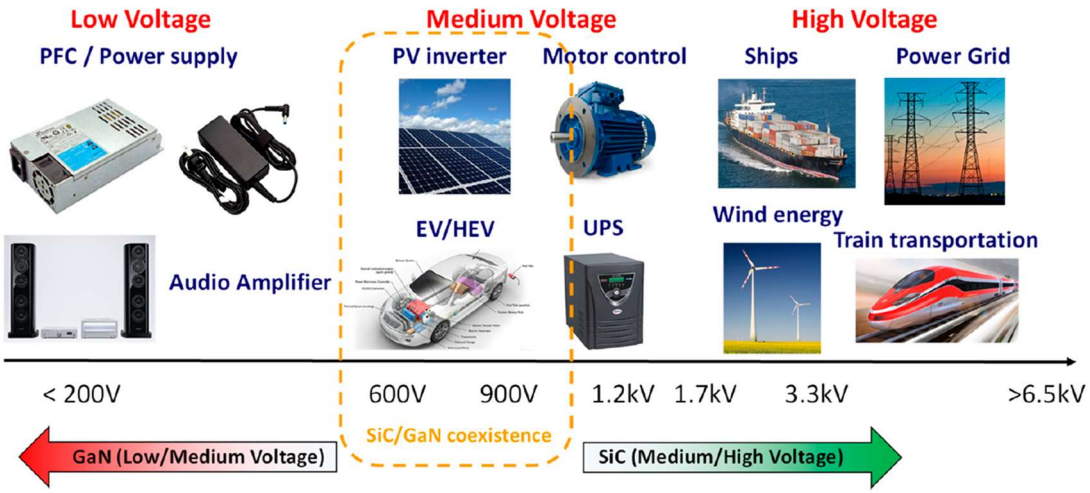


**Fig. 1.10 Power module applications as a function of operating voltage [40], © 2019 by authors, reproduced with license.**

### 1.4.2 Electrochemical migration

Electromigration (EM) and electrochemical migration (ECM) are known migration phenomena of metallic elements that cause failures in electronic components.

EM is mass transport caused by the gradual movement of ions in conductors such as metal wiring due to momentum transfer between conducting electrons and diffusing metal atoms. The vacancies and deposits created in the conductor by this movement of ions grow, eventually leading to a disconnection and a short circuit between adjacent conductors, respectively. The driving force of EM, $F_{\mathrm{EM}}$ is expressed as the product of the elementary charge, $e$, the effective charge number, $Z^*$ and the external electric field, $E$, as shown in Equation (1.3) [53].

$$F_{EM} = eZ^*E \tag{1.3}$$

The $Z^*$ of Al and Cu is about -1, while that of Sn is about -50 [54]. Since EM is more likely to occur with a larger absolute value of $Z^*$, Sn, the main component of solder, has lower EM resistance than Al and Cu.

ECM is the dissolution and movement of metal ions with chemical reactions in the presence of a potential, which results in the growth of a dendritic structure between the anode and cathode. This process significantly reduces the insulation between the electrodes, eventually leading to a short circuit. Among metals such as Ag, Cu, Sn, Pb, Ni, and Au that are commonly used in power modules, Ag is known to be the most susceptible to ECM [55, 56]. As shown in Fig.11, since the Ag in the Ag–Cu alloy layer is exposed against the inter-pattern at the edge of the Cu/AlN interface of the AMB substrate, there are a large number of Ag-ECM starting points on the AMB substrate.

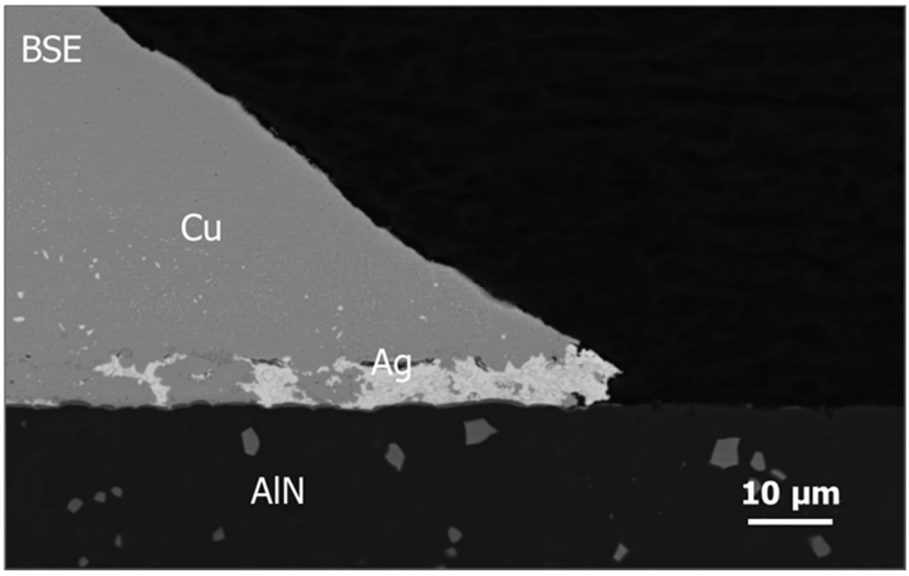


**Fig. 1.11 Cross-sectional BSE image of the edge of the Cu/AlN interface of an AMB substrate.**

Therefore, long-term use of AMB substrates with Ag at the Cu/ceramic bonding interface in high-voltage applications poses a potential risk of interelectrode breakdown due to Ag-ECM.

The following reaction mechanism for Ag-ECM has been proposed [57]. Ag dissolves at the anode and the electrolysis of water occurs at the cathode, as shown in Equations (1.4) and (1.5).

$$\text{Anode: } \mathrm{Ag} \rightarrow \mathrm{Ag^+} + e^- \tag{1.4}$$

$$\text{Cathode: } 2\mathrm{H_2O} + 2e^- \rightarrow \mathrm{H_2} + 2\mathrm{OH^-} \tag{1.5}$$

$\mathrm{Ag^+}$ dissolved at the anode and $\mathrm{OH^-}$ generated at the cathode move to the cathode while maintaining the equilibrium reaction shown in Equation (1.6). Since $\mathrm{AgOH}$ is thermally unstable, it quickly decomposes to $\mathrm{Ag_2O}$, which is dispersed as a colloid.

$$2\mathrm{Ag^+} + 2\mathrm{OH^-} \leftrightharpoons 2\mathrm{AgOH} \leftrightharpoons 2\mathrm{Ag_2O} + \mathrm{H_2O} \tag{1.6}$$

At the cathode, reduction of $\mathrm{Ag^+}$ occurs as shown in Equation (1.7) instead of water electrolysis, and $\mathrm{Ag}$ precipitates in a dendritic pattern.

$$\mathrm{Ag^+} + e^- \rightarrow \mathrm{Ag}\,(\downarrow) \tag{1.7}$$

These reactions are based on electrochemical redox reactions at each electrode, but the order of the ECM frequency is not consistent with the electrochemical series [58–60]. In addition to the electrochemical properties of the metal, the ECM frequency must take into

account the effects of reaction rate and pH on the electrode reactions [61]. This means that it is difficult to express the ECM frequency in terms of a single, well-defined indicator.

In general, several factors affect ECM, including temperature, relative humidity, and voltage bias. Lall et al. [62] and DiGiacomo [63] reported that dendritic propagation rates tend to increase as a function of temperature. Temperature is related to the ECM via chemical reaction rates given by the Arrhenius equation. Water vapor adhered to the substrate surface by hydrogen bonding can provide the electrolyte needed for the occurrence of ECM [64]. When the relative humidity is sufficiently high, water adsorbed on the substrate surface can reach a critical moisture level on the surface necessary for ECM. Zamanzadeh et al. [65] reported that the thickness of this critical moisture level is about 20 water monolayers. The higher the relative humidity, the faster the onset of ECM, and the dendrite growth can be seen in seconds in the water drop test. A voltage bias must be present for ECM to occur. The electric field created by voltage bias promotes the movement of positive ions along the field lines from the anode to the cathode via the ion transport path provided by the aqueous medium [66]. Zou et al. [67] reported that the probability of dendrite formation increases as the voltage gradient increases. Therefore, when power modules using AMB substrates with SiC, which can operate at high temperatures, are used at high voltage, the risk of dielectric breakdown due to ECM is very high.

## 1.5 Objective of this study

The objective of this study is to clarify the design guidelines for Cu/AlN bonding interfacial structures using Ag-free bonding materials based on the AMB method. The ultimate goal is to develop a Cu/AlN bonding technique using Ag-free bonding material

that is advantageous for high-voltage applications based on the design guidelines, and to obtain a Cu/AlN bonding interfacial structure with high reliability and high ECM resistance. In this study, the bonding mechanism of the AMB method with Ag and the general structure of the bonding interface between Cu and ceramics are examined. In addition, the Cu/AlN interfacial structures and their mechanical properties are systematically investigated using two types of Ag-free bonding materials, namely, Cu–Mg–Ti-based and Cu–P–Sn–Ti-based systems. This study is expected to provide a basis for designing interfacial structures for the development of highly reliable Cu/ceramic bonding technology using Ag-free bonding materials.

## 1.6 Scope of this study

This dissertation consists of six chapters, as outlined below (Fig. 1.12).

Chapter 1 presents the manufacturing methods and bonding interfacial structures of DBA, DBC, and AMB insulating substrates used in power modules. Of these substrates, the effect of Ag and Ti amounts on the Cu/AlN bonding interfacial structure of AMB substrates used for high-voltage applications and the potential risk of dielectric breakdown due to Ag-ECM are described. In addition, the objective of this dissertation and the outlines of the chapters are described.

To clarify the growth mechanism of TiN layer necessary to form a good Cu/AlN bonding interface by the AMB method, Chapter 2 describes microstructural observations focusing on the metallic grain boundary phase of TiN layer formed by heat treatment at 850 °C of single-crystal AlN substrates printed with Ag–Cu–$TiH_2$, Ag–$TiH_2$, and Cu–$TiH_2$ paste as metal layers.

In Chapter 3, detailed observations of the interfacial structures of Ag–Cu-brazed Cu on

TiN solid-phase sintered ceramic without metal grain boundary phase/TiN–Fe–Ni–C–$Mo_2C$ liquid-phase sintered ceramic at 850 °C in order to clarify the effects of the TiN particle formation process and metal grain boundary phase components on the formation of the metal/TiN particle bonding interface. In addition, in order to clarify the general structure of the metal/ceramic bonding interface, the above interfacial structures were compared with the interfacial structure of Ag–Cu-brazed Cu on WC–Co cemented carbide under the same conditions.

In Chapter 4, the aim is to clarify a Cu/AlN bonding interfacial structure using Ag-free bonding materials. Thus, Cu/AlN bonding interfacial structures were examined after bonding Cu with Mg–Ti co-deposited film on a polycrystalline AlN substrate between 800 °C and 950 °C. In addition, the peel strength of the Cu/AlN bonding interface was evaluated using the surface and interfacial cutting analysis system, which can characterize properties at specific depths. The results were compared with those for the Cu/AlN bonding interfacial structure. Furthermore, to clarify the effect of Fe addition on the Cu/AlN bonding interface based on the results in Chapter 3, the same evaluation was performed using Cu with Mg–Ti–Fe co-deposited films.

In Chapter 5, in order to clarify the effect of the Ag-free bonding material components on the Cu/AlN bonding interface, the Cu/AlN interfacial structures were examined by bonding Cu onto single-crystal AlN and polycrystalline AlN substrates between 800 °C and 950 °C using a commercial Cu–P–Sn–Ni brazing foil, which had a liquidus temperature close to the melting point of Mg as used in Chapter 4, and Ti layers. In addition, the relative strength was evaluated from the fracture probability of the Cu/AlN bonding interface by welding a Cu terminal to the Cu layer by ultrasonic welding, which applies high stress to the Cu/AlN bonding interface. The practicality of this is also

discussed. Furthermore, the ECM resistance of Cu–P-based AMB substrates was evaluated by the water drop test and compared with that of AMB substrates.

Chapter 6 concludes by summarizing the achievements of this study and results of each chapter in this dissertation.

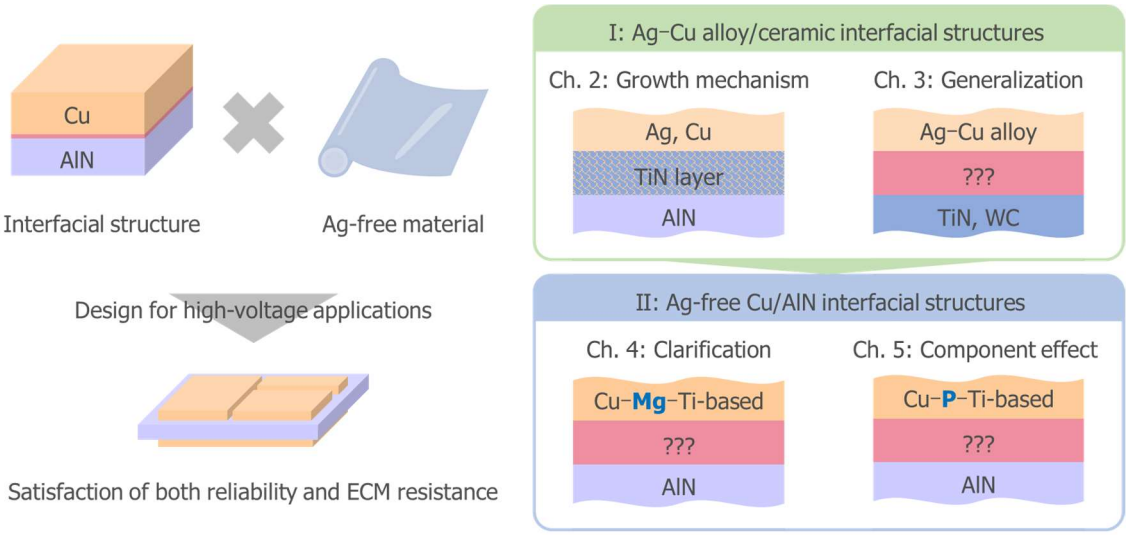


**Fig.1.12 Outline of the present dissertation.**

## References

[1] J. Rogelj, M. den Elzen, N. Höhne, T. Fransen, H. Fekete, H. Winkler, R. Schaeffer, F. Sha, K. Riahi, M. Meinshausen, Paris Agreement climate proposals need a boost to keep warming well below 2 °C, Nature, 534, 2016, 631–639.

[2] C.-F. Schleussner, T.K. Lissner, E.M. Fischer, J. Wohland, M. Perrette, A. Golly, J. Rogelj, K. Childers, J. Schewe, K. Frieler, M. Mengel, W. Hare, M. Schaeffer, Differential climate impacts for policy-relevant limits to global warming: the case of 1.5 °C and 2 °C, Earth System Dynamics, 7, 2016, 327–351.

[3] J. Rogelj, A. Popp, K.V. Calvin, G. Luderer, J. Emmerling, D. Gernaat, S. Fujimori, J. Strefler, T. Hasegawa, G. Marangoni, V. Krey, E. Kriegler, K. Riahi, D.P. van Vuuren, J. Doelman, L. Drouet, J. Edmonds, O. Fricko, M. Harmsen, P. Havlík, F. Humpenöder, E. Stehfest, M. Tavoni, Scenarios towards limiting global mean temperature increase below 1.5 °C, Nature Climate Change, 8, 2018, 325–332.

[4] M. Toriumi, H. Tanaka, H. Yoshida, The development of Al circuit substrate for power module, Proceedings of the IMC 1994, 1994, 104–109.

[5] C.-K. Kim, V.K. Sood, G.-S. Jang, S.-J. Lim, S.-J. Lee, HVDC Transmission: Power Conversion Applications in Power Systems, John Wiley & Sons Ltd., New York, 2009.

[6] M. Furuhashi, S. Tomohisa, T. Kuroiwa, S. Yamakawa, Practical applications of SiC–MOSFETs and further developments, Semiconductor Science and Technology, 31(3), 2016, 034003.

[7] L. Stevanovic, B. Rowden, M. Harfman-Todorovic, P. Losee, A. Bolotnikov, S. Kennerly, T. Schuetz, F. Carastro, R. Datta, F. Tao, R. Raju, P. Cioffi, High performance SiC MOSFET module for industrial applications, Proceedings of the

28th International Symposium on Power Semiconductor Devices and ICs, 2016, 479–482.

[8] M. Piton, B. Chauchat, J.F. Servière, Implementation of direct chip junction temperature measurement in high power IGBT module in operation - railway traction converter, Microelectronics Reliability, 88–90, 2018, 1305–1310.

[9] X.S. Ning, Y. Ogawa, K. Suganuma., Interface of aluminum/ceramic power substrates manufactured by casting-bonding process, Materials Research Society Symposium Proceedings, 445, 1996, 101–106.

[10] Y. Kuromitsu, Y. Nagatomo, H. Tonomura, K. Akiyama, C.M. Montesa, N. Shibata, Y. Ikuhara, Direct bonded aluminum on aluminum nitride substrates via a transient liquid phase and its application, Proceedings of 6th International Conference on Integrated Power Electronics Systems, 2010, 357–361.

[11] Y. Kuromitsu, Y. Nagatomo, K. Akiyama, N. Shibata, Y. Ikuhara, Direct-bonded aluminum on aluminum nitride substrates by transient liquid phase bonding, Journal of the Ceramic Society of Japan, 125(3), 2017, 165–167.

[12] J.F. Burgess, C.A. Neugebauer, G. Flanagan, R.E. Moore, The direct bonding of metals to ceramics and application in electronics, Electrocomponent Science and Technology, 2, 1976, 233–240.

[13] J. Schulz-Harder, Advantages and new development of direct bonded copper substrates, Microelectronics Reliability, 43(3), 2003, 359–365.

[14] H. Ning, J. Ma, F. Huang, Y. Wang, Q. Li, X. Li, Peroxidation of the Cu layer in direct bonding technology, Applied Surface Science, 211, 2003, 250–258.

[15] N.Yu. Taranets, H. Jones, Wettability of aluminum nitride based ceramics of different porosity by two active silver based brazing alloys, Materials Science and Engineering

A, 379, 2004, 251–257.

[16] N. Terasaki, T. Ohashi, Y. Nagatomo, Y. Kuromitsu, A.A. Shirzadi, A new method for liquid-phase bonding of copper plates to aluminum nitride (AlN) substrates used in high-power modules, Journal of Materials Science: Materials in Electronics, 30, 2019, 6552–6555.

[17] Y. Zhang, J. Zhang, J. Chen, Effect of interfacial microstructure evolution on the peeling strength and fracture of AMB Cu-metalized AlN substrate, Journal of the American Ceramic Society, 105, 2021, 577–589.

[18] Y. Nagatomo, T. Nagase, S. Shimamura, FEM analysis of thermal cycle properties of the substrates for power modules, Journal of Japan Institute of Electronics Packaging, 3(4), 2000, 330–334.

[19] N. Terasaki, K. Akiyama, Y. Nagatomo, Y. Kuromitsu. A. Kumamoto, N. Shibata, Y. Ikuhara, Interface analysis of aluminum and aluminum nitride bonding and its application, Fine Ceramic Report, 35(3), 2017, 121–123.

[20] A. Kumamoto, N. Shibata, K. Nayuki, T. Tohei, N. Terasaki, Y. Nagatomo, T. Nagase, K. Akiyama, Y. Kuromitsu, Y. Ikuhara, Atomic structures of a liquid-phase bonded metal/nitride heterointerface, Scientific Reports, 6, 2016, 22936.

[21] R.N. Lumley, T.B. Sercombe, G.B. Schaffer, Surface oxide and the role of magnesium during the sintering of aluminum, Metallurgical and Materials Transactions A, 30, 1999, 457–463.

[22] M.W. Chase, JANAF thermochemical tables, 3rd ed., the American Chemical Society, and the American Institute of Physics for the National Bureau of Standards, 1986.

[23] R. Klein, M.D. Brut, P. Ginet, A. Bellosi, J.Desmaison, Wettability of silicon nitride

ceramic composites by silver, copper and silver copper titanium alloys, Journal of the European Ceramic Society, 25(10), 2005, 1757–1763.

[24] X. Song, Y. Zhao, S. Hu, J. Cao, W. Fu, J. Feng, Wetting of AgCu–Ti filler on porous $Si_3N_4$ ceramic and brazing of the ceramic to TiAl alloy, Ceramics International, 44(5), 2018, 4622–4629.

[25] J. Yang, J. Huang, Z. Ye, S. Chen, R. Ji, Y. Zhao, Influence of interfacial reaction on reactive wettability of molten Ag–Cu–X wt.%Ti filler metal on SiC ceramic substrate and mechanism analysis, Applied Surface Science, 436, 2018, 768–778.

[26] H. Okamura, H. Shinohara, T. Funamoto, T. Shida, Bonding mechanism and microstructure of bonded zone of AlN ceramics with Ti-AgCu brazing metal, Quarterly Journal of the Japan Welding Society, 9(4), 1991, 494–501.

[27] Y. Nakao, K. Nishimoto, K. Saida, K. Murabe, Y. Fukaya, Microstructure of bonding layer in aluminum nitride to metals joints bonded by active brazing method, Quarterly Journal of the Japan Welding Society, 12(1), 1994, 115–121.

[28] D. Huh, D.-H. Kim, Joining of AlN to Cu using In-base active brazing fillers, Journal of Materials Research, 12(4), 1997, 1048–1055.

[29] O. Saitoh, A. Suzumura, H. Ogawa, The corrosion phenomena of ruby by active metal brazing filler (Ag–Cu–Ti) at the brazing interface, Quarterly Journal of the Japan Welding Society, 14(4), 1996, 717–722.

[30] S. Mandal, A.K. Ray, A.K. Ray, Correlation between the mechanical properties and the microstructural behaviour of $Al_2O_3$–(Ag–Cu–Ti) brazed joints, Materials Science and Engineering: A, 383(2), 2004, 235–244.

[31] M. Ali, K.M. Knowles, P.M. Mallinson, J.A. Fernie, Interfacial reactions between sapphire and Ag–Cu–Ti-based active brazed alloys, Acta Materialia, 103, 2016, 859–

869.

[32] B. Fan, J. Xu, H. Lei, L. Zhao, D. An, Z. Xie, Microstructure and mechanical properties of $Al_2O_3$/Cu joints brazed with Ag–Cu–Ti+Zn composite fillers, Ceramics International, 48(13), 2022, 18551–18557.

[33] S. Kato, T. Yano, T. Iseki, Interfacial structures between Ag-Cu-Ti alloys and sintered SiC with various additives, Journal of the Ceramic Society of Japan, 101(3), 1993, 325–330.

[34] F.-L. Sun, J.-C. Feng, D. Li, Bonding of CVD diamond thick films using an Ag-Cu-Ti brazing alloy, Journal of Materials Processing Technology, 115(3), 2001, 333–337.

[35] Y. Liu, Z.R. Huang, X.J. Liu, Joining of sintered silicon carbide using ternary Ag–Cu–Ti active brazing alloy, Ceramics International, 35(8), 2009, 3479–3484.

[36] M.C. Halbig, B.P. Coddington, R. Asthana, M. Singh, Characterization of silicon carbide joints fabricated using SiC particulate-reinforced Ag–Cu–Ti alloys, Ceramics International, 39(4), 2013, 4151–4162.

[37] J.Deng, H. Li, M. Deng, X. Xia, J. Liu, S. Fan, L. Zhang, L. Cheng, Brazing of graphite and stainless steel with Ag–Cu–Ti filler: Effects of brazing process parameters on microstructure and mechanical properties, Materials Today Communications, 28, 2021, 102544.

[38] N. Terasaki, Development of a high reliability power-module substrate via new bonding process using Ag free bonding material, Journal of Smart Processing, 7(5), 2018, 172–175.

[39] D. Sivaprahasam, T. Sujitha, U. Gowtham, B. Jayachandran, R. Gopalan, Microstructure and heat transfer characteristics of active brazed ceramic–metal joints, Ceramics International, 47, 2021, 16133–16140.

[40] F. Roccaforte, G. Greco, P. Fiorenza, F. Iucolano, An overview of normally-off GaN-based high electron mobility transistors, Materials, 12, 2019, 1599.

[41] J. Casarin, P. Ladoux, P. Lasserre, 10 kV SiC MOSFETs versus 6.5 kV Si-IGBTs for medium frequency transformer application in railway traction, International Conference on Electrical Systems for Aircraft, Railway, Ship Propulsion and Road Vehicles, 2015, 7101518.

[42] S. Sabri, E.V. Brunt, A. Barkley, B. Hull, M. O'Loughlin, A. Burk, S. Allen, J. Palmour, New generation 6.5 kV SiC power MOSFET, IEEE 5th Workshop on Wide Bandgap Power Devices and Applications, 2017, 246–6250.

[43] K. Kawahara, S. Hino, K. Sadamatsu, Y. Nakao, Y. Yamashiro, Y. Yamamoto, T. Iwamatsu, S. Nakata, S. Tomohisa, S. Yamakawa, 6.5 kV schottky-barrier-diode-embedded SiC-MOSFET for compact full-unipolar module, Proceedings of the International Symposium on Power Semiconductor Devices and ICs, 2017, 41–44.

[44] K. Kawahara, S. Hino, K. Sadamatsu, Y. Nakao, T. Iwamatsu, S. Nakata, S. Tomohisa, S. Yamakawa, Impact of embedding schottky barrier diodes into 3.3 kV and 6.5 kV SiC MOSFETs, Materials Science Forum, 924, 2018, 663–666.

[45] R. Kosugi, S. Ji, K. Mochizuki, K. Adachi, S. Segawa, Y. Kawada, Y. Yonezawa, H. Okumura, Breaking the theoretical limit of 6.5 kV-class 4H-SiC super-junction (SJ) MOSFETs by trench-filling epitaxial growth, Proceedings of the International Symposium on Power Semiconductor Devices and ICs, 2019, 39–42.

[46] T.J. Hammons, G. Palmason, S. Thorhallsson, Geothermal electric power generation in Iceland for the proposed Iceland/United Kingdom HVDC power link, IEEE Transactions on Energy Conversion, 6(2), 1991, 289–296.

[47] L. Bolduc, GIC observations and studies in the hydro-québec power system, Journal

of Atmospheric and Solar-Terrestrial Physics, 64(16), 2002, 1793–1802.

[48] P. Bresesti, W.L. Kling, R.L. Hendriks, R. Vailati, HVDC connection of offshore wind farms to the transmission system, IEEE Transactions on Energy Conversion, 22, 2007, 37–43.

[49] C.-K. Kim, V.K. Sood, G.-S. Jang, S.-J. Lim, S.-J. Lee, HVDC Transmission: Power Conversion Applications in Power Systems, John Wiley & Sons Ltd., New York, 2009.

[50] N. Flourentzou, V.G. Agelidis, G.D. Demetriades, VSC-based HVDC power transmission systems: An overview, IEEE Transactions on Power Electronics, 24(3), 2009, 592–602.

[51] C.M. Franck, HVDC circuit breakers: A review identifying future research needs, IEEE Transactions on Power Delivery, 26(2), 2011, art. 5686894, 998–1007.

[52] J. Echeverria, S. Kouro, M. Pérez, H. Abu-rub, Multi-modular cascaded DC-DC converter for HVDC grid connection of large-scale photovoltaic power systems, Proceedings of the IECON 2013, 39th Annual Conference of the IEEE Industrial Electronics Society, 2013, 6999–7005.

[53] H.B. Huntington, Diffusion in Solids (recent development) edited by A.S. Nowick, J.J. Burton, Academic press, New York, 1975, 303–352.

[54] R.J. Lloyd, K.-N. Tu, J. Jaspal, Handbook of Lead-Free Solder Technology for Microelectronic Assemblies, Marcel Dekker, New York, 2004

[55] G.T. Kohman, H.W. Hermance, G.H. Downes, Silver migration in electrical insulation, Bell System Technical Journal, 34(6), 1955, 1115–1147.

[56] Y.-L. Liu, J.-M. Long, X.-Y. Zhu, W.-J. Liu, Electrochemical migration characteristics of Ag-plated Cu powders in conductive thick film, Advanced

Materials Research, 146–147, 2011, 1070–1074.

[57] H. Okamoto, T. Takenouchi, S. Yoda, K. Shuto, T. Fujishiro, A. Okuno, S. Kijima, S. Takano, Analysis of ion Migration phenomena and investigation of ion migration mechanisms, The papers of technical meeting on dielectrics and electrical insulation, 96, 1996, 91.

[58] G. Milazzo, S. Caroli, V.K. Sharma, Tables of standard electrode potentials, Wiley, Chichester, 1978.

[59] A.J. Bard, R. Parsons, J. Jordan, Standard potentials in aqueous solutions, Marcel Dekker, New York, 1985.

[60] S.G. Bratsch, Standard electrode potentials and temperature coefficients in water at 298.15 K, Journal of Physical and Chemical Reference Data, 18, 1989, 1–21.

[61] T. Tsukui, Y. Yokosuka, Origins of ion migration patterns in printed wiring boards, Circuit technology: the journal of the Japan Institute of Printed Circuit, 9(3), 1994, 190–198.

[62] P. Lall, M. Pecht, E. Hakim, Influence of temperature on microelectronics and system reliability, A Physics of Failure Approach, CRC Press, New York, 1997.

[63] G. DiGiacomo, Metal migration (Ag, Cu, Pb) in encapsulated modules and time to fail model as a function of the environment and package properties, Proceedings of the IRPS, 1982, 27–33.

[64] O. Hallberg, D. Peck, Recent humidity accelerations, a base for testing standards, Quality and Reliability Engineering International, 7(3), 1991, 169–180.

[65] M. Zamanzadeh, S.L. Meilink, G.W. Warren, P. Wynblatt, B. Yan, Electrochemical examination of dendritic growth on electronic devices in HCl electrolytes, Corrosion, 46(8), 1990, 665–671.

[66] B. Rudra, D. Jennings, Electrochemical migration in multichip modules, Circuit World, 22(1), 1995, 67–70.

[67] L. Zou, C. Hunt, The effect of test voltage, test pattern and board finish on surface insulation resistance measurements for various fluxes, NPL Report CMMT(A), 1999, 222.

# Chapter 2: Growth mechanism of TiN reaction layers produced on AlN via AMB

## 2.1 Introduction

As described in Chapter 1, it is important to form a continuous defect-free TiN layer to obtain a good Cu/AlN bonding interface by the AMB method. Although Ag- and Cu-containing precipitates have been detected in the TiN layer, their effects on the TiN layer formation process have not been clarified. In addition, the detailed state of the bonding interface between the Ag–Cu alloy layer and the TiN layer has not been reported.

In this chapter, the microstructure of the TiN layer is investigated in detail to clarify the mechanism of TiN layer formation with contributions from Ag and Cu and to examine the interfacial structure of the Ag–Cu alloy layer/TiN layer [1].

## 2.2 Experimental procedure

### 2.2.1 Materials and sample fabrication

Powders of Ag ($D_{10}$ = 1.2 μm, $D_{50}$ = 1.6 μm, and $D_{90}$ = 2.8 μm), Cu ($D_{10}$ = 0.6 μm, $D_{50}$ = 0.8 μm, and $D_{90}$ = 1.1 μm), and $TiH_2$ ($D_{10}$ = 2.1 μm, $D_{50}$ = 5.2 μm, and $D_{90}$ = 10.7 μm) were added to an organic medium containing α-terpineol (96%), 2,2,4-trimethyl-1,3-pentanediol (98.5%), and polymethyl methacrylate and mixed using a mechanical mixer (ARE-250, THINKY) to produce a proprietary metal paste. Here, $D_{10}$, $D_{50}$, and $D_{90}$ correspond to the 10th, 50th, and 90th percentiles of particle size by volume, respectively. These metal powders had a purity of >99.0 wt%, with the balance being mostly C and O.

Concentrations of impurities related to the present work in these metal powders as determined by glow discharge mass spectrometry are shown in Table 2.1. The concentrations of Cu and Al in Ag powder were both 0.3 ppmw and those of Ag and Al in Cu powder were 9.8 ppmw and below the limit of detection (<0.01 ppmw), respectively. Compared with the Ag and Cu powders, the impurity concentrations were higher in the $TiH_2$ powder, with Ag, Cu, and Al concentrations of 61, 39, and 60 ppmw, respectively. $TiH_2$, which was available as a powder with a smaller particle size than Ti, was useful for improving the uniformity of the metal pastes.

**Table 2.1 Concentrations of impurities related to the present work (Ag, Cu, and $TiH_2$) powders as determined by glow discharge mass spectrometry. Dash (-): below the limit of detection [1], © 2022 by Springer Science Business Media, reproduced with license.**

| Powder | Concentration (ppmw) | | | |
|---|---|---|---|---|
| | Ag | Cu | Ti | Al |
| Ag | - | 0.3 | < 0.01 | 0.3 |
| Cu | 9.8 | - | < 0.01 | < 0.01 |
| $TiH_2$ | 6.1 | 39 | - | 60 |

Ag–26.4 wt% Cu–4.4 wt% $TiH_2$, Ag–6.0 wt% $TiH_2$, and Cu–14.3 wt% $TiH_2$ pastes were applied onto a commercially available $Al_2O_3$ sapphire $(0001)$ substrate (ø50.8 mm × 430 μm) on which a 1-μm-thick single-crystal epitaxial AlN film had been deposited as the AlN substrate (DOWA Electronics Materials Co., Ltd) using a screen-printing machine. The orientation relationship between the AlN film and the $Al_2O_3$ substrate was $(0001)$ AlN//$(0001)$ $Al_2O_3$, $[11\bar{2}0]$ AlN//$[1\bar{1}00]$ $Al_2O_3$, as observed in other studies [2, 3].

A cross-sectional bright-field (BF) transmission electron microscopy (TEM) image of the AlN/$Al_2O_3$ interface observed along the $[11\bar{2}0]$ AlN zone axis is shown in Fig. 2.1, together with electron diffraction patterns from the AlN and $Al_2O_3$. Strain contrast due to a large lattice mismatch between AlN and $Al_2O_3$ (11.6%) was observed around the AlN/$Al_2O_3$ interface. In addition, contrast due to the grain boundaries of the AlN film was observed along the direction perpendicular to the AlN/$Al_2O_3$ interface. Thus, columnar crystals of AlN with a grain size of up to 400 nm grew in the AlN film. These AlN columnar crystals were much smaller than the grain size of the polycrystalline AlN substrates examined by Zhang et al. [4]. It is reasonable to assume that the interfacial

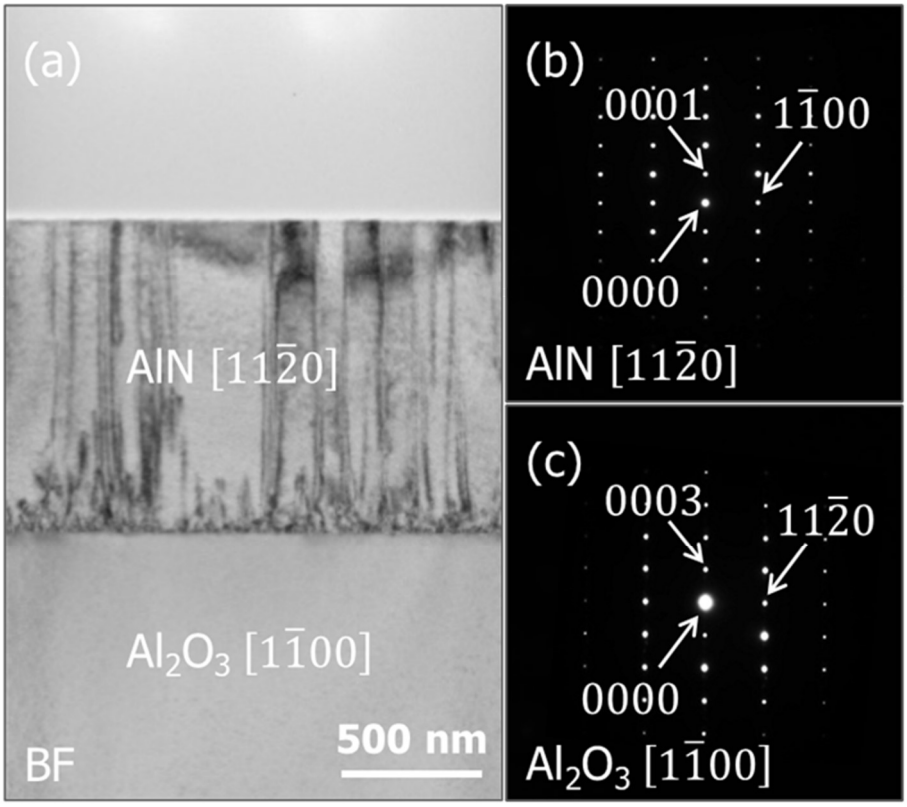


**Fig. 2.1 (a) A cross-sectional BF-TEM image of the AlN/$Al_2O_3$ interface observed along the $[11\bar{2}0]$ AlN zone axis, as shown in (b) in the SAED pattern. (c) Election diffraction pattern with the incident electron beam parallel to $[11\bar{2}0]$ AlN//$[1\bar{1}00]$ $Al_2O_3$ [1], © 2022 by Springer Science Business Media, reproduced with license.**

reaction between each paste and AlN was the same as that when using Ti. This is because the dehydrogenation of $TiH_2$ is completed at a heating temperature far below the Ag–Cu eutectic temperature (780 °C) [5, 6]. The amounts of Ag, Cu, and $TiH_2$ were about 6.3, 2.4, and 0.4 mg/cm$^2$, respectively. With these amounts of Ag and $TiH_2$, a continuous TiN layer was expected to form at the metal/AlN interface [5]. Furthermore, the ratio of Ag to Cu is near that at the eutectic composition [7]. After drying the samples at 150 °C for 10 min in air, each sample was placed inside a vacuum furnace and brazed (sintered) at 850 °C for 0.5 h, with heating and cooling rates of 10 °C/min.

### 2.2.2 Characterization

Cross-sections of these samples were observed using SEM before more detailed observations were undertaken by scanning transmission electron microscopy (STEM). Samples were mounted in an acrylic polymer at room temperature and polished using standard metallographic techniques and an argon-based ion beam polisher (ArBlade 5000, Hitachi High-Tech). The microstructures of all samples were analyzed using SEM (GeminiSEM 500, Carl Zeiss AG), which were operated at 1.8 kV.

Thin sections of the metal/AlN interface for STEM analysis were prepared using a focused ion beam (FIB) system (Scios, Thermo Fisher Scientific). These sections were reduced to a thickness between 30 and 100 nm with the FIB. Elemental analysis of the thin sections was performed using a Titan G2 ChemiSTEM equipped with an energy-dispersive X-ray spectroscopy (EDS) system (NSS7, Thermo Fisher Scientific) while tilted at $\pm 70°$ and a Talos F200X (Thermo Fisher Scientific) equipped with an EDS system (Super-X, Bruker), with an operating voltage of 200 kV for both systems.

## 2.3 Results and discussion

### 2.3.1 Formation of the TiN layer during the brazing reaction

A secondary electron (SE) image of the Ag–Cu–$TiH_2$/AlN interface after brazing at 850 °C for 0.5 h is shown in Fig. 2.2. This brazing temperature was above the liquidus temperature of the Ag–Cu–$TiH_2$ system used in this study (≈ 837 °C). Thus, the metal layer should be completely melted at the brazing temperature. The broken line in the figure corresponds to the position of the interface between AlN and $Al_2O_3$. Cu–Ti intermetallic compounds (IMCs) such as $Cu_2Ti$ (tetragonal, *Cmcm*, $a$ = 7.988 Å, $b$ = 4.458 Å, $c$ = 4.397 Å) and $Cu_4Ti$ (tetragonal, *Pnma*, $a$ = 4.526 Å, $b$ = 4.345 Å, $c$ = 1.292 Å) [8] were widely dispersed in the metal layer. This layer was composed of Ag-rich and Cu-rich phases arising from the melting of the Ag–Cu–$TiH_2$ paste. The TiN (cubic, $Fm\bar{3}m$, $a$

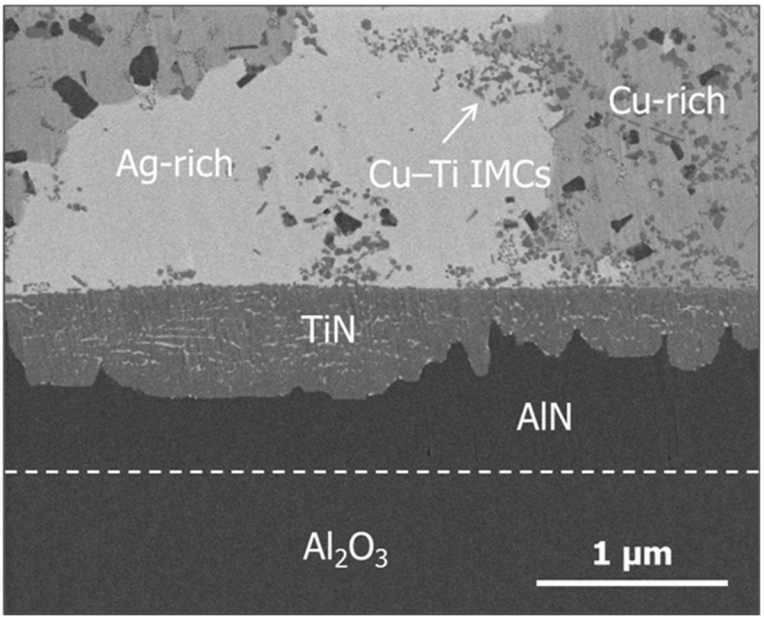


**Fig. 2.2 SE image of chemical reaction products at a Ag–Cu–$TiH_2$/AlN interface after brazing at 850 °C for 0.5 h [1], © 2022 by Springer Science Business Media, reproduced with license.**

= 4.239 Å) [9] reaction layer grew inward from the surface of the AlN toward the $Al_2O_3$ substrate and contained a large number of bright areas measuring <100 nm in size.

A high-angle annular dark-field (HAADF) image of the Ag–Cu–$TiH_2$/AlN interface together with elemental distributions is shown in Fig. 2.3. Bright areas between 40 nm and 200 nm in length that contain small particles are evident inside the TiN layer. These correspond to Ag- and Cu-containing phases. Their presence suggests that, when using AlN as a starting material in the AMB method, the growth process for the TiN layer cannot

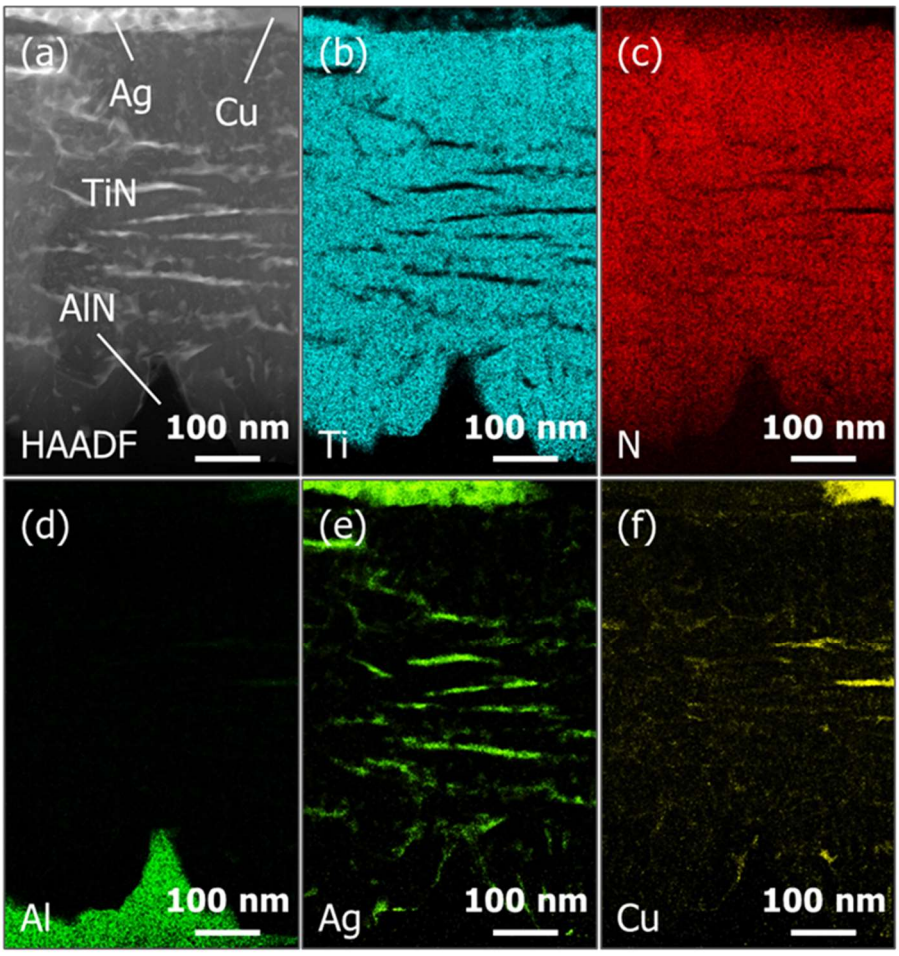


**Fig. 2.3 (a) HAADF image of a Ag–Cu–$TiH_2$/AlN interface after brazing at 850 °C for 0.5 h, together with elemental distributions of (b) Ti, (c) N, (d) Al, (e) Ag, and (f) Cu [1], © 2022 by Springer Science Business Media, reproduced with license.**

be simply described by the following single-substitution reaction:

$$Ti_{diss} + AlN \rightarrow TiN + Al_{diss} \quad (2.1)$$

where AlN and TiN are in the solid state and $Ti_{diss}$ and $Al_{diss}$ are dissolved in the Ag–Cu eutectic liquid phase [10]. This implies that the Ag- and/or Cu-containing liquid phase contributes significantly to the growth of the TiN layer. HAADF images, dark-field (DF) images, and electron diffraction patterns at each position on the Ti-containing metal layer side, at the center, and on the AlN side for the reaction layer at the Ag–Cu–$TiH_2$/AlN interface are shown in Fig. 2.4. These DF images were taken under the beam condition with diffraction vectors (***g***) as shown in Fig. 2.4(d1–6). The HAADF images are grouped into three pairs: a1 and a2, a3 and a4, and a5 and a6. Slight changes in the specimen orientation within each pair of HAADF images changes the electron diffraction patterns, as seen in the three corresponding pairs (d1) and (d2), (d3) and (d4), and (d5) and (d6). Examples of Ag- and Cu-containing areas in the corresponding HAADF images are circled.

These images show that the TiN layer is composed of TiN, Ag (cubic, $Fm\bar{3}m$, $a$ = 4.086 Å), and Cu (cubic, $Fm\bar{3}m$, $a$ = 3.615 Å) at each position. These observations suggest that the Ag–Cu liquid phase was intimately involved in the TiN growth process. Fig. 2.5(a) and (b) were obtained under conditions where the bright line evident in Fig. 2.5(a) was most sharp. Al from the AlN film appears to segregate together with Ag and Cu into the grain boundaries of the TiN layer, as shown by the line scan element analysis in Fig. 2.5(c) along the direction indicated by the arrow in Fig. 2.5(b). The peak concentrations of Ag, Cu, and Al were 1.5, 22.5, and 5.3 at%, respectively. This suggests that these Ag- or Cu-

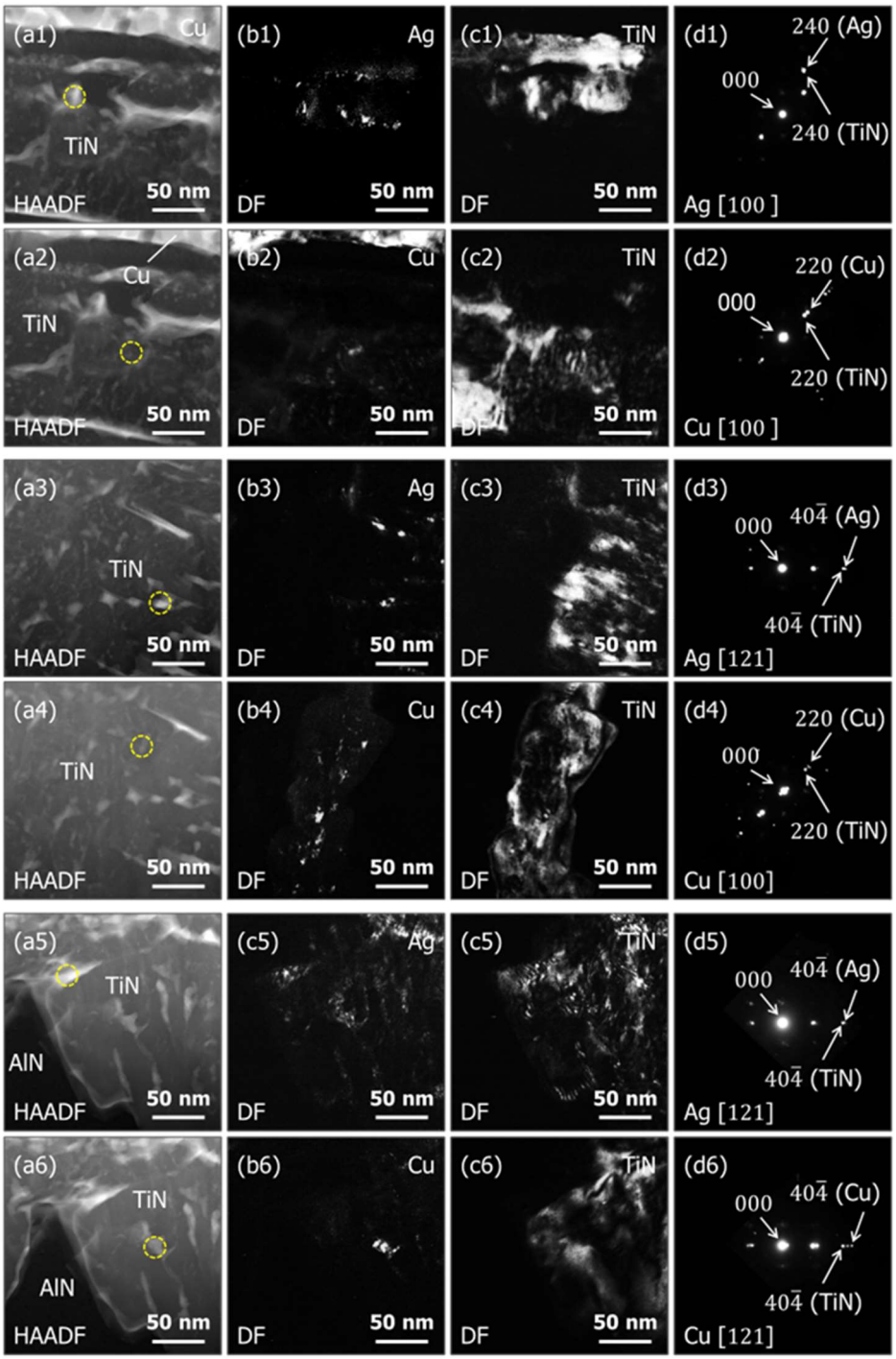


**Fig. 2.4 (a1–6) HAADF images of a Ag–Cu–$TiH_2$/AlN interface after brazing at 850 °C for 0.5 h, (b1, 3, 5) DF images for Ag, (b2, 4, 6) Cu, and (c1–6) TiN using *g* vectors as shown in the (d1–6) electron diffraction patterns. The HAADF images are grouped into three pairs: a1 and a2, a3 and a4, and a5 and a6. Slight changes in the specimen orientation within each pair of HAADF images changes the electron diffraction patterns, as shown in the three pairs d1 and d2, d3 and d4, and d5 and d6. Examples of Ag- and Cu-containing areas in the corresponding HAADF images are circled in yellow [1], © 2022 by Springer Science Business Media, reproduced with license.**

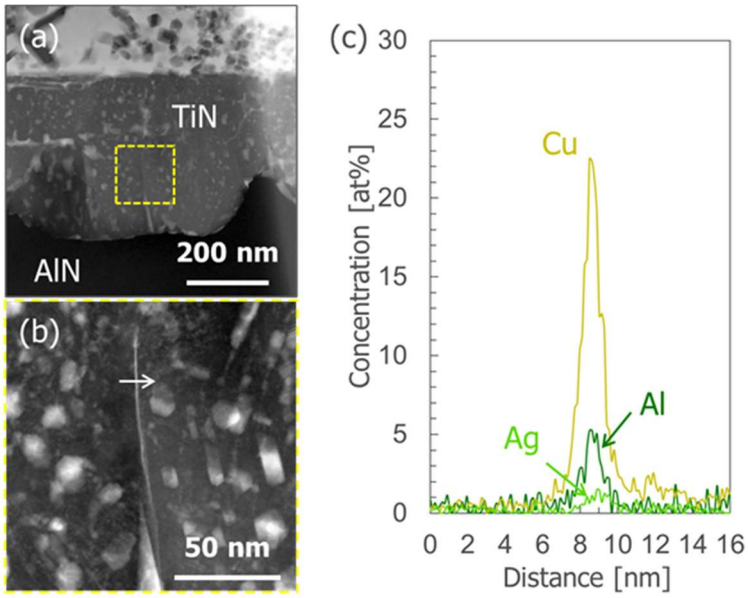


**Fig. 2.5 (a, b) HAADF images of a Ag–Cu–$TiH_2$/AlN interface after brazing at 850 °C for 0.5 h, and (c) EDS analysis along the direction indicated by the arrow in (b) [1], © 2022 by Springer Science Business Media, reproduced with license.**

based spherical metal phases contained Al derived from AlN in the same way as the TiN grain boundary phases. In other words, the spherical metal phases in the TiN layer defined its grain boundaries.

A detailed HAADF image of the TiN layer at the Ag–Cu–$TiH_2$/AlN interface is shown in Fig. 2.6. The TiN layer here was composed of TiN particles of <50 nm in size. Their grain boundaries contained Ag, Cu, and Al as shown by the line scan element analysis in Fig. 2.5(c). Therefore, each TiN grain was surrounded by metal-rich grain boundary phases that contained Ag, Cu, and Al and formed a network structure over the entire TiN layer. In addition, the direction of observation for the TiN layer caused a difference in appearance of the bright areas shown in Fig. 2.5(a) and (b). Thus, a metal-rich grain boundary phase of the TiN layer appeared as a spherical metal phase in the TiN layer when observed from the direction almost parallel to its grain boundary. The spatial distribution of the Cu phase in the TiN layer reconstructed in 3D based on the elemental

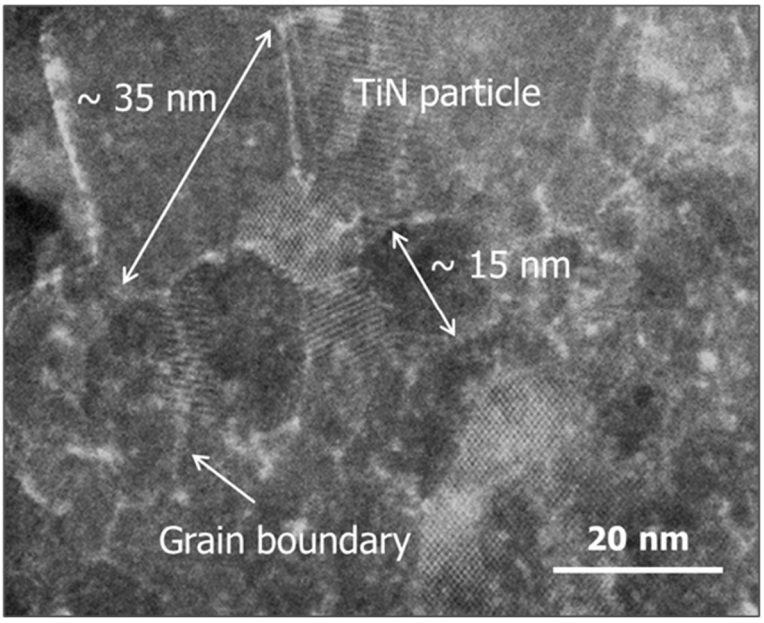


**Fig. 2.6 Detailed HAADF image of the TiN layer of a Ag–Cu–$TiH_2$/AlN interface after brazing at 850 °C for 0.5 h [1], © 2022 by Springer Science Business Media, reproduced with license.**

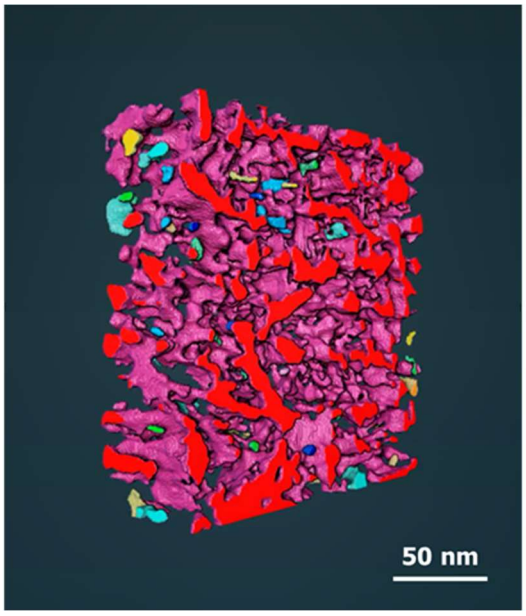


**Fig. 2.7 Spatial distribution of the Cu phase in the TiN layer of a Ag–Cu–$TiH_2$/AlN interface after brazing at 850 °C for 0.5 h.**

distribution image by the electron tomography method [11, 12] is shown in Fig. 2.7. The areas where the Cu phase was continuously present are shown in the same color. It can

be seen that the Cu phase formed a network structure covering the TiN particles, and that of the Cu phase can be linear or spherical, depending on the direction of observation of the TiN layer. This direct observation of the spatial distribution of the Cu phase in the TiN layer supports the differences in the shape distribution of the Cu phase shown in Figs. 2.5 and 2.6.

The HAADF images, elemental distributions, and line EDS profiles of the Ag/TiN particle and Cu/TiN particle interfaces after brazing at 850 °C for 0.5 h are shown in Figs. 2.8 and 2.9, respectively. The line EDS profiles were obtained along the yellow dotted arrows shown in Figs. 2.8(b) and 2.9(b). As shown in Fig. 2.8(d) and (f), an Al- and Cu-containing segregation layer was formed at the Ag/TiN particle interface. In addition, Fig. 2.8(g) shows that the peak position of Al was located at the outermost surface of the TiN particle, while the peak position of Cu was shifted into Ag by approximately 0.3 nm. In Fig. 2.9(d) and (g), on the other hand, not only was an Al-containing segregation layer formed on the outermost surface of the TiN particle, but an Al-depleted layer was also

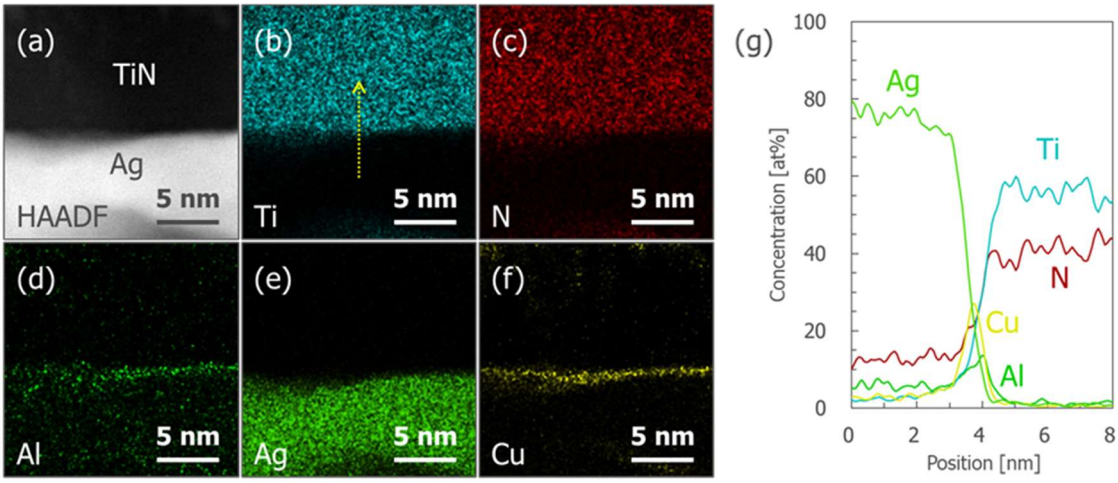


**Fig. 2.8 (a) HAADF images of a Ag/TiN particle interface after brazing at 850 °C for 0.5 h, together with elemental distributions of (b) Ti, (c) N, (d) Al, (e) Ag, and (f) Cu. (g) Line EDS profile obtained along the yellow dotted arrow shown in (b).**

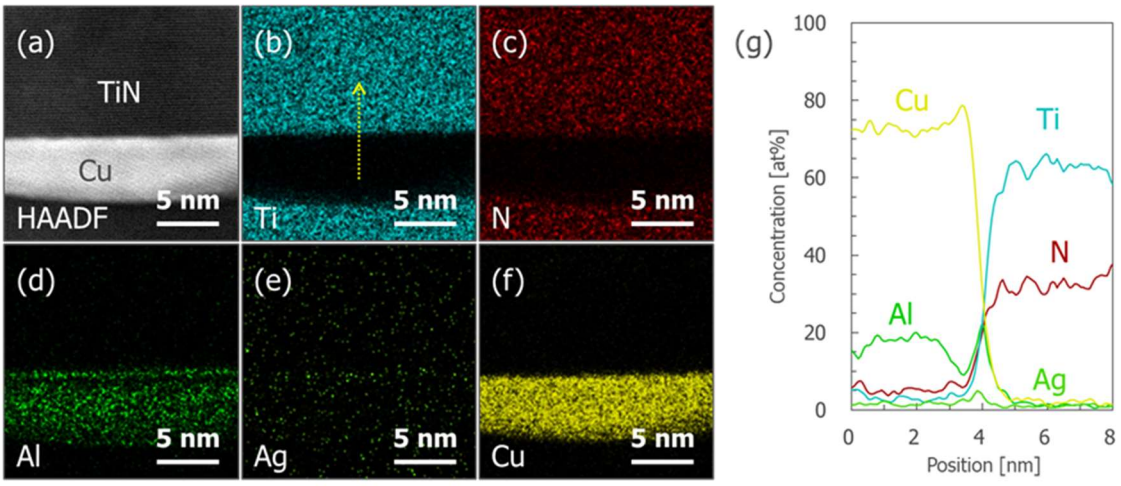


**Fig. 2.9 (a) HAADF images of a Cu/TiN particle interface after brazing at 850 °C for 0.5 h, together with elemental distributions of (b) Ti, (c) N, (d) Al, (e) Ag, and (f) Cu. (g) Line EDS profile obtained along the yellow dotted arrow shown in (b).**

formed on the outermost surface of the TiN particle, but an Al-depleted layer was also formed at the Cu/AlN interface, which was shifted approximately 0.6 nm from the peak position of Al to the Cu side. The presence of the Al-depleted layer indicates the formation of a Cu-containing segregation layer in the Cu layer. Taken together, these results suggest that the Ag–Cu alloy layer/TiN particle interfacial structure was essentially a Cu-containing segregation layer/Al-containing segregation layer/TiN particle structure when Cu was bonded onto AlN by the AMB method using Ag–Cu–Ti bonding material. This means that Ag is basically not required in the AMB method.

### 2.3.2 Formation of the TiN layer during the solid-phase sintering reaction

SE images of the Ag–$TiH_2$/AlN interface and the Cu–$TiH_2$/AlN interface after sintering at 850 °C for 0.5 h are shown in Fig. 2.10(a) and (b), respectively. As in Fig. 2.2, the broken lines in the figure correspond to the positions of the AlN/$Al_2O_3$ interface. In

contrast to the fully densified Ag–Cu eutectic structure, which was assisted by the Ag–Cu liquid phase generation (Fig. 2.2), the Ag-rich and Cu-rich sinters had remaining porosity. In addition, a layer of TiC (cubic, $Fm\bar{3}m$, $a$ = 4.328 Å) [13] and Cu–Ti IMCs is clearly visible in Fig. 2.10(a) and (b), respectively. Notably, the heating temperature (850 °C) used in these sintering experiments was below the melting point of Ag (961.8 °C), Cu (1084.6 °C), Ti (1668 °C), and also below the eutectic temperatures of the Ag–Ti system (960 °C) [14] and the Cu–Ti system (875 °C) [8]. Therefore, this suggests that the porosity in these sinters shown in Fig. 2.10(a) and (b) resulted from insufficient void shrinkage between metal powders during solid-phase sintering.

The surfaces of the Ag powder used in this study (Fig. 2.11) were covered with an organic medium, suggesting that TiC formed by reaction with $TiH_2$ powder in contact with the Ag powder particles during solid-phase sintering. In contrast to the results of solid-state sintering shown in Fig. 2.10(a), the Ag-rich phase densely precipitated

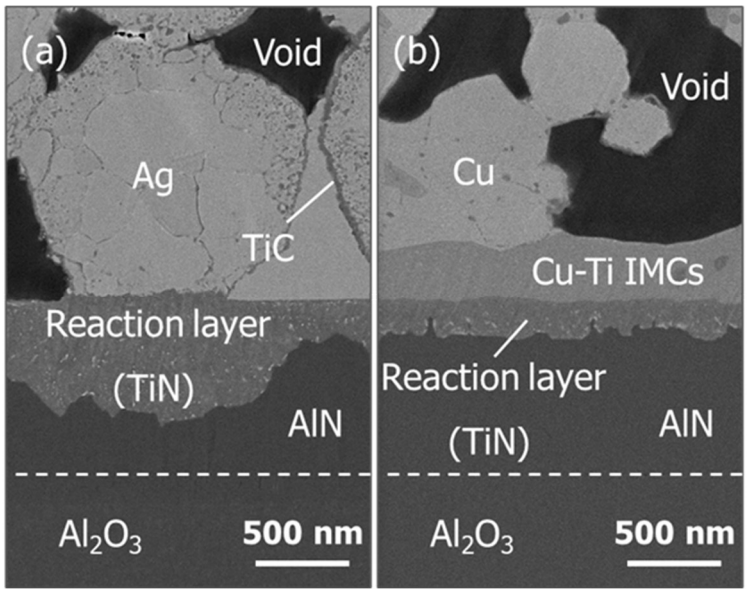


**Fig. 2.10 SE images of chemical reaction products at (a) a Ag–$TiH_2$/AlN interface after sintering at 850 °C for 0.5 h, and (b) a Cu–$TiH_2$/AlN interface after sintering at 850 °C for 0.5 h [1], © 2022 by Springer Science Business Media, reproduced with license.**

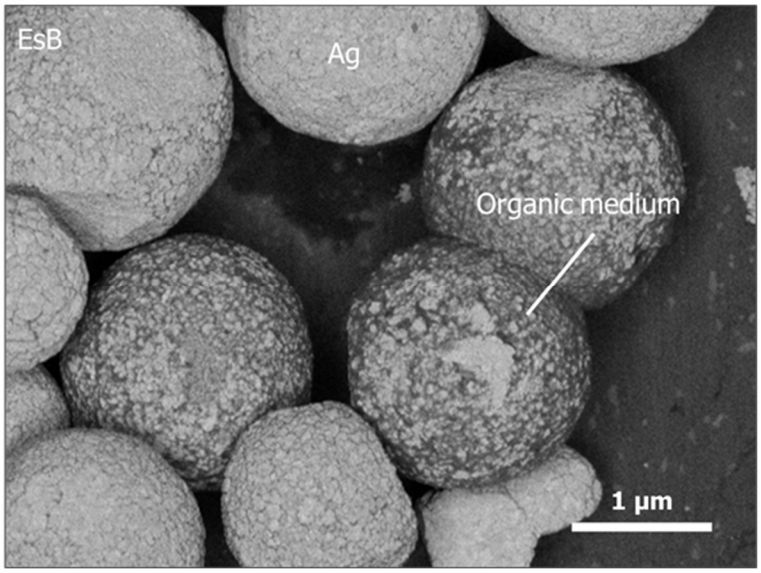


**Fig. 2.11 Surface EsB image of the Ag powder used in this study [1], © 2022 by Springer Science Business Media, reproduced with license.**

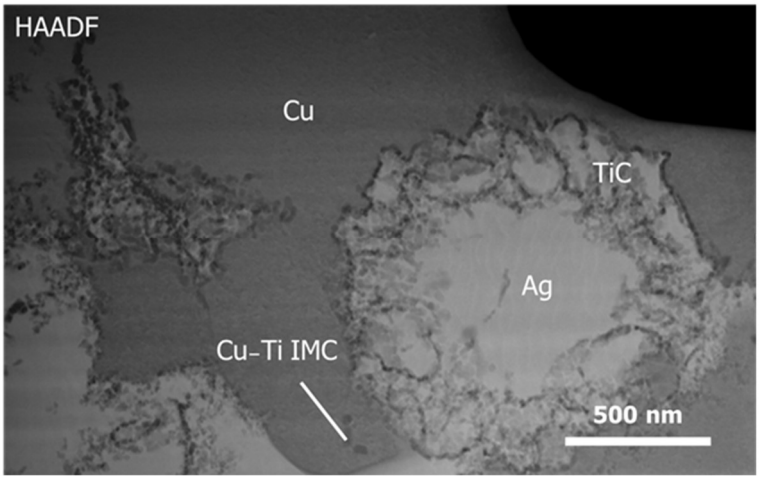


**Fig. 2.12 Cross-sectional HAADF image of a Ag–Cu alloy layer in the Ag–Cu–$TiH_2$ system after brazing at 850 °C for 0.5 h [1], © 2022 by Springer Science Business Media, reproduced with license.**

because TiC particles formed locally at the Ag–Cu–$TiH_2$/AlN interface, where liquid was present during the sintering process, as shown in Figs. 2.12, 2.13, and 2.14. Due to the proximity of the Ag–Mα and C–Kα lines, the apparent C concentration of Ag is high in Fig. 2.14(c). The uneven distribution of TiC particles at the Ag–Cu–$TiH_2$/AlN interface

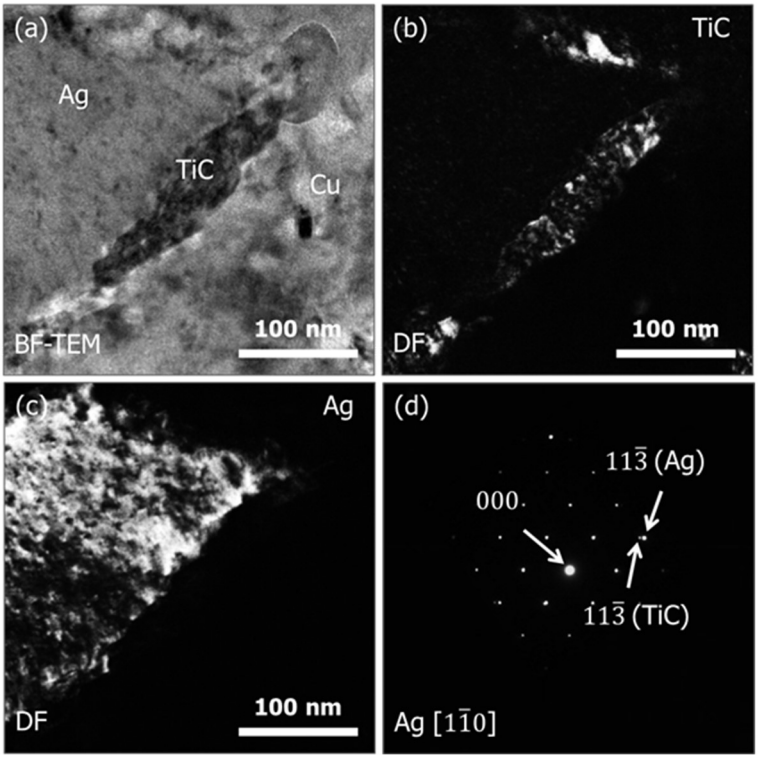


**Fig. 2.13 (a) BF-TEM image of a TiC particle in the Ag–Cu–$TiH_2$ system after brazing at 850 °C for 0.5 h, (b) DF image for TiC, and (c) for Ag using *g* vectors as shown in the electron diffraction pattern shown in (d) from this region [1], © 2022 by Springer Science Business Media, reproduced with license.**

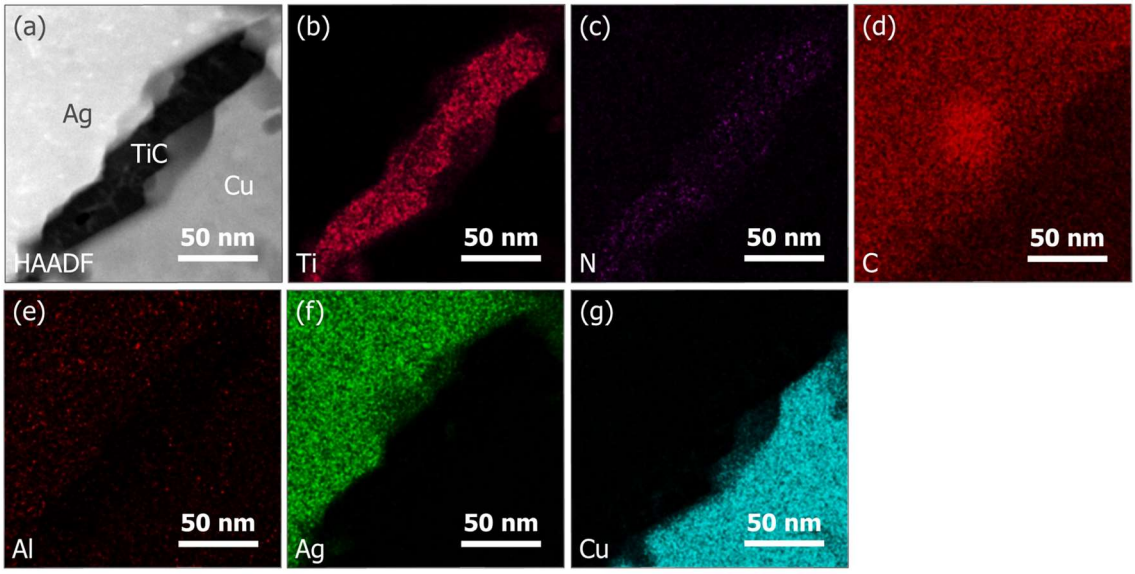


**Fig. 2.14 (a) HAADF image of a TiC particle in the Ag–Cu–$TiH_2$ system after brazing at 850 °C for 0.5 h, together with elemental distributions of (b) Ti, (c) N, (d) C, (e) Al, (f) Ag, and (g) Cu [1], © 2022 by Springer Science Business Media, reproduced with license.**

appears to be caused by the uneven distribution of the organic residue modifying the Ag particles and/or the convection of the Ag–Cu–Ti liquid phase. As in the case of Ag–Cu–$TiH_2$, the reaction layers between *M*–$TiH_2$ (*M* = Ag or Cu) and AlN grew inward from the AlN surface toward the $Al_2O_3$ substrate. These layers contained a large number of bright areas of <100 nm in size, which is similar to the size of Ag and Cu phases observed in the TiN layer in Fig. 2.2.

An HAADF image of the Ag–$TiH_2$/AlN interface together with elemental distributions is shown in Fig. 2.15. The reaction layer was composed of reaction products containing Ti and N, as well as Ag phases corresponding to the bright area observed in Fig. 2.10(a). The size of the Ag phases in the reaction layer was about 10% of the particle size of the Ag powder used in the Ag–$TiH_2$ paste. This implies that the generation of the Ag phase was completely different from the grain growth in the solid sintering process, meaning that a Ag-containing liquid phase was generated during the growth of the TiN layer. HAADF images, DF images, and selected area electron diffraction (SAED) patterns at each position on the Ti-containing metal layer side, at the center, and on the AlN side for the reaction layer at the Ag–$TiH_2$/AlN interface are shown in Fig. 2.16. The reaction layer was composed of TiN and Ag (cubic) at each position according to the SAED patterns shown in Fig. 2.16(d1–3). In addition, the coincidence of the zone axes of TiN and Ag suggests an epitaxial relationship between them, as at the Ag–Cu–$TiH_2$/AlN interface.

An HAADF image of the Cu–$TiH_2$/AlN interface together with elemental distributions is shown in Fig. 2.17. Corresponding to the bright area observed in Fig. 2.10(b), the Cu phases were distributed in the reaction layer, which was mainly composed of reaction products containing Ti and N, as at the Ag–$TiH_2$/AlN interface. The size of the Cu phase in the reaction layer was about 10% of the particle size of the Cu powder used in the Cu–

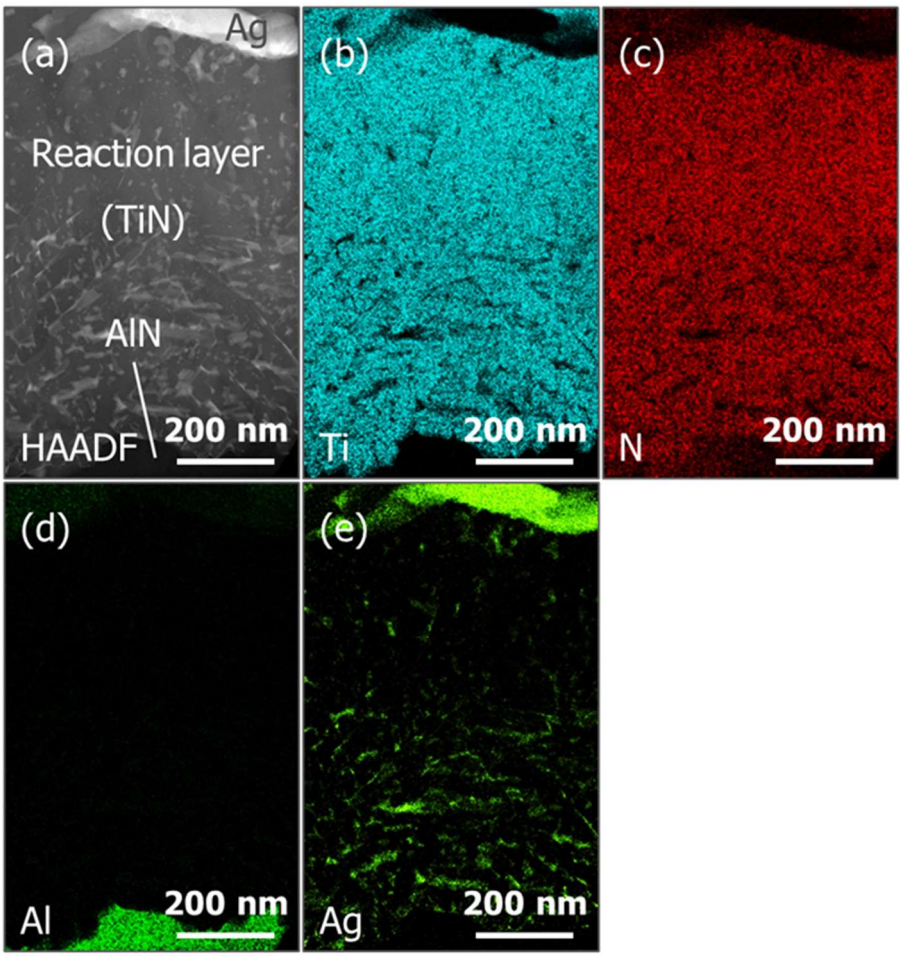


**Fig. 2.15 (a) HAADF image of a Ag–$TiH_2$/AlN interface after sintering at 850 °C for 0.5 h, together with elemental distributions of (b) Ti, (c) N, (d) Al, and (e) Ag [1], © 2022 by Springer Science Business Media, reproduced with license.**

$TiH_2$ paste. This also implies that the Cu phase in the Cu–$TiH_2$/AlN interfacial reaction layer was formed through the same reaction process as the Ag phase in the Ag–$TiH_2$/AlN interfacial reaction layer. HAADF images, DF images, and SAED patterns at each position on the Ti-containing metal layer side, at the center, and on the AlN side for the reaction layer at the Cu–$TiH_2$/AlN interface are shown in Fig. 2.18. Here, the reaction layer was composed of TiN and Cu (cubic) at each position, as evident from the SAED patterns shown in Fig. 2.18(d1–3). In addition, the coincidence of the zone axes of TiN and Cu suggests that there was an epitaxial relationship between them as in the Ag–Cu–

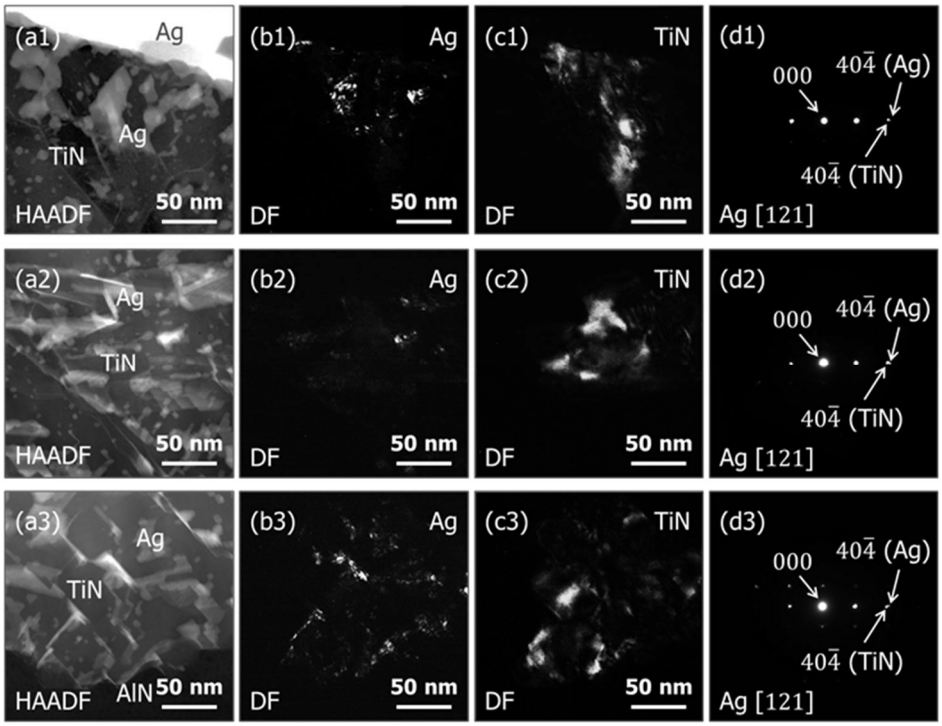


**Fig. 2.16 (a1–3) HAADF images of a Ag–$TiH_2$/AlN interface after sintering at 850 °C for 0.5 h, (b1–3) DF images for Ag, and (c1–3) for TiN using *g* vectors as shown in (d1–3) SAED patterns [1], © 2022 by Springer Science Business Media, reproduced with license.**

$TiH_2$/AlN interface.

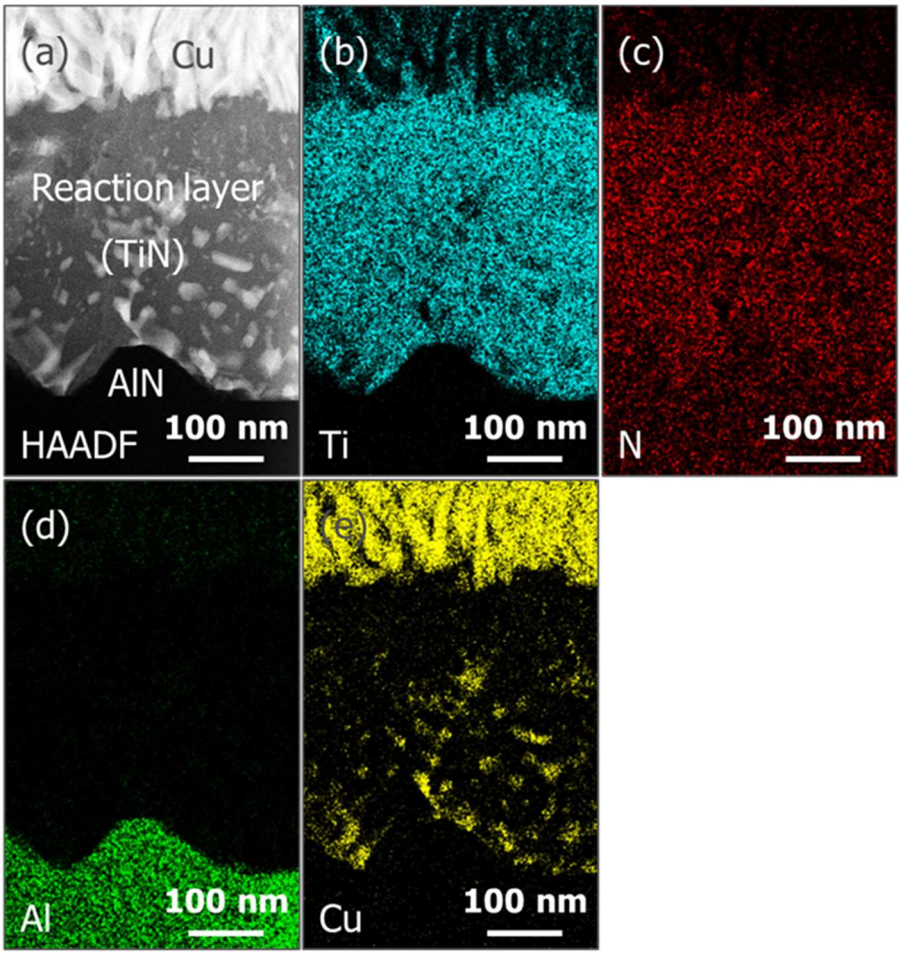


**Fig. 2.17 (a) HAADF image of a Cu–$TiH_2$/AlN interface after sintering at 850 °C for 0.5 h, together with elemental distributions of (b) Ti, (c) N, (d) Al, and (e) Cu [1], © 2022 by Springer Science Business Media, reproduced with license.**

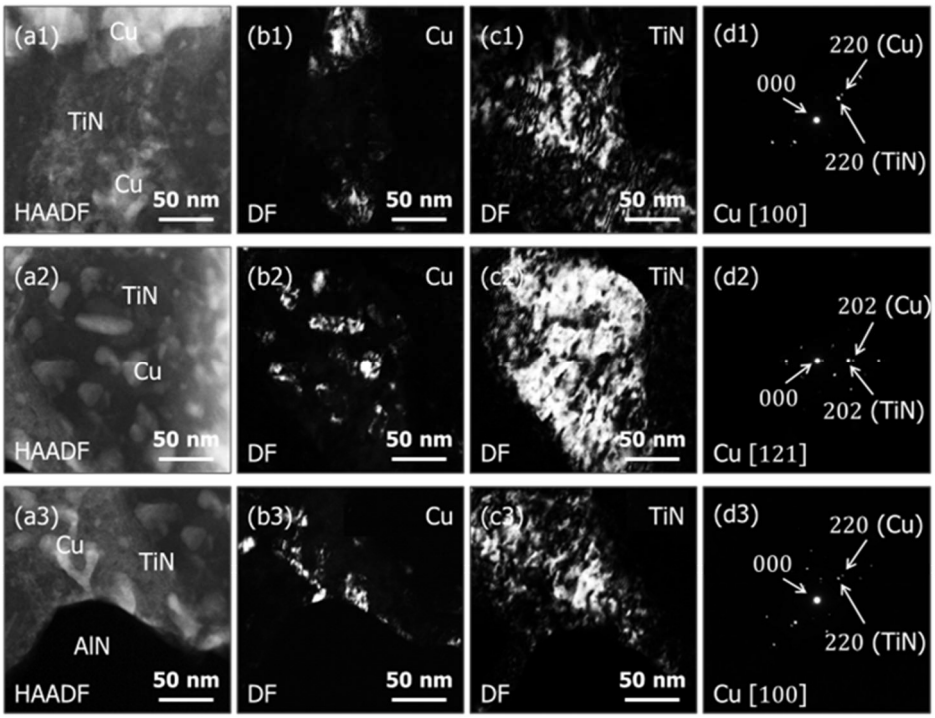


**Fig. 2.18 (a1–3) HAADF images of a Cu–$TiH_2$/AlN interface after sintering at 850 °C for 0.5 h, (b1–3) DF image for Cu, and (c1–3) for TiN using *g* vectors as shown in (d1–3) SAED patterns [1], © 2022 by Springer Science Business Media, reproduced with license.**

### 2.3.3 Growth mechanism of the TiN reaction layer

The results shown in Sections 2.3.1 and 2.3.2 indicate that the structural features of these TiN layers as shown Figs. 2.4, 2.16, and 2.18 did not depend on whether the Ti-containing metal layer was a liquid phase or a solid phase at the heat treatment temperature. Thus, the formation reaction of the TiN layer using AlN as a starting material via the AMB method consisted of TiN formation via a single-substitution reaction and a local liquid-phase formation reaction inside AlN.

Compositional analysis results for the Ag and the Cu phases in the TiN layer for three samples are shown in Tables 2.2 and 2.3, which were obtained from each phase shown in Figs. 2.4, 2.16, and 2.18. For the Ag–Cu–$TiH_2$ system, the Al concentration relative to the sum of the Ag, Cu, and Al concentrations is also shown in parentheses in Tables 2.2 and

**Table 2.2 Compositional analysis of the Ag phase in the TiN layer after brazing/sintering at 850 °C for 0.5 h as shown in Figs. 2.4 and 2.16. Dash (-): below the limit of detection [1], © 2022 by Springer Science Business Media, reproduced with license.**

| Sample | Position in the TiN layer | Concentration (at%) | | | | | Al/(Al+Ag(+Cu)) (at%) |
|---|---|---|---|---|---|---|---|
| | | Ag | Cu | Ti | Al | N | |
| Ag–Cu–$TiH_2$/AlN | Metal layer side | 46.7 | 10.2 | 15.9 | 0.9 | 26.3 | 1.9 (1.6) |
| | Center | 41.6 | 11.9 | 17.1 | 1.4 | 28.0 | 3.2 (2.5) |
| | AlN side | 17.8 | 4.7 | 35.4 | 0.7 | 41.4 | 3.8 (3.1) |
| Ag–$TiH_2$/AlN | Metal layer side | 30.3 | - | 37.3 | 2.0 | 30.4 | 6.2 |
| | Center | 23.7 | - | 42.3 | 2.8 | 31.2 | 10.5 |
| | AlN side | 14.3 | - | 47.4 | 2.5 | 35.8 | 14.7 |

**Table 2.3 Compositional analysis of Cu phase in the TiN layer after brazing/sintering at 850 °C for 0.5 h as shown in Figs. 2.4 and 2.18. Dash (-): below the limit of detection [1], © 2022 by Springer Science Business Media, reproduced with license.**

| Sample | Position in the TiN layer | Concentration (at%) | | | | | Al/(Al+Cu(+Ag)) (at%) |
|---|---|---|---|---|---|---|---|
| | | Ag | Cu | Ti | Al | N | |
| Ag–Cu–$TiH_2$/AlN | Metal layer side | 0.7 | 23.6 | 38.7 | 4.2 | 32.7 | 15.1 (14.7) |
| | Center | 0.3 | 17.1 | 40.7 | 3.3 | 38.7 | 16.1 (15.8) |
| | AlN side | 9.4 | 34.5 | 19.7 | 9.5 | 26.9 | 21.6 (17.8) |
| Cu–$TiH_2$/AlN | Metal layer side | - | 25.6 | 39.3 | 3.2 | 31.9 | 11.1 |
| | Center | - | 40.0 | 28.0 | 6.3 | 25.7 | 13.4 |
| | AlN side | - | 65.5 | 10.8 | 11.3 | 12.3 | 14.9 |

2.3. It can be seen that the Al concentration gradually decreased with increasing distance from AlN. This implies that the TiN grain boundaries functioned as diffusion paths and assisted in the transfer of elements between the Ti-containing metal layer and AlN. It is notable that Al dissolved better in Cu than Ag did in the Ag–Cu–$TiH_2$ system. In addition, the Al concentration dependence of the lattice constants of the Ag and Cu phases in the TiN layer for three samples are shown in Figs. 2.19 and 2.20, as estimated from the SAED

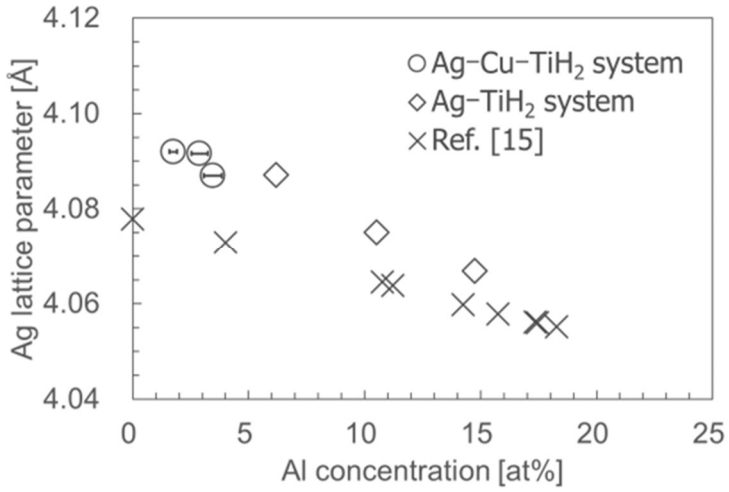


**Fig. 2.19 Al concentration dependence on the Ag lattice parameter [1], © 2022 by Springer Science Business Media, reproduced with license.**

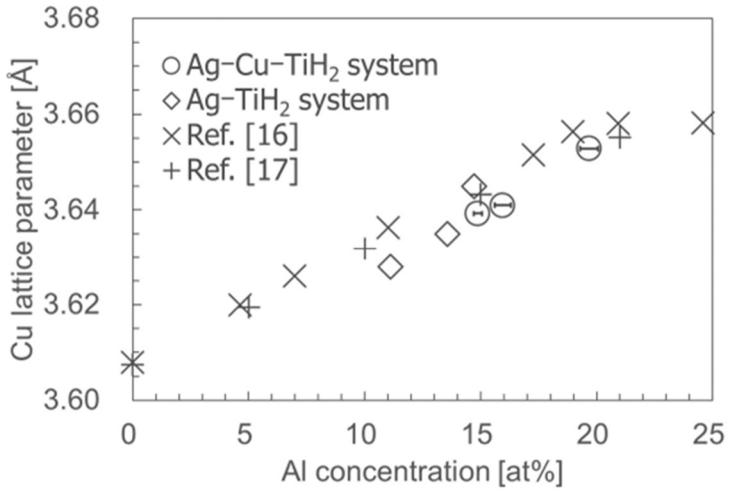


**Fig. 2.20 Al concentration dependence on the Cu lattice parameter [1], © 2022 by Springer Science Business Media, reproduced with license.**

patterns shown in Figs. 2.4, 2.16, and 2.18. The lattice constants of these phases are known to change linearly with respect to Al concentration in the Al solid solution region [14–16]. The changes in these lattice constants estimated in this work further support the proposition that there was a concentration gradient of *M* and Al in the TiN layer thickness direction.

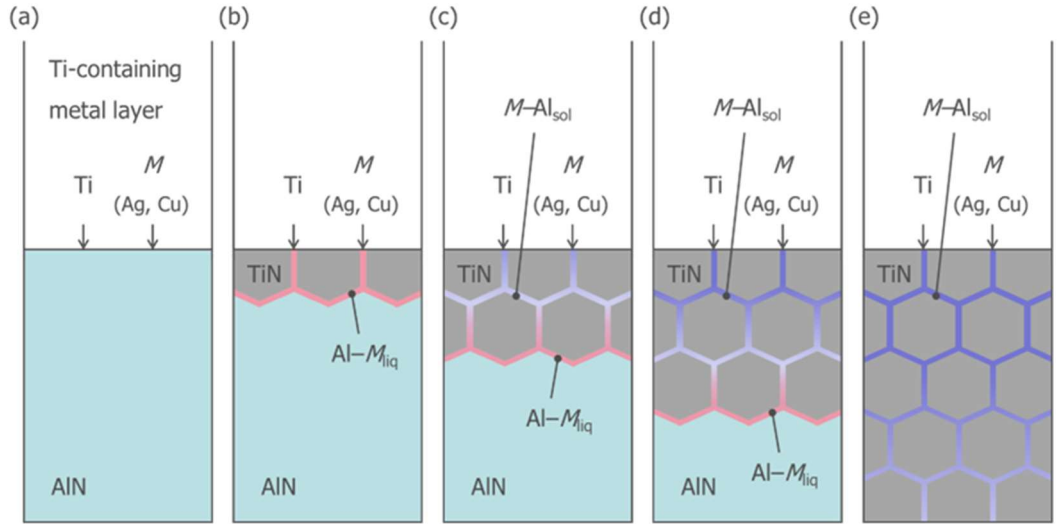


**Fig. 2.21 (a)–(e) Schematic mechanism for the formation reaction of the TiN layer at the interface between the Ti-containing metal layer and AlN. (a) Diffusion of Ti and *M* into the AlN surface. (b) Co-generation of TiN particles and the Al–*M* liquid phase according to Equations (2.2) and (2.3). (c, d) Growth of TiN layer toward the AlN interior and solidification of the Al–*M* liquid phase according to Equations (2.4) and (2.5), and finally (e) the TiN layer containing the *M*–Al solid phase with Al concentration distribution after complete solidification of the grain boundaries [1], © 2022 by Springer Science Business Media, reproduced with license.**

Combining the results of the three sets of interfacial reactions between a Ti-containing metal layer and AlN, a formation mechanism for the TiN layer via the AMB method is proposed, as illustrated in Fig. 2.21. First, an interfacial reaction occurs between Ti in the Ti-containing metal layer and AlN according to the following chemical reaction:

$$Ti + AlN \rightarrow TiN + Al_{liq} \tag{2.2}$$

This single-substitution reaction causes the co-generation of TiN particles and free liquid-phase Al ($Al_{liq}$) on the AlN surface at temperatures above the melting point of Al (660 °C). In addition, an element *M* (*M* = Ag and/or Cu) becomes eutectic with Al [18, 19] in the Ti-containing metal layer. Therefore, $Al_{liq}$ immediately forms Al–$M_{liq}$ as *M* dissolves in

$Al_{liq}$, as shown in Equation (2.3) and schematically in Fig. 2.21(b). It appears that Al–$M_{liq}$ contributes to lowering the energy of the entire interfacial reaction system.

$$Al_{liq} + M \rightarrow Al\text{–}M_{liq} \tag{2.3}$$

Furthermore, this Al–$M_{liq}$ is suggested to function as a diffusion path for supplying Ti from the Ti-containing metal layer to the interior of AlN. This means that Ti newly reaching the AlN surface via these diffusion paths propagates the co-generation of TiN particles and $Al_{liq}$ into the AlN interior by the chemical reaction in Equation (2.4), where $Al_{liq}$ is immediately integrated with Al–$M_{liq}$. Thus, the solidification reaction of Al–$M_{liq}$ of Equation (2.5) proceeds simultaneously with the single-substitution reaction of Equation (2.4) due to the increase in the concentration of *M* in Al–$M_{liq}$ on the Ti-containing metal layer side since *M* also diffuses through these diffusion paths into Al–$M_{liq}$ as shown in Fig. 2.21(c).

$$Ti + AlN + Al\text{–}M_{liq} \rightarrow TiN + Al\text{–}M_{liq} \tag{2.4}$$

$$Al\text{–}M_{liq} + M \rightarrow M\text{–}Al_{sol} \tag{2.5}$$

Therefore, the single-substitution reaction of Equation (2.2) promotes continuous interfacial reactions between the Ti-containing metal layer and AlN, and the reaction forming the TiN layer proceeds inside the AlN through repeated occurrence of local reactions of Equations (2.4) and (2.5), as shown schematically in Fig. 2.21(d). Consequently, the TiN layer is composed of TiN particles and grain boundaries with a concentration gradient of *M* and Al in the thickness direction of the TiN layer. This

corresponds to a high *M* concentration on the Ti-containing metal layer side and a high Al concentration on the AlN side, respectively, as shown in Fig. 2.21(e). In the TiN formation reaction using AlN as a starting material via the AMB method, the local Al–$M_{liq}$ plays an important role in the progress of the interfacial reaction between the Ti-containing metal layer and AlN, and Al–$M_{liq}$ and $M$–$Al_{sol}$ derived from this local liquid phase act as diffusion paths promoting transfer between the Ti-containing metal layer and AlN at all stages of the interfacial reaction.

## 2.4 Conclusions

This chapter presented a detailed investigation of the microstructure of TiN layers formed by the interfacial reactions in the AMB method between three Ti-containing metal layers—namely, Ag–Cu–$TiH_2$, Ag–$TiH_2$, and Cu–$TiH_2$—and a single-crystal AlN substrate. These interfacial structures were summarized in Fig. 2.22. The main conclusions were as follows:

1. The TiN layer grown inside the AlN substrate at the Ag–Cu–$TiH_2$/AlN interface consisted of a grain boundary phase composed of Ag and Cu in solid solution with Al derived from AlN surrounding TiN particles of <50 nm in size.
2. Ag was not essential in the formation of the Ag–Cu alloy layer/TiN particle interface, whereas TiN particles with an Al-containing segregation layer on the outermost surface were bonded to the Ag–Cu alloy layer via a Cu-containing segregation layer.
3. Interfacial reactions between AlN and Ti-containing metal layers that do not melt at 850 °C, such as Ag–$TiH_2$ and Cu–$TiH_2$, produced TiN layers with the same structure as the TiN layer grown at the Ag–Cu–$TiH_2$/AlN interface.

4. When AlN used as the starting material in the AMB process, TiN layers grew toward the AlN interior due to interfacial reactions involving the formation of a localized Al-based eutectic liquid phase and the transport of elements via this eutectic liquid phase.

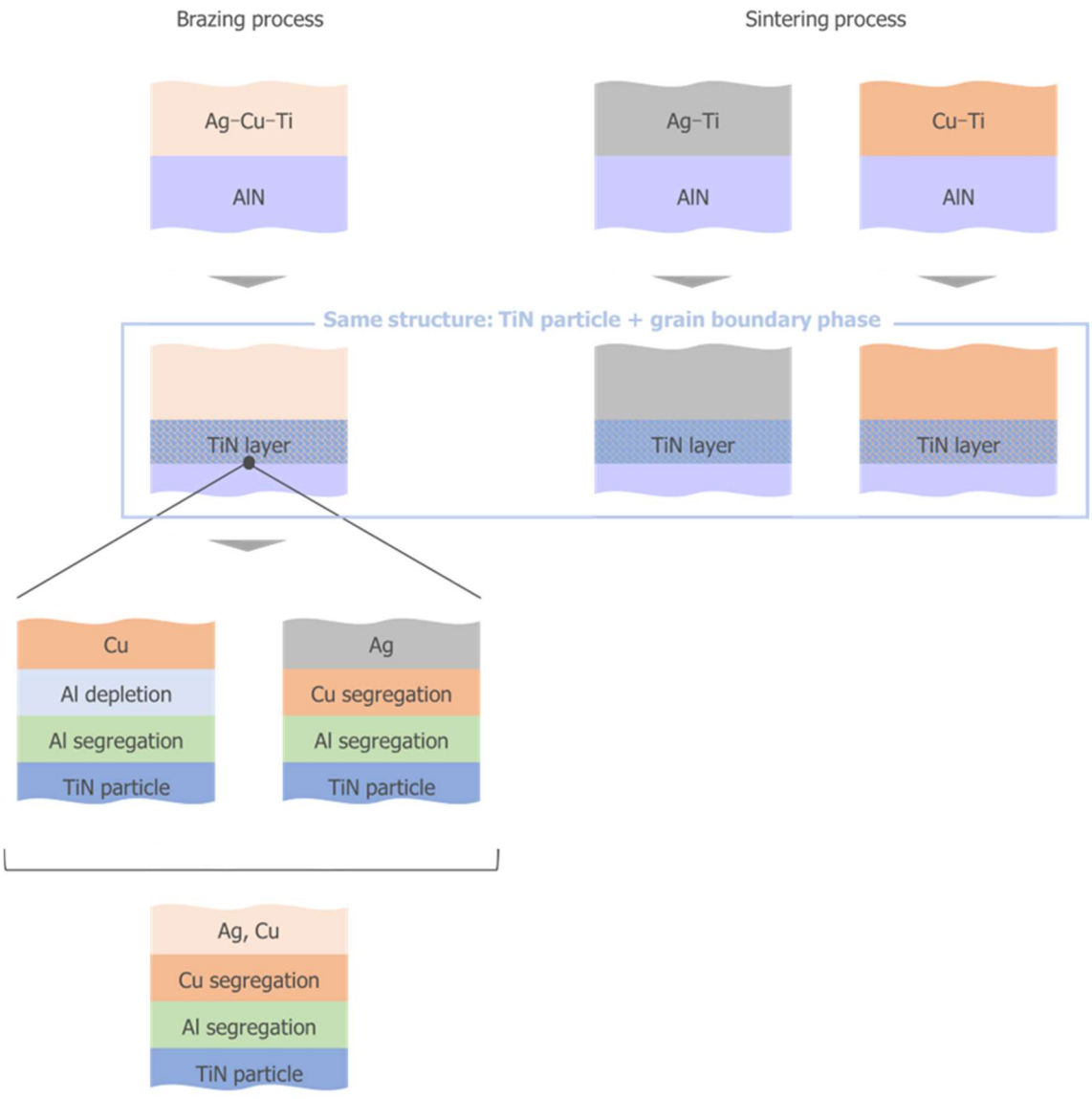


**Fig.2.22 Cu/ceramic interfacial structures discussed in this chapter.**

## References


[1] N. Terasaki, M. Sakaguchi, H. Chiba, T. Ohashi, Y. Nagatomo, Y. Kuromitsu, T. Sekino, K.M. Knowles, Growth mechanism of TiN reaction layers produced on AlN via active metal bonding, Journal of Materials Science, 57, 2022, 13300–13313.

[2] Th. Kehagias, Ph. Komninou, G. Nouet, P. Ruterana, Th. Karakostas, Misfit relaxation of the AlN/$Al_2O_3$ (0001) interface, Physical Review B, 64, 2001, art. 195329.

[3] Y. Tokumoto, Y. Sato, T. Yamamoto, N. Shibata, Y. Ikuhara, Atomic structure of AlN/$Al_2O_3$ interfaces fabricated by pulsed-laser deposition, Journal of Materials Science, 41, 2006, 2553–2557.

[4] Y. Zhang, J. Zhang, J. Chen, Effect of interfacial microstructure evolution on the peeling strength and fracture of AMB Cu-metalized AlN substrate, Journal of the American Ceramic Society, 105, 2021, 577–589.

[5] M.W. Chase, JANAF thermochemical tables, 3rd ed., the American Chemical Society, and the American Institute of Physics for the National Bureau of Standards, 1986.

[6] V. Bhosle, E.G. Baburaj, M. Miranova, K. Salama, Dehydrogenation of $TiH_2$, Materials and Engineering A, 356, 2003, 190–199.

[7] N. Terasaki, T. Ohashi, Y. Nagatomo, Y. Kuromitsu, A.A. Shirzadi, A new method for liquid-phase bonding of copper plates to aluminum nitride (AlN) substrates used in high-power modules, Journal of Materials Science: Materials in Electronics, 30(7), 2019, 6552–6555.

[8] H. Okamoto, Cu–Ti (Copper-Titanium), Journal of Phase Equilibria, 23(6), 2002, 549–550.

[9] C. Vahlas, B.D. Ladouce, P.Y. Chevalier, C. Bernard, L. Vandenbulcke, A thermodynamic evaluation of the Ti–N system, Thermochimica Acta, 180, 1991, 23–

37.

[10] Q. Chen, B. Sundman, Thermodynamic assessment of the Ti–Al–N system, Journal of Phase Equilibria, 19(2), 1998, 146–153.

[11] H. Jinnai, Y. Nishikawa, T. Ikehara, T. Nishi, Emerging technologies for the 3D analysis of polymer structures, Advances in Polymer Science, 170, 2004, 115.

[12] H. Jinnai, Novel structural analyses of polymeric materials by three-dimensional microscopy, Journal of the Surface Science Society of Japan, 28(8), 2007, 467-474.

[13] H. Okamoto, Comment on C–Ti (Carbon-Titanium), Journal of Phase Equilibria, 16(6), 1995, 532–533.

[14] J.L. Murray, K.J. Bhansali, The Ag–Ti (Silver-Titanium) system, Bulletin of Alloy Phase Diagrams, 4(2), 1983, 178–183.

[15] I. Obinata, G. Wassermann, Röntgenographische Untersuchung der Löslichkeit von Aluminium in Kupfer, Naturwissenschaften, 21, 1933, 382–385.

[16] A.J. Bradley, H.J. Goldschmidt, X-ray study of slowly cooled iron-copper-aluminium alloys Part I. -Alloys rich in iron and copper, Journal of the Institute of Metals, 65, 1939, 389–401.

[17] W.B. Pearson, A Handbook of Lattice Spacings and Structures of Metals and Alloys, Pergamon Press, London, 1958.

[18] J.L. Murray, The aluminum–copper system, International Metals Reviews, 30(5), 1985, 211–233.

[19] A.J. McAlister, The Ag–Al (Silver-Aluminum) system, Bulletin of Alloy Phase Diagrams, 8(6), 1987, 526–533.

# Chapter 3: Interfacial structure of Ag–Cu eutectic brazing to TiN-based and WC-based ceramics

## 3.1 Introduction

In Chapter 2, the TiN layer formed by the interfacial reaction between the Ag–Cu–$TiH_2$ brazing alloy and AlN was shown to be a composite of TiN particles and Ag- and Cu-containing grain boundary phases. In addition, it was demonstrated that Cu-containing and Al-containing segregation layers were formed at the Ag–Cu alloy layer/TiN particle interface. However, it is unclear how the Ag–Cu alloy, the TiN particles and the formation of these segregation layers contribute to the formation of the Ag–Cu alloy layer/TiN particle interface, since the formation reaction of TiN particles, Cu-containing and Al-containing segregation layers at the Ag–Cu alloy layer/TiN particle interface are all completed during active brazing.

In this chapter, based on Ag–Cu brazing, in order to clarify the effects of TiN particle formation and metal components of the grain boundary phase on the formation of the metal/TiN particle bonding interface, the Ag–Cu alloy layer/TiN particle interface was investigated by using a TiN solid-phase sintered ceramic without a metal grain boundary phase and a TiN liquid-phase sintered ceramic with a mainly Fe-containing grain boundary phase which is different from Ag–Cu alloy. In addition, to clarify the general structure of the metal/ceramics bonding interface formed by Ag–Cu brazing, the interfacial structure of the Ag–Cu alloy layer/WC–Co cemented carbide, which is a different material system from the TiN sintered ceramic, is investigated [1, 2].

## 3.2 Experimental procedure

### 3.2.1 Materials and sample fabrication

In this study, as the sintered materials for brazing Cu, two TiN sintered ceramics with different sintering methods were used as TiN layers and a WC–Co cemented carbide was used as a different material system from TiN. One of the TiN sintered ceramics was a commercial TiN solid-phase sintered ceramic (ø50.8 mm × 6 mm) fabricated by the solid-phase sintering method, in which there was no grain boundary phase composed of metal components, and this was cut into a 10 mm × 10 mm × 6 mm rectangular parallelepiped. The other was TiN–8.4 wt% Fe–2.2 wt% Ni–1.1 wt% C–3.8 wt% $Mo_2C$, which was fabricated by the liquid-phase sintering method (referred to as TiN liquid-phase sintered ceramic). Powders of TiN ($D_{50}$ = 1.3 μm), Fe ($D_{50}$ = 6.1 μm), Ni ($D_{50}$ = 2.5 μm), C ($D_{50}$ = 4.7 μm), and $Mo_2C$ ($D_{50}$ = 1.8 μm) were added to ethanol and mixed for 40 h in a ball mill together with WC balls (ø3 mm). $D_{50}$ is the 50th percentile of particle size by volume. The resulting mixture was dried at 150 °C for 3 h under vacuum, and then formed into a cylinder (ø20 mm × 8 mm) under pressure of 200 MPa. The molding was sintered at 1400 °C for 2 h in $N_2$ containing 3 vol% $H_2$ at atmospheric pressure and then formed into a 10 mm × 10 mm × 6 mm rectangular parallelepiped by grinding. The relative densities of these solid- and liquid-phase sintered ceramics were 81.9% and 99.8%, respectively, indicating that the TiN liquid-phase sintered ceramics were almost fully densified. In addition, the area ratio of TiN grains to the grain boundary phase was about 80:20 on the surface to be bonded to the TiN liquid-phase sintered ceramic. The concentrations of impurities in the TiN solid-phase sintered ceramic as found by inductively coupled plasma

optical emission spectrometry (ICP-OES) are shown in Table 3.1. The TiN solid-phase sintered ceramic had purity of >99.9 wt%. Of nine impurities including Al, K, and Ca, the one with the highest concentration was Fe (0.018 wt%). These impurities would be derived from the TiN grains used as a raw material for the TiN solid-phase sintered ceramic, or from the Ti material used as a raw material for the TiN grains. In addition, this Fe impurity concentration was about 0.2% of the Fe concentration in the TiN liquid-phase sintered ceramic. WC–Co cemented carbide using only Co as the binder, which was finished to a surface roughness of 0.15 μm by grinding, was also used and was cut into a 10 mm × 10 mm × 6 mm rectangular parallelepiped. Oxygen-free copper (OFC, 10 mm × 10 mm × 0.8 mm) was brazed onto the sintered materials using a Ag–Cu eutectic brazing foil (Ag–28 wt% Cu [3], 10 mm × 10 mm × 0.05 mm). These materials were laminated in the order of Cu, Ag–Cu brazing foil, and the sintered materials. The laminated specimen was vacuum brazed at 850 °C for 0.5 h under pressure of 1 MPa, with heating and cooling rates of 10 °C/min, and ultimate vacuum of about $5 \times 10^{-3}$ Pa.

**Table 3.1 Concentrations of impurities related to the TiN solid-phase sintered ceramic as measured by ICP-OES [2], © 2022 by authors, reproduced with license.**

| Concentration (wt%) | | | | | | | | |
|---|---|---|---|---|---|---|---|---|
| Al | K | Ca | Cr | Mn | Fe | Co | Nb | Mo |
| 0.012 | 0.015 | 0.002 | 0.002 | 0.005 | 0.018 | 0.010 | 0.002 | 0.003 |

## 3.2.2 Characterization

The surface and cross-section of the TiN sintered ceramics and the WC–Co cemented carbide were observed by SEM and auger electron spectroscopy (AES). AES analysis and SEM observation of these sinter surfaces were performed using a PHI 700 system

(ULVAC-PHI, Inc.) operated at 10 kV. For cross-sectional SEM analysis of these sinters, metallography specimens mounted in an acrylic polymer at room temperature were polished using standard metallographic techniques, with final polishing performed using an argon-based ion beam polisher (ArBlade 5000, Hitachi High-Tech). The microstructures of all cross-sectional specimens were observed using a GeminiSEM 500 system (Carl Zeiss AG) operated at an operating voltage of 1.8 kV. In addition, cross-sections of Cu/TiN sintered ceramic brazed specimens and Cu/WC–Co cemented carbide brazed specimen, which were prepared in the same way as the sintered specimens before brazing, were observed by SEM before more detailed observations were undertaken by STEM. SEM observation and elemental analysis of the cross-sections were performed using the GeminiSEM 500 system with an EDS system (NORAN System7, Thermo Fisher Scientific), which were operated at 1.8 kV and 7 kV, respectively. Cu/TiN thin sections for STEM analysis were prepared using a FIB system (Scios, Thermo Fisher Scientific), and their thickness was adjusted between 30 and 100 nm. The elemental distributions of the thin sections were evaluated using a Titan G2 ChemiSTEM system (Thermo Fisher Scientific) equipped with an EDS system (NSS7, Thermo Fisher Scientific) operated at 200 kV.

## 3.3 Results and discussion

### 3.3.1 Surface and cross-sectional microstructures of TiN solid-phase and liquid-phase sintered ceramics and WC–Co cemented carbide

Cross-sectional SE images of the near surface of the TiN solid-phase sintered ceramic

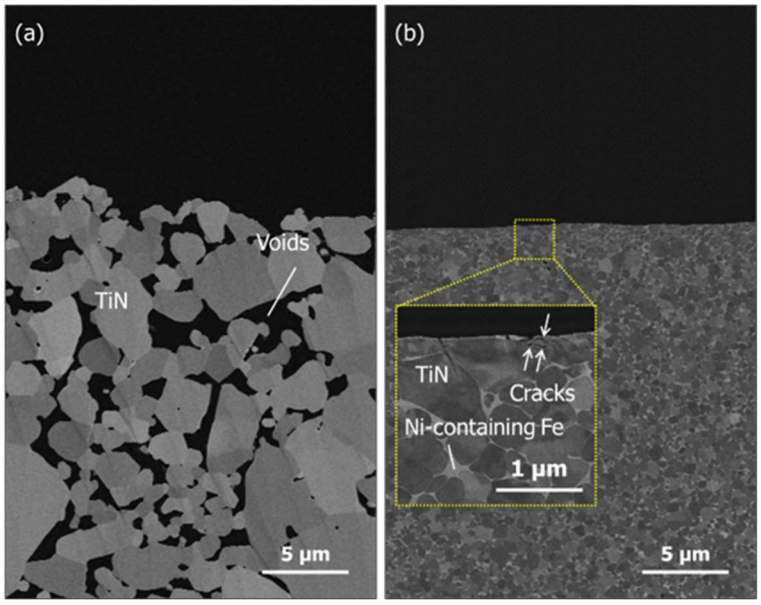


**Fig. 3.1 Cross-sectional SE images of (a) the TiN solid-phase sintered ceramic and (b) the TiN liquid-phase sintered ceramic near the surface [2], © 2022 by authors, reproduced with license.**

and the TiN liquid-phase sintered ceramic before brazing are shown in Fig. 3.1. The TiN solid-phase sintered ceramic contained a large number of voids, owing to the low sinterability of TiN grains [4]. In contrast, the TiN liquid-phase sintered ceramic had a dense structure due to the bonding of the TiN grains through a crystalline grain boundary phase consisting of a Ni-containing Fe phase (Fe–44 at% Ni, cubic, $Fm\bar{3}m$, $a$ = 3.586 Å) [5–7] and $Mo_2C$ (hexagonal, $P6_3/mmc$, $a$ = 2.994 Å, $c$ = 4.732 Å) [8]. In addition, although the surface of the TiN liquid-phase sintered ceramic finished by grinding had some fine cracks, it was flatter than the TiN solid-phase sintered ceramic. Surface SE images of the TiN solid-phase sintered ceramic and the TiN liquid-phase sintered ceramic before brazing, together with the AES spectra obtained from these surfaces, are shown in Fig. 3.2. Some voids were present on the surface of the TiN solid-phase sintered ceramic and appeared to be connected to the voids inside the ceramic as shown in Fig. 3.1(a). In addition, the shape of the AES spectra suggests that the impurities shown in Table 3.1

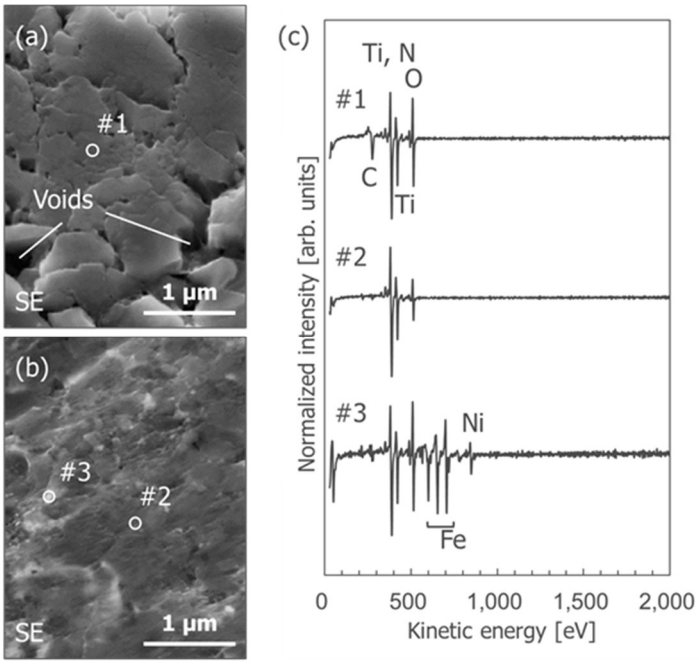


**Fig. 3.2 Surface SE images of (a) the TiN solid-phase sintered ceramic and (b) the TiN liquid-phase sintered ceramic. (c) AES spectrum obtained from areas marked by white open circles in (a) and (b) [2], © 2022 by authors, reproduced with license.**

were not significantly segregated on the TiN grain surface (#1). In contrast, the SE image of the TiN liquid-phase sintered ceramic shows regions of different brightness regions (Fig. 3.1(b)). According to the AES spectrum, the dark contrast region (#2) appears to be composed of the TiN phase with C and O, while the bright contrast region (#3) appears to be composed of the Ni-containing Fe phase in addition to the aforementioned TiN phase. Thus, no grain boundary phase components were present on the surface of the TiN grains on the surface to be bonded to the TiN liquid-phase sintered ceramics.

An SE image of the WC–Co cemented carbide surface before brazing, together with its Co distribution and AES spectrum, is shown in Fig. 3.3. The SE image shows two regions of different brightness. Based on the Co distribution shown in Fig. 3.3(b), the bright and dark regions appear to correspond to WC grains (#4) and the grain boundaries composed of Co (#5), respectively. In addition, the area ratio of Co distributed in the WC

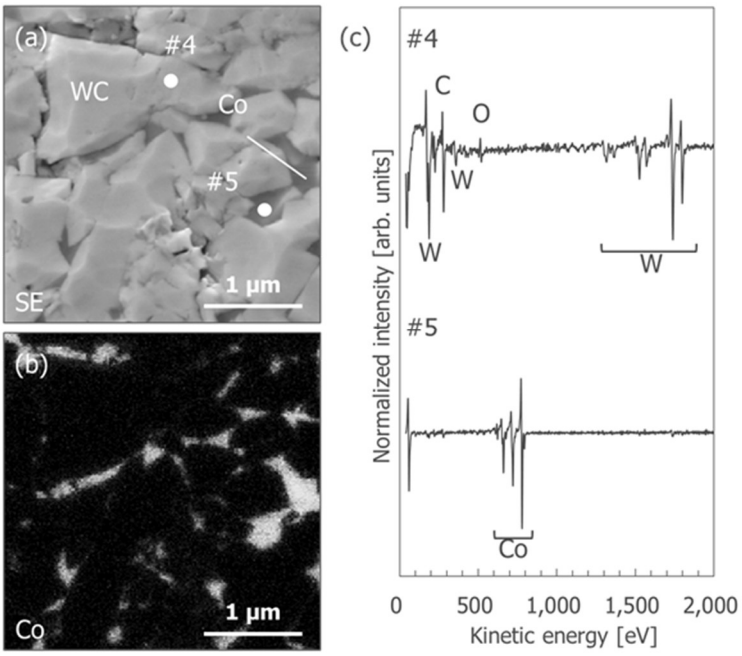


**Fig. 3.3 (a) SE image, (b) Co distribution, and (c) AES spectrum of the WC–Co cemented carbide surface [1], © 2022 by Elsevier B.V., reproduced with license.**

grain boundaries to the entire WC–Co cemented carbide surface to be brazed was about 10%. It can be seen that Co-containing different phases were not present on the WC grain surfaces shown in Fig. 3.3(c), as the WC–Co cemented carbide surface to be brazed was finished by grinding.

### 3.3.2 Interfacial structure of Ag- and Cu-rich phase/TiN solid-phase and liquid-phase sintered ceramics

The appearance of the TiN solid-phase sintered ceramic and that of the Cu plates brazed with Ag–Cu eutectic brazing foil at 850 °C for 0.5 h are shown in Fig. 3.4. Poor adhesion can be seen between the Ag–Cu alloy layer and the TiN grains. This result is different from the state of bonding at the Ag–Cu alloy layer/TiN layer interface involving the interfacial reaction between the Ag–Cu–Ti liquid phase and the AlN substrate in the AMB

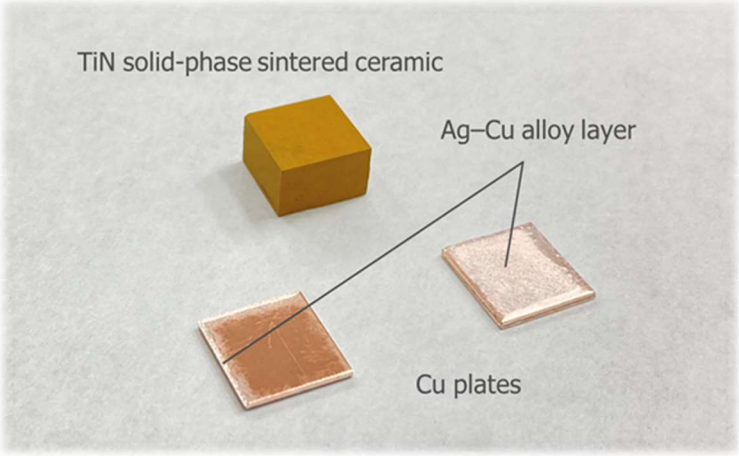


**Fig. 3.4 Appearance of the TiN solid-phase sintered ceramic and Cu plates brazed with a Ag–Cu eutectic brazing foil after heating at 850 °C for 0.5 h [2], © 2022 by authors, reproduced with license.**

method. In addition, Ag–Cu alloy layers were formed on the entire bonding surface of the Cu plate and on the edge of its non-bonding surface. This suggests that a sufficient amount of Ag–Cu liquid phase was generated during heating but did not penetrate into the voids leading from the surface to interior of the TiN solid-phase sintered ceramic shown in Figs. 3.1(a) and 3.2(a). Thus, good bonding was not achieved between the Ag–Cu alloy layer and the TiN grains by mechanical bonding, such as the anchor effect [9].

A cross-sectional energy-selective backscattered electron (EsB) image of the interface between the Cu and TiN liquid-phase sintered ceramic after bonding at 850 °C for 0.5 h, together with the elemental distributions, is shown in Fig. 3.5. In contrast to the bonding state between Cu and the TiN solid-phase sintered ceramic shown in Fig. 3.4, here the Cu/TiN liquid-phase sintered ceramic brazing interface appears to show a ceramic morphology without any macroscopic gaps or pores. The most significant feature of the cross-sectional microstructure of the Cu/TiN liquid-phase sintered ceramic is that the Ni-containing Fe phase was substituted for the Cu-rich and Ag-rich phases from the Cu/TiN liquid-phase sintered ceramic brazing interface to the interior of the TiN liquid-phase

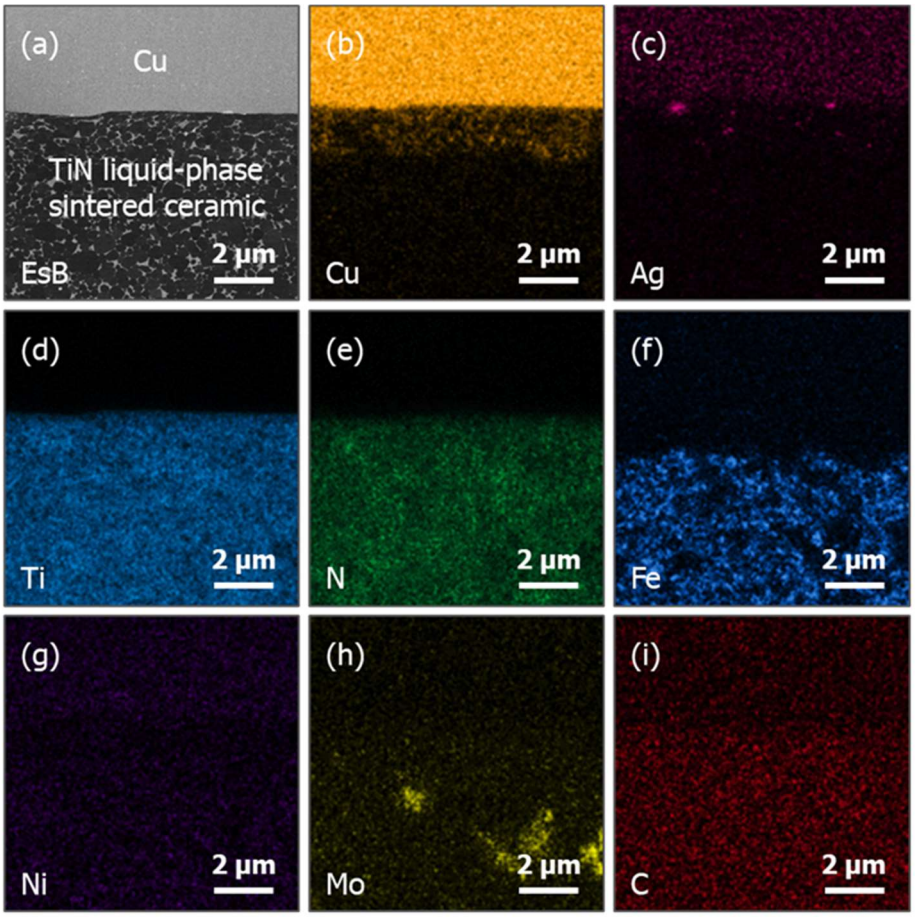


**Fig. 3.5 (a) Cross-sectional EsB image of the Cu/TiN liquid-phase sintered ceramic interface after bonding at 850 °C for 0.5 h. (b)–(i) Elemental distributions of (b) Cu, (c) Ag, (d) Ti, (e) N, (f) Fe, (g) Ni, (h) Mo, and (i) C [2], © 2022 by authors, reproduced with license.**

sintered ceramic to a depth of about 2 μm. This suggests that interdiffusion of the Ni-containing Fe phase with the Cu(Ag)-rich phase could result in replacement of these phases while maintaining the shape near the brazed surface of the TiN liquid-phase sintered ceramics. In addition, no distinct Fe or Ni signals can be seen in the Ag–Cu alloy layer, suggesting that the concentrations of these elements are below the limit of detection due to their diffusion to the Cu surface side. The macroscopic structures of the Cu/TiN liquid-phase sintered ceramic interface can be divided into three types. The first is the Ag–Cu alloy layer/TiN brazing interface formed by the interfacial reaction between the Ag–Cu liquid phase and the TiN grains (Interface I). The second is the substituted Ag–

Cu phase/TiN interface, where the grain boundary phases of the TiN liquid-phase sintered ceramic are substituted for the Ag–Cu brazing filler components (Interface II). The third is the interface between the TiN grains and the grain boundary phase without substitution by the Cu-rich and Ag-rich phases in the TiN liquid-phase sintered ceramic (Interface III).

An HAADF image and elemental distributions of Interface I after brazing at 850 °C for 0.5 h are shown in Figs. 3.6 and 3.7 for the Cu-rich phase/TiN grain interface and the Ag-rich phase/TiN grain interface, respectively. The highest signal in the Fe and Ni maps is located uniformly at Interface I between the Cu-rich phase and TiN grain (Fig. 3.6(f) and (g)). By comparison, a Cu signal is detected at Interface I between the Ag-rich phase and a TiN grain in addition to the Fe and Ni signals (Fig. 3.7(b), (f), and (g)). Cu segregates with Fe and Ni at Interface I between the Ag-rich phase and a TiN grain, while the regions where these elements do not segregate correspond to very small voids of 1 to 2 nm in size. Line EDS profiles of Interface I after brazing at 850 °C for 0.5 h are shown in Figs. 3.6(j) and 3.7(j), where the line EDS profiles correspond to the white dashed arrows in Figs. 3.6(b) and 3.7(b), respectively. The peak positions of the Fe and Ni signals at the interface between the Cu-rich phase and a TiN grain almost overlap, as shown in Fig. 3.6(j). The overlap of the peak positions between these elements was also detected at Interface I between the Ag-rich phase and a TiN grain (Fig. 3.7(j)), while the peak position of the Cu signal was shifted toward the Ag-rich phase with respect to the peak positions of the Fe and Ni signals. The difference in peak widths of Fe and Ni signals between the Cu-rich phase/TiN grain interface and the Ag-rich phase/TiN grain interface may be due to the curvature of TiN grains in the thickness direction of the Cu/TiN thin sections for STEM analysis. No Fe or Ni was present on the TiN grain surface of the TiN liquid-phase sintered ceramic before brazing (#2 in Fig. 3.2(c)). These results suggest that

the segregation layers containing Fe and Ni were formed by the interfacial reaction between the TiN grains and the Ag–Cu liquid phase, which contained Fe and Ni components derived from the grain boundary phase of the TiN liquid-phase sintered ceramic. This means that neither the Cu-rich phase nor the Ag-rich phase was directly bonded to TiN grains. On the other hand, such interfacial reactions seemed not to occur during brazing in the TiN solid-sintered ceramic system because the dissolution of TiN grains into the Ag–Cu liquid phase did not provide enough Fe, one of the impurities shown in Table 3.1. In addition, a Cu-containing segregation layer appeared to be present between the Ag-rich phase and the Fe- and Ni-containing segregation layer at Interface I between the Ag-rich phase and TiN grains.

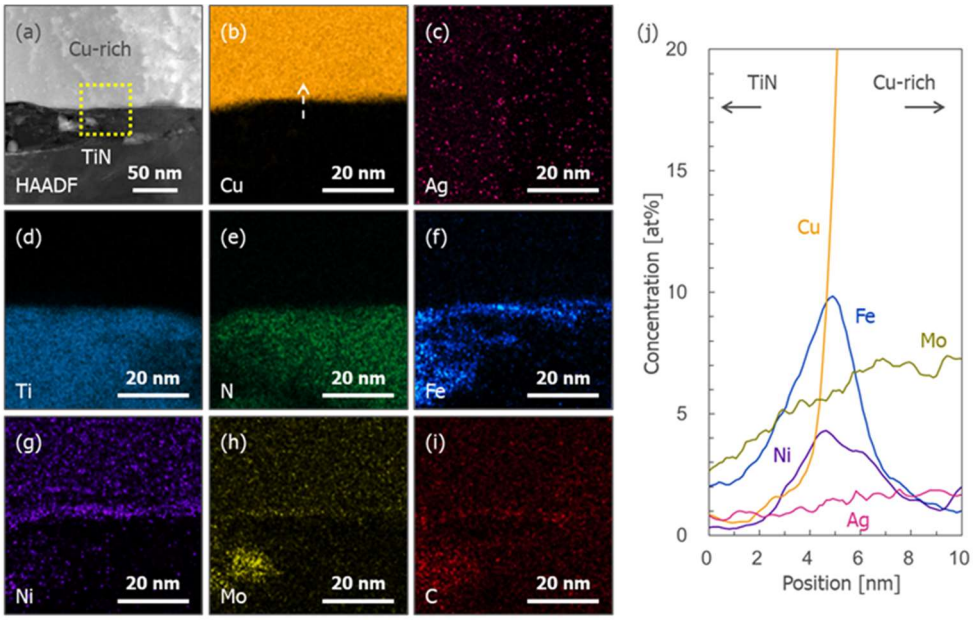


**Fig. 3.6 (a) Cross-sectional HAADF image of the Cu-rich phase/TiN grain interface after brazing at 850 °C for 0.5 h. (b)–(i) Elemental distributions of (b) Cu, (c) Ag, (d) Ti, (e) N, (f) Fe, (g) Ni, (h) Mo, and (i) C obtained from the selected area marked in (a). (j) Line EDS profile obtained along the white dashed arrow shown in (b) [2], © 2022 by authors, reproduced with license.**

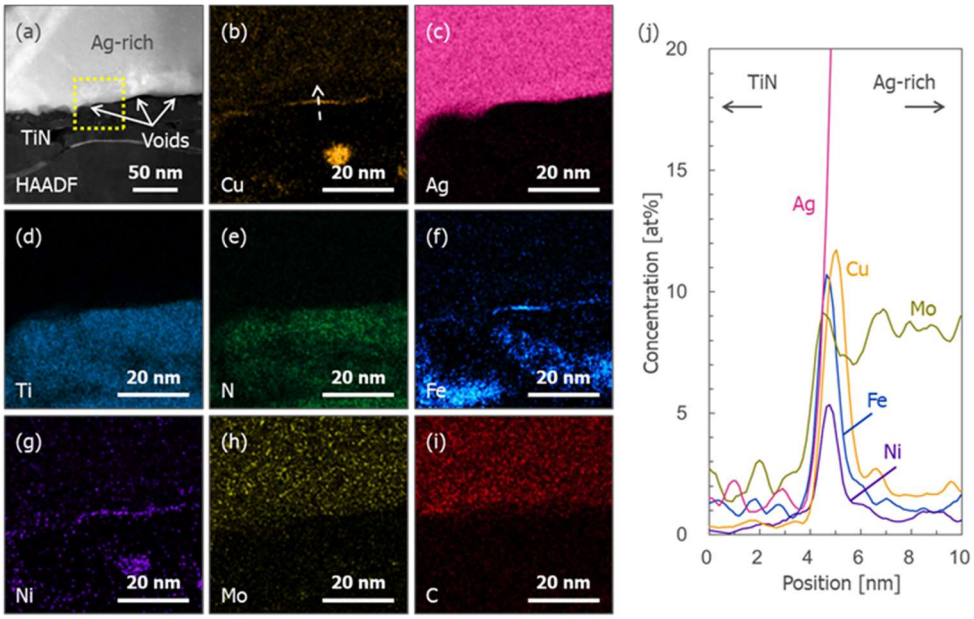


**Fig. 3.7 (a) Cross-sectional HAADF image of the Ag-rich phase/TiN grain interface after brazing at 850 °C for 0.5 h. (b)–(i) Elemental distributions of (b) Cu, (c) Ag, (d) Ti, (e) N, (f) Fe, (g) Ni, (h) Mo, and (i) C obtained from the selected area marked in (a). (j) Line EDS profile obtained along the white dashed arrow shown in (b) [2], © 2022 by authors, reproduced with license.**

An HAADF image and elemental distributions of Interface II after brazing at 850 °C for 0.5 h are shown in Figs. 3.8 and 3.9 for the substituted Cu-rich phase/TiN grain interface and the substituted Ag-rich phase/TiN grain interface, respectively. As shown in Fig. 3.8(f) and (g) and Fig. 3.9(f) and (g), the highest signal in the Fe and Ni maps was uniformly located between the Cu-rich and Ag-rich phases and a TiN grain at Interface II, similar to Interface I (Figs. 3.6 and 3.7). In addition, a Cu signal was detected at Interface II between the substituted Ag-rich phase and a TiN grain in addition to the Fe and Ni signals (Fig. 3.9(b), (f), and (g)). The line EDS profiles of Interface II in Figs. 3.8(j) and 3.9(j), corresponding to the white dashed arrows in Figs. 3.8(b) and 3.9(b), show that the Fe and Ni peak positions coincided with the Cu-rich phase/TiN grain interface. In addition, the Cu peak position was shifted toward the Ag-rich phase compared with the Fe and Ni peak positions coinciding with the Ag-rich phase/TiN grain interface. Compared to the

Ag signal at the Ag-rich phase/TiN grain interface, the Cu signal at the Cu-rich phase/TiN grain interface is detected within TiN grains, which may be due to the curvature of TiN grains in the thickness direction of Cu/TiN thin sections for STEM analysis as in Interface I. Most importantly, these features of Interface II formed by interdiffusion between the grain boundary phase and the Ag–Cu liquid phase are in perfect agreement with those of Interface I formed by the interfacial reaction during brazing. Specifically, the interfacial structure across the Fe- and Ni-containing segregation layer is a feature common to both the Cu-rich phase/TiN grain interface and the Ag-rich phase/TiN grain interface. Also, a Cu-containing segregation layer may have been present between the Ag-rich phase and Fe- and Ni-containing segregation layer at the Cu-rich/TiN grain interface for Interfaces I and II. The (a) annular bright-field (ABF) and (b) HAADF images of the substituted Cu-rich phase/TiN grain interface are shown in Fig. 3.10. These were observed along the TiN [001] direction. In Fig. 3.10(a), the local dark contrast corresponds to the Ti or N columns of TiN. Comparing Fig. 3.10(a) and (b) suggests that the 3–4 layers from the surface of the TiN particle are substituted by elements heavier than Ti and N, while maintaining the rock-salt structure of TiN. On the other hand, no clear atomic columns corresponding to Cu-containing segregation layers were observed in the Cu-rich phase. This suggests that the Cu-containing segregation layer does not have a specific structure. A detailed HAADF image of the substituted Cu-rich phase/TiN grain phase interface, together with elemental distributions, is shown in Fig. 3.11. Here, the elemental distribution of Fe coincides well with the region substituted by relatively heavy elements on the TiN grain surface. This suggests that the outermost surface of the TiN grains was modified to $Ti_{1-x}Fe_xN$ [10].

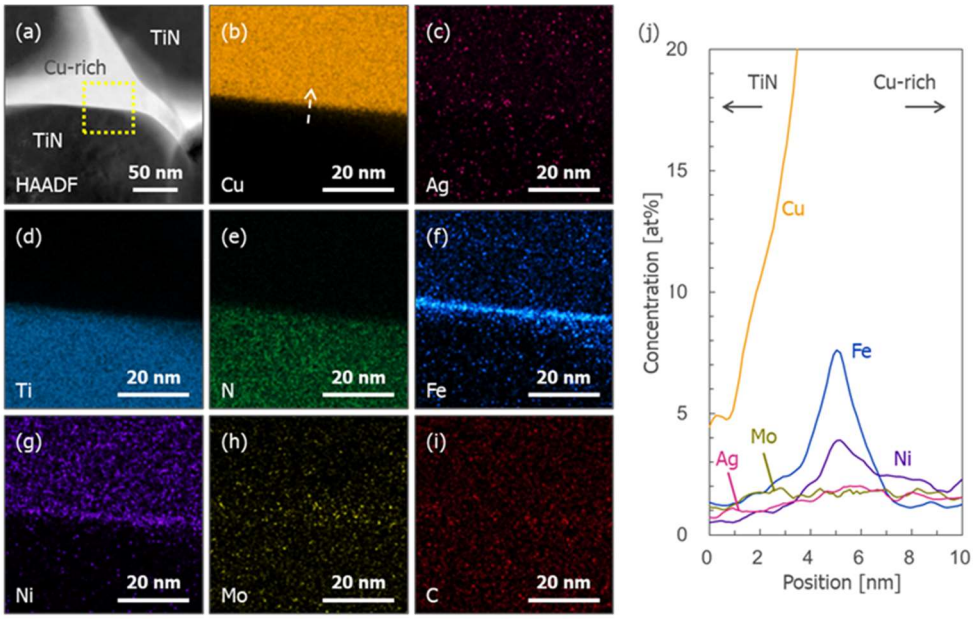


**Fig. 3.8 (a) Cross-sectional HAADF image of the substituted Cu-rich phase/TiN grain interface after brazing at 850 °C for 0.5 h. (b)–(i) Elemental distributions of (b) Cu, (c) Ag, (d) Ti, (e) N, (f) Fe, (g) Ni, (h) Mo, and (i) C obtained from the selected area marked in (a). (j) Line EDS profile obtained along the white dashed arrow shown in (b) [2], © 2022 by authors, reproduced with license.**

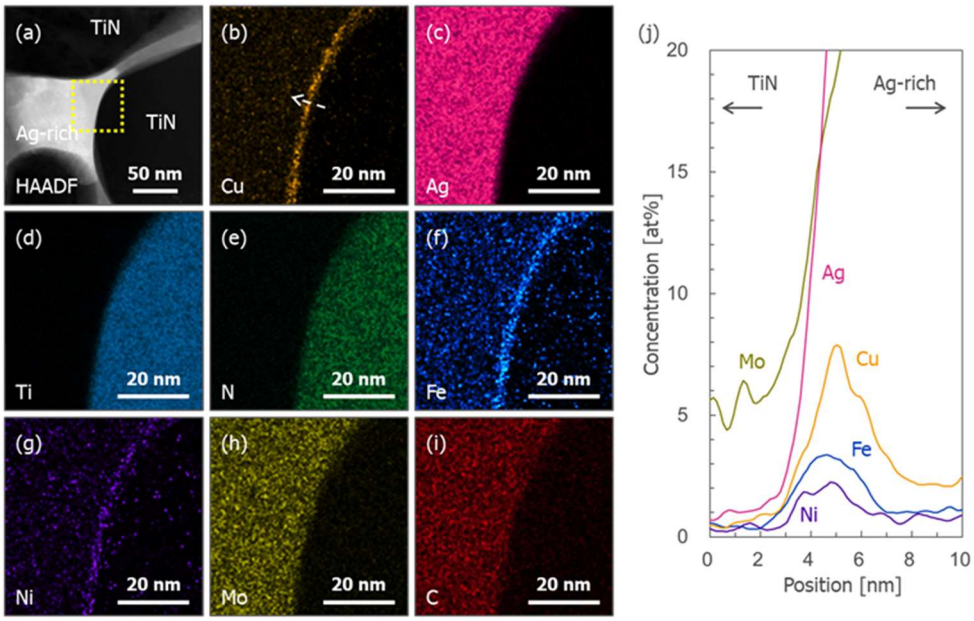


**Fig. 3.9 (a) Cross-sectional HAADF image of the substituted Ag-rich phase/TiN grain interface after brazing at 850 °C for 0.5 h. (b)–(i) Elemental distributions of (b) Cu, (c) Ag, (d) Ti, (e) N, (f) Fe, (g) Ni, (h) Mo, and (i) C obtained from the selected area marked in (a). (j) Line EDS profile obtained along the white dashed arrow shown in (b) [2], © 2022 by authors, reproduced with license.**

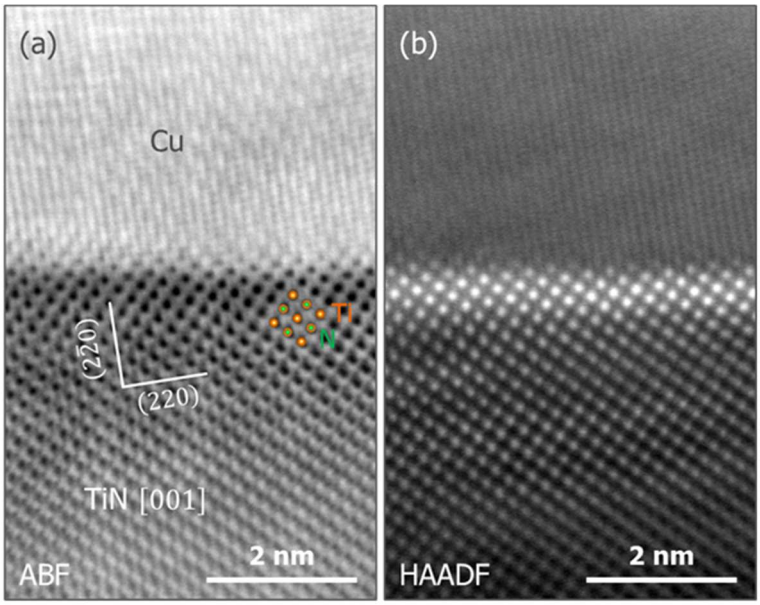


**Fig. 3.10 (a) ABF and (b) HAADF images of the substituted Cu-rich phase/TiN grain interface after brazing at 850 °C for 0.5 h.**

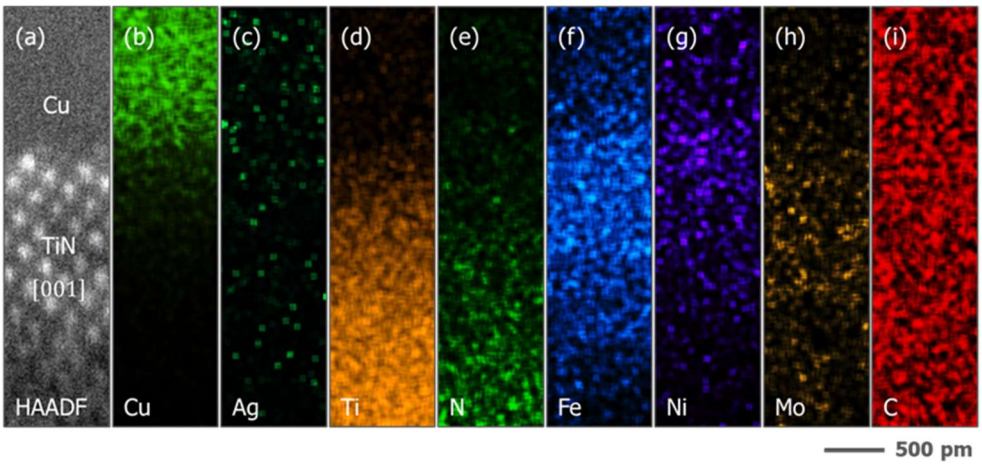


**Fig. 3.11 (a) HAADF image of the substituted Cu-rich phase/TiN grain phase interface with elemental distributions of (b) Cu, (c) Ag, (d) Ti, (e) N, (f) Fe, (g) Ni, (h) Mo, and (i) C.**

An HAADF image, elemental distributions, and a line EDS profile at Interface III ($Mo_2C$/TiN grain) after brazing at 850 °C for 0.5 h are shown in Fig. 3.12. The elemental distributions and line EDS profile were obtained from the selected area shown in Fig. 3.12(a) and the white dashed arrow shown in Fig. 3.12(b), respectively. The highest uniform signal in the Fe map can be clearly seen at Interface III in Fig. 3.12(f). In addition, the Ni concentration of 6.2 at% at the Ni peak position is close to the value of about 4.9 at% in $Mo_2C$, which might not be immediately clear. However, the Ni peak position was consistent with the Fe peak position in the line EDS profile in Fig. 3.12(j). This suggests that the surfaces of TiN grains constituting the TiN liquid-phase sintered ceramic were covered by an Fe- and Ni-containing layer due to an interfacial reaction during the liquid-phase sintering process above the Ag–Cu brazing temperature. This means that the TiN grains were bonded to the grain boundary phase through the Fe- and Ni-containing

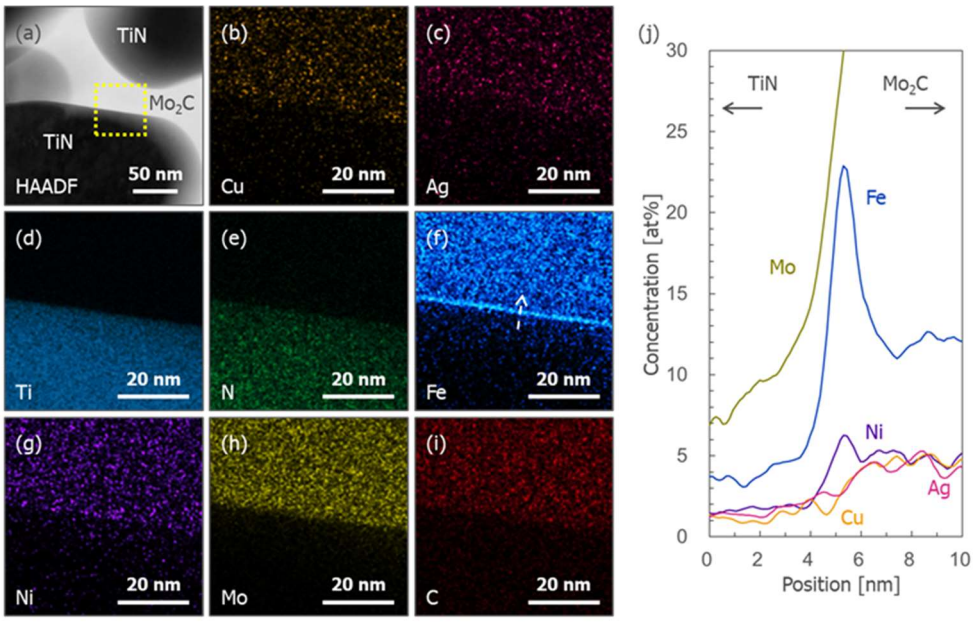


**Fig. 3.12 (a) Cross-sectional HAADF image of the $Mo_2C$/TiN grain interface after brazing at 850 °C for 0.5 h. (b)–(i) Elemental distributions of (b) Cu, (c) Ag, (d) Ti, (e) N, (f) Fe, (g) Ni, (h) Mo, and (i) C obtained from the selected area marked in (a). (j) Line EDS profile obtained along the white dashed arrow shown in (f) [2], © 2022 by authors, reproduced with license.**

segregation layer in the TiN liquid-phase sintered ceramic used in this work.

Combining the results of brazing between the Ag–Cu brazing filler metal and the TiN solid-phase sintered ceramic and the results for the three sets of interfacial structures for the Cu brazed TiN liquid-phase sintered ceramic, a bonding mechanism for TiN grains to Cu-rich and Ag-rich phases is proposed, as illustrated in Fig. 3.13. During the liquid-phase sintering process (1400 °C), which was used to fabricate the TiN liquid-phase sintered ceramic, the surfaces of TiN grains were covered with an Fe- and Ni-containing segregation layer due to the interfacial reaction between the TiN grains and the grain boundary components consisting mainly of Fe. The TiN liquid-phase sintered ceramic used in this study was formed by the bonding of TiN grains with a grain boundary phase such as the Ni-containing Fe phase and $Mo_2C$ via this Fe- and Ni-containing segregation layer. The surface to be bonded to the TiN liquid-phase sintered ceramic consisted of flat TiN grains and a grain boundary phase due to the grinding process, as shown in Fig. 3.13(a). Therefore, no Fe- and Ni-containing segregation layer was present on the surfaces of the TiN liquid-phase sintered ceramics to be bonded. As shown schematically in Fig. 3.13(b), the grain boundary components of the TiN liquid-phase sintered ceramic first dissolved into the Ag–Cu liquid phase above the Ag–Cu eutectic temperature, causing erosion of its grain boundary phases. Then, as this erosion progresses, the concentrations of Fe and Ni in the Ag–Cu liquid phase increased, promoting the interfacial reaction with TiN grains to form the Fe- and Ni-containing segregation layer on the surface of TiN grain, as shown in Fig. 3.13(c). While this interfacial reaction was occurring, interdiffusion occurred between the grain boundary phase and the Ag–Cu liquid phase. After brazing, the Ag–Cu liquid phase separated into the Cu-rich and Ag-rich phases by solidification. Most importantly, the following interfacial structure was formed through this Fe- and Ni-

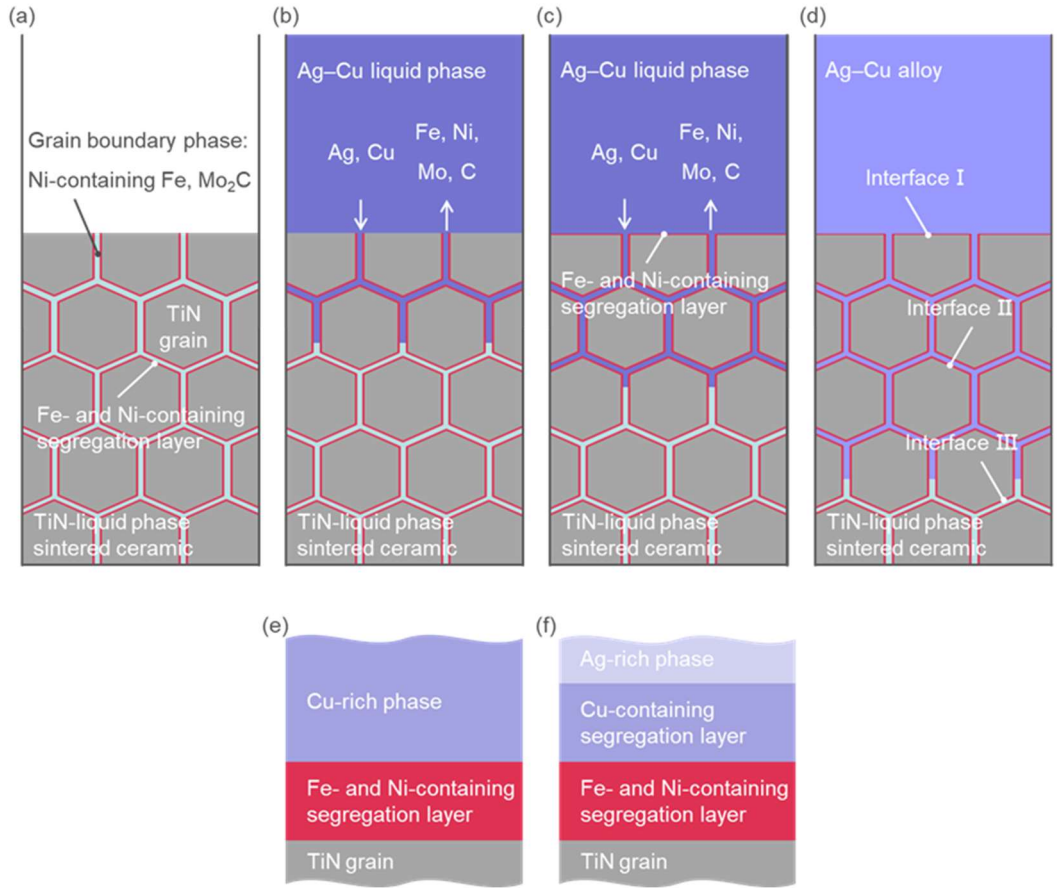


**Fig. 3.13 (a)–(d) Schematic mechanism for the interfacial reaction between the TiN liquid-phase sintered ceramic and Ag–Cu eutectic brazing filler metal during heating above the Ag–Cu eutectic temperature. Details of the interfacial structures at (e) the Cu-rich phase/TiN grain interface and (f) the Ag-rich phase/TiN grain interface for Interface I and Interface II after heating [2], © 2022 by authors, reproduced with license.**

containing layer: Cu-rich phase/Fe- and Ni-containing segregation layer/TiN grain and Ag-rich phase/Cu-containing segregation layer/Fe- and Ni-containing segregation layer/TiN grain (Fig. 3.13(d) and (e), respectively). This suggests that the Fe- and Ni-containing segregation layer contributed to lowering the energy of the entire interfacial reaction system, and furthermore that the formation of the Cu-containing segregation layer between the Ag-rich phase and the Fe- and Ni-containing segregation layer promoted stabilization of the interfacial structure. Thus, a Cu-containing segregation layer may have been present between the Ag-rich phase and the Fe- and Ni-containing

segregation layer. The Cu-containing segregation layer may also have been present between the Cu-rich phase and the Fe- and Ni-containing segregation layer, but it would be difficult to distinguish the Cu signal derived from the Cu-rich layer from that of the Cu-containing segregation layer. Taken together with the results of Ag–Cu brazing of the Cu plate onto the TiN solid-phase sintered ceramic, in which there was no grain boundary phase composed of metal components, the addition of elements to the interfacial reaction system capable of forming a segregation layer between the metal phase and the TiN grain is a key for achieving Ag–Cu brazing onto TiN grains.

### 3.3.3 Interfacial structure of Ag- and Cu-rich phase/WC–Co cemented carbide

A cross-sectional SE image and the elemental distributions of the Cu/WC–Co cemented carbide interface after brazing at 850 °C for 0.5 h are shown in Fig. 3.14. The SEM observation shows that there is no macroscopic interfacial structure at the Cu/WC–Co cemented carbide interface. However, both Ag and Cu, which make up the brazing material, penetrated down to a depth of about 1 μm from the surface of WC–Co cemented carbide. In addition, comparison of Fig. 3.14(a)–(c) shows that the distributions of Ag and Cu coincided well with the grain boundary phase of the WC–Co cemented carbide. These results suggest that Co, which makes up the grain boundary phase of WC–Co cemented carbide, was substituted for Ag and Cu during brazing. This means that Co dissolved into the molten Ag–Cu phase during brazing and mutually diffused with Ag and Cu. Similar to the macroscopic interfacial structure of Cu/TiN liquid-phase sintered ceramics, that of Cu/WC–Co cemented carbides can also be divided into three types of interfaces. The first is the Ag–Cu alloy layer/WC brazing interface (Interface I), which was formed by the

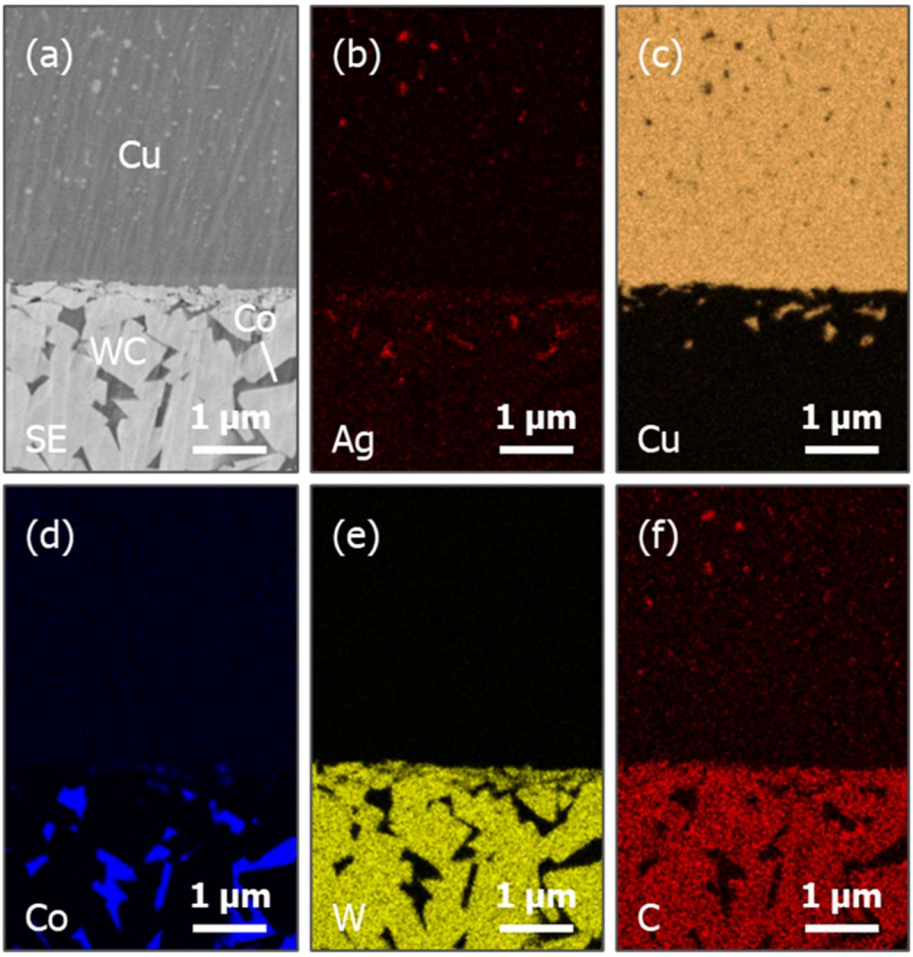


**Fig. 3.14 (a) Cross-sectional SE image of a Cu/WC–Co cemented carbide brazed at 850 °C for 0.5 h with elemental distributions of (b) Ag, (c) Cu, (d) Co, (e) W, and (f) C [1], © 2022 by Elsevier B.V., reproduced with license.**

interfacial reaction between the Ag–Cu liquid phase and WC grains. The second is the substituted Ag–Cu phase/WC interface (Interface II), in which the grain boundary phase of the WC–Co cemented carbide was substituted by the Ag–Cu brazing filler component. The third is the interface between the WC grains and Co without substitution by the Cu-rich and Ag-rich phases in the WC–Co cemented carbide (Interface III).

An HAADF image and elemental distributions of Interface I after brazing at 850 °C for 0.5 h are shown in Figs. 3.15 and 3.16 for the Cu-rich phase/WC grain interface and the Ag-rich phase/WC grain interface, respectively. The highest signal in the Co map was

uniformly located at Interface I between the Cu-rich phase and a WC grain (Fig. 3.15(f)). By comparison, a Cu signal was detected at Interface I between the Ag-rich phase and a WC grain in addition to the Co signal (Fig. 3.16(c) and (d)). Line EDS profiles of Interface I after brazing at 850 °C for 0.5 h are shown in Figs. 3.15(g) and 3.16(g), where the line EDS profiles correspond to the yellow dashed arrows in Figs. 3.15(a) and 3.16(a), respectively. Fig. 3.16(g) shows that the peak position of the Cu signal was shifted toward the Ag-rich phase relative to the peak position of the Co signal, but it is not clear from Fig. 3.15(g) whether a Cu peak signal was present because of the strong Cu signal from the Cu-rich phase. The difference in peak width of Co signal between the Cu-rich phase/WC grain interface and the Ag-rich phase/WC grain interface may be due to the curvature of WC grains in the thickness direction of the Cu/WC thin sections for STEM analysis as in the Cu/TiN thin sections. There was no Co on the WC grain surface of the

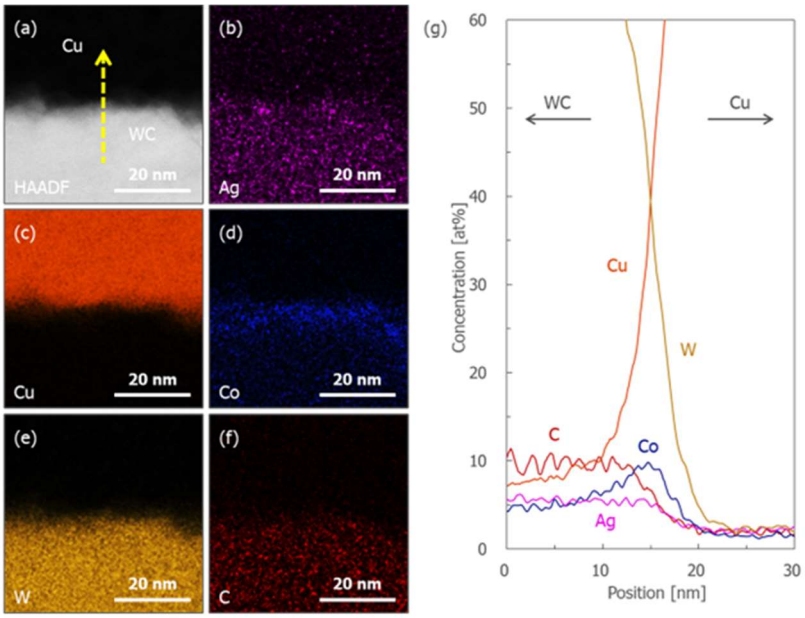


**Fig. 3.15 (a) HAADF image of a Cu-rich phase/WC grain interface after brazing at 850 °C for 0.5 h with elemental distributions of (b) Ag, (c) Cu, (d) Co, (e) W, and (f) C. (g) Line EDS profile is acquired along the yellow arrow shown in (a) [1], © 2022 by Elsevier B.V., reproduced with license.**

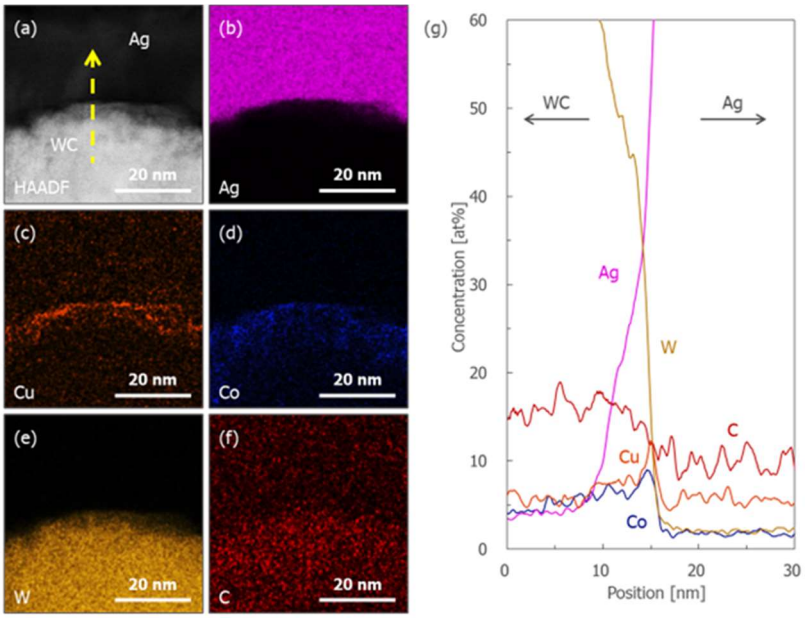


**Fig. 3.16 (a) HAADF image of a Ag-rich phase/WC grain interface after brazing at 850 °C for 0.5 h with elemental distributions of (b) Ag, (c) Cu, (d) Co, (e) W, and (f) C. (g) Line EDS profile is acquired along the yellow arrow shown in (a) [1], © 2022 by Elsevier B.V., reproduced with license.**

WC–Co cemented carbide before brazing (#4 in Fig. 3.3(c)). These results suggest that the Co-containing segregation layer was formed by the interfacial reaction between the WC grains and the Ag–Cu liquid phase, which contained Co derived from the grain boundary phase of the WC–Co cemented carbide. Thus, neither the Cu-rich phase nor Ag-rich phase was not directly bonded to the WC grain.

An HAADF image and elemental distributions of Interface II after brazing at 850 °C for 0.5 h are shown in Figs. 3.17 and 3.18 for the substituted Cu-rich phase/WC grain interface and the substituted Ag-rich phase/WC grain interface, respectively. The highest signal in the Co map is located uniformly between the Cu-rich and Ag-rich phases and the WC grain at Interface II, similar to Interface I (Figs. 3.15 and 3.16), as shown in Figs. 3.17(d) and 3.18(d). In addition, a Cu signal was detected at Interface II between the substituted Ag-rich phase and a WC grain in addition to the Co signal (Fig. 3.18(c) and

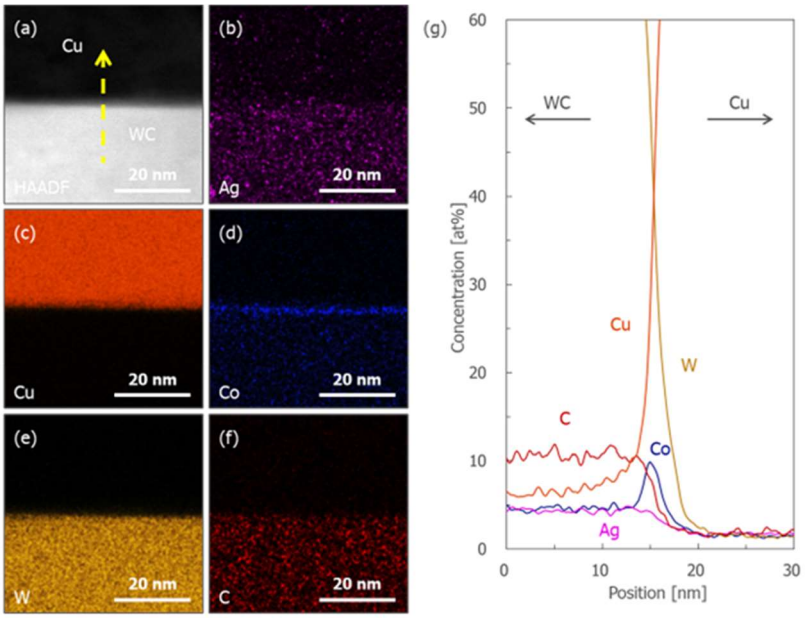


**Fig. 3.17 (a) HAADF image of a substituted Cu-rich phase/WC grain interface after brazing at 850 °C for 0.5 h with elemental distributions of (b) Ag, (c) Cu, (d) Co, (e) W, and (f) C. (g) Line EDS profile is acquired along the yellow arrow shown in (a).**

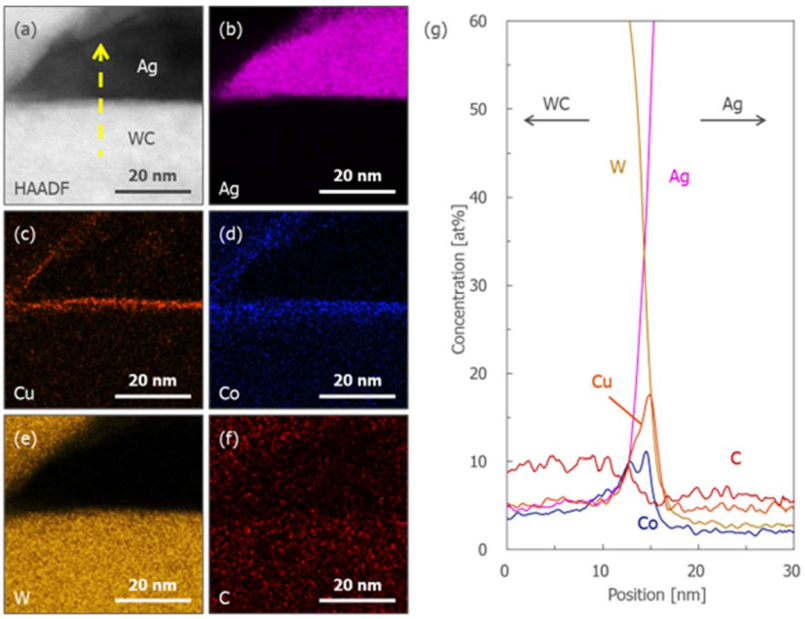


**Fig. 3.18 (a) HAADF image of a substituted Ag-rich phase/WC grain interface after brazing at 850 °C for 0.5 h with elemental distributions of (b) Ag, (c) Cu, (d) Co, (e) W, and (f) C. (g) Line EDS profile is acquired along the yellow arrow shown in (a).**

(d)). The line EDS profiles of Interface II are shown in Figs. 3.17(g) and 3.18(g), corresponding to the yellow dashed arrows in Figs. 3.17(a) and 3.18(a), respectively. In addition, the Cu peak position was shifted toward the Ag-rich phase compared with the Co peak position coinciding with the Ag-rich phase/WC grain interface. The difference in peak width of Co signal between the Cu-rich phase/WC grain interface and the Ag-rich phase/WC grain interface may be due to the curvature of WC grains in the thickness direction of the Cu/WC thin sections for STEM analysis as in Interface I. Most importantly, these features of Interface II formed by interdiffusion between the grain boundary phase and the Ag–Cu liquid phase are in perfect agreement with those of Interface I formed by the interfacial reaction during brazing. The (a) ABF and (b) HAADF images of the substituted Cu-rich phase/WC grain interface and the substituted Ag-rich phase/WC grain interface are shown in Figs. 3.19 and 3.21, respectively. These were observed along the WC $[10\bar{1}0]$ direction. In Figs. 3.19(a) and 3.21(a), most local dark

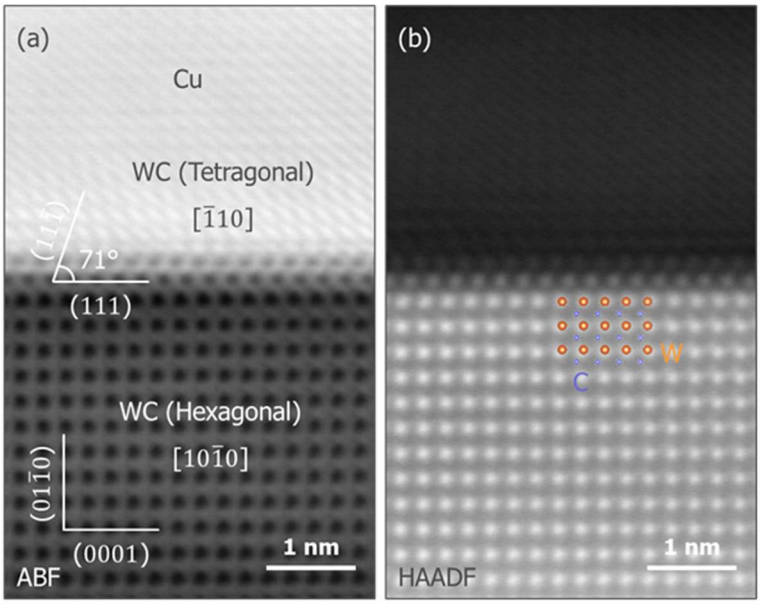


**Fig. 3.19 (a) ABF and (b) HAADF images of the substituted Cu-rich phase/WC grain interface after brazing at 850 °C for 0.5 h.**

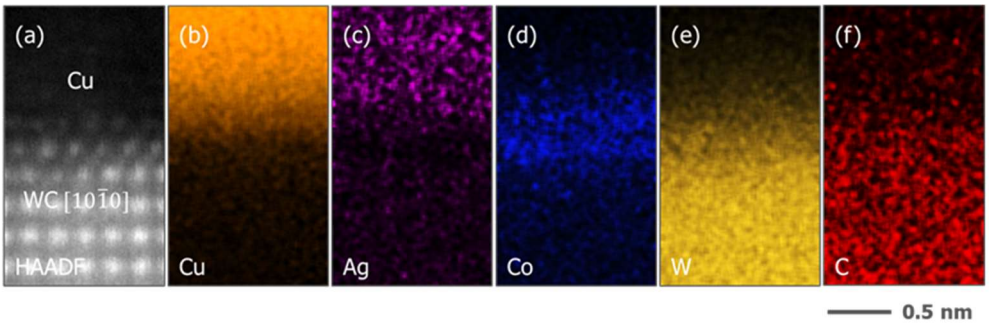


**Fig. 3.20 (a) Detailed HAADF image of the substituted Cu-rich phase/WC grain interface with elemental distributions of (b) Cu, (c) Ag, (d) Co, (e) W, and (f) C.**

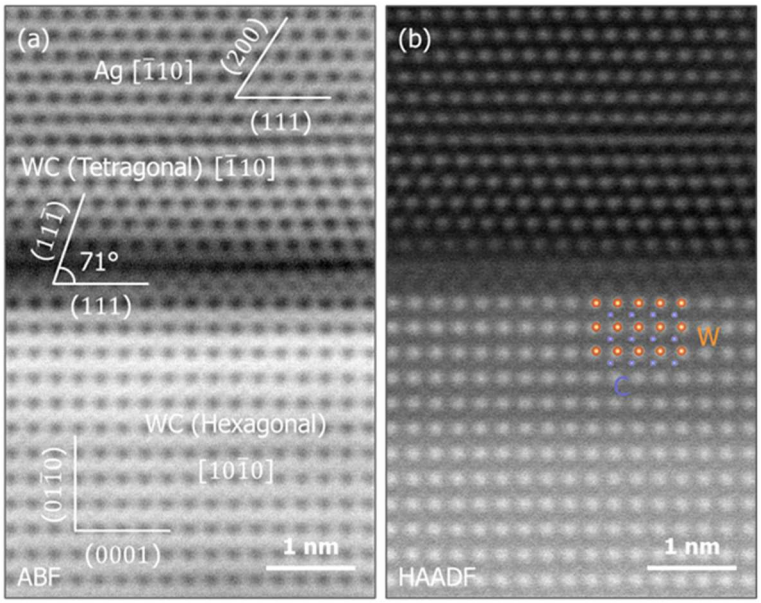


**Fig. 3.21 (a) ABF and (b) HAADF images of the substituted Ag-rich phase/WC grain interface after brazing at 850 °C for 0.5 h.**

contrast corresponds to the W column of hexagonal WC. Ag columns corresponding to the Ag-rich phase observed along the Ag $[\bar{1}10]$ direction are observed in Fig. 3.21, while no Cu columns corresponding to the Cu-rich phase are observed in Fig. 3.19. These results suggest that the Cu-containing segregation layer observed at the Ag–Cu alloy layer/WC grain interface did not have a specific structure, which is consistent with the Cu-containing segregation layer observed at the Ag–Cu alloy layer/TiN grain interface. In

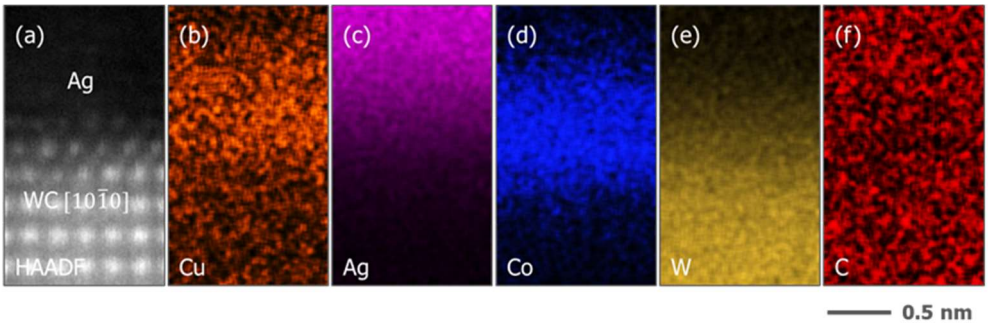


**Fig. 3.22 (a) Detailed HAADF image of the substituted Ag-rich phase/WC grain interface with elemental distributions of (b) Cu, (c) Ag, (d) Co, (e) W, and (f) C.**

addition, comparison of Figs. 3.19, 3.20, 3.21, and 3.22 suggests that the Co-containing segregation layer formed at the Ag–Cu alloy layer/WC grain interface was tetragonal WC formed on the surface of hexagonal WC [11]. Furthermore, Figs. 3.19 and 3.21 show that the orientation relationship between tetragonal WC and hexagonal WC is $[\bar{1}10]$ tetragonal WC//$[10\bar{1}0]$ hexagonal WC, with $(111)$ tetragonal WC//$(0001)$ hexagonal WC. This means that the outermost surface of the hexagonal WC grains was modified to tetragonal $W_xCo_{1-x}C$ [11].

## 3.4 General bonding interfacial structure between Cu and ceramic via Ag–Cu brazing

In Section 3.3.2, it was demonstrated that the Cu-rich phase/Fe- and Ni-containing segregation layer/TiN grain interfacial structure and the Ag-rich phase/Fe- and Ni-containing segregation layer/TiN grain interfacial structure were formed at the Ag–Cu brazed Cu/TiN–Fe–Ni–C–$Mo_2C$ liquid-phase sintered ceramic interface. The Fe- and Ni-containing segregation layer was suggested to be $Ti_xFe_{1-x}N$, in which the outermost surface of TiN grains was modified by the interfacial reaction between Fe and Ni, and TiN grains. In Section 3.3.3, it was demonstrated that the Cu-rich phase/Co-containing

segregation layer/WC grain interfacial structure and the Ag-rich phase/Co-containing segregation layer/WC grain interfacial structure were formed at the Ag–Cu brazed Cu/WC–Co cemented carbide interface. The Co-containing segregation layer was suggested to be $W_xCo_{1-x}C$, in which the outermost surface of the WC grain was modified by the interfacial reaction between Co and WC grains. These results suggest that the interfacial structure formed by Ag–Cu brazing between Cu and ceramic was commonly a Cu-containing segregation layer/modified layer on the ceramic surface/ceramic. Thus, during the bonding process, the formation of the Cu/ceramic bonding interfacial structure required chemical reactions on the ceramic surface, which do not necessarily require Ag. In addition, the general bonding interfacial structure demonstrated in this chapter appeared to be consistent with a bonding interfacial structure consisting of an Al-containing segregation layer as described in Section 2.3.1. Thus, the Al-containing segregation layer at the Ag–Cu alloy layer/TiN grain interface formed by the AMB method was $Ti_xAl_{1-x}N$ [12, 13], in which the outermost surface of the TiN grains was modified by the interfacial reaction with Al when AlN was used as the starting material.

## 3.5 Conclusions

In this chapter, Cu was bonded onto TiN solid/liquid-phase sintered ceramics using Ag–Cu brazing, and the effects of TiN grain formation and metal components of the grain boundary phase on the formation of Ag–Cu alloy layer/TiN grain interface were investigated. In addition, the general structure of the Cu/ceramic bonding interface was discussed based on a comparison of the Ag–Cu alloy layer/TiN grain interfacial structure and the Ag–Cu alloy layer/WC grain interfacial structure obtained by bonding Cu onto WC–Co cemented carbide using Ag–Cu brazing. These interfacial structures were

summarized in Fig. 3.23. The main conclusions were as follows:

1. Ag–Cu brazing does not produce a bonding interfacial structure between Cu and TiN solid-phase sintered ceramic without a metal grain boundary phase
2. Ag–Cu brazing of Cu onto a TiN–Fe–Ni–C–$Mo_2C$ liquid-phase sintered ceramic with an Fe-based grain boundary phase produced an interfacial structure of Cu(Ag)-rich phase/Cu-containing segregation layer/Fe- and Ni-containing segregation layer/TiN grain.
3. The Fe- and Ni-containing segregation layer was $Ti_xFe_{1-x}N$, in which the outermost

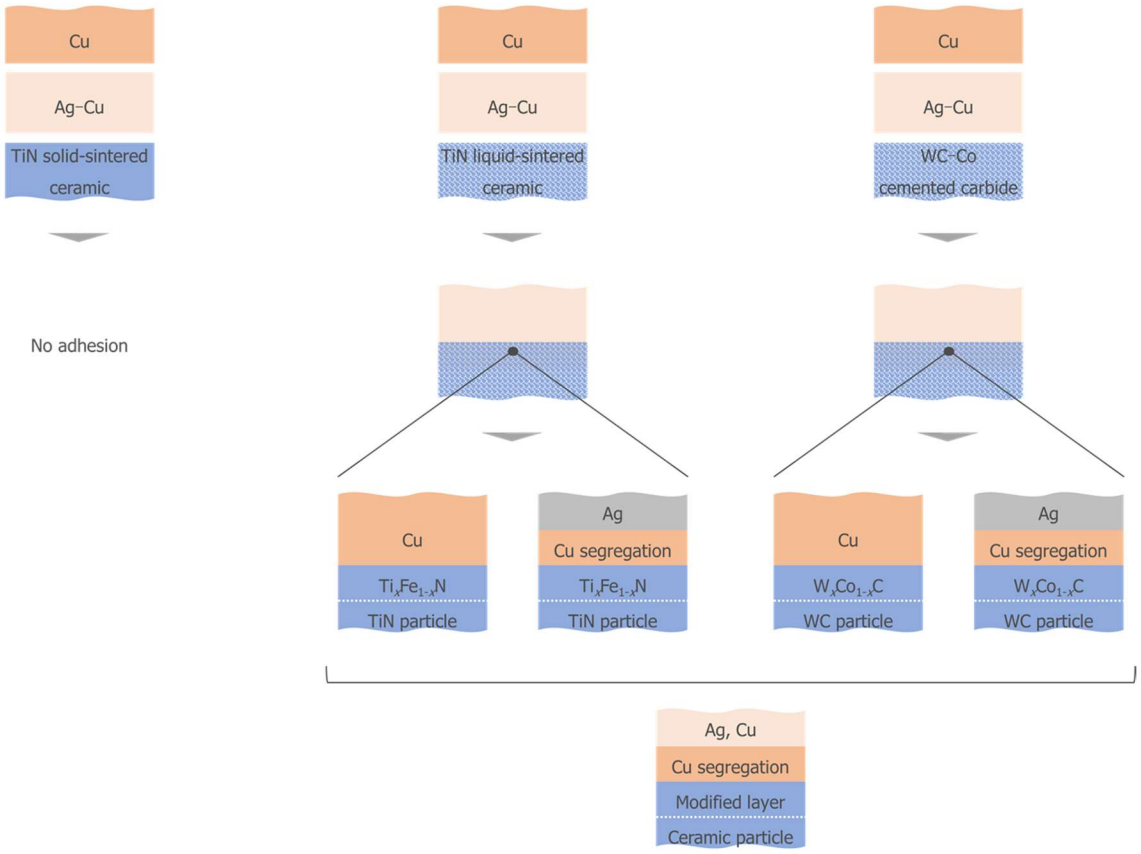


**Fig.3.23 Cu/ceramic interfacial structures discussed in this chapter.**

surface of TiN grains was modified by interfacial reaction with Fe and Ni.

4. Ag–Cu brazing of Cu onto WC–Co cemented carbide produced a Cu(Ag)-rich phase/Cu-containing segregation layer/Co-containing segregation layer/WC grain interfacial structure.
5. The Co-containing segregation layer was tetragonal $W_xCo_{1-x}C$, in which the outermost surface of WC grains was modified by interfacial reaction with Co.
6. The general Cu/ceramic bonding interfacial structure by Ag–Cu brazing was found to be a Cu-containing segregation layer/modified layer on the ceramic surface/ceramic structure, in which Ag was not an essential component.

## References

[1] N. Terasaki, N. Kon, H. Chiba, T. Ohashi, T. Sekino, Co segregation on WC grain formed in an interfacial reaction between WC–Co cemented carbide and Ag–Cu eutectic brazing material, Materials Letters, 332, 2023, 133551.

[2] N. Terasaki, N. Kon, H. Chiba, T. Ohashi, T. Sekino, Interfacial structure between TiN sintered ceramics with and without an Fe-containing grain boundary phase and Ag–Cu eutectic brazing filler material, SN Applied Sciences, 5, 2023, 46.

[3] P.R. Subrumanian, J.H. Perepezko, The Ag–Cu (Silver-Copper) system, Journal of Phase Equilibria, 14(1), 1993, 62–75.

[4] M.A. Kuzenkova, P.S. Kislyi, Vacuum sintering of titanium nitride, Soviet Powder Metallurgy and Metal Ceramics 10, 1971, 125–128.

[5] E.A. Owen, A.H. Sully, On the migration of atoms in iron-nickel alloys, The London, Edinburgh, and Dublin Philosophical Magazine and Journal of Science, 31(207), 1941, 314–338.

[6] K. Ono, Y. Ueda, A. Yamaguchi, J. Moriyama, Thermodynamic study of Fe–Ni solid solution, Transactions of the Japan Institute of Metals, 18, 1977, 610–616.

[7] L.J. Swartzendruber, V.P. Itkin, C.B. Alcock, The Fe–Ni (Iron-Nickel) System, Journal of Phase Equilibria, 12, 1991, 288–312.

[8] V.N. Eremenko, T.Y. Velikanova, The type of crystallization and composition of the higher molybdenum carbide, Soviet Powder Metallurgy and Metal Ceramics, 4, 1965, 30–32.

[9] J. Qin, Q. Huang, X. Wang, X. Suo, J. Wang, H. Li, Interfacial metal/ceramic bonding mechanism for metallization of ceramics via cold spraying, Journal of Materials Processing Technology, 288, 2021, 116845.

[10] H. Ohtani, M. Hillert, A thermodynamic assessment of the Fe–N–Ti system, Calphad, 15(1), 1991, 41–52.

[11] A.M. Augustine, P. Ravindran, Role of W-site substitution on mechanical and electronic properties of cubic tungsten carbide, Journal of Physics: Condensed Matter, 32(14), 2020, 145701.

[12] K. Kutschej, P.H. Mayrhofer, M. Kathrein, P. Polcik, R. Tessadri, C. Mitterer, Structure, mechanical and tribological properties of sputtered $Ti_{1-x}Al_xN$ coatings with $0.5 \leq x \leq 0.75$, Surface and Coatings Technology, 200(7), 2005, 2358–2365.

[13] K. Yamamoto, Y. Tatsuhira, Y. Iwai, The Relationship between coating property and solid particle erosion resistance of AIP-deposited TiAlN coatings with different Al contents, Coatings, 11, 2021, 992.

# Chapter 4: Effects of interfacial structure on peel strength between Cu and AlN bonded with a Mg–Ti-based co-deposited film

## 4.1 Introduction

Chapters 2 and 3 demonstrated that Ag is not essential in bonding between Cu and TiN and that the surface of TiN particles must be modified by interfacial reactions with Al or Fe.

In this chapter, in order to clarify a Cu/AlN bonding interfacial structure using Ag-free bonding materials that can completely eliminate Ag-ECM, the structure of the Cu/AlN interface bonded using Mg–Ti [1] and Mg–Ti–Fe co-deposited films was investigated. The melting point of Mg (650 °C) and the Cu-rich Cu–Mg eutectic temperature (726 °C) are roughly equivalent to the melting range of Ag–Cu based active brazing alloys [2]. In addition, Mg hardly forms a solid solution with Ti, and these two metals do not form intermediate phases with each other [3]. Therefore, the Cu–Mg–Ti system is not expected to inhibit the interfacial reaction between Ti and AlN. Furthermore, the relationship between the peel strength of the Cu/AlN bonding interface by surface and interfacial cutting analysis system (SAICAS) test and the structure of the Cu/AlN bonding interface was considered [1]. Assuming that a Cu/AlN bonding interface equivalent to the Cu/AlN bonding interface in the Ag–Cu–Ti system is formed in the Cu–Mg–Ti system, the intentional addition of Fe is expected to replace the modified layer formed on the TiN particle surface from $Ti_xAl_{1-x}N$ to $Ti_xFe_{1-x}N$. Therefore, the effects of Fe addition on the Cu/AlN interfacial structure and its peel strength were also investigated.

## 4.2 Experimental procedure

### 4.2.1 Materials and sample fabrication

OFC (37 mm × 37 mm × 0.3 mm) with six different Mg–Ti-based co-deposited films on one side of a Cu plate was used as a source of Mg and Ti to fabricate a Cu–Mg–Ti ternary system by transient liquid phase (TLP) bonding [4–6]. The AMB method, in which TLP bonding is applied between a Cu plate and an AlN substrate via Ag–Ti-based paste, has been reported to be effective in the formation reaction of the Cu–Ag liquid phase and the TiN layer at the Cu/AlN interface as well as in the use of Cu–Ag–Ti-based alloys [7, 8]. This bonding method between metal and ceramic is called active TLP bonding [5]. The composition of each Mg–Ti-based co-deposited film and the amounts of Mg, Ti, and Fe are shown in Table 4.1. For the Mg–11.5 wt% Ti, Mg–17.8 wt% Ti, and Mg–30.2 wt% Ti co-deposited films, the amount of Mg ($w_{\mathrm{Mg}}$) was commonly about 1.04 mg/cm$^2$ while the amount of Ti ($w_{\mathrm{Ti}}$) was about 0.14, 0.23, and 0.45 mg/cm$^2$, respectively. For the Mg–15.0 wt% Ti–15.7 wt% Fe, Mg–13.5 wt% Ti–23.7 wt% Fe, and Mg–11.0 wt% Ti–38.3 wt% Fe co-deposited films, $w_{\mathrm{Mg}}$ and $w_{\mathrm{Ti}}$ were commonly about 1.04 mg/cm$^2$ and 0.23 mg/cm$^2$, while the amount of Fe ($w_{\mathrm{Fe}}$) was about 0.24, 0.39, and 0.79 mg/cm$^2$, respectively. Both $w_{\mathrm{Mg}}$ and $w_{\mathrm{Ti}}$ correspond to the amounts of Ag and Ti that can form a good Cu/AlN interface using Ag–Ti paste [7, 8]. $w_{\mathrm{Fe}}$ = 0.24 mg/cm$^2$ corresponds to the amount of Fe dissolved from the TiN liquid-phase sintered ceramic into the molten Ag–Cu phase based on the composition ratio of the grain boundary phase in the TiN liquid-phase sintered ceramic presented in Chapter 3, while $w_{\mathrm{Fe}}$ = 0.39 mg/cm$^2$ is based on the assumption that the TiN grain boundary phase is entirely

**Table 4.1 Amounts of Mg, Ti, and Fe in Mg–Ti-based co-deposited films.**

| Mg–Ti-based co-deposited film | Element amount [mg/cm²] | | |
|---|---|---|---|
| | $w_{Mg}$ | $w_{Ti}$ | $w_{Fe}$ |
| Mg–11.5 wt% Ti | 1.04 | 0.14 | 0.00 |
| Mg–17.8 wt% Ti | 1.04 | 0.23 | 0.00 |
| Mg–30.2 wt% Ti | 1.04 | 0.45 | 0.00 |
| Mg–15.0 wt% Ti–15.7 wt% Fe | 1.04 | 0.23 | 0.24 |
| Mg–13.5 wt% Ti–23.7 wt% Fe | 1.04 | 0.23 | 0.39 |
| Mg–11.0 wt% Ti–38.3 wt% Fe | 1.04 | 0.23 | 0.79 |

composed of Fe and $w_{\mathrm{Fe}}$ = 0.79 mg/cm$^2$ on the assumption that excess Fe dissolves into the molten Ag–Cu phase [9]. Commercially available sintered AlN (50 mm × 50 mm × 1 mm) was used as the AlN substrate, which contained $Y_2O_3$, a sintering additive, as a second phase. The Cu plate was stacked so that the Mg–Ti-based co-deposited film faced the AlN substrate. The stacked specimens were vacuum heated between 800 °C and 950 °C for 0.5 h under a constant pressure of 1 MPa, with heating and cooling rates of 10 °C/min.

### 4.2.2 Characterization

Cross-sections of the Cu/AlN bonded specimens were observed by SEM. The bonded specimens were mounted in acrylic polymer at room temperature and polished using standard metallographic techniques, followed by a final polishing using an argon-based ion beam polisher (ArBlade 5000, Hitachi High-Tech) to obtain a smooth surface for observation. The microstructures of all cross-sectional specimens were evaluated using a GeminiSEM 500 system (Carl Zeiss AG), which was operated at 1.8 kV. In addition, the

microstructures of the AlN surface and the cross-sectional Cu/AlN interface after the SAICAS test, as described in Section 4.2.3, were analyzed using an electron probe micro analyzer (EPMA) and SEM, respectively. SEM observations and elemental analysis of the AlN surface were performed using a JXA–8530F system (JEOL) operated at 15 kV. Cross-sections of Cu/AlN bonded specimens, which were fabricated as described the previous section, were analyzed using a GeminiSEM 500 system operated at 1.8 kV. In addition, the microstructural details of the Cu/AlN interface were evaluated using STEM. Thin Cu/AlN sections for STEM observations were prepared using a focus ion beam system (Scios, Thermo Fisher Scientific) with thickness between 30 and 100 nm. A Titan G2 ChemiSTEM system (Thermo Fisher Scientific) with an EDS system (NSS7, Thermo Fisher Scientific) operating at 200 kV was used to evaluate the elemental distributions of the thin sections.

### 4.2.3 SAICAS test

The peel strength of the Cu/AlN interface was evaluated using the SAICAS [10]. End milling (10-mm diameter) was performed to reduce the Cu plate thickness of the Cu/AlN bonded specimens from 0.3 mm to 0.03 mm. Using the SAICAS (EN, DAIPLA WINTES) shown in Fig. 4.1, the reduced Cu plates were cut using a diamond cutting blade with a rake angle of 20°, a clearance angle of 10°, and a blade width ($w$) of 0.3 mm at a vertical speed of 0.1 μm/s and a horizontal speed of 2 μm/s. Two-axis motion of the diamond cutting blade was used in the early stage of cutting, and the motion was then controlled to single-axis motion after reaching the Cu/AlN interface. The peel strength ($P$) at the Cu/AlN interface by the SAICAS test was determined using Equation (4.1):

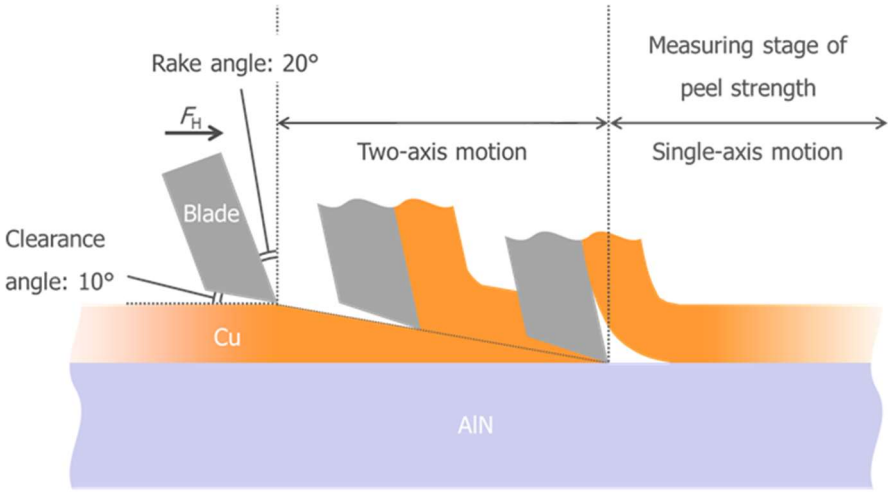


**Fig. 4.1 Schematic diagram of the SAICAS system [1], © 2023 by authors, reproduced with license.**

$$P = {}^{F_H}/_{w} \tag{4.1}$$

Here, $F_H$ is the average horizontal force acting on the diamond cutting blade during single-axis motion, which is calculated using data obtained during the time period 350–500 s.

## 4.3 Results and discussion

### 4.3.1 Development of Cu/AlN interfacial structure for various Ti amounts and bonding temperatures

A relatively low-magnification cross-sectional SE image of the interface between Cu and AlN bonded at 800 °C for 0.5 h with $w_{Mg}$ = 1.04 mg/cm$^2$ and $w_{Ti}$ = 0.14 mg/cm$^2$ is shown in Fig. 4.2. It can be seen that Cu and AlN form a good bonding interface without microscale gaps and voids through the TiN layer. In addition, Cu–Mg IMCs such as

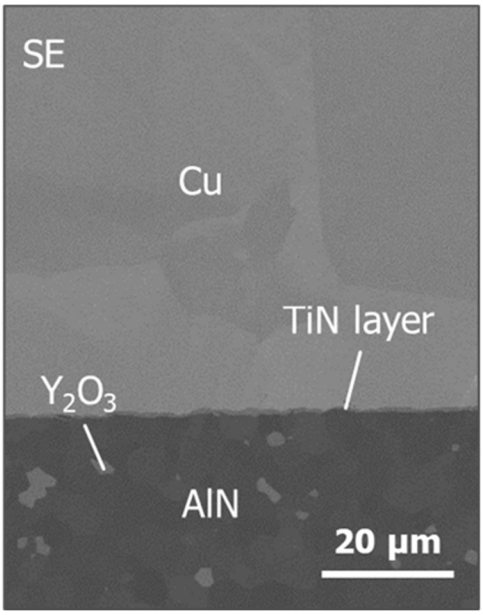


**Fig. 4.2 Cross-sectional SE image of the Cu/AlN interface bonded at 800 °C for 0.5 h with $w_{Mg}$ = 1.04 mg/cm$^2$ and $w_{Ti}$ = 0.14 mg/cm$^2$ [1], © 2023 by authors, reproduced with license.**

$Cu_2Mg$ (cubic, $Fd\bar{3}m$, $a$ = 7.034 Å) and $CuMg_2$ (orthorhombic, $Fddd$, $a$ = 5.275 Å, $b$ = 9.044 Å, $c$ = 18.328 Å) did not form near the Cu/AlN interface [2, 11]. Thus, the interfacial reaction between the molten Cu–Mg–Ti phase and AlN proceeded sufficiently, and the isothermal solidification was completed by the diffusion of Mg into the Cu plate, indicating that active TLP bonding using the Cu–Mg–Ti ternary system was as beneficial for bonding between Cu and AlN as conventional methods using the Cu–Ag–Ti system, such as brazing and active TLP bonding.

A collection of cross-sectional EsB images of the Cu/AlN interface bonded for 0.5 h between 800 °C and 950 °C is shown in Fig. 4.3. The values of $w_{Ti}$ in each Mg–Ti co-deposited film were 0.14 mg/cm$^2$, 0.23 mg/cm$^2$, and 0.45 mg/cm$^2$ for Fig. 4.3(a1–4), (b1–4), and (c1–4), respectively. For all bonding temperatures ($T_B$) and $w_{Ti}$, TiN layers consisting of two phases with different brightness were formed at the Cu/AlN interface. In the TiN layer, the dark gray phase corresponds to TiN (cubic, $Fm\bar{3}m$, $a$ = 4.239 Å) [12],

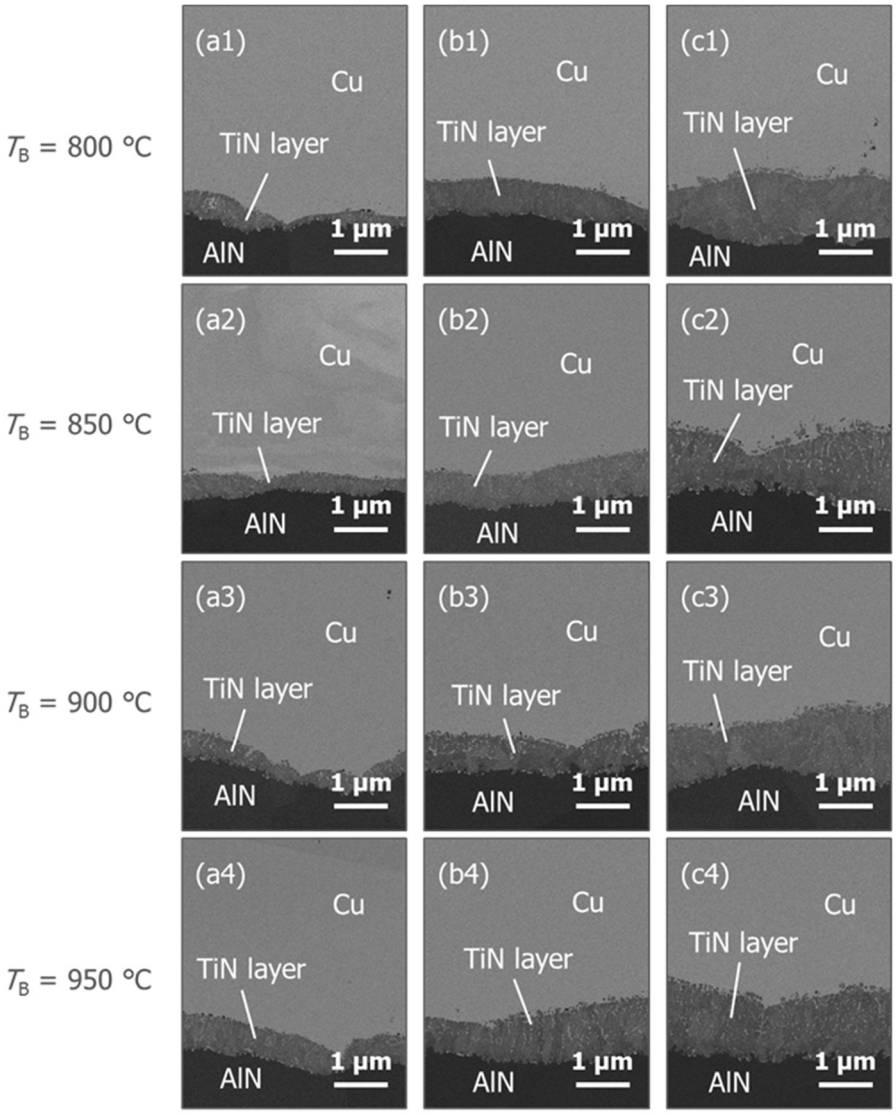


**Fig. 4.3 Collection of cross-sectional EsB images of the Cu/AlN interface bonded for 0.5 h between 800 °C and 950 °C with $w_{Mg}$ = 1.04 mg/cm$^2$ and $w_{Ti}$ = (a1–4) 0.14 mg/cm$^2$, (b1–4) 0.23 mg/cm$^2$, and (c1–4) 0.45 mg/cm$^2$ [1], © 2023 by authors, reproduced with license.**

while the brightness of the light gray phase coincides well with that of the Cu plate. This suggests that the TiN layer formed by the interfacial reaction between the molten Cu–Mg–Ti phase and AlN had a composite structure consisting of TiN particles and a Cu-containing grain boundary phase. The $T_B$ dependence of the TiN layer thickness ($t_{TiN}$) at the Cu/AlN interface bonded for 0.5 h between 800 °C and 950 °C is shown in Fig. 4.4. The dotted lines correspond to the $t_{TiN}$ per unit area estimated from each amount of Ti

using Equation (4.3) for the single-substitution reaction shown in Equation (4.2):

$$\mathrm{Ti} + \mathrm{AlN} \rightarrow \mathrm{TiN} + \mathrm{Al} \tag{4.2}$$

$$t_{\mathrm{TiN}} = V_{\mathrm{TiN}} \cdot n_{\mathrm{TiN}} = V_{\mathrm{TiN}} \cdot n_{\mathrm{Ti}} = {}^{M_{\mathrm{TiN}}}/_{d_{\mathrm{TiN}}} \cdot {}^{w_{\mathrm{Ti}}}/_{M_{\mathrm{Ti}}} \tag{4.3}$$

Here, $V_{\mathrm{TiN}}$, $n_{\mathrm{TiN}}$, $n_{\mathrm{Ti}}$, $M_{\mathrm{TiN}}$, $M_{\mathrm{Ti}}$, and $d_{\mathrm{TiN}}$ are the molar volume of TiN, the molar amounts of TiN and Ti, the molar masses of TiN and Ti, and the density of TiN, respectively. The amounts of TiN and Ti that are produced and consumed are equal according to Equation (4.2). These parameters are as follows: $M_{\mathrm{TiN}}$ = 61.8737 g/mol, $M_{\mathrm{Ti}}$ = 47.867 g/mol, and $d_{\mathrm{TiN}}$ = 5.22 g/cm$^3$. It can be seen that $t_{\mathrm{TiN}}$ increases with increasing $T_{\mathrm{B}}$ and $w_{\mathrm{Ti}}$. In addition, $t_{\mathrm{TiN}}$ obtained from SEM observations was greater

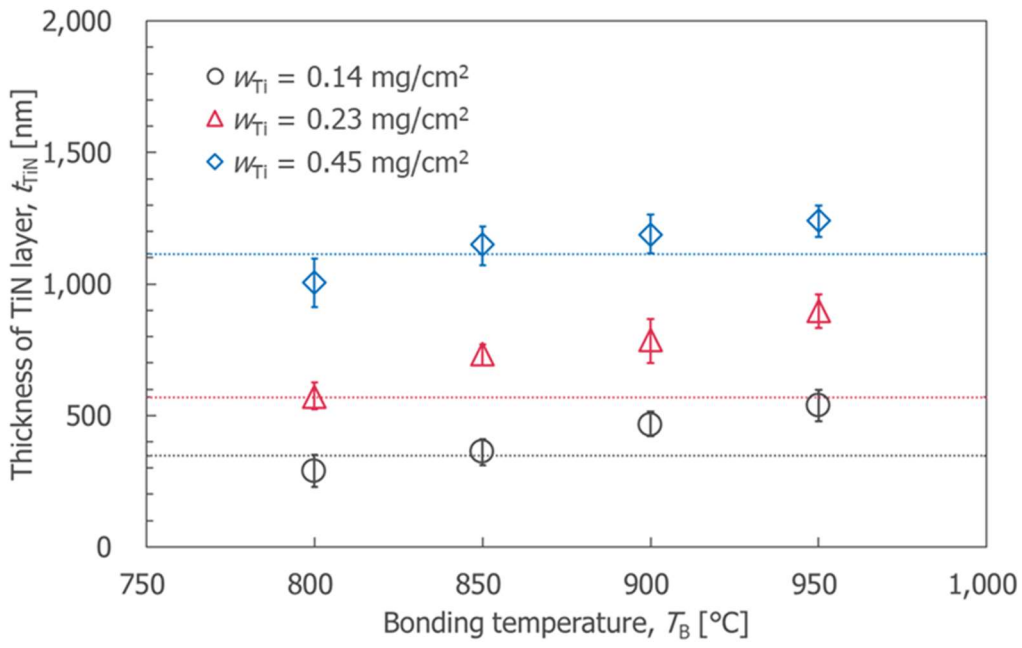


**Fig. 4.4 TiN layer thickness at the Cu/AlN interface versus bonding temperature. The dotted lines correspond to the TiN layer thickness estimated from the amount of Ti [1], © 2023 by authors, reproduced with license.**

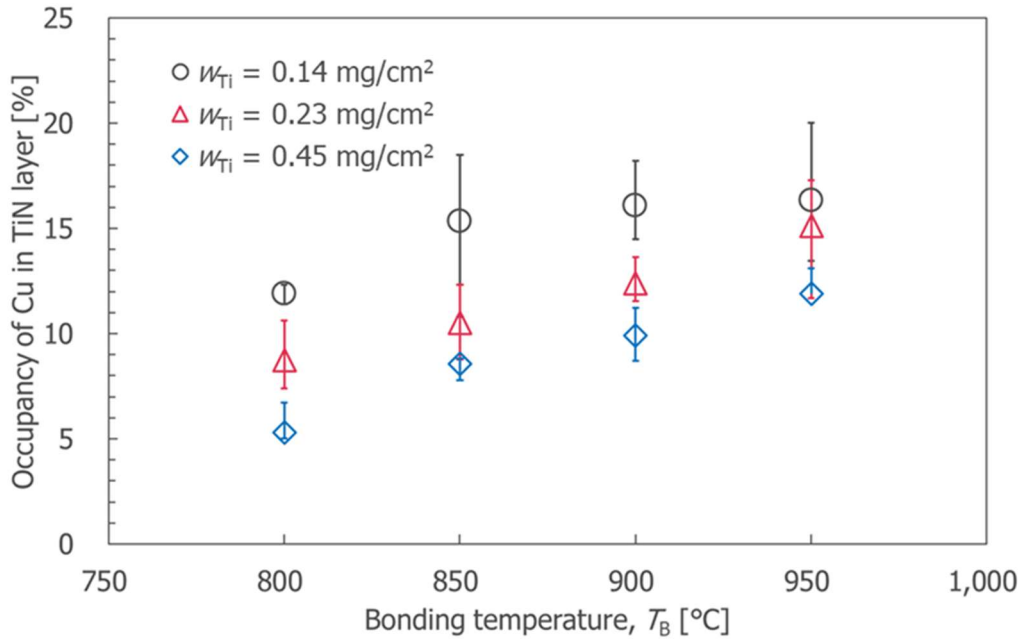


**Fig. 4.5 Cu occupancy in TiN layer at the Cu/AlN interface versus bonding temperature [1], © 2023 by authors, reproduced with license.**

than that estimated using Equation (4.3) when $T_B$ was higher than about 850 °C. This suggests that the increase in the occupancy of Cu in the TiN layer with increasing $T_B$ shown in Fig. 4.5 increased the apparent thickness of the TiN layer grown by the interfacial reaction between the molten Cu–Mg–Ti phase and AlN. This means that increasing $T_B$ strongly induced mixing of TiN particles with the molten Cu–Mg–Ti phase.

### 4.3.2 Peel strength of Cu/AlN interface by the SAICS test

The $w_{Ti}$ dependence of peel strength ($P$) at the Cu/AlN interface is shown in Fig. 4.6. The dotted lines correspond to the average $P$ at each $T_B$. No Cu/AlN bonded specimens fractured in the Cu plate in this study. $P$ was approximately constant for each $T_B$, with no dependence on $w_{Ti}$. In addition, $P$ increased threefold with increasing $T_B$ from about 5 N/mm at $T_B$ = 800 °C to about 15 N/mm at $T_B$ = 950 °C. Fig. 4.7 clearly shows that $P$

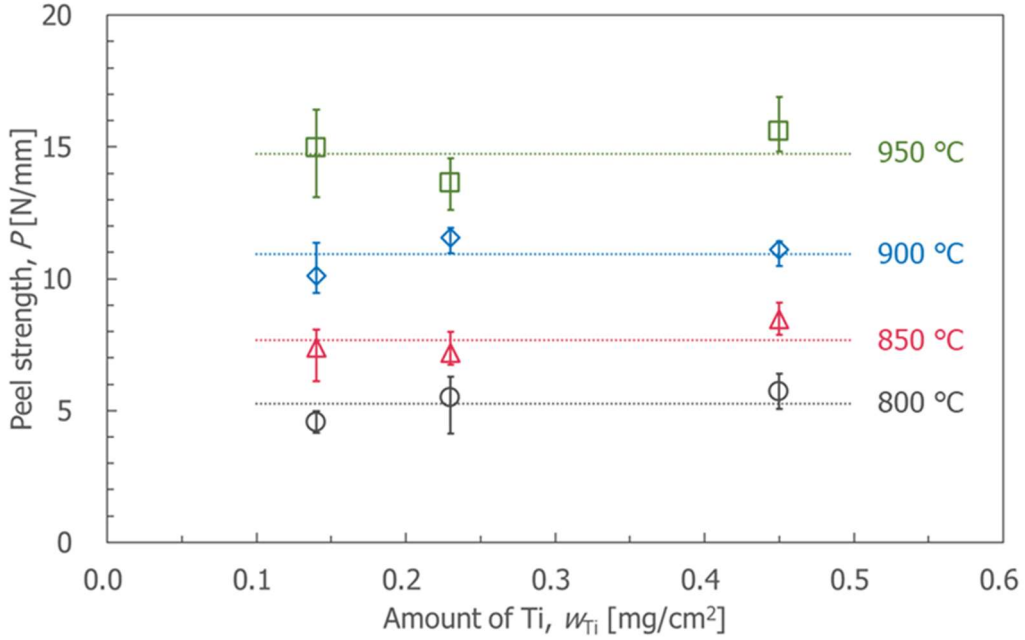


**Fig. 4.6 Peel strength at the Cu/AlN interface as a function of the amount of Ti [1], © 2023 by authors, reproduced with license.**

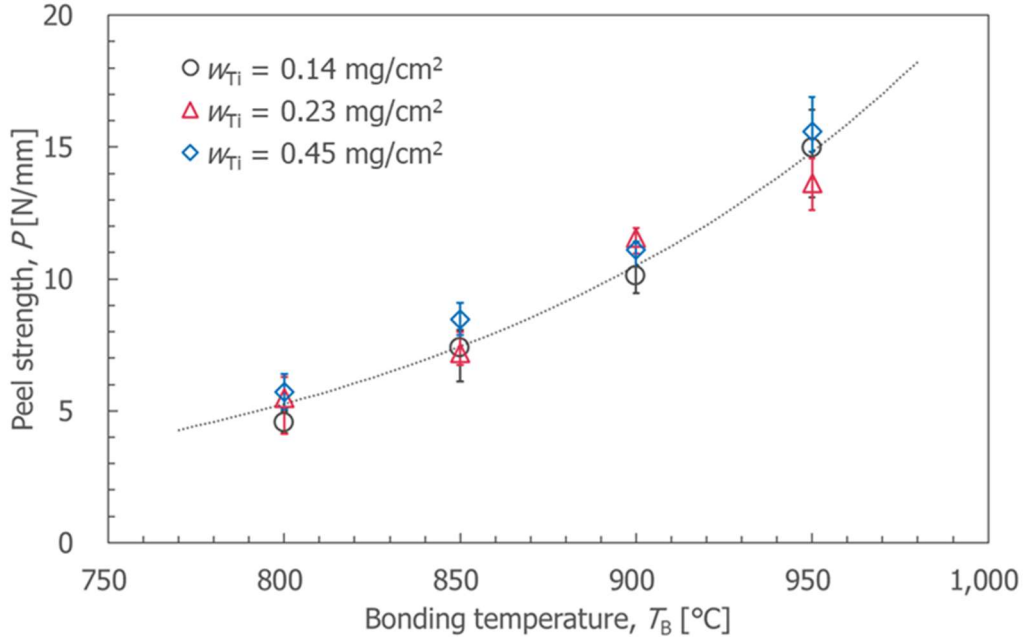


**Fig. 4.7 Peel strength at the Cu/AlN interface as a function of bonding temperature [1], © 2023 by authors, reproduced with license.**

increased exponentially with $T_B$ between 800 °C and 950 °C. When compared with the $T_B$ dependence of $t_{TiN}$ shown in Fig. 4.4, this suggests that the effect of $t_{TiN}$ on $P$ was relatively small, meaning that this behavior of $P$ was dominated by $T_B$ when the interfacial reaction between the molten Cu–Mg–Ti phase and AlN could form a TiN layer between Cu and AlN to achieve a good Cu/AlN interface.

Surface optical images of Cu/AlN bonded specimens prepared at 800 °C and 950 °C for 0.5 h with $w_{Ti}$ = 0.45 mg/cm$^2$ according to SAICAS tests are shown in Figs. 4.8 and 4.9, respectively. The cutting direction is from left to right. Surface backscattered electron (BSE) images with elemental distributions of the Cu/AlN bonded specimens shown in Figs. 4.8(b)–(g) and 4.9(b)–(g) were obtained from the yellow dotted area in Figs. 4.8(a) and 4.9(a), respectively. The cross-sectional EsB images of the Cu/AlN interface shown

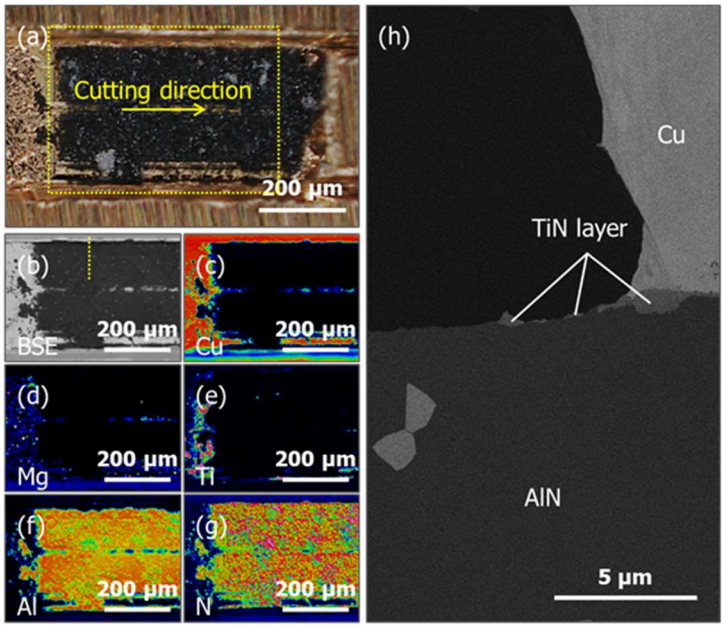


**Fig. 4.8 (a) Optical image of a specimen bonded at 800 ℃ for 0.5 h after the SAICAS test. $w_{Mg}$ and $w_{Ti}$ were 1.04 mg/cm$^2$ and 0.45 mg/cm$^2$, respectively. (b) BSE image with elemental distributions: (c) Cu, (d) Mg, (e) Ti, (f) Al, and (g) N obtained from the yellow dotted area in (a). (h) Cross-sectional EsB image at a Cu/AlN interface obtained along the yellow dotted line in (b) [1], © 2023 by authors, reproduced with license.**

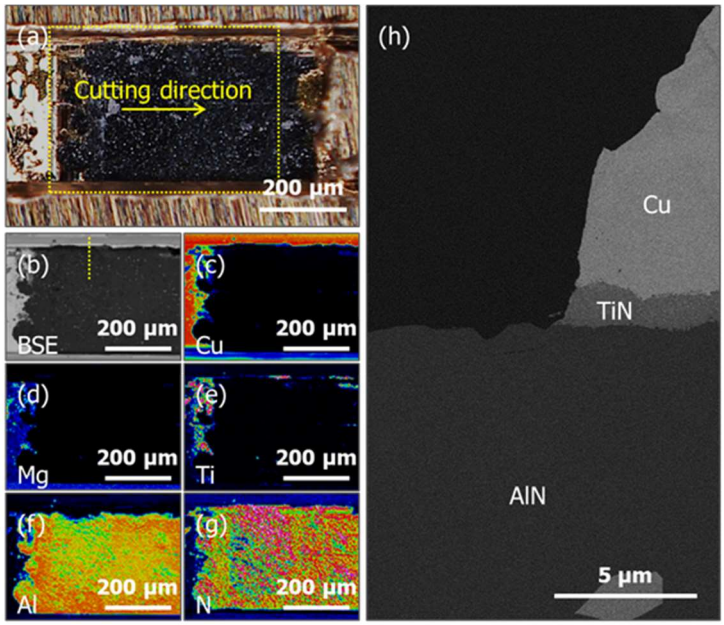


**Fig. 4.9 (a) Optical image of a specimen bonded at 950 °C for 0.5 h after the SAICAS test. $w_{Mg}$ and $w_{Ti}$ were 1.04 mg/cm$^2$ and 0.45 mg/cm$^2$, respectively. (b) BSE image with elemental distributions: (c) Cu, (d) Mg, (e) Ti, (f) Al, and (g) N obtained from the yellow dotted area in (a). (h) Cross-sectional EsB image at a Cu/AlN interface obtained along the yellow dotted line in (b) [1], © 2023 by authors, reproduced with license.**

in Figs. 4.8(h) and 4.9(h) were obtained from the yellow dotted lines in Figs. 4.8(b) and 4.9(b), respectively. In Fig. 4.8(a), it can be seen that the cutting surface of the Cu/AlN bonded specimen, where the Cu plate was peeled off after the SAICAS test, consists of light gray areas and black areas. The appearance of these light gray areas, which were small on the cutting surface, is consistent with that of the original AlN substrate. This suggests that fractures partially occurred within the AlN substrate during the SAICAS test. However, comparison between Fig. 4.8(a) and Fig. 4.8(c)–(g) reveals that the large black areas on the cutting surface are not TiN, but rather AlN. In addition, Fig. 4.8(h) shows that although the TiN layer partially remains on the cutting surface, mainly AlN is exposed. Surface and cross-sectional observations of Cu/AlN bonded specimens after the SAICAS test suggest that the main fracture mode of the Cu/AlN interface in the SAICAS

test was TiN/AlN interfacial fracture. By comparing Fig. 4.9(a) and Fig. 4.9(b)–(g), it can be seen that the cutting surface after the SAICAS test of the Cu/AlN bonded specimen fabricated at $T_B$ = 950 °C was dominated by the black area corresponding to AlN. In addition, the cross-sectional EsB image of the Cu/AlN interface shown in Fig. 4.9(h) reveals that fracture occurred at the TiN layer/AlN interface regardless of the increase in $t_{TiN}$ with increasing $T_B$. Most importantly, taken together with the EPMA and SEM observations, the characteristics of the Cu/AlN interfacial fracture mode in the Cu/AlN bonded specimen fabricated at $T_B$ = 800 °C, which was classified in the lowest Cu/AlN interfacial peel strength group shown in Fig. 4.8, were completely consistent with those in the highest Cu/AlN interfacial peel strength group fabricated at $T_B$ = 950 °C, as shown in Fig. 4.9. This suggests that the threefold difference in peel strength at the Cu/AlN interface between $T_B$ = 800 °C and $T_B$ = 950 °C corresponded to a difference in bond strength at the TiN layer/AlN interface, meaning that the bond strength of the TiN layer/AlN interface, which consisted of a TiN particle/AlN interface and a Cu grain boundary phase/AlN interface, was lower than that of the Cu plate/TiN layer interface and the Cu grain boundary phase/TiN particle interface, which consists of a Cu phase/TiN particle interface.

Cross-sectional HAADF images of the TiN layer/AlN interface bonded at $T_B$ = 800 °C for 0.5 h with $w_{Ti}$ = 0.14 mg/cm$^2$ are shown in Fig. 4.10(a)–(c). The line EDS profiles of the TiN layer/AlN interface shown in Fig. 4.10(d) and (e) were obtained from the yellow dotted arrows shown in Fig. 4.10(b) and (c), respectively. The regions of bright contrast observed in the TiN layer correspond to signals from the Cu-containing grain boundary phases. It can be seen that the TiN layer/AlN interface consisted of two different interfaces: one where TiN particles and AlN were bonded via the Cu-containing grain

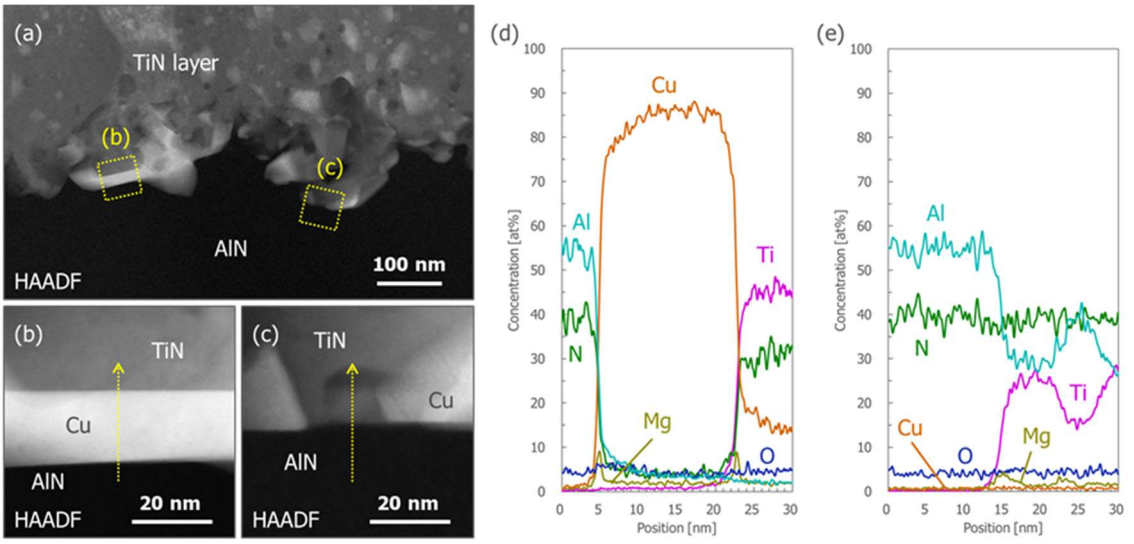


**Fig. 4.10 (a–c) Cross-sectional HAADF images of a TiN layer/AlN interface bonded at 800 °C for 0.5 h. $w_{Mg}$ and $w_{Ti}$ were 1.04 mg/cm$^2$ and 0.45 mg/cm$^2$, respectively. Line EDS profiles of (d) TiN/AlN indirect interface and € TiN/AlN direct interface. The line EDS profiles in (d) and (e) were obtained along the yellow dotted arrows in (b) and (c), respectively [1], © 2023 by authors, reproduced with license.**

boundary phase (Fig. 4.10(b)), and another where TiN particles and AlN were directly bonded (Fig. 4.10(c)). In Fig. 4.10(d), the Mg signal has peaks at both the Cu-containing grain boundary phase/AlN interface and the TiN particle/Cu-containing grain boundary phase interface. The Mg concentrations at these peak positions were 9.1 at% and 8.9 at%, respectively. In addition, Fig. 4.10(e) shows that the Mg signal at the TiN particle/AlN interface also has a peak where the Mg concentration was 4.4 at%. Furthermore, the Al concentration in the TiN particles in direct contact with AlN was higher than that in the TiN particles in contact with AlN via the Cu-containing grain boundary phase. The Al-rich TiN grains are expected to be composed of a metastable phase, $Ti_{1-x}Al_xN$, with a rock-salt structure [13, 14].

Cross-sectional HAADF images of the TiN layer/AlN interface bonded at $T_B$ = 950 °C for 0.5 h with $w_{Ti}$ = 0.45 mg/cm$^2$ are shown in Fig. 4.11(a)–(c). The line EDS profiles of the TiN layer/AlN interface shown in Fig. 4.11(d) and (e) were obtained from the yellow

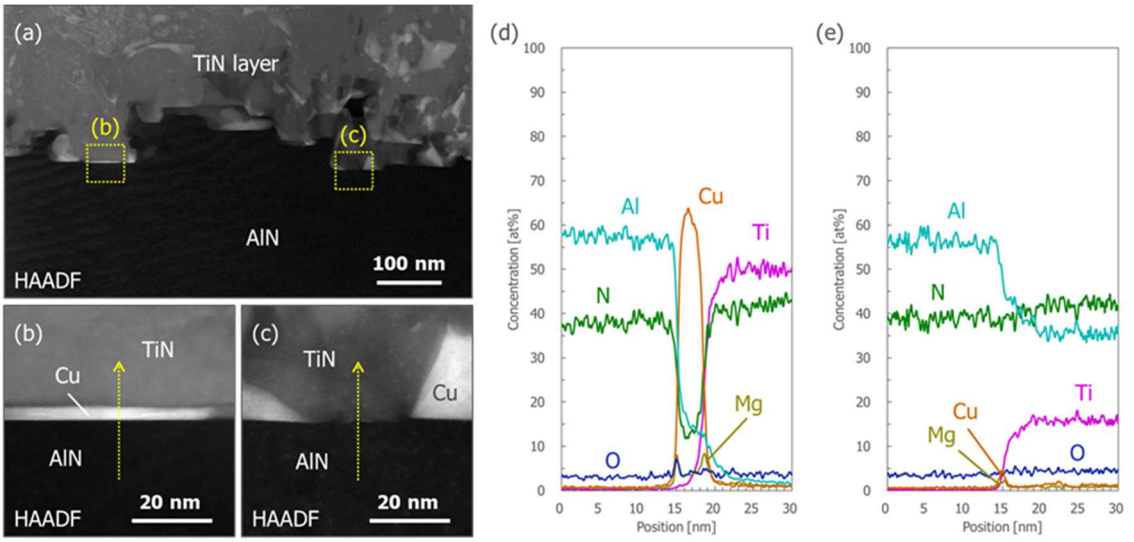


**Fig. 4.11 (a–c) Cross-sectional HAADF images of a TiN layer/AlN interface bonded at 950 °C for 0.5 h. $w_{Mg}$ and $w_{Ti}$ were 1.04 mg/cm$^2$ and 0.45 mg/cm$^2$, respectively. Line EDS profiles of (d) TiN/AlN indirect interface and (e) TiN/AlN direct interface. The line EDS profiles in (d) and (e) were obtained along the yellow dotted arrows in (b) and (c), respectively [1], © 2023 by authors, reproduced with license.**

dotted arrows shown in Fig. 4.11(b) and (c), respectively. In Fig. 4.10(d), the signal peak positions of Mg and O match well at the Cu-containing grain boundary phase/AlN interface. The concentrations of Mg and O were 7.8 at% and 7.1 at%, respectively, giving a ratio of approximately 1:1. As reported by Takakuwa et al. [15], MgO (cubic, $Fm\bar{3}m$, $a$ = 4.212 Å) [16] is formed at the Cu/AlN interface by the interfacial reaction between the molten Cu–Mg binary liquid phase and polycrystalline AlN. In addition, Kumamoto et al. [17] reported that the MgO phase is formed at the Al/AlN interface by the interfacial reaction between the molten Al–Mg-based liquid phase and single-crystal AlN. This suggests that the formation of the MgO phase at the interface between the Mg-containing liquid phase and AlN by the interfacial reaction contributed to stabilizing the interfacial structure in the presence of O derived from the surface oxide films of bonding materials such as Cu, Al, Mg, and AlN. This means that the MgO phase can develop by the modification of the amorphous Al–O phase present on the AlN surface, as discussed in

Section 1.2.1. Furthermore, Fig. 4.11(d) shows a plateau in the Al signal at the Mg signal peak position of the TiN particle/Cu-containing grain boundary phase interface. This suggests that the outermost surface of the TiN particle was modified by $Ti_{1-x}Al_xN$ [13, 14] and/or $Ti_{1-x}Mg_xN$ [18, 19] at the TiN particle/Cu-containing grain boundary phase interface. More interestingly, Fig. 4.11(e) shows that the Al signal plateau in Fig. 4.11 (d) was located at the Al-rich TiN particle/AlN interface, where both Cu and Mg signals were enhanced. This suggests that the outermost surface of the TiN particle was modified by $Ti_{1-x}Al_xN$ [13, 14] and/or $Ti_{1-x}Mg_xN$ [18, 19], even at the Cu-containing segregation phase/TiN particle interface. However, the O signal peak derived from the MgO phase was not clearly seen at the interface between the Cu-containing segregation phase and AlN. Since the concentration of Mg was at most 2.2 at%, which is less than the background concentration of O (4.0 at%), it is reasonable that no O signal peak was observed, even if a MgO phase actually formed.

Taken together with the interfacial structure analysis and the peel strength evaluation by the SAICAS test of these Cu/AlN bonded specimens, these results suggest that the bonding strength of the interface between the Cu plate and AlN substrate bonded through the Mg–Ti co-deposited film was dominated by that between AlN and Cu phases, such as the Cu-containing grain boundary phase and the Cu-containing segregation phase, since no fracture occurred at the interface between Cu phases and TiN particles surface-modified by $Ti_xMg_{1-x}N$. In addition, the development of MgO with increasing bonding temperature suggests an increase in bonding strength between AlN and Cu phases. These imply that sufficient formation of MgO formation at the Cu phase/AlN interface is important for achieving high-strength Cu/AlN bonding using Ag-free Cu–Mg–Ti bonding materials.

### 4.3.3 Effect of Fe addition on the Cu/AlN interfacial structure

The $T_B$ dependence of $t_{TiN}$ at the Cu/AlN interface bonded for 0.5 h between 800 °C and 950 °C with four different $w_{Fe}$ is shown in Fig. 4.12(a). Here, $w_{Mg}$ and $w_{Ti}$ were commonly 1.04 mg/cm$^2$ and 0.23 mg/cm$^2$, respectively. Here, $t_{TiN}$ increased with increasing $T_B$, while the growth of $t_{TiN}$ was suppressed with increasing $w_{Fe}$. The cross-sectional EsB images of the Cu/AlN interface bonded at 950 °C for 0.5 h with $w_{Fe}$ = 0.00 mg/cm$^2$ and $w_{Fe}$ = 0.79 mg/cm$^2$ are shown in Fig. 4.12(b) and (c), respectively. It can be seen that TiN layers with bright spots derived from the Cu-containing grain boundary phase were uniformly formed at both of the Cu/AlN interfaces. In addition, Fig. 4.12(c) shows that $TiFe_2$ (hexagonal, $P6_3/mmc$, $a$ = 4.794 Å, $c$ = 7.834 Å) [20, 21] was formed by the addition of Fe to the Mg–Ti co-deposited film. The decrease in $t_{TiN}$ with increasing $w_{Fe}$ suggests that the formation of $TiFe_2$ suppressed the TiN formation reaction. Thus, the TiN formation reaction competes with the $TiFe_2$ formation reaction.

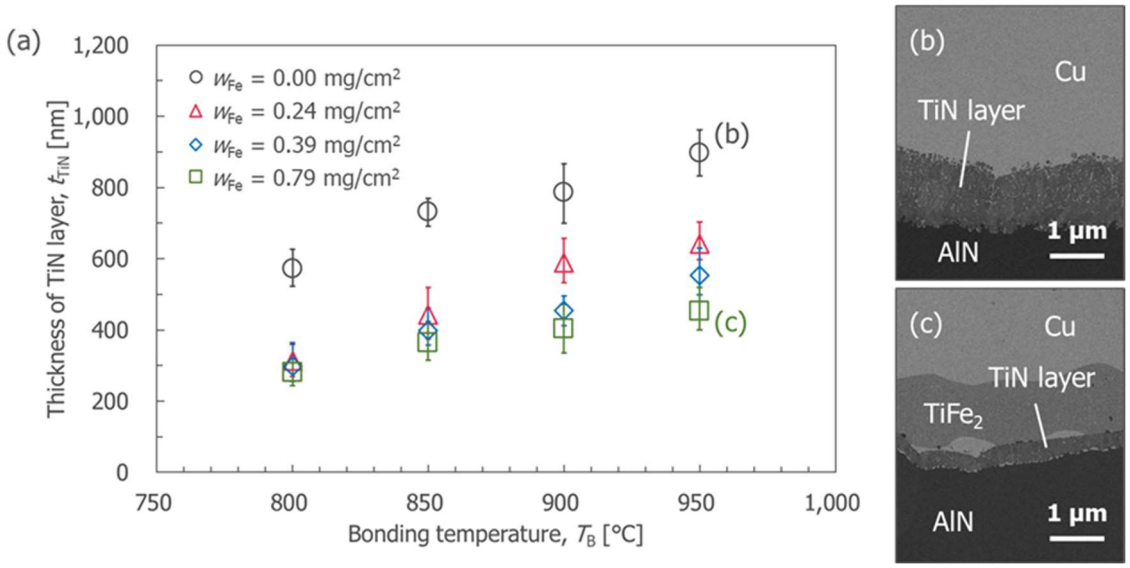


**Fig. 4.12 (a) TiN layer thickness at the Cu/AlN interface versus bonding temperature. Cross-sectional EsB images of the Cu/AlN interface bonded at 950 °C for 0.5 h with $w_{Mg}$ = 1.04 mg/cm$^2$, $w_{Ti}$ = 0.23 mg/cm$^2$, and $w_{Fe}$ = (b) 0.00 mg/cm$^2$, and (c) 0.79 mg/cm$^2$.**

### 4.3.4 Effect of Fe addition on peel strength of Cu/AlN interface

The $T_B$ dependence of $P$ at the Cu/AlN interface is shown in Fig. 4.13. The Cu/AlN bonded specimens did not fracture in the Cu plate even when Fe was added to the Mg–Ti co-deposited film. This suggests that there was no Cu/AlN bonding interfacial fracture caused by $TiFe_2$. It can be seen that $P$ was roughly constant between $w_{Fe}$ = 0.24 mg/cm$^2$ and $w_{Fe}$ = 0.79 mg/cm$^2$ for each $T_B$. In addition, $P$ was about 10 N/mm for $T_B$ below 850 °C, where the $T_B$ dependence was very small, whereas $P$ increased for $T_B$ above 900 °C, ultimately reaching about 13 N/mm at $T_B$ = 950 °C. From the comparison with $w_{Fe}$ = 0.00 mg/cm$^2$, it can be seen that the effect of $P$ enhancement by Fe addition decreased with increasing $T_B$ and disappeared for $T_B$ above 900 °C. Comparison with the $T_B$ dependence of $t_{TiN}$ shown in Fig. 4.12 suggests that the effect of $t_{TiN}$ on $P$ was very small. Surface optical images of Cu/AlN bonded specimens prepared at 800 °C and

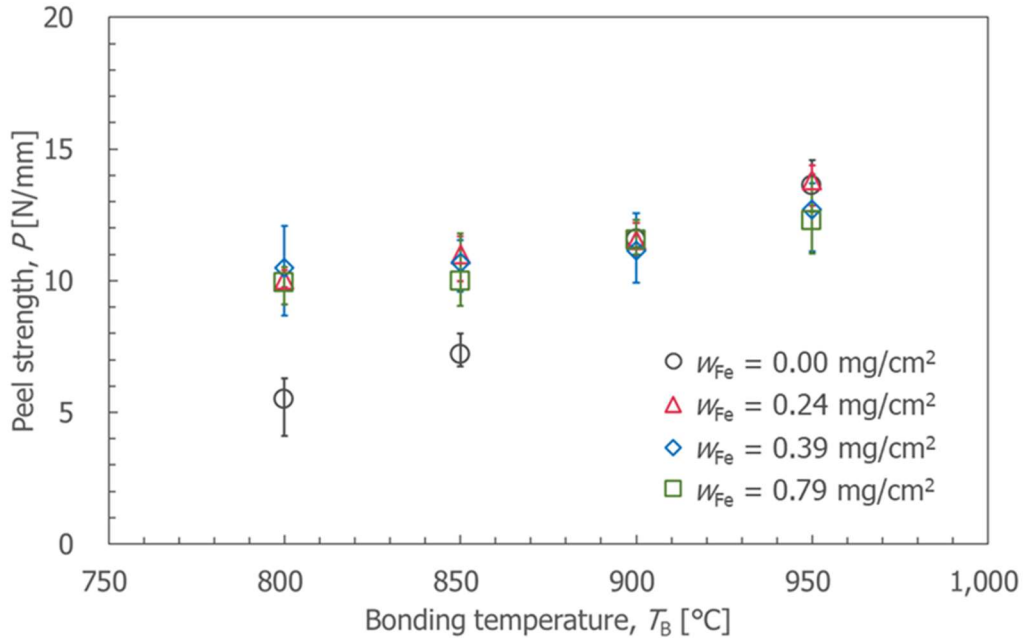


**Fig. 4.13 Peel strength at the Cu/AlN interface as a function of bonding temperature.**

950 °C for 0.5 h with $w_{Fe}$ = 0.79 mg/cm$^2$ according to the SAICAS test are shown in Figs. 4.14(a) and 4.15(a), respectively. The cutting direction was from left to right. The SE and BSE images of the surface shown in Figs. 4.14(b)–(i) and 4.15(b)–(i), with elemental distributions of the Cu/AlN bonded specimens were obtained from the yellow dotted areas in Figs. 4.14(a) and 4.15(a), respectively. In Figs. 4.14(a) and 4.15(a), the cutting surface of the Cu/AlN bonded specimens, where the Cu plate was peeled off after the SAICAS test, is black, although there are some light gray areas that partially match the appearance of the original AlN substrate. By comparing Figs. 4.14(d)–(i) and 4.15(d)–(i), it can be seen that the black areas are composed of AlN as described in Section 4.3.2. This suggests that the fracture mode of the Cu/AlN interface by the SAICAS test remained fracture of the TiN layer/AlN interface even when Fe was added.

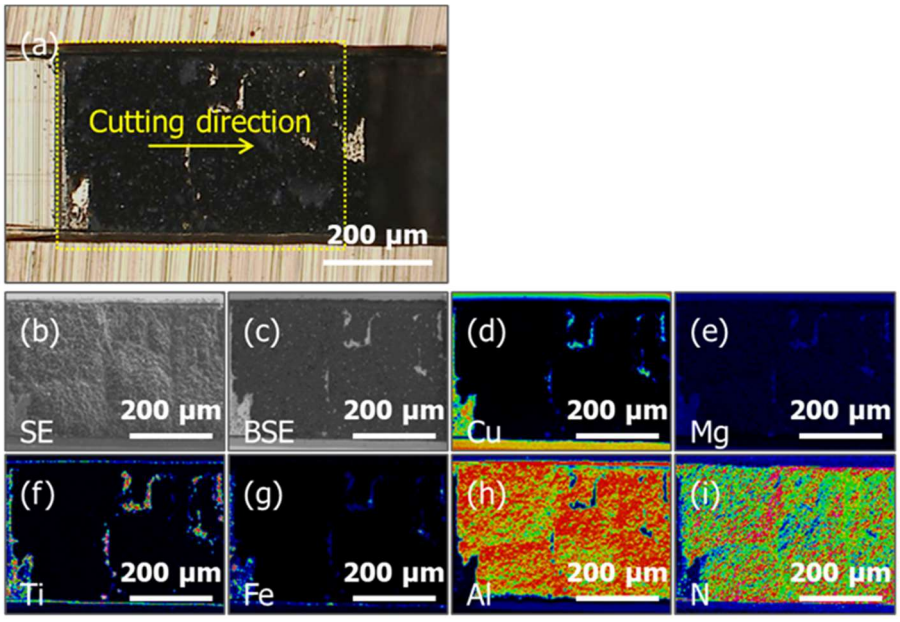


**Fig. 4.14 (a) Optical image of a specimen bonded at 800 °C for 0.5 h after the SAICAS test. $w_{Mg}$, $w_{Ti}$, and $w_{Fe}$ were 1.04 mg/cm$^2$, 0.23 mg/cm$^2$, and 0.79 mg/cm$^2$, respectively. (b) SE and (c) BSE images with elemental distributions: (d) Cu, (e) Mg, (f) Ti, (g) Fe, (h) Al, and (i) N obtained from the yellow dotted area in (a).**

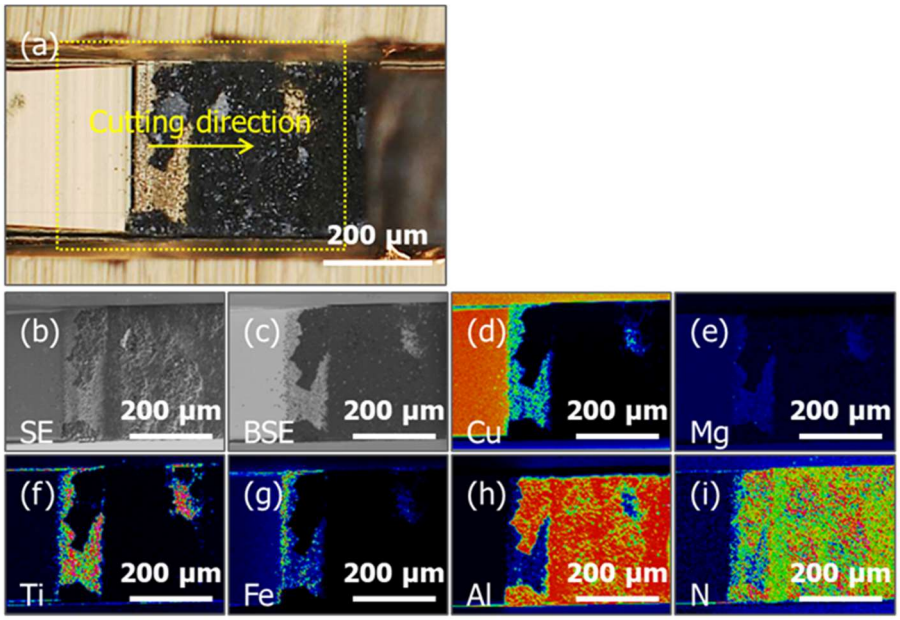


**Fig. 4.15 (a) Optical image of a specimen bonded at 950 °C for 0.5 h after the SAICAS test. $w_{Mg}$, $w_{Ti}$, and $w_{Fe}$ were 1.04 mg/cm$^2$, 0.23 mg/cm$^2$, and 0.79 mg/cm$^2$, respectively. (b) SE and (c) BSE images with elemental distributions: (d) Cu, (e) Mg, (f) Ti, (g) Fe, (h) Al, and (i) N obtained from the yellow dotted area in (a).**

Cross-sectional HAADF images of the TiN layer bonded at $T_B$ = 800 °C for 0.5 h with $w_{Fe}$ = 0.79 mg/cm$^2$ are shown in Fig. 4.16(a) and (b). The line EDS profiles of the Cu-containing grain boundary phase/TiN particle interface shown in Fig. 4.16(c) was obtained from the yellow dotted arrows shown in Fig. 4.16(b). In Fig. 4.16(c), the Fe signal has a peak at the Cu-containing grain boundary phase/TiN particle interface, suggesting that the outermost surface of TiN particles was modified to $Ti_xFe_{1-x}N$ [22] by interfacial reactions with Fe dissolved in the molten Cu–Mg–Ti phase. This is consistent with the Cu-rich phase/TiN grain interfacial structure at the Ag–Cu brazed Cu/TiN–Fe–Ni–C–$Mo_2C$ liquid-phase sintered ceramic interface described in Section 3.3.2. In addition, comparison of Figs. 2.9, 4.11, and 4.12 reveals that the contribution of Fe to the surface modification of TiN particles was higher than the contributions of Al and Mg.

Cross-sectional HAADF images of the TiN layer/AlN interface bonded at $T_B$ = 800 °C

and $T_B$ = 950 °C for 0.5 h with $w_{Fe}$ = 0.79 mg/cm$^2$ are shown in Fig. 4.17(a) and (b) and Fig. 4.18(a) and (b), respectively. The line EDS profiles of the TiN/AlN interface shown in Figs. 4.17(c) and 4.18(c) were obtained from the yellow dotted arrows shown in Figs. 4.17(b) and 4.18(b), respectively. In Fig. 4.17(c), the TiN/AlN interface formed at $T_B$ = 800 °C has a sharp Mg signal peak and broad Fe signal peak, which are located on the AlN side and the TiN side, respectively. The atomic ratio of Mg to Fe at the Mg peak position was Mg/(Mg+Fe) ≈ 0.79. The broad signal peak of Fe located on the TiN side suggests that the outermost surface of the TiN particles was modified to $Ti_xFe_{1-x}N$ [22], which is consistent with the surface state of the TiN particles at the Cu-containing grain boundary phase/TiN particle interface shown in Fig. 4.16. On the other hand, Fig. 4.18(c) shows that Fe was almost absent at the peak position of the Mg signal at the

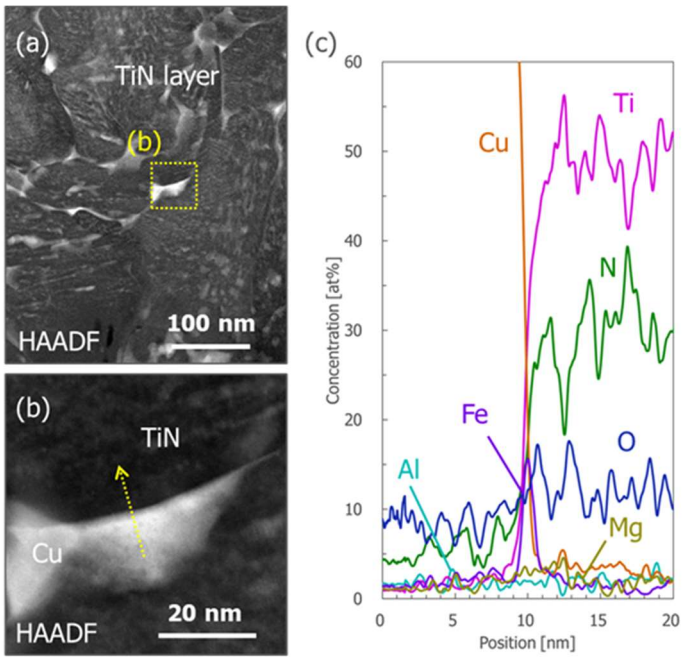


**Fig. 4.16 (a, b) Cross-sectional HAADF images of a TiN layer bonded at 800 °C for 0.5 h. $w_{Mg}$, $w_{Ti}$, and $w_{Fe}$ were 1.04 mg/cm$^2$, 0.23 mg/cm$^2$, and 0.79 mg/cm$^2$, respectively. Line EDS profiles of (c) Cu-containing grain boundary phase/TiN particle interface. T The line EDS profiles in (c) were obtained along the yellow dotted arrow shown in (b).**

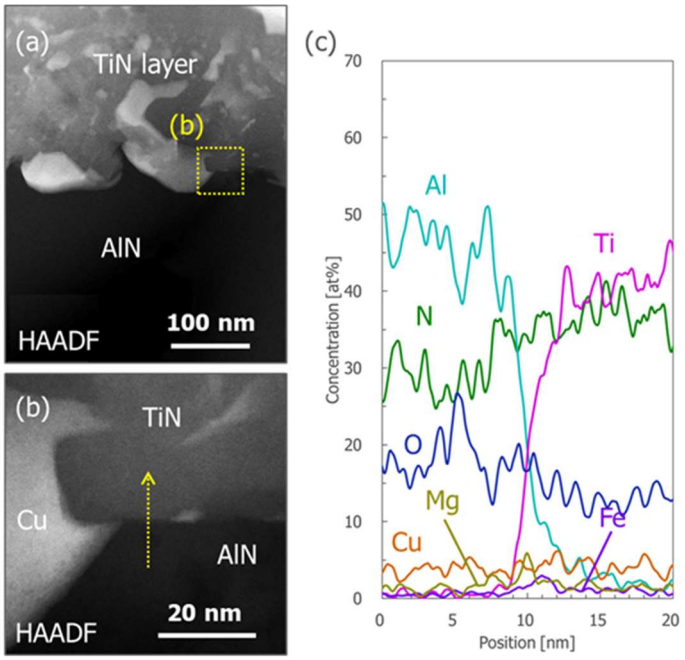


**Fig. 4.17 (a, b) Cross-sectional HAADF images of a TiN layer/AlN interface bonded at 800 °C for 0.5 h. $w_{Mg}$, $w_{Ti}$, and $w_{Fe}$ were 1.04 mg/cm$^2$, 0.23 mg/cm$^2$, and 0.79 mg/cm$^2$, respectively. Line EDS profiles of (c) TiN/AlN interface. The line EDS profiles in (c) were obtained along the yellow dotted arrow shown in (b).**

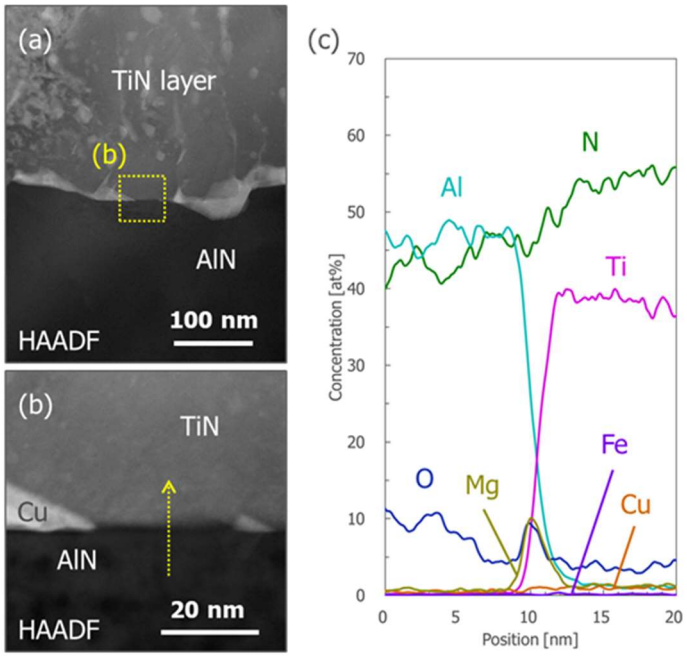


**Fig. 4.18 (a, b) Cross-sectional HAADF images of a TiN layer/AlN interface bonded at 950 °C for 0.5 h. $w_{Mg}$, $w_{Ti}$, and $w_{Fe}$ were 1.04 mg/cm$^2$, 0.23 mg/cm$^2$, and 0.79 mg/cm$^2$, respectively. Line EDS profiles of (c) TiN/AlN interface. The line EDS profiles in (c) were obtained along the yellow dotted arrow shown in (b).**

TiN/AlN interface formed at $T_B$ = 950 °C, where Mg/(Mg+Fe) ≈ 0.99. The very small Fe peak is located on the TiN side, and the Fe concentration at the peak position was 0.35 at%. This suggests that a single phase of MgO developed at the TiN/AlN interface at $T_B$ = 950 °C. This could explain why the the peel strength at the Cu/AlN interface in the Cu–Mg–Ti–Fe system was consistent with that in the Cu–Mg–Ti system, as shown in Fig. 4.13. In addition, the comparison between Figures 4.16, 4.17, and 4.18 suggests that the bonding strength at the interface between Cu phase and TiN particle surface-modified with $Ti_xFe_{1-x}N$ as well as that surface-modified with $Ti_xMg_{1-x}N$ is higher than the bonding strength between Cu phase and AlN interface through the Mg- and O-containing phase. The atomic and effective ionic radii of Mg, Al, Ti, Fe, Ni, Cu, and Ag are listed in Tables 4.2 and 4.3 [23]. Here, the effective ionic radii are for a coordination number of 6, based on the observation that the modified layer on the TiN particle surface has a cubic structure as shown in Fig. 3.10. The observations of the Cu/AlN bonding interface in Chapters 2 to 4 indicate that Mg, Al, Fe, and Ni are elements that can substitute for Ti in the modified layer on the TiN particle surface, while Cu and Ag cannot substitute for Ti. It can be seen from Table 4.2 that the atomic radii of these elements are smaller than that of Ti, regardless of their substitutability with Ti. It can also be seen from Table 4.3 that the valence and ionic radius of the cations are not clear indicators of the substitutability with Ti, as is the atomic radius. These results suggest that the indicators of modification layer

**Table 4.2 Atomic radii of Mg, Al, Ti, Fe, Ni, Cu, and Ag.**

| Atomic radius [Å] | | | | | | |
|---|---|---|---|---|---|---|
| Mg | Al | Ti | Fe | Ni | Cu | Ag |
| 1.45 | 1.18 | 1.76 | 1.56 | 1.49 | 1.45 | 1.65 |

**Table 4.3 Effective ionic radii of Mg, Al, Ti, Fe, Ni, Cu, and Ag for a coordination number of 6 [31]. LS and HS are low and high spin states, respectively.**

| Effective ionic radius [Å] | | | | | | | | | | | | | | |
|---|---|---|---|---|---|---|---|---|---|---|---|---|---|---|
| $Mg^{2+}$ | $Al^{3+}$ | $Ti^{3+}$ | $Fe^{2+}$, LS | $Fe^{2+}$, HS | $Fe^{3+}$, LS | $Fe^{3+}$, HS | $Ni^{2+}$ | $Ni^{3+}$, LS | $Ni^{3+}$, HS | $Cu^{+}$ | $Cu^{2+}$ | $Cu^{3+}$ | $Ag^{+}$ | $Ag^{3+}$ |
| 0.72 | 0.54 | 0.67 | 0.61 | 0.78 | 0.55 | 0.65 | 0.69 | 0.56 | 0.60 | 0.77 | 0.73 | 0.54 | 1.15 | 0.75 |

formation should not be based on bulk properties, but rather on the influence of potential fields from Cu and ceramics.

The $T_B$ dependence of Mg/(Mg+Fe) at the TiN/AlN interface bonded between 800 °C and 950 °C for 0.5 h is shown in Fig. 4.19, where $w_{Mg}$, $w_{Ti}$ and $w_{Fe}$ were 1.04 mg/cm$^2$, 0.23 mg/cm$^2$, and 0.79 mg/cm$^2$, respectively. It can be seen that Mg/(Mg+Fe) gradually

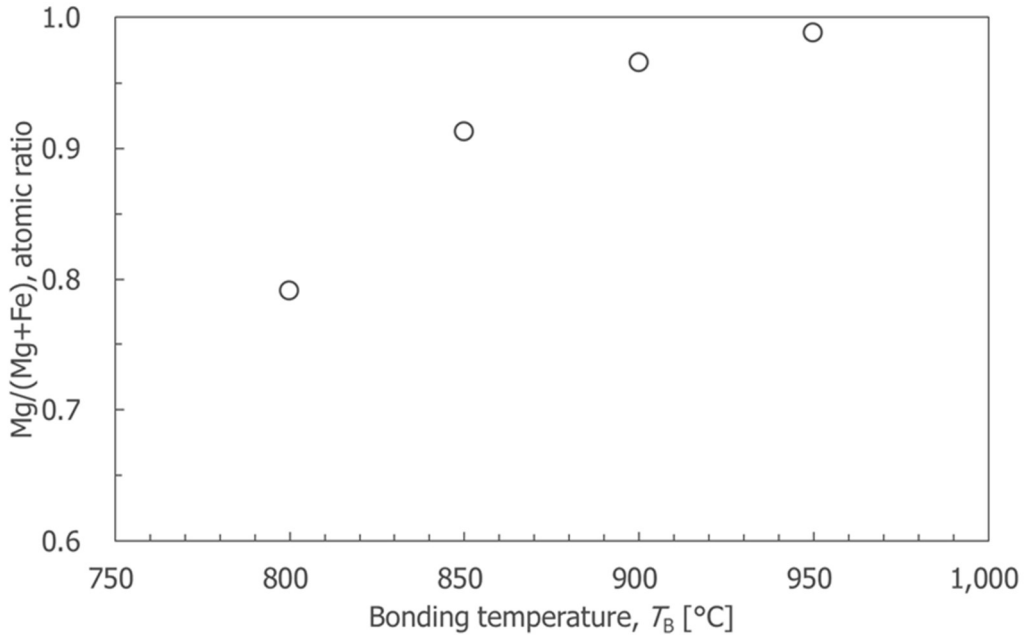


**Fig. 4.19 Mg/(Mg+Fe) at the TiN/AlN interface bonded for 0.5 h between 800 °C and 950 °C with $w_{Mg}$, $w_{Ti}$, and $w_{Fe}$ were 1.04 mg/cm$^2$, 0.23 mg/cm$^2$, and 0.79 mg/cm$^2$ as a function of bonding temperature.**

approached 1.0 with increasing $T_B$. Hashemi et al. [24, 25] reported that the Mg–Fe binary system does not form any IMCs and that the solid solubility limit of each in the other is very small. Taken together with the microstructural observation of the Fe-containing Cu/AlN interface, it is expected that Fe-coexisting with Mg at the TiN/AlN interface would be present as iron oxides.

Three stable iron oxides can be formed: FeO (cubic, $Fm\bar{3}m$, $a$ = 4.3536 Å), $Fe_3O_4$ (cubic, $Fd\bar{3}m$, $a$ = 8.396 Å), and $Fe_2O_3$ (trigonal, $R\bar{3}c$, $a$ = 5.4277 Å) [26]. In the presence of MgO, these iron oxides have been reported to form the MgO + spinel $MgFe_2O_4$ phase for Mg/(Mg+Fe) ≈ 0.79 and 0.91 at $T_B$ = 800 °C and 850 °C, respectively, as shown in Fig. 4.19 [27–31]. This suggests that the formation of $MgFe_2O_4$ below $T_B$ = 850 °C contributed to the higher peel strength of the Fe-containing Cu/AlN bonding interface compared with the Fe-free Cu/AlN bonding interface. On the other hand, the Mg/(Mg+Fe) ≈ 0.99 obtained at $T_B$ = 950 °C suggests that $MgFe_2O_4$, which was expected to form stably at $T_B$ = 950 °C, did not actually form. Thus, with increasing $T_B$, sufficient Fe for $MgFe_2O_4$ formation was not supplied to the AlN surface because of the enhanced $TiFe_2$ and $Ti_xFe_{1-x}N$ formation reactions. The supply of Fe to the AlN surface, which is the main surface for interfacial reactions, played an important role in improving Cu/AlN bonding interfacial strength by Fe addition.

## 4.4 Conclusions

In this chapter, Cu plates were bonded onto AlN substrates using Mg–Ti-based co-deposited films as an Ag-free bonding material that could completely eliminate Ag-ECM, and the effect of Cu/AlN interfacial structure on peel strength by the SAICAS tests was

investigated. These interfacial structures were summarized in Fig. 4.20. The main conclusions were as follows:

1. The TiN layer with Cu-containing grain boundary phase was formed at the Cu/AlN interface bonded by using Mg–Ti-based co-deposited films, which was equivalent to the Cu/AlN bonding interfacial structure when using the AMB method.
2. The Fe-free Cu/AlN bonding interface fractured at the TiN layer/AlN interface. The peel strength of the Cu/AlN bonding interface increased exponentially with increasing $T_B$ between 800 °C and 950 °C, reaching approximately 15 N/mm at $T_B$ = 950 °C.
3. The growth of the MgO phase at the TiN layer/AlN interface of the Fe-free Cu/AlN bonded specimens with increasing $T_B$ appeared to contribute to the increase in peel strength at the Cu/AlN bonding interface.
4. For Fe addition between 0.24 mg/cm$^2$ and 0.79 mg/cm$^2$, the peel strength of the Fe-containing Cu/AlN bonding interface increased by a maximum of approximately 1.8-fold below 850 °C and the peel strength for bonding above 900 °C was equivalent to that of the Fe-free Cu/AlN bonding interface.
5. The results suggest that formation of the Fe–Mg–O phase at the TiN layer/AlN interface of the Fe-containing Cu/AlN bonded samples contributed to the increase in peel strength, and this phase transitioned to MgO with increasing $T_B$.
6. These Mg-based oxide phases at the TiN layer/AlN interface imply that the amorphous Al–O phase on the AlN surface is modified.

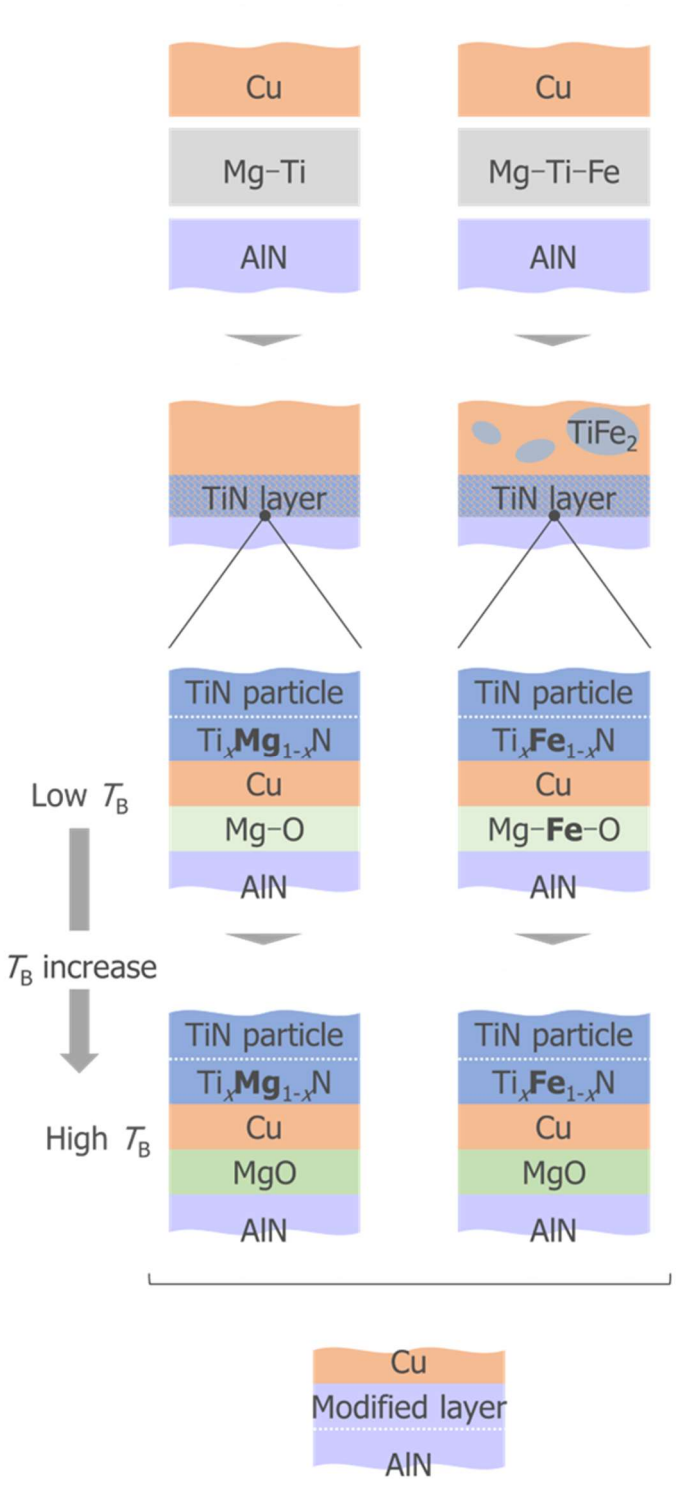


**Fig.4.20 Cu/ceramic interfacial structures discussed in this chapter.**

## References

[1] N. Terasaki, N. Kon, H. Chiba, T. Ohashi, T. Sekino, Effect of interfacial structure on peel strength between Cu and AlN bonded with a Mg–Ti co-deposited film, Discover Materials, 3, 2023.

[2] H. Okamoto, Cu–Mg (Copper-Magnesium), Journal of Phase Equilibria, 13, 1992, 213–214.

[3] J.L. Murray, The Mg−Ti (Magnesium-Titanium) system, Bulletin of Alloy Phase Diagrams, 7, 1986, 245–248.

[4] A.A. Shirzadi, E.R. Wallach, New approaches for transient liquid phase diffusion bonding of aluminium based metal matrix composites, Materials Science and Technology, 13(2), 1997, 135–142.

[5] R. Asthana, Reinforced cast metals: part II evolution of the interface, Journal of Materials Science, 1998, 33, 1959–1980.

[6] G.O. Cook, C.D. Sorensen, Overview of transient liquid phase and partial transient liquid phase bonding, Journal of Materials Science, 46, 2011, 5305–5323.

[7] N. Terasaki, T. Ohashi, Y. Nagatomo, Y. Kuromitsu, A.A. Shirzadi, A new method for liquid-phase bonding of copper plates to aluminum nitride (AlN) substrates used in high-power modules, Journal of Materials Science: Materials in Electronics, 30, 2019, 6552–6555.

[8] Y. Zhang, J. Zhang, J. Chen, Effect of interfacial microstructure evolution on the peeling strength and fracture of AMB Cu-metalized AlN substrate, Journal of the American Ceramic Society, 105, 2021, 577–589.

[9] N. Terasaki, N. Kon, H. Chiba, T. Ohashi, T. Sekino, Interfacial structure between TiN sintered ceramics with and without an Fe-containing grain boundary phase and Ag–Cu

eutectic brazing filler material, SN Applied Sciences, 5(46), 2023.

[10] Y. Kishima, I. Nishiyama, Characteristic evaluation for interface of different materials by SAICAS system, Journal of the Adhesion Society of Japan, 41(6), 2005, 234–241.

[11] J. Miettinen, Thermodynamic description of Cu–Mg–Ni and Cu–Mg–Zn systems, CALPHAD: Computer Coupling of Phase Diagrams and Thermochemistry, 32, 2008, 389–398.

[12] C. Vahlas, B.D. Ladouce, P.Y. Chevalier, C. Bernard, L. Vandenbulcke, A thermodynamic evaluation of the Ti–N system, Thermochimica Acta, 180, 1991, 23–37.

[13] K. Kutschej, P.H. Mayrhofer, M. Kathrein, P. Polcik, R. Tessadri, C. Mitterer, Structure, mechanical and tribological properties of sputtered $Ti_{1-x}Al_xN$ coatings with $0.5 \leq x \leq 0.75$, Surface and Coatings Technology, 200(7), 2005, 2358–2365.

[14] K. Yamamoto, Y. Tatsuhira, Y. Iwai, The Relationship between coating property and solid particle erosion resistance of AIP-deposited TiAlN coatings with different Al contents, Coatings, 11, 2021, 992.

[15] S. Takakuwa, N. Terasaki, N. Kon, T. Ohashi, N. Nita, Y. Nagatomo, Y. Kuromitsu, A new transient liquid phase bonding method using magnesium foil to bond copper plates to aluminum nitride substrates, Journal of Materials Science: Materials in Electronics, 33, 2022, 10486–10493.

[16] H.A. Wriedt, The Mg−O (Magnesium-Oxygen) system, Bulletin of Alloy Phase Diagrams, 8(3), 1987, 227–233.

[17] A. Kumamoto, N. Shibata, K. Nayuki, T. Tohei, N. Terasaki, Y. Nagatomo, T. Nagase, K. Akiyama, Y. Kuromitsu, Y. Ikuhara, Atomic structures of a liquid-phase bonded

metal/nitride heterointerface, Scientific Reports, 6, 2016, 22936.

[18] M.A. Gharavi, R. Armiento, B. Alling, P. Eklund, Theoretical study of phase stability, crystal and electronic structure of $MeMgN_2$ (Me = Ti, Zr, Hf) compounds, Journal of Materials Science, 53, 2018, 4294–4305.

[19] S.R. Bauers, A. Holder, W. Sun, C.L. Melamed, R.W-Robinson, J. Mangum, J. Perkins, W. Tumas, B. Gorman, A. Tamboli, G. Ceder, S. Lany, A. Zakutayev, Ternary nitride semiconductors in the rocksalt crystal structure, Applied Physical Sciences, 116(30), 2019, 14829–14834.

[20] J.L. Murray, The Fe−Ti (Iron-Titanium) system, Bulletin of Alloy Phase Diagrams 2, 1981, 320–334.

[21] P.J. Brown, J. Deportes, B. Ouladdiaf, Magnetic structure of the laves phase compound $TiFe_2$, Journal of Physics: Condensed Matter, 4, 1992, 10015.

[22] H. Ohtani, M. Hillert, A thermodynamic assessment of the Fe–N–Ti system, Calphad, 15(1), 1991, 41–52.

[23] R.D. Shannon, Revised effective ionic radii and systematic studies of interatomic distances in halides and chalcogenides, Acta Crystallographica Section A, A32, 1976, 751–767.

[24] N.A.A. Hashemi, J.B. Clark, L.J. Swartzendruber, The Fe–Mg (iron-magnesium) System, Bulletin of Alloy Phase Diagrams, 6, 1985, 235–238.

[25] N.A.A. Hashemi, J.B. Clark, L.J. Swartzendruber, Fe–Mg (iron-magnesium), Binary Alloy Phase Diagrams, II Ed., Ed. T.B. Massalski, 2, 1990, 1722–1723.

[26] H.A Wriedt, The Fe–O (iron-oxygen) system, Journal of Phase Equilibria, 12, 1991, 170–200.

[27] A.E. Paladino, Phase equilibria of the ferrite region of the system $FeO–MgO–Fe_2O_3$,

Journal of the American Ceramic Society, 43(4), 1960, 183–191.

[28] B. Phillips, S. Somiya, A. Muan, Melting relations of magnesium oxide-iron oxide mixtures in air, Journal of the American Ceramic Society, 44(4), 1961, 167–169.

[29] B. Phillips, A. Muan, Phase equilibria in the system MgO–FeO–$Fe_2O_3$ in the temperature range of 1400 to 1800 °C, Journal of the American Ceramic Society, 45(12), 1962, 588–591.

[30] D.H. Speidel, Phase equilibria in the system MgO–FeO–$Fe_2O_3$: the 1300 °C isothermal section and extrapolations to other temperatures, Journal of the American Ceramic Society, 50(5), 1967, 243–248.

[31] V. Raghavan, Fe–Mg–O (iron-magnesium-oxygen), Journal of Phase Equilibria and Diffusion, 31, 2010, 368.

# Chapter 5: Development of the interfacial structure between AlN and Cu–P–Sn–Ni brazing alloy for different initial Ti layer thicknesses

## 5.1 Introduction

In Chapter 4, it was demonstrated that Cu can be bonded onto AlN via a TiN layer when a Mg–Ti-based co-deposited film was used as the Ag-free bonding material, and this was similar to the AMB method using a Ag-containing bonding material.

In this chapter, in order to clarify the effect of the Ag-free bonding material components on the Cu/AlN bonding interface, the structures of the Cu/AlN interface bonded using a commercial Cu–P eutectic-based brazing foil with a liquidus temperature whose melting range is almost equivalent to the Cu–Mg system used in Chapter 4 and Ti layers were investigated [1, 2]. P and Sn contained in this commercial brazing foil are known to form multiple IMCs with Ti [3–8]. Therefore, it is expected that the combination of Ag-free Cu–P eutectic brazing material and Ti will enable the evaluation of the interfacial structure and its formation process when the interfacial reaction between Ti and AlN competes with the IMC formation reaction between Ti and Ag-free bonding material components. In addition, in order to evaluate the practicality of the Ag-free bonding technique, the relative strength of the Cu/AlN interface was evaluated based on the fracture probability of the Cu/AlN interface after ultrasonic welding of Cu terminals to the Cu layer. Furthermore, the effect of using a Ag-free bonding material on the ECM resistance was evaluated.

## 5.2 Experimental procedure

### 5.2.1 Materials and sample fabrication

An amorphous brazing alloy composed of Cu–6.3 wt% P–9.3 wt% Sn–7 wt% Ni, which can be supplied as a foil material suitable for bonding flat plates, with a thickness of 25 μm was used as the Ag-free material for bonding between Cu and AlN substrates. The amounts of Cu, P, Sn and Ni were 16.0, 1.3, 1.9 and 1.4 mg/cm$^2$, respectively. The solidus and liquidus temperatures of this Cu–rich alloy are 600 °C and 630 °C, respectively, the lowest commercially available. P and Sn lower the melting temperature of Cu via the eutectic reaction, and Ni suppresses the formation of $Cu_3P$ (hexagonal, $P6_3cm$, $a$ = 7.07 Å, $c$ = 7.135 Å) [9], which is the single brittle Cu–P IMC formed in the Cu–P binary system. In this study, Ti layers with three different thicknesses of 0.5, 1, and 5 μm were prepared. The two thinner layers were deposited on one side of a 300-μm-thick polycrystalline foil of OFC by physical vapor deposition (PVD). For the thickest layer, a 5-μm-thick TPC270C Ti foil was used. According to Japan Industrial Standards (JIS), TPC270C foil has the highest purity of all commercially available pure Ti materials. It is notable for its softness and excellent workability. Ti thicknesses of 0.5, 1, and 5 μm correspond to Ti amounts of 0.23, 0.45, and 2.25 mg/cm$^2$, respectively. In addition, AlN substrates prepared by two different manufacturing processes were used. One type was a 1-mm-thick AlN polycrystalline substrate, which is commonly used for high-voltage power module applications. These substrates all contained yttria ($Y_2O_3$) as a sintering additive. The other type was a commercially available $Al_2O_3$ sapphire (0001) substrate (ø50.8 mm × 430 μm) upon which a 1-μm-thick single-crystal epitaxial AlN film was

deposited as the AlN substrate (DOWA Electronics Materials Co., Ltd.). The orientation relationship between the AlN film and the $Al_2O_3$ substrate was $(0001)$ AlN//$(0001)$ $Al_2O_3$, $[11\bar{2}0]$ AlN// $[1\bar{1}00]$ $Al_2O_3$, as observed in other studies [10, 11]. These materials were all cut into 5 mm × 10 mm rectangular pieces and were then stacked in the order: Cu, Ti deposited film or Ti foil, Cu–P–Sn–Ni brazing foil, and AlN substrate. The stacked samples were brazed in a vacuum at 650, 750, 850, and 950 °C for 1 h under a compressive stress of 1 MPa, with heating and cooling rates of 10 °C/min. The grain size of the polycrystalline Cu was >50 μm after heating under these conditions.

### 5.2.2 Characterization

Cross-sections of the resulting bonds were observed by EPMA, SEM, and STEM equipped with EDS. Metallography samples for SEM and EPMA mounted in an acrylic polymer at room temperature were polished using conventional metallographic techniques. In addition, the final polishing for these samples was performed using an argon-based ion beam polisher (ArBlade 5000, Hitachi High-Tech) to obtain the final flat cross-sections before coating with a thin carbon layer. The microstructures and elemental distributions of all samples were analyzed using an EPMA apparatus (JXA–8530F, JEOL) operated at 15 kV. The thickness of the Cu/AlN thin sections for STEM analysis, prepared using a FIB system (Scios, Thermo Fisher Scientific), ranged from 30 to 100 nm. Elemental distributions of the thin sections were evaluated on a STEM (Titan G2 ChemiSTEM, Thermo Fisher Scientific) equipped with an EDS system (NSS7, Thermo Fisher Scientific) operated at 200 kV. Cu/AlN bonding interfaces with a single-crystal epitaxial AlN substrate were observed along the AlN $\langle 11\bar{2}0 \rangle$ direction. This direction is highly effective for distinguishing between Al and N rows in AlN, and in these directions

these rows of atoms do not overlap with each other.

### 5.2.3 Ultrasonic welding

The bonding reliability of the Cu/AlN interface was determined from observations of Cu/AlN interfacial delamination and AlN cracking by SAT of the Cu/AlN interfaces after ultrasonic welding of a Cu terminal to the Cu layer. For these observations, Cu/AlN/Cu bonded substrates consisting of OFC (20 mm × 20 mm × 300 μm) and polycrystalline AlN (25 mm × 25 mm × 635 μm) were prepared using the same bonding procedure with a 0.5-μm-thick Ti film as described in Section 5.2.1, but with the polycrystalline AlN substrates bonded on both sides to Cu. Cu terminals (OFC, 5 mm × 10 mm × 1 mm) were welded onto these substrates using an ultrasonic welder (60C–904, Ultrasonic Engineering) in collapse mode, where the load, collapse distance, and welding area were 500 N, 0.45 mm and 3 mm × 3 mm, respectively. For each bonding temperature, 30 samples were prepared in this way. After welding, the Cu/AlN interfaces were assessed for failure using SAT (FSP8 V, Hitachi Power Solutions). Cross-sections of ultrasonic welding samples were mounted in an acrylic polymer at room temperature and polished using standard metallographic techniques. These samples were observed by SEM (S-3400N, Hitachi High-Tech) operated at 15 kV.

### 5.2.4 Water drop test

The ECM resistance was evaluated by the water drop test [12–14]. In this test, since the electrode and insulating layer were covered with deionized water droplets, the humidity, which was close to 100% relative humidity, accelerated the dissolution and migration of the metal contained in the electrode, which can promote the ECM

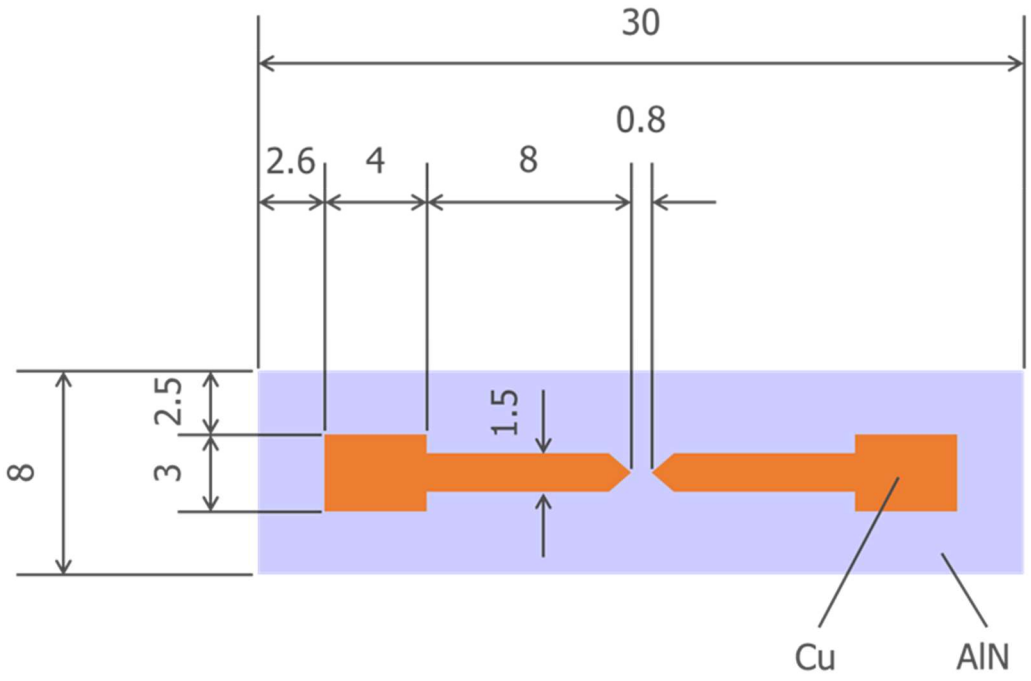


**Fig. 5.1 Cu electrode pattern for the water drop test.**

phenomenon in a short time. A Ag-free Cu/AlN bonding substrate consisting of OFC (29 mm × 7 mm × 300 μm) and polycrystalline AlN (30 mm × 8 mm × 1 mm) was fabricated using the same bonding procedure with 0.5-μm-thick Ti film as described in Section 5.2.1. In addition, a Ag-containing Cu/AlN bonding substrate was fabricated at 850 °C for 0.5 h with a Ag amount of 6.29 mg/cm$^2$ and a Ti amount of 0.29 mg/cm$^2$ using the AMB method based on the interdiffusion process described in Section 1.3. These substrates were etched by standard techniques to the electrode pattern shown in Fig. 5.1. A 50 V DC was applied between the Cu electrodes covered with deionized water. The electrical resistance between the Cu electrodes was measured at 1 s intervals up to 10 s after applying the voltage. The elemental distributions of the naturally dried AlN substrate surface after the water drop test were analyzed using an EPMA as described in Section 5.2.2.

## 5.3 Results and discussion

### 5.3.1 Development of Cu/AlN interfacial structure depending on initial Ti layer thickness

Cross-sectional BSE images of the Cu/AlN interfaces bonded at 650 °C for 1 h are shown in Fig. 5.2, where the initial Ti layer thicknesses were 0.5, 1, and 5 μm, respectively. At this temperature just above the liquidus temperature of the Cu–P–Sn–Ni brazing foil, the Cu/AlN bonding interface appeared to fit the surface shape of the polycrystalline AlN substrate well, with no gaps or pores. This suggests that the Cu–P–Sn–Ni liquidus phase had good wettability to the AlN substrate due to the presence of the initial Ti active metal. For all the images in Fig. 5.2, the Cu layer is divided into two regions by the Ti-containing layer formed about 8 μm from the surface of the AlN substrate.

The reaction between the Cu–P–Sn–Ni brazing foil and the Ti films with thickness of 1 μm or less consumed the entire Ti film. The products of this reaction were mainly $Ti_5P_3$

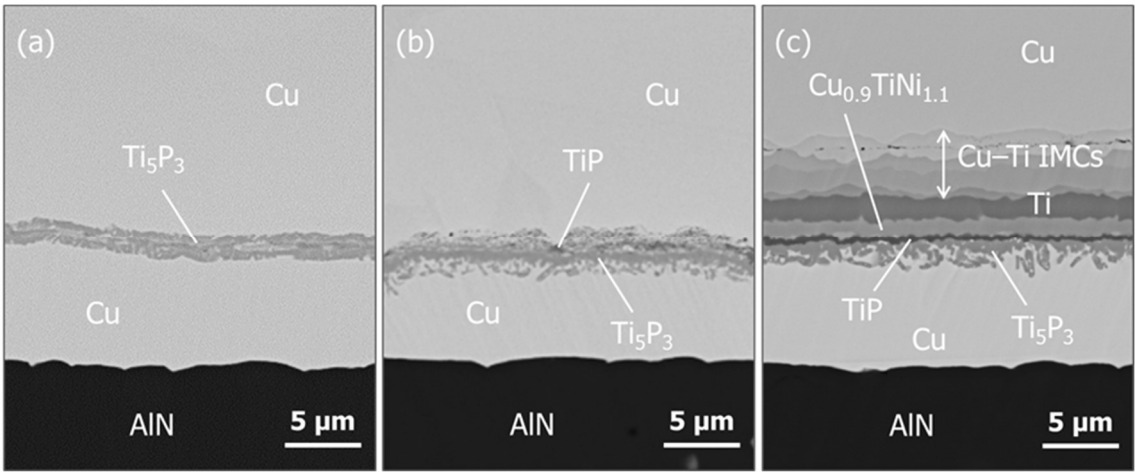


**Fig. 5.2 Cross-sectional BSE images of a Cu/AlN bonding interface after bonding at 650 °C for 1 h with initial Ti layers (a) 0.5 μm, (b) 1 μm, and (c) 5 μm thick.**

(hexagonal, $P6_3/mcm$, $a$ = 7.234 Å, $c$ = 5.090 Å) [5, 7], which was formed as a discontinuous layer for the 0.5-μm-thick Ti layer and a continuous layer for the 1-μm-thick Ti layer. In contrast, there was still unreacted Ti foil after the chemical reaction between the Cu–P–Sn–Ni brazing foil and the 5-μm-thick Ti foil, as shown in Fig. 5.2(c). Here, this unreacted Ti foil is called a residual Ti layer. From the residual Ti layer to the AlN substrate, the cross-sectional structure was composed of the following compounds: $Cu_{0.9}TiNi_{1.1}$ (tetragonal, $I4/mmm$, $a$ = 3.12 Å, $c$ = 7.965 Å) [11], TiP (hexagonal, $P6_3/mmc$, $a$ = 3.499 Å, $c$ = 11.700 Å) [3, 6, 7], $Ti_5P_3$ [5, 7] and Cu (cubic, $Fm\bar{3}m$, $a$ = 3.615 Å). The brightness of the BSE image also increased gradually from the residual Ti layer toward the Cu surface. This suggests that multiple Cu–Ti IMCs with different composition ratios such as $Cu_4Ti$ (orthorhombic, $Pnma$, $a$ = 4.525 Å, $b$ = 4.341 Å, $c$ = 12.953 Å) [16–18], $Cu_4Ti_3$ (tetragonal, $I4/mmm$, $a$ = 3.126 Å, $c$ = 19.964 Å) [17, 18], CuTi (tetragonal, $P4/nmm$, $a$ = 3.107 Å, $c$ = 5.919 Å) [17, 18], and $CuTi_2$ (tetragonal, $I4/mmm$, $a$ = 2.944 Å, $c$ = 10.786 Å) [17, 18] were formed in layers by solid-phase diffusion bonding between the Cu layer and the Ti foil. In addition, a number of voids were distributed in the Cu–Ti IMCs, as shown in Fig. 5.2(c). This suggests that the oxide films present on the surface of the Cu plate and Ti foil inhibited the interdiffusion between Cu and Ti.

Cross-sectional BSE images together with elemental distributions of the Cu/AlN interface bonded at 650 °C are shown in Figs. 5.3, 5.4, and 5.5, for the initial 0.5-, 1-, and 5-μm-thick Ti layers, respectively. The gray area in the AlN layer shown in Figs. 5.3(a) and 5.5(a) are yttria, a sintering additive in the AlN substrate. Sn diffused beyond the P-containing IMC layer toward the Cu surface side when using the Ti layer with thickness of 1 μm or less, as evident from Figs. 5.3(c) and 5.4(c), where the diffusion length of Sn

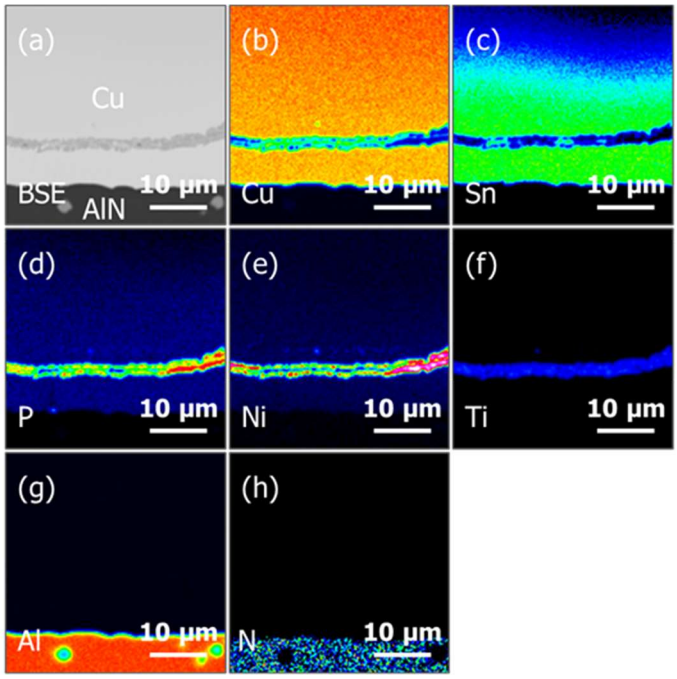


**Fig. 5.3 (a) BSE image of a Cu/AlN bonding interface after bonding at 650 °C for 1 h with an initially 0.5-μm-thick Ti film, together with elemental distributions of (b) Cu, (c) Sn, (d) P, (e) Ni, (f) Ti, (g) Al, and (h) N.**

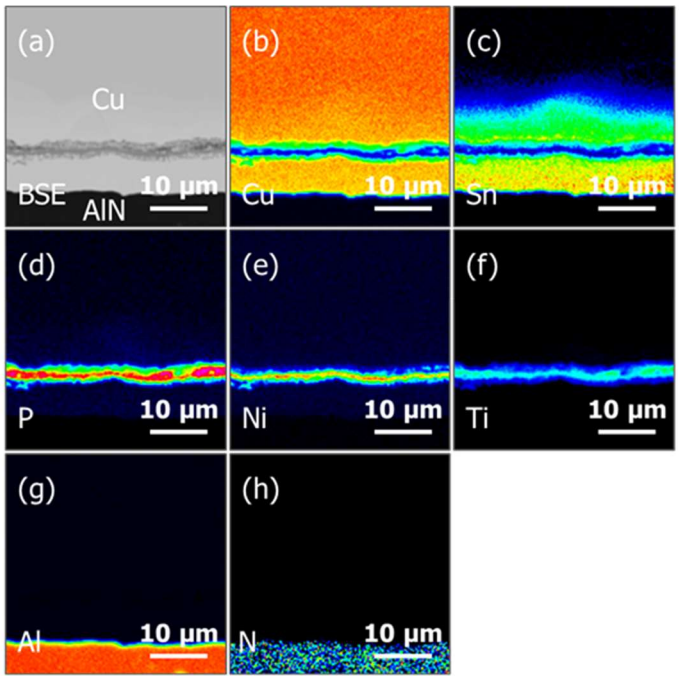


**Fig. 5.4 (a) BSE image of a Cu/AlN bonding interface after bonding at 650 °C for 1 h with an initially 1-μm-thick Ti film, together with elemental distributions of (b) Cu, (c) Sn, (d) P, (e) Ni, (f) Ti, (g) Al, and (h) N [2], © 2022 by Springer Science Business Media, reproduced with license.**

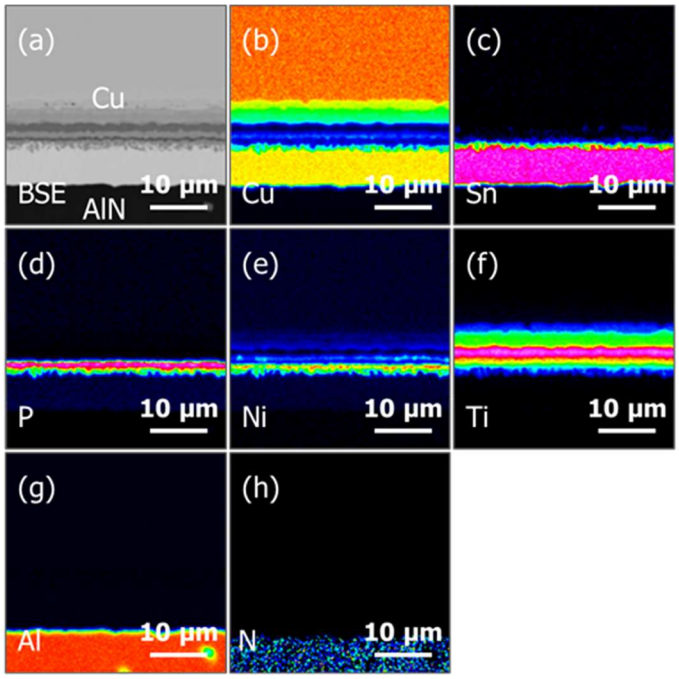


**Fig. 5.5 (a) BSE image of a Cu/AlN bonding interface after bonding at 650 °C for 1 h with an initially 5-μm-thick Ti film, together with elemental distributions of (b) Cu, (c) Sn, (d) P, (e) Ni, (f) Ti, (g) Al, and (h) N [2], © 2022 by Springer Science Business Media, reproduced with license.**

was longer for a 0.5-μm-thick Ti layer than for a 1-μm-thick Ti layer. By contrast, the Sn was localized between the P-containing layer and the AlN substrate when using the 5-μm-thick Ti layer, as shown in Fig. 5.5(c). This suggests that the difference in Sn distribution was due to a difference in the degree of dissolution of the TiN layer into the Cu–P–Sn–Ni liquid phase. P-containing IMC particles were precipitated by the reaction between Ti and P when dissolving the entire Ti layer with thickness of 1 μm or less in the Cu–P–Sn–Ni liquid phase, forming a layered dispersion structure or a dense layered structure. Consumption of P, a melting point-lowering element in the Cu–P–Sn–Ni brazing foil, promoted solidification from the P-containing IMC layer side to the AlN side. Sn that concentrated at the Cu/AlN interface during the isothermal solidification process eventually diffused into Cu toward the Cu surface side. The difference in Sn diffusion

length between the Ti layer thicknesses of 0.5 μm and 1 μm is suggested to arise from the difference in the lifetime of the liquid phase, which has a faster diffusion rate. This same solidification process is expected to occur when using the 5-μm-thick Ti layer. However, the formation of the residual Ti layer present in Figs. 5.2(c) and 5.5(a) suggests that not all of the Ti layer is dissolved into the Cu–P–Sn–Ni liquid phase. In addition, the diffusion length of Sn into Ti is only ~1 nm after 1 h at 650 °C [19]. Hence, the residual Ti layer functioned as a diffusion-inhibiting layer and suppressed the diffusion of Sn toward the Cu surface side. Furthermore, Figs. 5.3(a)–(c), 5.4(a)–(c), and 5.5(a)–(c) show that there was no precipitation of either $Cu_3Sn$ (orthorhombic, *Cmcm*, $a$ = 5.529 Å, $b$ = 47.75 Å, $c$ = 4.323 Å) or $Cu_6Sn_5$ (monoclinic, *C*2/*c*, $a$ = 11.022 Å, $b$ = 7.282 Å, $c$ = 9.827 Å, $\beta$ = 98.84°) in the regions where both Cu and Sn were present [20–22]. This supports the formation of a dense Cu layer without Kirkendall void generation [23, 24] at the Cu/AlN interface.

Cross-sectional BSE images and TEM images of a Cu/AlN interface, together with nano-beam electron diffraction (NBD) patterns of a Cu/AlN interfacial reaction layer after bonding for 1 h between 650 °C and 950 °C with the 0.5-μm-thick Ti layer are shown in Fig. 5.6. In the BSE images, the gray area in the AlN layer is yttria. The NBD patterns were acquired from the areas circled in yellow in the corresponding TEM images. The BSE images show that a Ti-containing layer composed of $Ti_5P_3$ was formed at a distance of ~8 μm from the surface of the AlN substrate at all the heating temperatures used. Within this range of bonding temperatures, the morphology of these Ti-containing layers was essentially independent of the bonding temperature. In addition, the NBD patterns in Fig. 5.6 show that the Cu/AlN interfacial reaction layers were composed of an amorphous phase at 750 °C or lower, and a crystalline phase at 850 °C or higher. The thicknesses of

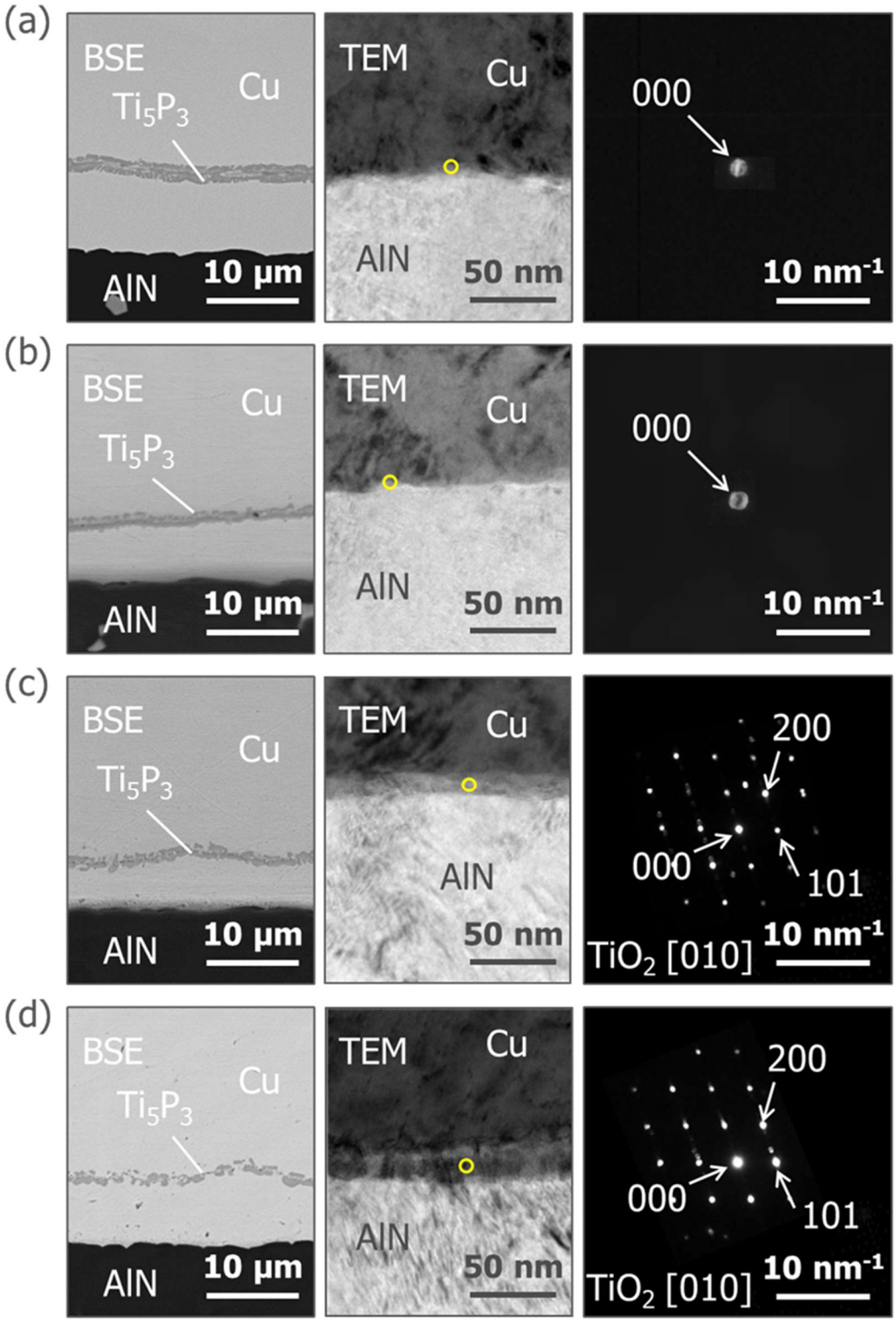


**Fig. 5.6 Cross-sectional BSE and TEM images of a Cu/AlN bonding interface with NBD patterns of the interfacial reaction layer after bonding for 1 h with an initially 0.5-μm-thick Ti film at (a) 650 °C, (b) 750 °C, (c) 850 °C, and (d) 950 °C.**

these crystalline phases were ~13 nm at 850 °C and ~20 nm at 950 °C, respectively. This suggests that the crystalline Cu/AlN interfacial reaction layer consisted of rutile $TiO_2$ (tetragonal, $P4_2/mnm$, $a$ = 4.5937 Å, $c$ = 2.9581 Å) [25], in consideration of the NBD patterns shown in Fig 5.6. The observations in Fig. 5.6 show that, as expected from other studies of active brazes, Ti could efficiently diffuse through the liquid braze to the braze/AlN interface during the bonding process.

Cross-sectional BSE images and TEM images of a Cu/AlN interface, together with NBD patterns of a Cu/AlN interfacial reaction layer after bonding for 1 h between 650 °C and 950 °C with the 1-μm-thick Ti layer, are shown in Fig. 5.7. In the BSE images, the gray area in the AlN layer is yttria. The NBD patterns were acquired from the areas circled in yellow in the corresponding TEM images. The BSE images show that the Ti-containing layer composed of TiP and $Ti_5P_3$ was formed at a distance of ~8 μm from the surface of the AlN substrate at all these heating temperatures. P was the main melting point-lowering element in the Cu–P–Sn–Ni brazing alloy. This therefore suggests that its consumption through the IMC formation reaction with Ti caused the Cu–P–Sn–Ni liquid phase to solidify in the early stages of the heating process, meaning that the interfacial reaction between Cu and AlN when using the Ti films of 1-μm-thick or less proceeded mainly in the solid phase. Furthermore, the NBD patterns in Fig. 5.7 show that the Cu/AlN interfacial reaction layers were composed of an amorphous phase at 750 °C or lower, and a crystalline phase at 850 °C or higher. The thicknesses of these crystalline phases were ~7 nm at 850 °C and ~35 nm at 950 °C, respectively. EDS line profiles after bonding for 1 h at (a) 850 °C and (b) 950 °C with this initial 1-μm-thick Ti film are shown in Fig. 5.8. The EDS line profiles were acquired from the lines indicated by the yellow arrows in the corresponding TEM images in Fig. 5.7(c) and (d), respectively. In the Cu/AlN interfacial

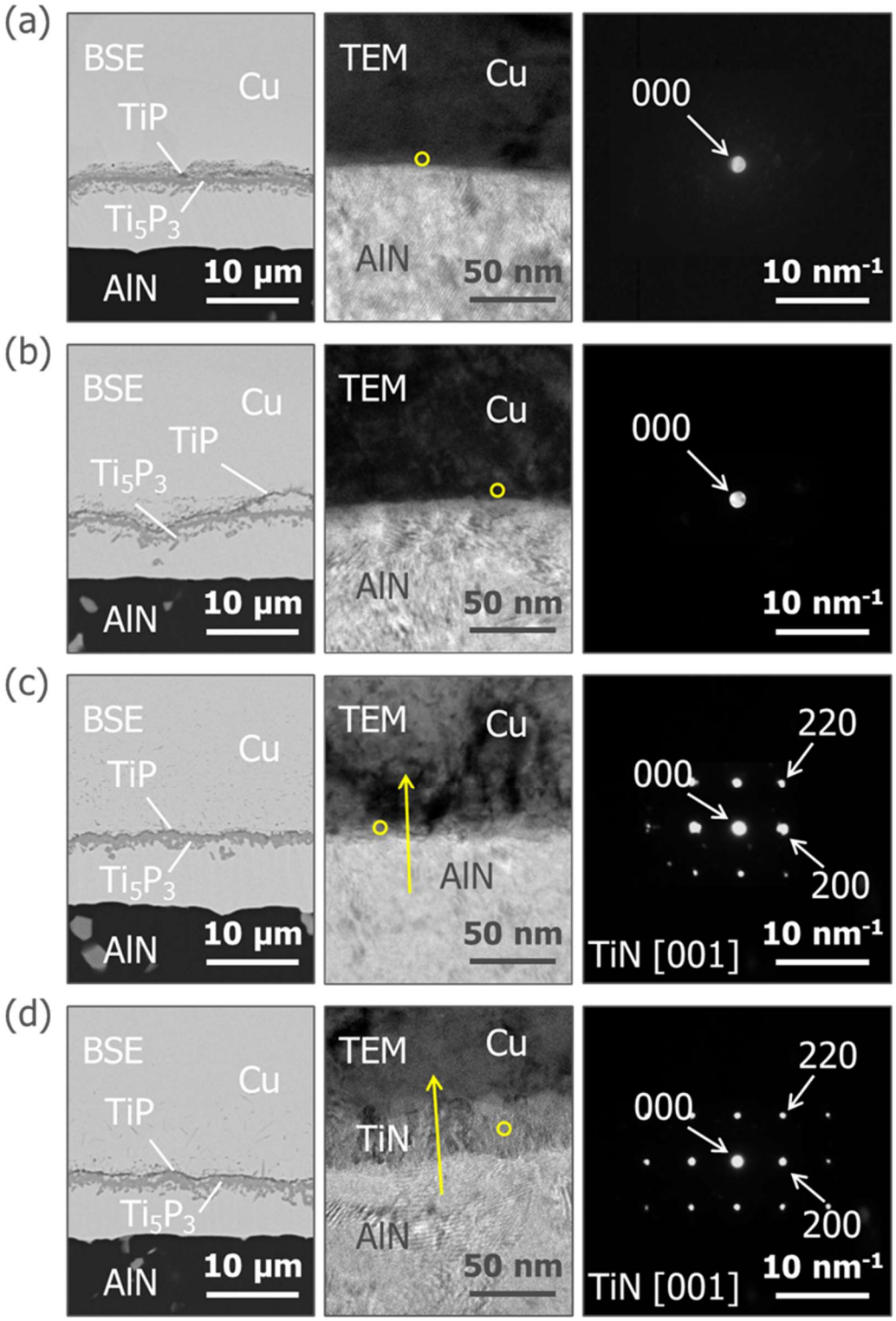


**Fig. 5.7 Cross-sectional BSE and TEM images of a Cu/AlN bonding interface with NBD patterns of the interfacial reaction layer after bonding for 1 h with an initially 1-μm-thick Ti film at (a) 650 °C, (b) 750 °C, (c) 850 °C, and (d) 950 °C [2], © 2022 by Springer Science Business Media, reproduced with license.**

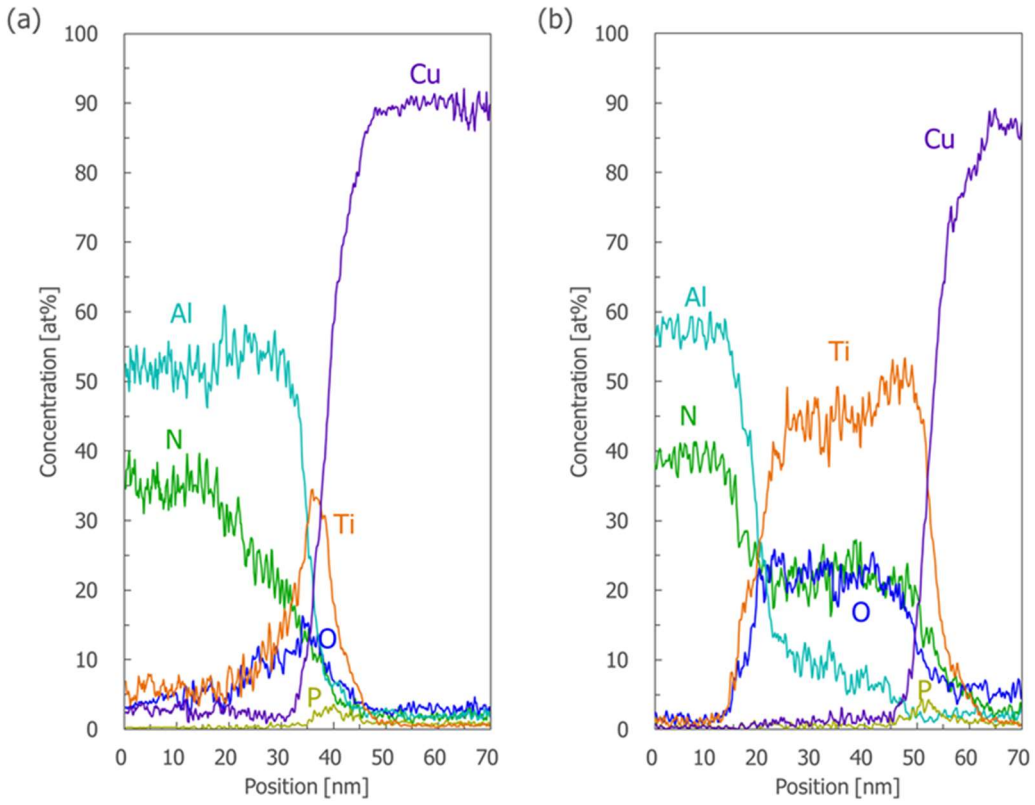


**Fig. 5.8 EDS analyses of a Cu/AlN interfacial reaction layer after bonding for 1 h with an initially 1-μm-thick Ti film at (a) 850 °C and (b) 950 °C. These EDS line profiles were acquired along the yellow arrows shown in the corresponding TEM images in Fig. 5.7(c) and (d), respectively [2], © 2022 by Springer Science Business Media, reproduced with license.**

reaction layer, the O and N signals overlapped with the Ti signal. This suggests that the crystalline Cu/AlN interfacial reaction layer consisted of an O-containing TiN phase, given the NBD patterns shown in Fig 5.7. These NBD patterns can be indexed in terms of TiN, which has the rock-salt crystal structure and occurs over a wide range of stoichiometries within the Ti–N system. Substitution of oxygen for nitrogen within this phase can also occur to give an extensive phase field within the ternary Ti–O–N system in which rock-salt titanium oxynitrides of the general composition $TiO_xN_y$ are formed [26–30].

Cross-sectional BSE images and TEM images of a Cu/AlN bonding interface, together

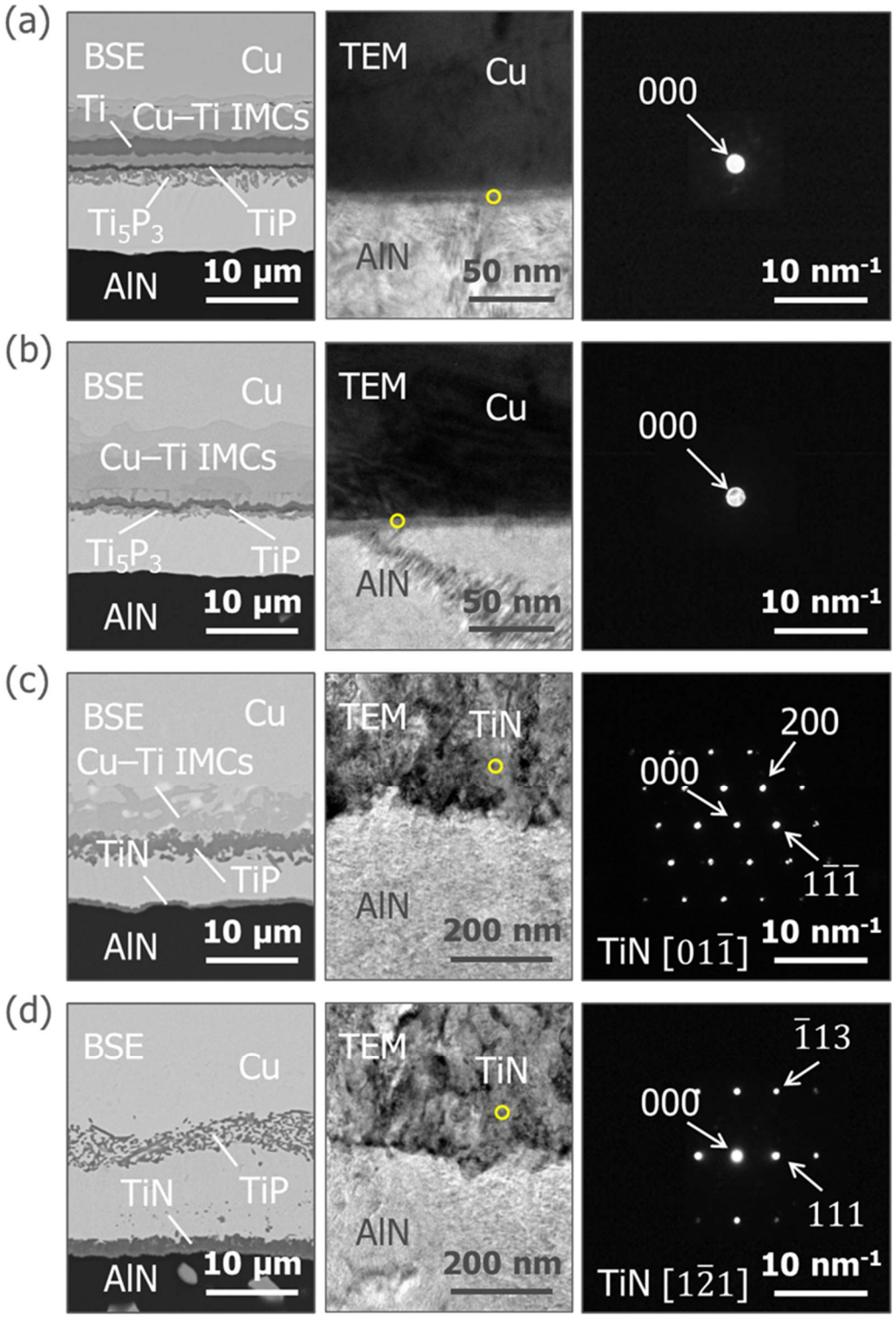


**Fig. 5.9 Cross-sectional BSE and TEM images of a Cu/AlN bonding interface with NBD patterns of the interfacial reaction layer after bonding for 1 h with an initially 5-μm-thick Ti film at (a) 650 °C, (b) 750 °C, (c) 850 °C, and (d) 950 °C [2], © 2022 by Springer Science Business Media, reproduced with license.**

with NBD patterns of a Cu/AlN interfacial reaction layer after bonding for 1 h between 650 °C and 950 °C with the 5-μm-thick Ti layer, are shown in Fig. 5.9. In the BSE images, the gray area in the AlN layer shown is yttria. The NBD patterns were acquired from the areas circled in yellow in the corresponding TEM images. As the heating temperature was increased from 650 °C to 750 °C, the residual Ti layer disappeared because of the growth of the Cu–Ti IMC layer. In addition, the layer of Cu–Ti IMCs disappeared and an obvious interfacial reaction layer was formed at the AlN interface at 850 °C or higher. The thickness of these interfacial reaction layers, which were identified as the crystalline TiN phase from the NBD patterns shown in Fig. 5.9, are ~0.5 μm at 850 °C and ~1 μm at 950 °C, respectively.

The Cu/AlN interfacial reaction layers were composed of an amorphous phase at a heating temperature of 750 °C or lower when using the 5-μm-thick Ti foil. This was the same as with the Cu/AlN interfacial structure when using Ti films with an initial thickness of 1 μm or less, as shown in Figs. 5.6 and 5.7. Cross-sectional HAADF images, together with elemental distributions of the Cu/AlN interface bonded at 650 °C and 750 °C for 1 h with initial 0.5 μm Ti layers, are shown in Figs. 5.10 and 5.11, respectively. Both Sn and Ni are omitted from these elemental maps but were present in solid solution within Cu near the Cu/AlN bonding interface. The highest signals in the P, Ti, and O maps were located at the Cu/AlN bonding interface, as can be seen in Fig. 5.10(c)–(e). By comparison, only Ti and O signals were uniformly distributed at the Cu/ AlN interfacial reaction layer, whereas P was enriched at the interface between Cu and interfacial reaction layer, as shown in Fig. 5.11(c)–(e), despite the base signal of P in the Cu in Fig. 5.11(c) being relatively high. When using the Ti foil with the smallest initial thickness of 0.5 μm shown in Figs. 5.10 and 5.11, the transformation of the elemental distribution at the

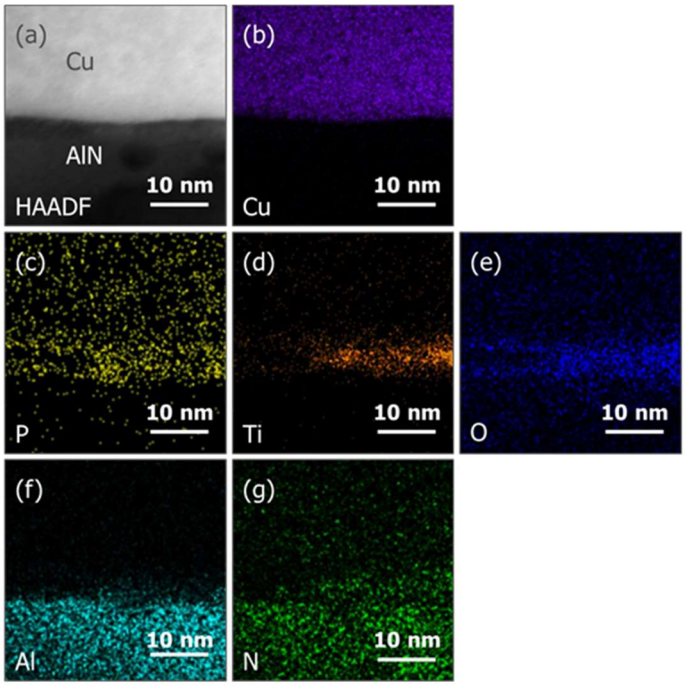


**Fig. 5.10 (a) HAADF image of a Cu/AlN bonding interface after bonding at 650 °C for 1 h with an initially 0.5-μm-thick Ti film, together with elemental distributions of (b) Cu, (c) P, (d) Ti, (e) O, (f) Al, and (g) N.**

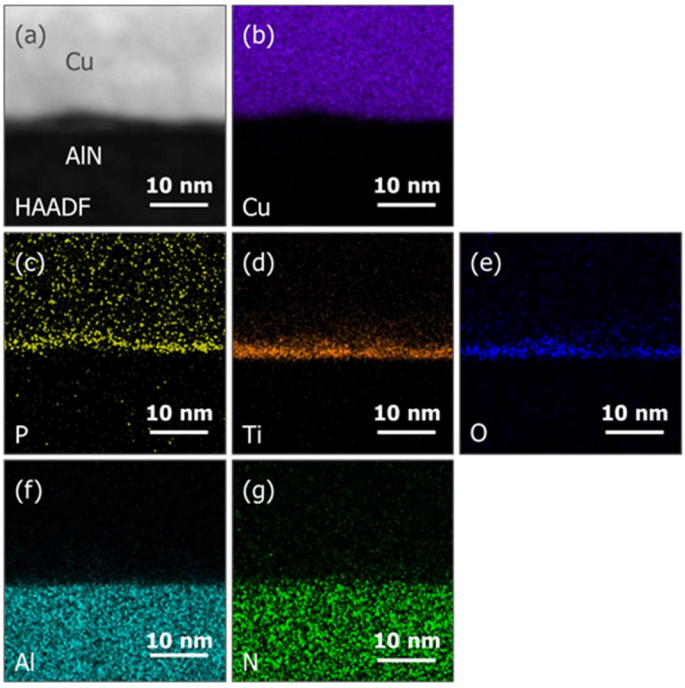


**Fig. 5.11 (a) HAADF image of a Cu/AlN bonding interface after bonding at 750 °C for 1 h with an initially 0.5-μm-thick Ti film, together with elemental distributions of (b) Cu, (c) P, (d) Ti, (e) O, (f) Al, and (g) N.**

Cu/AlN bonding interface was consistent with that when using the Ti foil with the greatest initial thickness of 5 μm as shown in Figs. 5.12 and 5.13. This suggests that at 650 °C and 750 °C the reaction between Cu and AlN did not depend on the thickness of the initial Ti layer. Furthermore, the thickness of these Ti–O based phases observed at the Cu/AlN bonding interface under these bonding conditions was at most 10 nm for 0.5–5-μm-thick Ti material, regardless of whether the source of the Ti material was a film or a foil. This suggests that the oxygen component of the Ti–O-based phases was derived mainly from the surface oxide layer of the AlN and the brazing material, rather than from any oxygen from the surface and grain boundaries of the Ti material. This implies that the Ti–O-based phase can be formed by modification of the amorphous Al–O phase on the AlN surface.

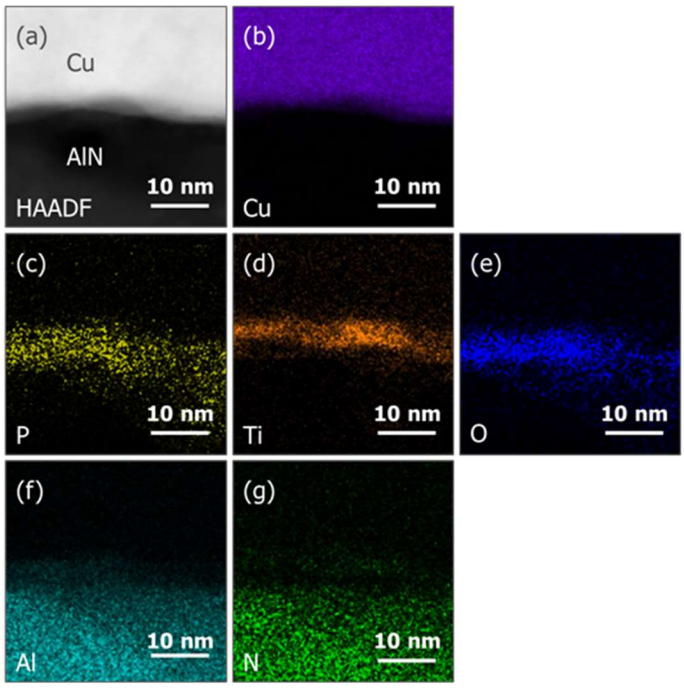


**Fig. 5.12 (a) HAADF image of a Cu/AlN bonding interface after bonding at 650 °C for 1 h with an initially 5-μm-thick Ti foil, together with elemental distributions of (b) Cu, (c) P, (d) Ti, (e) O, (f) Al, and (g) N [2], © 2022 by Springer Science Business Media, reproduced with license.**

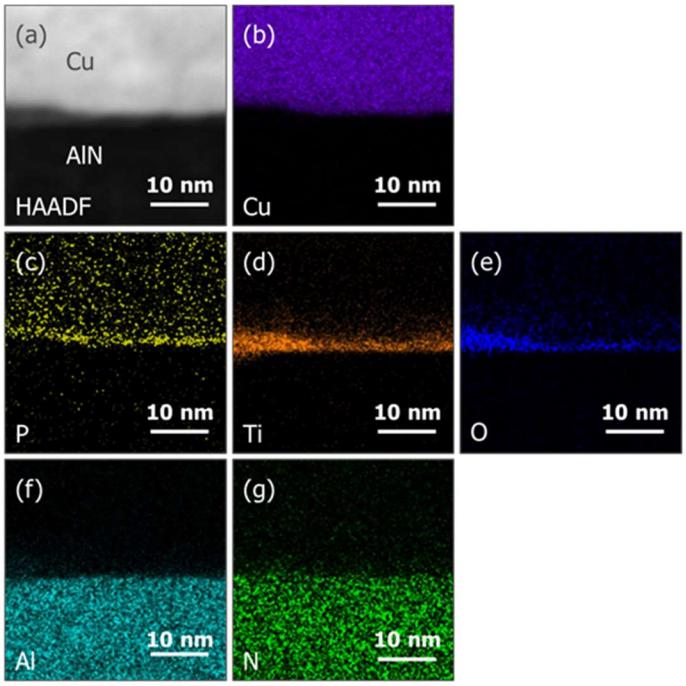


**Fig. 5.13 (a) HAADF image of a Cu/AlN bonding interface after bonding at 750 °C for 1 h with an initially 5-μm-thick Ti foil, together with elemental distributions of (b) Cu, (c) P, (d) Ti, (e) O, (f) Al, and (g) N [2], © 2022 by Springer Science Business Media, reproduced with license.**

Quantitative analysis using EPMA of the Cu phase 4 μm away from a Cu/AlN bonding interface after bonding at 650 °C and 750 °C for 1 h is shown in Table 5.1. The Sn concentration decreased by more than half between 650 °C and 750 °C when using the Ti films with thickness of 1 μm or less, whereas there was only a 5% decrease using the 5-μm-thick Ti foil. This is consistent with the Ti residual layer and/or the thick Cu–Ti IMC layer strongly inhibiting the diffusion of Sn into the Cu surface side. This Sn concentration, which was relatively insensitive to the 100 °C temperature rise for the 5-μm-thick Ti foil, was larger than the solid solubility of Sn in Cu at 850 °C (5.6 at%) [21–23]. This implies that the Cu–Sn liquid phase generated by the remelting of the Cu phase in contact with the AlN substrate melted the layer of Cu–Ti IMCs above 850 °C. Thus, the Ti-containing liquid phase generated at a relatively high heating temperature helped

**Table 5.1 Quantitative analysis of the Cu phase 4 μm away from a Cu/AlN bonding interface after bonding for 1 h at the specified temperatures.**

| Thickness of Ti film/foil (μm) | Temperature (°C) | Concentration (at%) | | | | |
|---|---|---|---|---|---|---|
| | | Cu | P | Sn | Ni | Ti |
| 0.5 | 650 | 94.9 | 1.5 | 3.0 | 0.5 | 0.1 |
| | 750 | 98.4 | 0.0 | 1.2 | 0.3 | 0.1 |
| 1 | 650 | 95.6 | 0.4 | 3.8 | 0.2 | 0.1 |
| | 750 | 97.8 | 0.0 | 1.9 | 0.2 | 0.1 |
| 5 | 650 | 92.8 | 0.5 | 6.1 | 0.2 | 0.4 |
| | 750 | 93.7 | 0.0 | 5.8 | 0.1 | 0.4 |

to promote the single-substitution reaction between Ti and AlN on the surface of the AlN substrate, in a manner similar to the AMB method using Ag.

### 5.3.2 Development process of the rutile $TiO_2$ structure at the Cu/AlN bonding interface

A relatively low-magnification cross-sectional BF-TEM image of the Cu/single-crystal AlN interface bonded at 650 °C for 1 h and viewed along the $[11\bar{2}0]$ AlN zone axis is shown in Fig. 5.14. The Cu/AlN bonding interface appeared to be flat with no gaps and/or pores. This suggests that significant morphological changes between Cu and AlN did not occur during this bonding procedure just above the liquidus temperature of the Cu–P–Sn–Ni brazing foil.

Higher-magnification cross-sectional BF-TEM images of Cu/AlN interfaces bonded at temperatures between 650 and 950 °C for 1 h are shown in Fig. 5.15. The reaction layer formed at 650 °C had a thickness of 2–5 nm. On the other hand, a uniform reaction layer

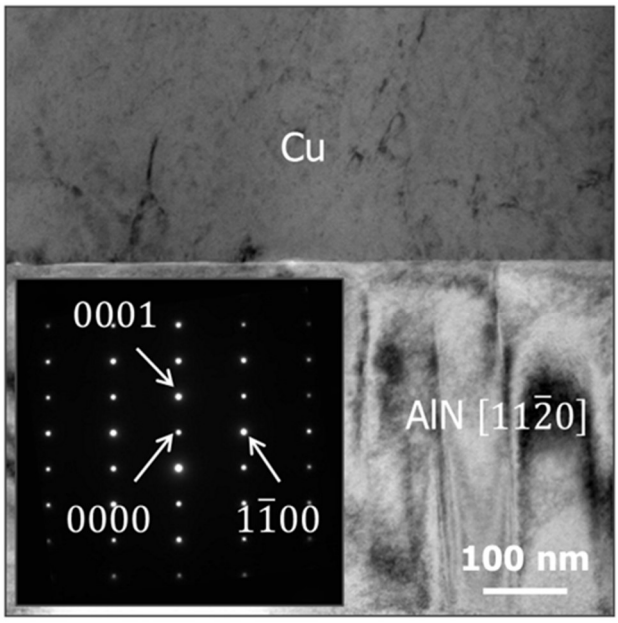


**Fig. 5.14 A cross-sectional TEM image of the Cu/AlN interface bonded at 650 °C for 1 h with an initially 0.5-μm-thick Ti film. AlN as observed along the [$11\bar{2}0$] direction, which is shown in the inset SAED pattern [1], © 2021 by Springer Science Business Media, reproduced with license.**

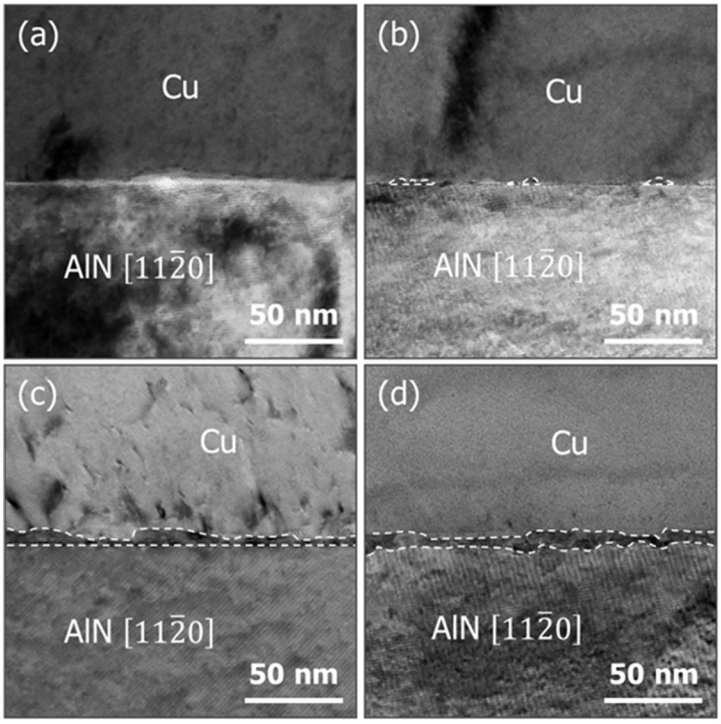


**Fig. 5.15 Cross-sectional BF-TEM images of Cu/AlN bonding interfaces after bonding for 1 h at (a) 650 °C, (b) 750 °C, (c) 850 °C, and (d) 950 °C with an initially 0.5-μm-thick Ti film [1], reproduced with license.**

formed at the Cu/AlN interface above 850 °C with a thickness of up to 10 nm, which was partially grown at 750°C. The surface of AlN remained flat when it was in contact with Cu/AlN interfacial reaction layers for bonding temperatures between 650 °C and 850 °C. However, this flatness was lost at the bonding temperature of 950 °C. This sequence of observations is consistent with the interfacial reaction(s) between the Cu braze and AlN occurring first on the surface of the AlN before proceeding into the bulk of the AlN.

HAADF images and elemental distributions of the Cu/AlN interfaces bonded at 650 °C and 750 °C for 1 h are shown in Figs. 5.16 and 5.17, respectively. Sn and Ni, not shown in these elemental maps, were both in solid solution within the Cu. The highest signals in the P, Ti and O maps were located at the Cu/AlN interfacial reaction layer, as shown in Fig. 5.16(c)–(e). By comparison, only Ti and O signals were detected uniformly in the

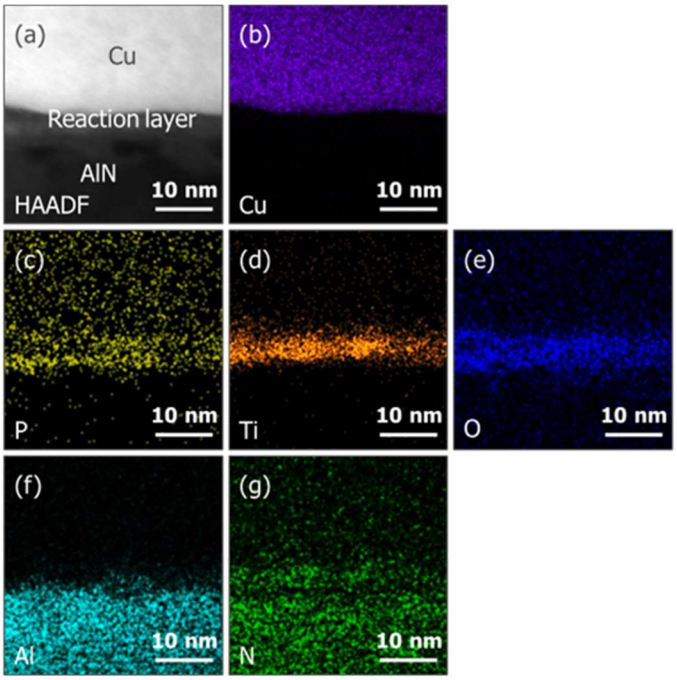


**Fig. 5.16 (a) HAADF image of a Cu/AlN bonding interface bonded at 650 °C for 1 h, together with elemental distributions of (b) Cu, (c) P, (d) Ti, (e) O, (f) Al, and (g) N with an initially 0.5-µm-thick Ti film [1], © 2021 by Springer Science Business Media, reproduced with license.**

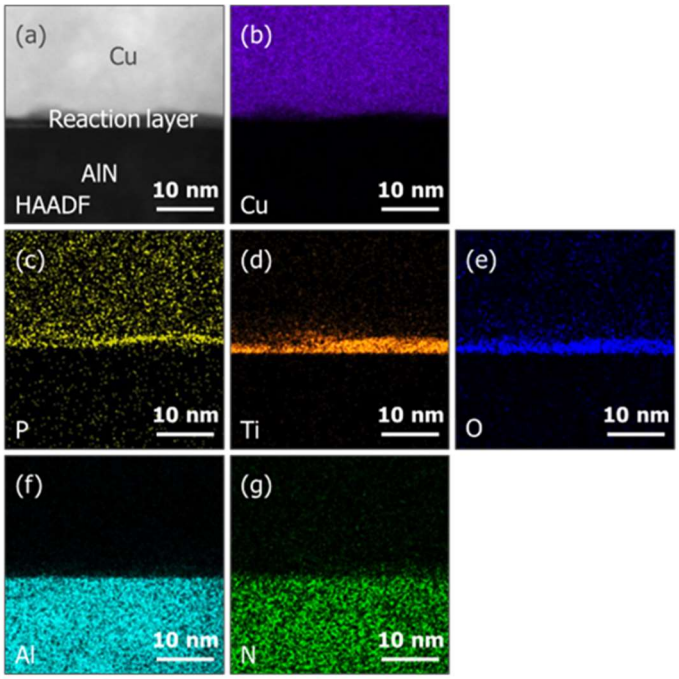


**Fig. 5.17 (a) HAADF image of a Cu/AlN bonding interface bonded at 750 °C for 1 h, together with elemental distributions of (b) Cu, (c) P, (d) Ti, (e) O, (f) Al, and (g) N with an initially 0.5-μm-thick Ti film [1], © 2021 by Springer Science Business Media, reproduced with license.**

Cu/AlN interfacial reaction layer, whereas P was concentrated at the interface between Cu and interfacial reaction layer, as shown in Fig. 5.17(c)–(e). The behavior of P, Ti, and O at the Cu/AlN bonding interface was the same for both polycrystalline AlN and single-crystal AlN.

BF-TEM and high-resolution TEM images of the Cu/AlN bonding interfaces after bonding for 1 h between 650 °C and 950 °C, together with NBD images acquired from each reaction layer of the Cu/AlN bonding interface, are shown in Fig. 5.18. All observations were made along the $[11\bar{2}0]$ AlN direction. Given the elemental distribution of the Cu/AlN interfacial reaction layer formed at 650 °C for 1 h as shown in Fig. 5.16(c)–(e), the Cu/AlN interfacial reaction layer was identified as amorphous P–Ti–O.

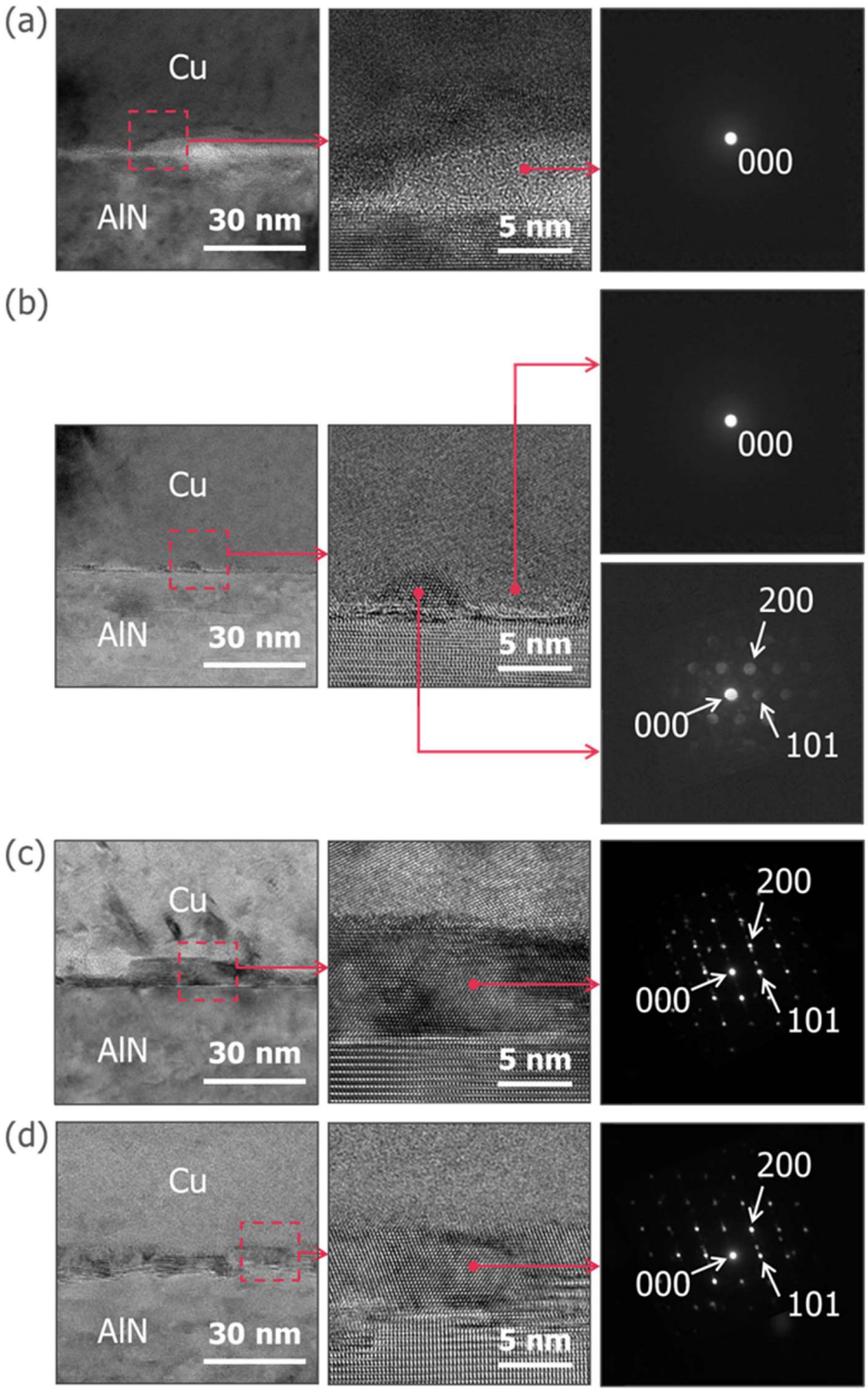


**Fig. 5.18 Cross-sectional BF-TEM and HRTEM images of Cu/AlN bonding interfaces with NBD patterns of the interfacial reaction layer observed along $[11\bar{2}0]$ AlN after bonding for 1 h at (a) 650 °C, (b) 750 °C, (c) 850 °C and (d) 950 °C with an initially 0.5-μm-thick Ti film [1], © 2021 by Springer Science Business Media, reproduced with license.**

From the NBD patterns acquired from the Cu/AlN interfacial reaction layer above 850 °C shown in Fig. 5.18(c)–(d), these Cu/AlN interfacial reaction layers were identified as rutile $TiO_2$ with a [010] zone axis observed at each bonding temperature. At the highest bonding temperature of 950 °C, the rutile $TiO_2$ was able to attack the underlying AlN substrate. In addition, from the NBD pattern acquired from the Cu/AlN interfacial reaction layer formed at 850 °C for 1 h shown in Fig. 5.18(b), a third phase, which is also composed of Ti and O, was identified as amorphous Ti–O. These results suggest that rutile $TiO_2$ was formed by the crystallization of amorphous Ti–O by the outward diffusion of P from amorphous P–Ti–O into the adjacent Cu. Here, the amorphous P–Ti–O phase grown from the amorphous Al–O phase that is present on the AlN surface is expected to be a titanophosphate glass [31]. The glass can be composed of conventional glass former, $P_2O_5$, which can be vitrified alone, and non-conventional glass former, $TiO_2$, which can be vitrified in a multi-component system [32]. The enrichment of P at the Cu/amorphous Ti–O interface at 750 °C is thought to have facilitated the crystallization of the amorphous Ti–O phase. This implies that P, as a Cu–P-based eutectic system, is useful as an element for the formation of the liquid phase that fills the gaps between the Cu plate and the AlN substrate, while it is an inhibiting element for the formation of $TiO_2$, the interfacial reaction layer. In addition, according to Ellingham's diagram [33], if the amorphous Al–O phase is considered to be $Al_2O_3$, a comparison of the standard free energy of $P_2O_5$ and $TiO_2$, which form titanophosphate glass, with that of $Al_2O_3$ shows that $P_2O_5$, $TiO_2$, and $Al_2O_3$ are lower in that order. It is suggested that $Al_2O_3$ is the most stable of these oxides in the oxide formation reaction starting from the amorphous Al–O phase, which is not consistent with the observed Cu/AlN bonding interfacial structure. This implies that, similar to the modified layers on the surface of TiN particles discussed in Section 4.3.4,

modified layers grown from the amorphous Al–O phase need to be discussed in terms of stability, including the influence of potential fields from Cu and ceramics, as well as thermodynamic stability as bulk materials.

Cross-sectional BF-STEM and HAADF images at the rutile $TiO_2$/AlN interface along [010] rutile $TiO_2$//[11$\bar{2}$0] AlN after bonding at 750 °C for 1 h are shown in Fig. 5.19(a) and (b), respectively. Local dark contrast in the BF-STEM image shown in Fig. 5.19(a) corresponds either to the position of Ti or O columns in the rutile $TiO_2$ bulk, or that of Al or N columns in the AlN bulk, respectively. By comparing Fig. 5.19(a) with the HAADF image shown in Fig. 5.19(b), where the atomic columns with heavier atoms have brighter intensities, it can be seen that the columns with strongest intensities in the BF-STEM image correspond to the cation Ti columns. Similarly, the columns with strong intensity

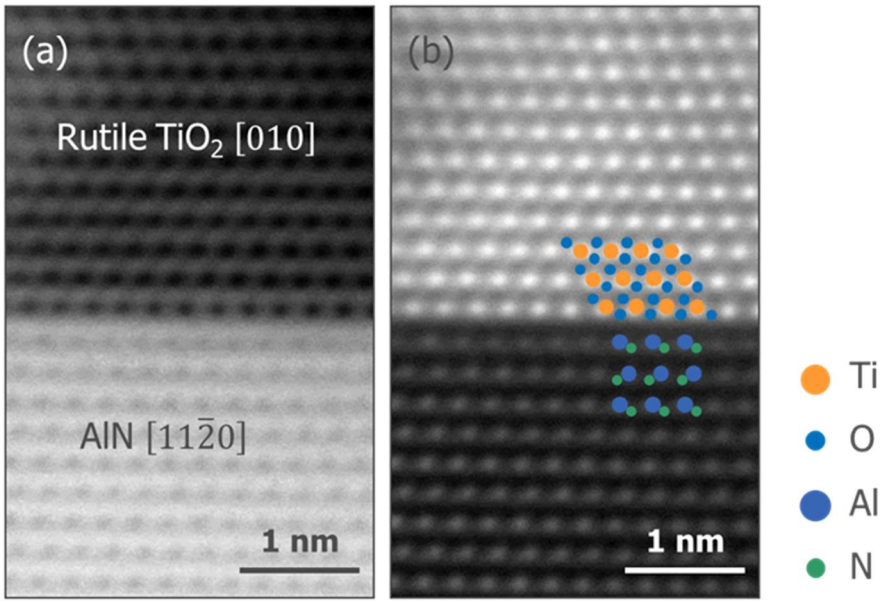


**Fig. 5.19 Cross-sectional (a) BF-STEM and (b) HAADF images of the rutile $TiO_2$/AlN interface after bonding at 750 °C for 1 h with an initially 0.5-μm-thick Ti film [1], © 2021 by Springer Science Business Media, reproduced with license.**

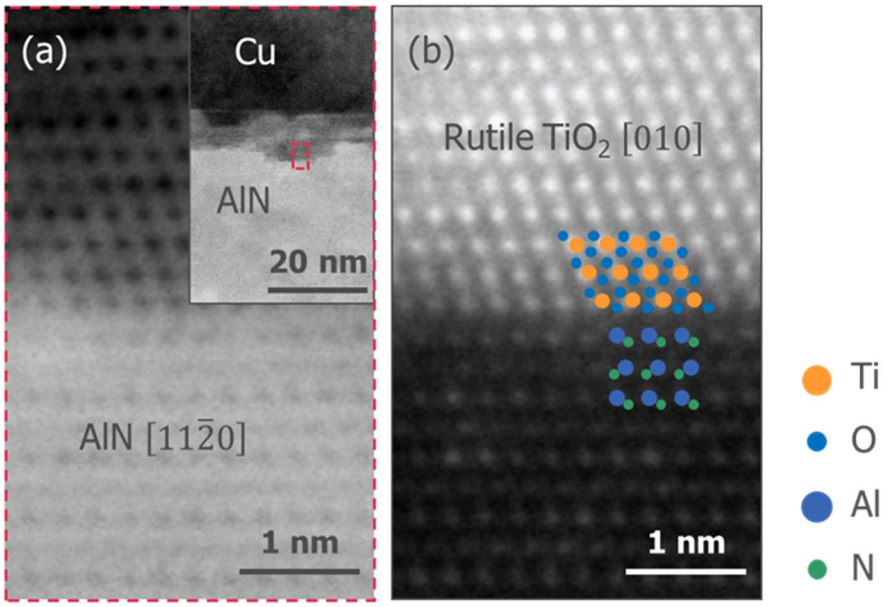


**Fig. 5.20 Cross-sectional (a) BF-STEM and (b) HAADF images of the rutile $TiO_2$/AlN interface after bonding at 950 °C for 1 h with an initially 0.5-μm-thick Ti film [1], © 2021 by Springer Science Business Media, reproduced with license.**

in the AlN bulk region of the BF-STEM image correspond to the cation Al columns. In addition, in consideration of the distribution of bright contrast in the AlN bulk, the AlN substrate is suggested to have an Al–polar growth direction, as shown in the inset of Fig. 5.19(b). Furthermore, Fig. 5.19 shows that here the orientation relationship between rutile $TiO_2$ and AlN is $[010]$ rutile $TiO_2$//$[11\bar{2}0]$ AlN, with $(101)$ rutile $TiO_2$//$(0001)$ AlN.

Cross-sectional BF-STEM and HAADF images at the rutile $TiO_2$/AlN interface seen along $[010]$ rutile $TiO_2$//$[11\bar{2}0]$ AlN after bonding at 950 °C for 1 h are shown in Fig. 5.20(a) and (b), respectively. At this bonding temperature, the rutile $TiO_2$ eroded the AlN, as shown in the inset of Fig. 5.20(a). The orientation relationship between rutile $TiO_2$ and AlN was the same as that after bonding at 750 °C for 1 h (Fig. 5.19). Therefore, rutile $TiO_2$ could chemically attack the AlN layer while maintaining this orientation relationship.

Using three-index notation rather than four-index notation for AlN, it is evident that

the orientation relationship between rutile and AlN shown in Figs. 5.19 and 5.20 is equivalent to $(011)$ rutile $TiO_2$// $(001)$ AlN and $[100]$ rutile $TiO_2$// $[100]$ AlN. Simple mismatch calculations between rutile $TiO_2$ and AlN (hexagonal, $P6_3mc$, $a$ = 3.11 Å, $c$ = 4.98 Å) [34] show that within the parallel planes $(011)$ rutile $TiO_2$ and $(001)$ AlN, the misfit between the parallel vectors $[200]$ rutile $TiO_2$ and $[300]$ AlN, defined with respect to the AlN crystal structure, was –1.5%, while that between the parallel vectors $[01\bar{1}]$ rutile $TiO_2$ and $[120]$ AlN, defined again with respect to the AlN crystal structure, was +1.4%. These lattice mismatches are very low and are consistent with the arrangement of the cations in the HAADF images shown in Figs. 5.19 and 5.20.

Quantitative compositional analysis of the rutile $TiO_2$ from bonding for 1 h at 850 °C and 950 °C is shown in Table 5.2. In the rutile $TiO_2$ heated to 950 °C where the AlN was visibly eroded, the N concentration was 10.7 at%, which is 4.5 at% higher than that in the rutile $TiO_2$ heated to 850 °C where the AlN was not visibly eroded. By comparison, the Al concentration of the rutile $TiO_2$ at both bonding temperatures was about 4–5 at%. The rutile $TiO_2$ remained fully coherent with respect to the AlN bulk structure when it could attack it chemically, meaning that the growth kinetics of the rutile $TiO_2$ into AlN will be strongly affected by its local interfacial crystallography with AlN.

**Table 5.2 Quantitative compositional analysis of rutile $TiO_2$ after bonding for 1 h at the specified temperatures with an initially 0.5-µm-thick Ti film [1], © 2021 by Springer Science Business Media, reproduced with license.**

| Temperature (°C) | Concentration (at%) | | | | | | | |
|---|---|---|---|---|---|---|---|---|
| | Cu | P | Sn | Ni | Ti | O | Al | N |
| 850 | 0.9 | 1.0 | 0.3 | 0.4 | 65.9 | 20.5 | 4.8 | 6.2 |
| 950 | 1.2 | 1.2 | 0.8 | 0.8 | 58.6 | 22.3 | 4.4 | 10.7 |

A simple schematic of the Cu/AlN interfacial structure bonded for 1 h between 650 °C and 950 °C as a function of bonding temperature and thickness of the initial Ti layer is shown in Fig. 5.21. The Cu/AlN interfacial structure transformed from the amorphous P–Ti–O phase to the amorphous Ti–O phase independently of the Ti layer thickness at 750 °C or lower. Above 750 °C, the interfacial reaction phase formed at the Cu/AlN bonding interface depended on the thickness of the Ti layer, specifically, rutile $TiO_2$ for a 0.5-μm-thick Ti film, $TiO_xN_y$ for a 1-μm-thick Ti film, and TiN for a 5-μm-thick Ti foil. Ti concentrations in the amorphous P–Ti–O phase and the amorphous Ti–O phase as a function of the initial Ti material in the range of thickness 0.5–5 μm are shown in Fig.5.22.

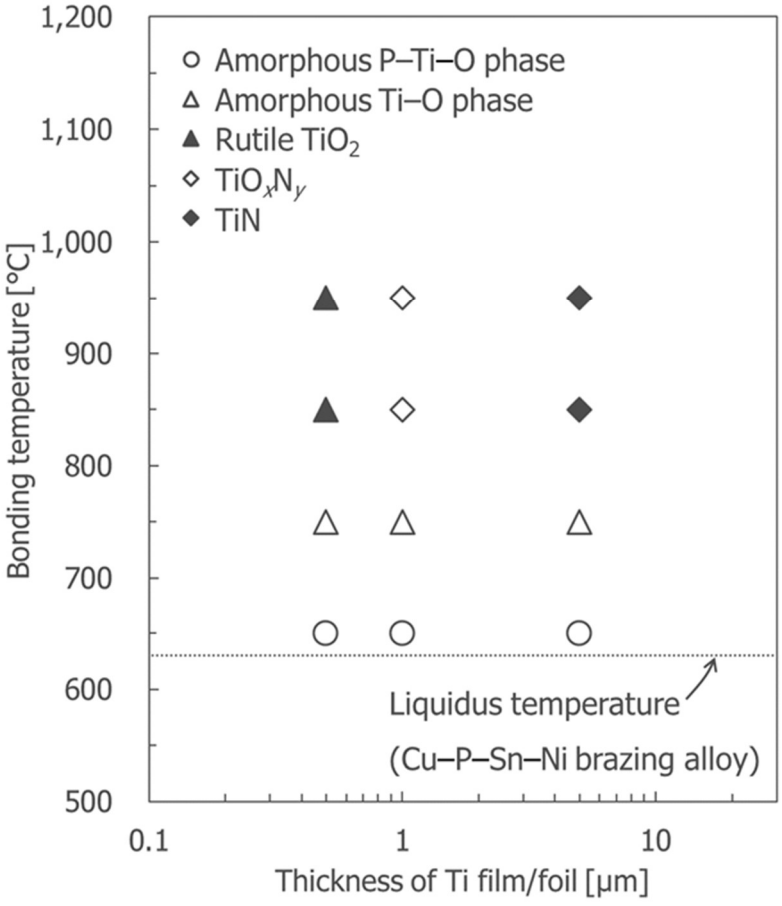


**Fig. 5.21 Classification of Cu/AlN interfacial structure as a function of temperature and Ti film/foil thickness [2], © 2022 by Springer Science Business Media, reproduced with license.**

The Ti concentration in the amorphous Ti–O phase increased with increasing Ti layer thickness, however, within experimental error, the Ti concentration of the highest Ti concentration of 43.0 at% was observed in the amorphous Ti–O phase at 750 °C when using a 5-μm-thick Ti foil. In addition, the N concentration in the rutile $TiO_2$ phase increased from 6.2 at% to 10.7 at%, as shown in Table 5.2, with increasing heating temperature amorphous P–Ti–O phase was independent of the initial thickness of the Ti material. The from 850 °C to 950 °C when using a 0.5-μm-thick Ti film. This implies that

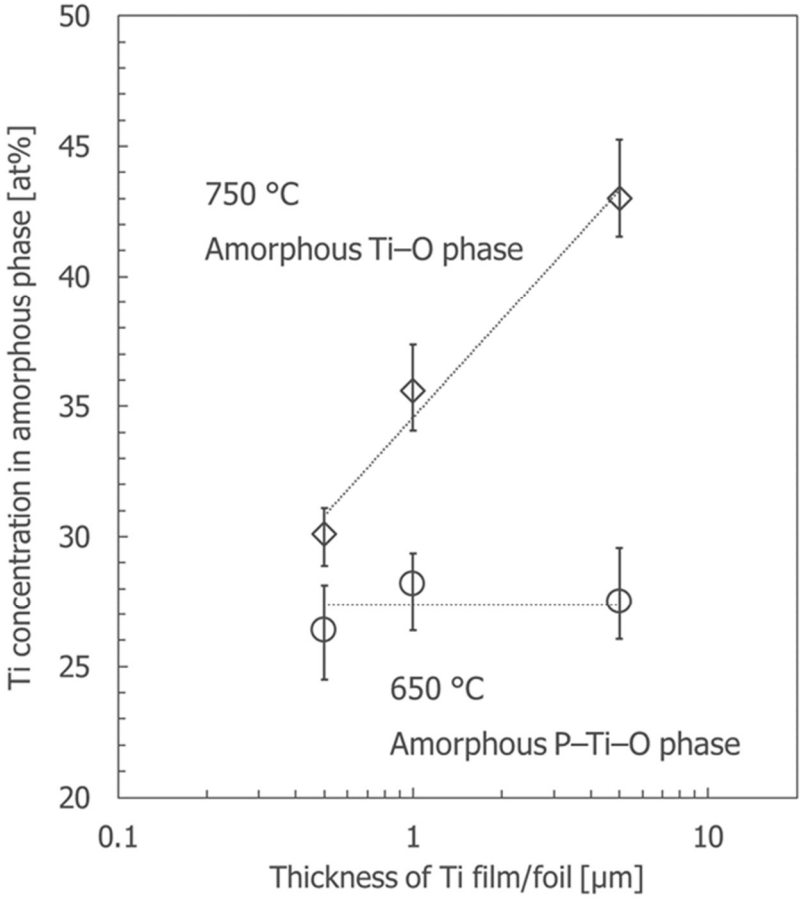


**Fig. 5.22 Dependence of the Ti concentration in the amorphous phase of a Cu/AlN bonding interface on the initial Ti film/foil thickness after bonding for 1 h at 650 °C and 750 °C. Within the experimental error for the 0.5–5-μm thickness range shown, the Ti concentration of the amorphous P–Ti–O phase was independent of the initial thickness of the Ti material, whereas that of the amorphous Ti–O phase increased with increasing initial thickness of the Ti material [2], © 2022 by Springer Science Business Media, reproduced with license.**

the difference in Cu/AlN interfacial reaction layer between the initial 0.5- and 1-μm-thick Ti films was caused by the difference in the amount of erosion of the AlN substrate through the Ti concentration in the amorphous (P–)Ti–O phase. Hence, an increase in the N concentration at the Cu/AlN interface promoted the formation of $TiO_xN_y$, rather than rutile $TiO_2$, as the crystallization product of the amorphous Ti–O phase. This growth process of the $TiO_xN_y$ phase for a 1-μm-thick Ti film was completely different from the formation process of the TiN phase, which was similar to the process in the Ag–Cu–Ti-based system. This was a consequence of the melting of the Cu phase in the case of the 5-μm-thick Ti foil.

### 5.3.3 Reliability of the Cu/AlN bonding interface by ultrasonic welding of Cu terminals

The probability of Cu/AlN interfacial fracture after ultrasonic welding Cu terminals to Cu/AlN/Cu substrates bonded for 1 h at temperatures between 650 °C and 950 °C is shown in Fig. 5.23(a). Here, the Cu/AlN interfacial fracture probability gradually decreased from 43.3% (13 out of 30 samples tested) for bonding at 650 °C to 33.3% (10/30) for bonding at 750 °C, decreasing further to 0% (0/30) at a bonding temperature of 850 °C or higher. These data show that the commercial production of reliable Cu/AlN bonding interfaces for practical use is very likely possible via the Ag-free AMB method using a Cu–P-based material if the bonding temperature is 850 °C or higher.

Examples of cross-sectional BSE images of the Cu/AlN bonding interface after ultrasonic welding of the Cu terminal to the Cu/AlN/Cu substrates bonded for 1 h at 650 °C and 850 °C are shown in Fig. 5.23(b) and (c), respectively. In the bond produced

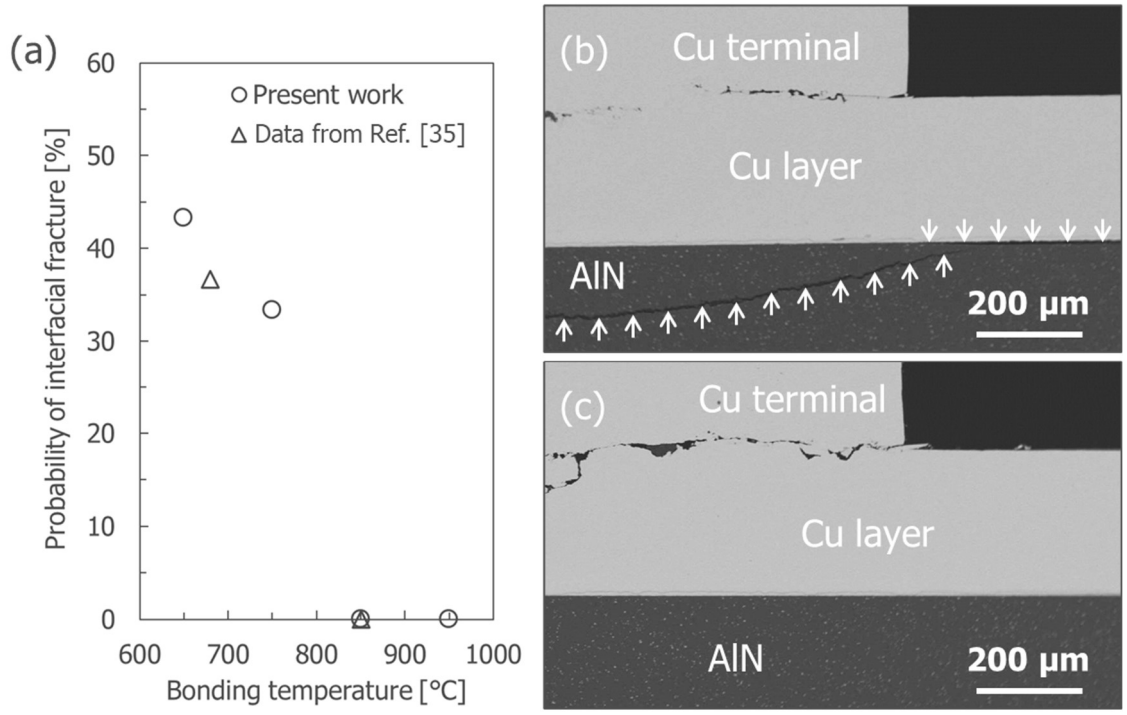


**Fig. 5.23 (a) Effects of heating temperature on the probability of Cu/AlN interfacial fracture after ultrasonic welding of a Cu terminal to the Cu/AlN/Cu substrate, together with examples of cross-sectional BSE images of the Cu terminal/Cu/AlN interface after bonding for 1 h at (b) 650 °C and (c) 850 °C with an initially 0.5-μm-thick Ti film. Cracks in the AlN substrate and at the Cu/AlN interface are indicated by arrows in (b) [1], © 2021 by Springer Science Business Media, reproduced with license.**

at 650 °C, cracks formed inside the AlN just below where the Cu terminal was ultrasonically welded to the Cu layer. Furthermore, delamination of the Cu/AlN interface occurred near the approaching crack, just below the edge of the Cu terminal. This suggests that local delamination of the Cu/AlN bonding interface occurred due to the ultrasonic vibration when the welding of the Cu terminal caused cracks in AlN. By comparison, no 650 °C and 850 °C are shown in Fig. 5.23(b) and (c), respectively. In the bond produced at 650 °C, cracks formed inside the AlN just below where the Cu terminal was ultrasonically welded to the Cu layer. Furthermore, delamination of the Cu/AlN interface occurred near the approaching crack, just below the edge of the Cu terminal. This suggests that local delamination of the Cu/AlN bonding interface occurred due to the ultrasonic

**Table 5.3 Density comparison in amorphous and crystalline phases of metals and oxides.**

| | Density | | |
|---|---|---|---|
| | Amorphous phase [g/cm³] | Crystalline phase [g/cm³] | Difference [%] |
| Cu [36] | 8.83 | 8.96 | 1.5 |
| Al [36] | 2.68 | 2.70 | 0.7 |
| Au [36] | 18.57 | 19.30 | 3.8 |
| Ni [36] | 8.76 | 8.90 | 1.6 |
| $Al_2O_3$ [37, 40] | 2.8–3.2 | 3.69 | 13.3–24.1 |
| $WO_3$ [38, 41] | 5.0–5.6 | 7.16 | 21.8–30.2 |
| $Ta_2O_5$ [39, 42] | 7.31–7.68 | 8.36 | 8.1–12.6 |

fracture events, such as the delamination of Cu/AlN bonding interface or the production of AlN internal cracks, were observed in the AlN substrate bonded at 850 °C. Table 5.3 compares the density of the amorphous and crystalline phases of metals and oxides [36–42]. It can be seen that the density of the amorphous phase is lower than that of the crystalline phase, whose difference is larger than in oxides than in metals. Generally, ceramics such as oxides contain numerous defects. When ceramics are compressed, cracks caused by defects grow steadily. On the other hand, when the ceramic is pulled, cracks propagate rapidly under low stress. Thus, the ceramics have high compressive strength and low tensile strength [43]. These suggest that crystallization of the amorphous Ti–O phase restrained by Cu and AlN generates compressive stresses in rutile $TiO_2$ and increases the strength of the Cu/AlN bonding interface. Taken together with the microstructural observations on the bonding of Cu onto AlN, these observations indicate that the formation of rutile $TiO_2$ at the braze/AlN interface is a key aspect in realizing reliable Cu/AlN bonds using Ag-free bonding material based on the Cu–P eutectic system

with Ti as an active metal.

### 5.3.4 Effect of the bonding material on the ECM resistance between electrodes

The relationship between the electrical resistance between Cu electrodes and duration of voltage application on the Ag-free Cu/AlN bonding substrate and Ag-containing Cu/AlN bonding substrate in the water drop test is shown in Fig. 5.24. The electrical resistance between Cu electrodes before the test was approximately $10^{13}$ Ω regardless of the bonding material, but it rapidly decreased to approximately $10^{6}$ Ω after 1 s of voltage application. In addition, as the duration of voltage application progressed, the electrical resistance between the Cu electrodes decreased further, reaching $2 \times 10^{4}$ Ω after 2–4 s for the Ag-containing Cu/AlN bonding substrate and after 7 s for the Ag-free Cu/AlN bonding substrate, respectively. These results suggest that the rate of decrease in the

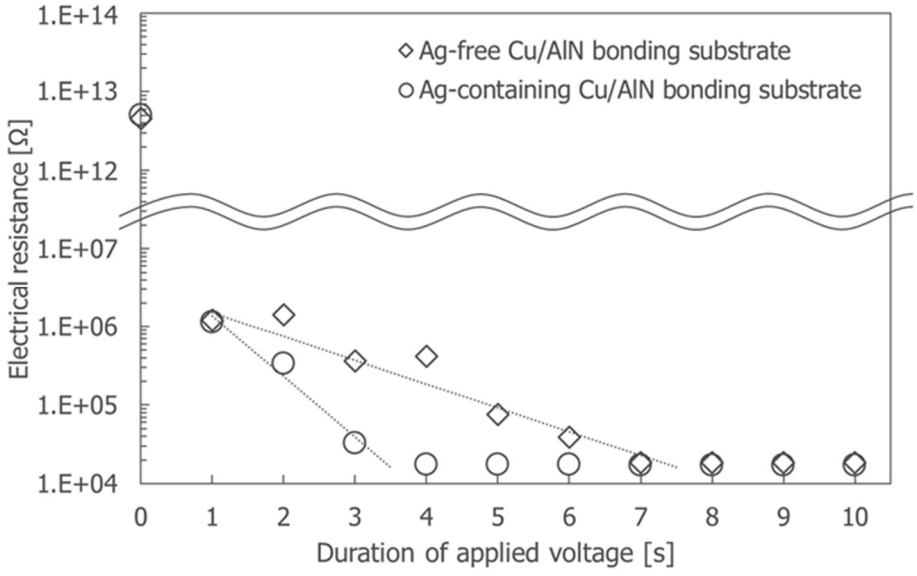


**Fig. 5.24 Electrical resistance between Cu electrodes versus duration of applied voltage.**

electrical resistance between Cu electrodes of the Ag-free Cu/AlN bonding substrate is approximately half that of the Ag-containing Cu/AlN bonding substrate. Thus, the ECM resistance of the Ag-free Cu/AlN bonding substrate was approximately three times higher than that of the Ag-containing Cu/AlN bonding substrate.

The SE image and elemental distributions between the Cu electrodes of Ag-free Cu/AlN bonding substrate and Ag-containing Cu/AlN bonding substrate after the water drop test are shown in Figs. 5.25 and 5.26, respectively. Cu, P, and Sn were distributed between the Cu electrodes for the Ag-free Cu/AlN bonding substrate as shown in Fig. 5.25(b)–(d), where no Ni was detected. On the other hand, Cu and Ag were distributed between the Cu electrodes for the Ag-containing Cu/AlN bonding substrate as shown in Fig. 5.26(b) and (c). Since the frequency of ECM occurrence for the detected elements is known to increase in the order of Ag, Cu, and Sn, the difference in the rate of decrease in electrical resistance between the Cu electrodes for the Ag-free Cu/AlN bonding substrate

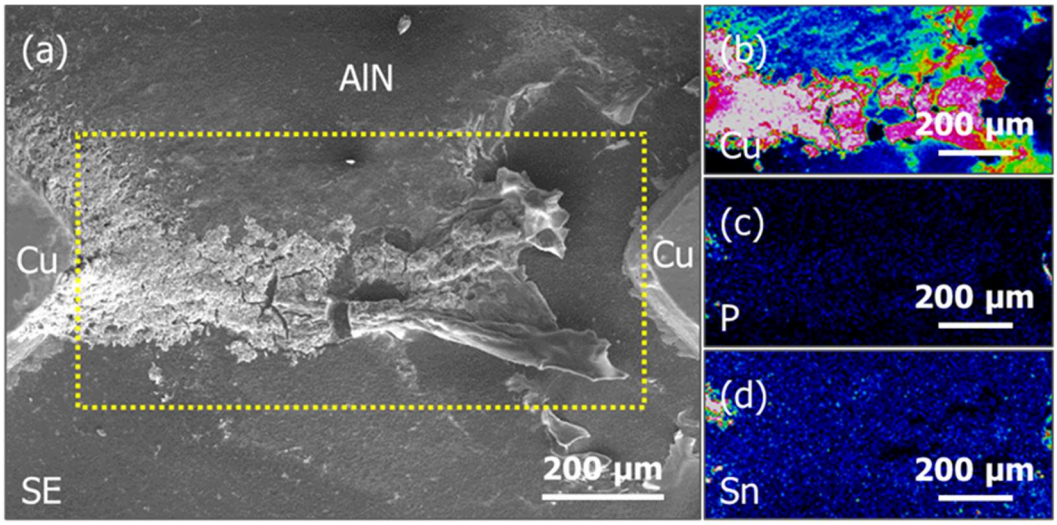


**Fig. 5.25 (a) SE image of an AlN surface of a Ag-free Cu/AlN bonding substrate after the water drop test, together with elemental distributions of (b) Cu, (c) P, and (d) Sn obtained from the yellow dotted area shown in (a).**

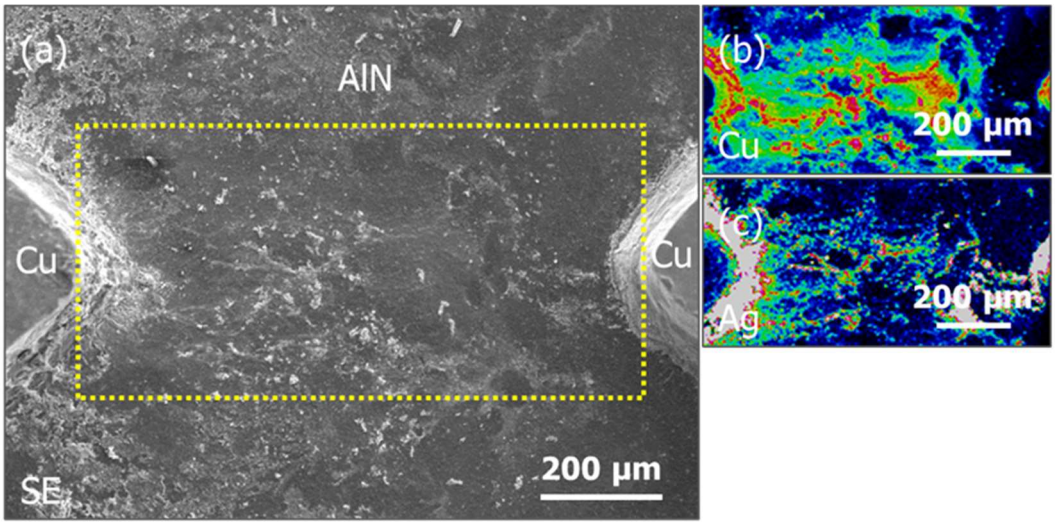


**Fig. 5.26 (a) SE image of an AlN surface of a Ag-containing Cu/AlN bonding substrate after the water drop test, together with elemental distributions of (b) Cu and (c) Ag obtained from the yellow dotted area shown in (a).**

and the Ag-containing Cu/AlN bonding substrate was due to the migration of Ag ions. This demonstrates that the bonding method between Cu and AlN using Ag-free bonding material is a useful and practical method for manufacturing insulating substrates used in power modules for high-voltage applications where there is a potential risk of insulation failure.

## 5.4 Conclusions

This chapter presented an investigation into the dependence of Cu/AlN interfacial structures bonded by using a combination of Cu–P–Sn–Ni brazing foil and Ti layers on the initial Ti layer thickness and bonding temperature, the relative Cu/AlN strength of the interfaces, and their ECM resistance. These interfacial structures were summarized in Fig. 5.27. The main conclusions were as follows:

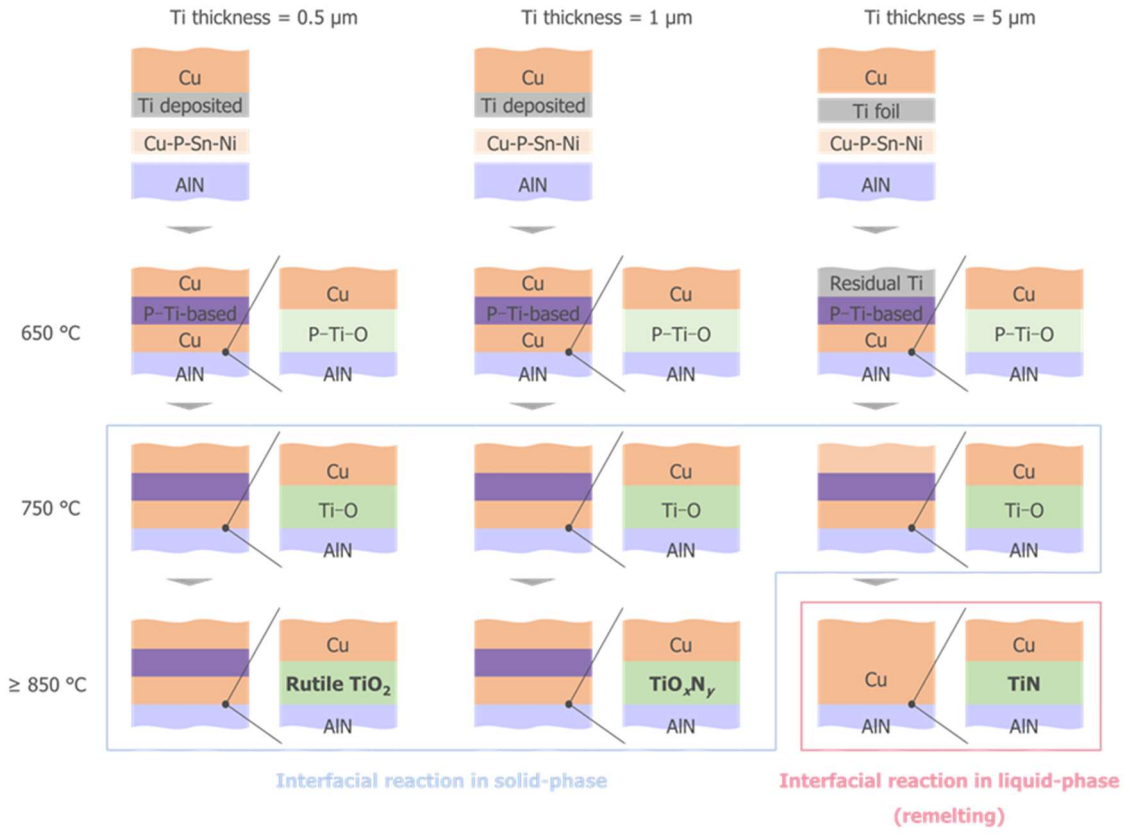


**Fig.5.27 Cu/ceramic interfacial structures discussed in this chapter.**

1. The Cu/AlN bonding interfacial structure produced by combining Cu–P–Sn–Ni brazing foil and a Ti layer resulted in five different phases depending on the initial Ti layer thickness and the bonding temperature: an amorphous P–Ti–O phase, an amorphous Ti–O phase, rutile $TiO_2$, rock-salt $TiO_xN_y$, and TiN, and these are different from the Cu/AlN bonding interfacial structure when using the Cu–Mg–Ti-based system.
2. The novel Cu/AlN bonding interfacial structure, in which a titanium oxide phase was formed by an interfacial reaction with a nitride ceramic, AlN, had the following orientation relationship: [010] rutile $TiO_2$// $[11\bar{2}0]$ AlN, (101) rutile $TiO_2$//(0001) AlN.

3. These Ti–O-based phases were suggested to be formed by modification of the amorphous Al–O phase on the AlN surface.
4. When using Cu–P-based Ag-free bonding materials, a reliable Cu/AlN bonding interface for practical use was achieved by rutile $TiO_2$ dominating the Cu/AlN bonding interface at bonding temperatures of 850 °C or higher.
5. The ECM resistance of Ag-free Cu/AlN bonding substrates using Cu–P-based Ag-free bonding materials was approximately three times higher than that of Ag-containing Cu/AlN bonding substrates.

## References


[1] N. Terasaki, N. Kon, H. Chiba, T. Ohashi, Y. Nagatomo, Y. Kuromitsu, K.M. Knowles, Interfacial structures between aluminum nitride and Cu–P–Sn–Ni brazing alloy with Ti film, Journal of Materials Science, 56, 2021, 8778–8788.

[2] N. Terasaki, A. Nii, H. Chiba, T. Ohashi, K.M. Knowles, T. Sekino, Development of the interfacial microstructure between aluminum nitride and Cu–P–Sn–Ni brazing alloy for different initial titanium layer thicknesses, Journal of Materials Science, 57, 2022, 21731–21742.

[3] N. Schönberg, An X-ray investigation of transition metal phosphides, Acta Chemica Scandinavica, 8(2), 1954, 226–239.

[4] P. Pietrokowsky, E.P. Frink, A constitution diagram for the alloy system titanium tin, Transactions of the American Society for Metals, 49, 1957, 339–358.

[5] G. Brauer, K. Gingerich, M. Knausenberger, Kristallstruktur des Titanphosphids $Ti_5P_3$, Angewandte Chemie, 76(4), 1964, 187.

[6] T. Lundström, P.-O. Snell, Studies of the crystal structures and phase relationships in the Ti–P system, Acta Chemica Scandinavica, 21(5), 1967, 1343–1352.

[7] H. Okamoto, P–Ti (Phosphorus-Titanium), Journal of Phase Equilibria and Diffusion, 28(6), 2007, 587.

[8] H. Okamoto, Sn–Ti (Tin-Titanium), Journal of Phase Equilibria and Diffusion, 31, 2010, 202–203.

[9] P. Thadani, L.E. Toth, J. Zbasnik, Low temperature heat capacities of transition metal phosphidest†, Journal of Physics and Chemistry of Solids, 36(9), 1975, 987–991.

[10] Y. Tokumoto, Y. Sato, T. Yamamoto, N. Shibata, Y. Ikuhara, Atomic structure of $AlN/Al_2O_3$ interfaces fabricated by pulsed-laser deposition, Journal of Materials

Science, 41, 2006, 2553–2557.

[11] Th. Kehagias, Ph. Komninou, G. Nouet, P. Ruterana, Th. Karakostas, Misfit relaxation of the AlN/$Al_2O_3$ (0001) interface, Physical Review B, 64, 2001, art. 195329.

[12] K. Fujimoto, K. Tanaka, S. Nakata, Evaluation method for sensitivity of electrochemical migration by quantity of electricity for electrochemical reaction in water drop test, Quarterly Journal of the Japan Welding Society, 18(1), 2000, 146–152.

[13] A. Matsumura, H. Noguchi, S. Okada, Analysis on initiation process of ionic migration of Ag with the aid of low voltage, Journal of Japan Institute of Electronics Packaging, 6(7), 2003, 546–549.

[14] Y.H. Xia, W. Jillek, E. Schmitt, In-situ observation on electrochemical migration of lead-free solder joints under water drop test, Proceedings of 2008 International Conference on Electronic Packaging Technology and High Density Packaging, 2008, 4607147.

[15] F.J.J.V. Loo, G.F. Bastin, A.J.H. Leenen, Phase relations in the ternary Ti–Ni–Cu system at 800 and 870 °C, Journal of the Less-Common Metals, 57, 1978, 111–121.

[16] H. Okamoto, Cu–Ti (Copper-Titanium), Journal of Phase Equilibria, 23(6), 2002, 549–550.

[17] H.-U. Pfeifer, S. Bahn, K. Schubert, Zum Aufbau des Systems Ti–Ni–Cu und einiger quasihomologer Legierungen, J. Less-Common Metals 14(3), 1968, 291–302.

[18] P. Villars, L.D. Calvert, Pearson's Handbook of Crystallographic data for Intermetallic Phases, Volume 2, American Society for Metals, Metals Park, Ohio, 2037–2038.

[19] R.A. Pérez, M. Behar, F. Dyment, Diffusion study of Sn implanted in α-Ti, Philosophical Magazine A, 75, 1997, 993–1004.

[20] N. Saunders, A.P. Miodownik, The Cu–Sn (Copper-Tin) system, Bulletin of Alloy Phase Diagrams, 11(3), 1190, 278–287.

[21] S. Fürtauer, D. Li, D. Cupid, H. Flandorfer, The Cu–Sn phase diagram, Part I: New experimental results, Intermetallics, 34, 2013, 142–147.

[22] D. Li, P. Franke, S. Fürtauer, D. Cupid, H. Flandorfer, The Cu–Sn phase diagram, Part I: New thermodynamic assessment, Intermetallics, 34, 2013, 148–158.

[23] J. Wang, J. Chen, L. Zhang, Z. Zhang, Y. Han, X. Hu, H. Lu, S. Zhang, Forming mechanism and growth of Kirkendall voids of Sn/Cu joints for electronic packaging: A recent review, Journal of Advanced Joining Processes, 6, 2022, 100125.

[24] B. Wang, W. Li, S. Zhang, X. Liu, K. Pan, Effect of electric current stressing on mechanical performance of solders and solder joints: A review, Journal of Materials Science, 57, 2022, 17533–17562.

[25] J. L. Murray, H. A. Wriedt, O–Ti (Oxygen–Titanium), Binary Alloy Phase Diagrams, 2nd. Edition, Ed. T.B. Massalski, H. Okamoto, P.R. Subramanian, L. Kacprzak, ASM International, Materials Park, OH, 3, 1990, 2924–2927.

[26] C.H. Shin, G. Bugli, G. Djega-Mariadassou, Preparation and characterization of titanium oxynitrides with high specific surface areas, Journal of Solid State Chemistry, 95, 1991, 145–155.

[27] H. Yang, P.G. McCormick, Synthesis of titanium oxynitride by mechanical milling, Journal of Materials Science, 28, 5663–5667.

[28] G. Hyett, M.A. Green, I.P. Parkin, The use of combinatorial chemical vapor deposition in the synthesis of $Ti_{3-\delta}O_4N$ with $0.06 < \delta < 0.25$: a titanium oxynitride

phase isostructural to anosovite, Journal of the American Chemical Society, 129, 2007, 15541–15548.

[29] S.G. Seo, C.-H. Park, H.-Y. Kim, W.H. Nam, M. Jeong, Y.-N. Choi, Y.S. Lim, W.-S. Seo, S.-J. Kim, J.Y. Lee, Y.S. Cho, Preparation and visible-light photocatalysis of hollow rock-salt $TiO_{1-x}N_x$ nanoparticles, Journal of Materials Chemistry A, 1(11), 2013, 3639–3644.

[30] K. Rees, E. Lorusso, S.D. Cosham, A.N. Kulak, G. Hyett, Combining single source chemical vapour deposition precursors to explore the phase space of titanium oxynitride thin films, Dalton Transactions, 47, 2018, 10536–10543.

[31] Y. Shi, N.T. Lonnroth, R.E. Youngman, S.J. Rzoska, M. Bockowski, M.M. Smedskjaer, Pressure-induced structural changes in titanophosphate glasses studied by neutron and X-ray total scattering analyses, Journal of Non-Crystalline Solids, 483, 2018, 50–59.

[32] H. Rawson, Inorganic glass-forming systems, Academic press, New York, 1967.

[33] H.J.T. Ellingham, Reducibility of oxides and sulphides in metallurgical processes, Journal of the Society of Chemical Industry, 63(5), 1944, 125–160.

[34] H.A. Wriedt, Al–N (Aluminum–Nitrogen), Binary Alloy Phase Diagrams, 2nd. Edition, Ed. T.B. Massalski, H. Okamoto, P.R. Subramanian, L. Kacprzak, ASM International, Materials Park, OH, 1, 1990, 176–177.

[35] N. Terasaki, Development of a high reliability power-module substrate via new bonding process using Ag free bonding material, Journal of Smart Processing, 7(5), 2018, 172–175.

[36] D. Weaire, M.F. Ashby, J. Logan, M.J. Weins, On the use of pair potentials to calculate the properties of amorphous metals, Acta Metallurgica, 19(8), 1971, 779–

788.

[37] I. Levin, D. Brandon, Metastable alumina polymorphs: crystal structures and transition sequences, Journal of the American Ceramic Society, 81, 1998, 1995–2012.

[38] M.S. Mattsson, Cation intercalation in sputter-deposited W oxide films, Physical Review B, 58, 1998, 11015.

[39] D. Lützenkirchen-Hecht, R. Frahm, Structural investigations of sputter deposited thin films: reflection mode EXAFS, specular and non specular X-ray scattering, Physica B: Condensed Matter, 283, 2000, 108–113.

[40] G. Gutiérrez, B. Johansson, Molecular dynamics study of structural properties of amorphous $Al_2O_3$, Physical Review B, 65, 2002, 104202.

[41] Y. Kimura, C. Kaito, Characteristic crystal growth from amorphous $WO_3$ film by vacuum heating, Journal of Crystal Growth, 250, 2003, 450 – 457.

[42] Y.-N. Wu, L. Li, H.-P. Cheng, First-principles studies of $Ta_2O_5$ polymorphs, Physical Review B, 83, 2011, 144105.

[43] R.T. Qu, Z. Zhang, A universal fracture criterion for high-strength materials, Scientific Reports, 3, 2013, 1117.

# Chapter 6: General conclusions

The potential risk of dielectric breakdown due to Ag-ECM in conventional AlN–AMB substrates was an issue that needed to be addressed in order to improve the long-term insulation reliability of power modules used in high-voltage applications. The objective of this dissertation was to clarify Cu/AlN bonding interfacial structures with high reliability and high ECM resistance using Ag-free bonding material that can completely eliminate the influence of Ag-ECM. The results of this dissertation are summarized below, together with the schematic diagram of the Cu/ceramic bonding interfacial structures clarified in this dissertation, as shown in Fig. 6.1.

In Chapter 2, the objective was to clarify the growth mechanism of the TiN layer necessary to form a good Cu/AlN bonding interface in the AMB method. The TiN layer formed at the Ag–Cu–$TiH_2$/AlN interface during the brazing process at 850 °C was found to be a complex of TiN particles of <50 nm in size and a grain boundary phase composed of Al solid solution of Ag and Cu. In addition, the interfacial structure between the TiN particles and these grain boundary phases was found to be essentially a Cu-containing segregation layer/Al-containing segregation layer/TiN particles. Furthermore, the TiN layer structure formed at the *M*–$TiH_2$ (*M* = Ag or Cu)/AlN interface during the solid-phase sintering process at 850 °C was equivalent to that formed during the brazing process. Based on the comparison of these TiN layer structures, a TiN layer growth mechanism was proposed in which propagation of the localized interfacial reaction into the AlN interior with the generation of Al-based liquid phase strongly contributes to the TiN layer formation.

In Chapter 3, the objective was to clarify the effects of TiN grain formation and metal components of the grain boundary phase on the formation of metal/TiN grain bonding interfaces and the general structure of metal/ceramic bonding interfaces. At a bonding temperature of 850 °C, the Ag–Cu brazing interfacial structure between Cu and TiN liquid-phase sintered ceramic, where Fe was the main grain boundary component, was found to be a Cu-containing segregation layer/Fe- and Ni-containing segregation layer/TiN grain interfacial structure. The outermost surface of the TiN grains, which formed Fe- and Ni-containing segregation layer, was modified into $Ti_xFe_{1-x}N$ by the interfacial reaction between the TiN grains and the Fe-containing liquid phase. In addition, the Ag–Cu brazing interfacial structure between Cu and WC–Co cemented carbide at 850 °C was found to be a Cu-containing segregation layer/Co-containing segregation layer/hexagonal WC grain interfacial structure. The outermost surface of the hexagonal WC grains, which were Co-containing segregation layer, was modified into tetragonal WC by the interfacial reaction between the hexagonal WC grains and the Co-containing liquid phase. The commonality of these interfacial structures revealed that the general bonding interfacial structure between Cu and ceramics, which requires an interfacial reaction, is a Cu-containing segregation layer/modified layer on the ceramic surface/ceramic. In this interfacial structure, Ag is not an essential component.

In Chapter 4, the objective was to clarify a Cu/AlN bonding interfacial structure using Ag-free bonding materials. The Cu/AlN bonding interfacial structure bonded between 800 °C and 950 °C using Mg–Ti(–Fe) co-deposited films was found to be an interfacial structure where Cu was bonded to AlN via a TiN layer composed of TiN particles and a Cu-containing grain boundary phase, similar to typical AMB substrates fabricated using Ag–Cu–Ti-based bonding materials. Fracture of the Cu/AlN bonding interface by the

SAICAS test was found to occur at the TiN layer/AlN interface. The peel strength of the Fe-free Cu/AlN bonding interface increased exponentially between 800 °C and 950 °C, but was independent of the amount of Ti between 0.14 mg/cm$^2$ and 0.45 mg/cm$^2$. The bond strength at the TiN/AlN interface was found to increase with growth of the MgO phase at the TiN/AlN interface, where the amorphous Al–O phase on the AlN surface was modified. On the other hand, the peel strength of the Fe-containing Cu/AlN interface increase below 850 °C: for Fe amounts between 0.24 mg/cm$^2$ and 0.79 mg/cm$^2$, the peel strength above 900 °C was equivalent to that of the Fe-free Cu/AlN interface, which was added based on the results in Chapter 3. This demonstrated that the Fe–Mg–O phase-dominant TiN layer/AlN interfacial structure formed by the modification of the amorphous Al–O phase transitions to the MgO-dominant TiN layer/AlN interfacial structure with increasing bonding temperature.

In Chapter 5, the objective was to clarify the effect of Ag-free bonding material components on the Cu/AlN bonding interface. The Cu/AlN bonding interfacial structures bonded between 650 °C and 950 °C using Cu–P–Sn–Ni brazing foils and Ti layers were found to develop five interfacial reaction layers: amorphous P–Ti–O phase, amorphous Ti–O phase, rutile $TiO_2$, rock-salt $TiO_xN_y$, TiN, depending on the bonding temperature and initial Ti layer thickness. Of these phases, Ti–O-based phases were found to be formed by modification of the amorphous Al–O phase on the AlN surface. In particular, when using an initial Ti layer thickness of 0.5 μm, fracture at the Cu/AlN bonding interface was sufficiently suppressed at bonding temperatures of 850°C or higher, where rutile $TiO_2$ growing from the amorphous (P–)Ti–O phase was dominant. It was concluded that crystallization of the amorphous Ti–O phase contributed to realizing a Cu/AlN bonding interface that had small lattice mismatch with AlN, which in turn improved the

strength of the Cu/AlN bonding interface. In addition, the ECM resistance of the Ag-free Cu/AlN bonding substrate was approximately three times higher than that of the Ag-containing Cu/AlN bonded substrate, indicating that the development of Cu/AlN bonding technology using Ag-free bonding material can improve the long-term reliability of insulation for power modules using in high-voltage environments.

Based on the discussion in Chapters 2 through 5, guidelines for designing bonding materials capable of suppressing ECM are summarized. First, the ECM resistance of the components of the bonding material must be equal to or greater than that of the metal components constituting the circuit layer. Second, when bonding flat plates such as circuit layer metal plates and ceramic substrates, it is necessary to physically fill the gap between the plates. Therefore, it is suitable to form a liquid phase by melting this highly ECM-resistant bonding material itself or by eutectic formation by interdiffusion between the circuit layer and this bonding material during the bonding process. In particular, when using eutectic systems, it is practical to use a eutectic composition in which the main component of the circuit layer is dominant, which can suppress the amount of liquid phase, since IMC derived from excess liquid phase contributes to ceramic fracture. Third, since thermal stress derived from the difference in expansion coefficients between metal and ceramic promotes ceramic fracture, the upper temperature limit of the melting range of the bonding material should be equal to or lower than that of the Ag–Cu eutectic-based brazing material already in practical use. Finally, the bonding material should contain elements that can form modified layer(s) with respect to the main phase of the ceramic substrate or the surface natural oxide film present on the main phase by interfacial reactions during bonding. Here it is considered desirable that the free energy of the reaction system is reduced by the formation of the modified layer, but further

experimental and computational approaches are needed as future work to determine the design guidelines for the formation of the modified layer.

For Cu/AlN bonding interfacial structures that have high reliability and high ECM resistance using Ag-free bonding materials suitable for high-voltage applications, Cu/AlN bonding interfacial structures are proposed that use two types of Ag-free bonding material: a Cu–Mg–Ti-based system and a Cu–P–Sn–Ti-based system, which can achieve long-term insulation reliability for power modules in high-voltage environments. Since the thermal energy applied to the Cu/AlN bonding interfacial structure in the thermal cycling test between -40 °C and 200 °C at high temperatures, which is a typical durability test of insulating substrates for power modules, is very small compared to that in the bonding process, the macro-scale structures such as TiN layers and IMCs that compose the proposed Cu/AlN bonding interfacial structures show no change before and after the thermal cycling test. While these macroscale structures are thermodynamically stable in this temperature range, it is necessary to evaluate the stability of the Cu/AlN bonding interfacial structures at the nano- and atomic-scale in the future. In addition, guidelines for designing highly ECM-resistant bonding materials based on these Cu/AlN bonding interfacial structures are proposed. Since no principles have been found that can consistently explain all the structures and elements in the modified layer formed at the Cu/AlN bonding interface, it is necessary in the future to refine the design guidelines for the modified layer from both structural analysis based on detailed observation of the Cu/AlN bonding interface structure and analysis of adhesion energies based on DFT calculations. It is hoped that the knowledge presented in this dissertation on the Cu/AlN bonding interfacial structure using Ag-free bonding materials and guidelines for designing highly ECM-resistant bonding materials will, through further evaluation,

provide useful guidelines for the development of new Cu/ceramic bonding technology based on ceramic surface modification in the future.

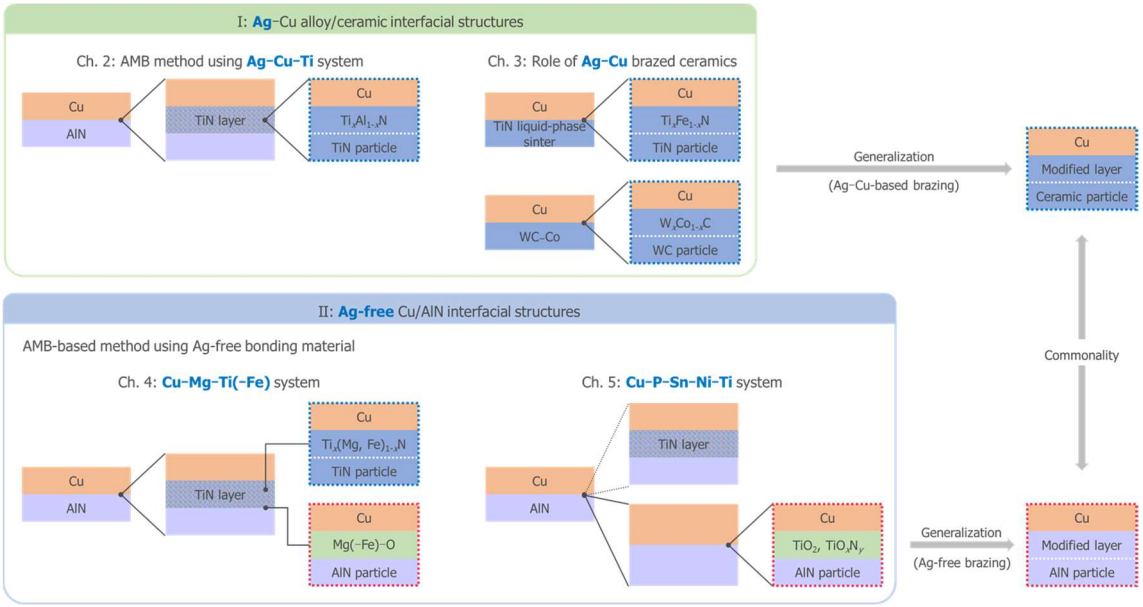


**Fig.6.1 Schematic diagram of the Cu/ceramic bonding interfacial structures clarified in this dissertation.**

# Research achievement

## Peer-reviewed journal articles

1. **N. Terasaki**, M. Sakaguchi, H. Chiba, T. Ohashi, Y. Nagatomo, Y. Kuromitsu, T. Sekino, K.M. Knowles, Growth mechanism of TiN reaction layers produced on AlN via active metal bonding, Journal of Materials Science, 57, 2022, 13300–13313.
2. **N. Terasaki**, A. Nii, H. Chiba, T. Ohashi, K.M. Knowles, T. Sekino, Development of the interfacial microstructure between aluminum nitride and Cu–P–Sn–Ni brazing alloy for different initial titanium layer thicknesses, Journal of Materials Science, 57, 2022, 21731–21742.
3. **N. Terasaki**, N. Kon, H. Chiba, T. Ohashi, T. Sekino, Co segregation on WC grain formed in an interfacial reaction between WC–Co cemented carbide and Ag–Cu eutectic brazing material, Materials Letters, 332, 2023, 133551.
4. **N. Terasaki**, N. Kon, H. Chiba, T. Ohashi, T. Sekino, Interfacial structure between TiN sintered ceramics with and without an Fe-containing grain boundary phase and Ag–Cu eutectic brazing filler material, SN Applied Sciences, 5, 2023, 46.
5. **N. Terasaki**, N. Kon, H. Chiba, T. Ohashi, T. Sekino, Effect of interfacial structure on peel strength between Cu and AlN bonded with a Mg–Ti co-deposited film, Discover Materials, 3, 2023.

## Related peer-reviewed journal articles

1. A. Kumamoto, N. Shibata, K. Nayuki, T. Tohei, **N. Terasaki**, Y. Nagatomo, T. Nagase, K. Akiyama, Y. Kuromitsu, Y. Ikuhara, Atomic structures of a liquid-phase bonded

metal/nitride heterointerface, Scientific Reports, 6, 2016, 22936.

2. **N. Terasaki**, Development of a high reliability power-module substrate via new bonding process using Ag free bonding material, Journal of Smart Processing, 7(5), 2018, 172–175.
3. **N. Terasaki**, T. Ohashi, Y. Nagatomo, Y. Kuromitsu, A.A. Shirzadi, A new method for liquid-phase bonding of copper plates to aluminum nitride (AlN) substrates used in high-power modules, Journal of Materials Science: Materials in Electronics, 30, 2019, 6552–6555.
4. **N. Terasaki**, N. Kon, H. Chiba, T. Ohashi, Y. Nagatomo, Y. Kuromitsu, K.M. Knowles, Interfacial structures between aluminum nitride and Cu–P–Sn–Ni brazing alloy with Ti film, Journal of Materials Science, 56, 2021, 8778–8788.
5. S. Takakuwa, **N. Terasaki**, N. Kon, T. Ohashi, N. Nita, Y. Nagatomo, Y. Kuromitsu, A new transient liquid phase bonding method using magnesium foil to bond copper plates to aluminum nitride substrates, Journal of Materials Science: Materials in Electronics, 33, 2022, 10486–10493.

## Journal articles

1. **N. Terasaki**, K. Akiyama, Y. Nagatomo, Y. Kuromitsu, A. Kumamoto, N. Shibata, Y. Ikuhara, Interface analysis between aluminum and aluminum nitride and its application, Fine Ceramic Report, 35(3), 2017, 121–123.
2. **N. Terasaki**, Development of highly reliable power module substrates using new Cu/ceramics bonding technology, Braze, 124, 2019, 15–22.
3. T. Ohashi, **N. Terasaki**, S. Takakuwa, Bonding technology between copper and nitride ceramics for development of insulating substrates for power modules, Optical and

electro-optical engineering contact, 60(7), 2022, 26–33.

## Conference proceedings

1. S. Nishimoto, A. Sengoku, **N. Terasaki,** Y. Nagatomo, T. Nagase, Y. Kuromitsu, Development of Ag sintered film formation technique on Al surface using Ag paste with glass frit, in the 19th Symposium on Microjoining and Assembly Technology in Electronics, 19, 2013, 449-454.
2. **N. Terasaki**, Y. Nagatomo, T. Nagase, Y. Kuromitsu, New power module structures consist of both copper and aluminum bonded on aluminum nitride substrates with an aluminum base plate, 8th International conference on lntegrated power Electronics systems, 2014, 456–460.
3. **N. Terasaki**, Y. Nagatomo, T. Nagase, Y. Kuromitsu, Reliability and thermal resistance evaluation of Cu–Al composite insulating substrates for power modules, Journal of MMIJ, 130(6), 2014, 363–367.
4. S. Takakuwa, **N. Terasaki**, T. Ohashi, Development of a new bonding technique between Cu and $Si_3N_4$ by using Ag free bonding material, in the 26th Symposium on Microjoining and Assembly Technology in Electronics, 26, 2020, 281–284.

## Oral presentations

1. **N. Terasaki**, Y. Nagatomo, T. Nagase, Y. Kuromitsu, New power module structures consist of both copper and aluminum bonded on aluminum nitride substrates with an aluminum base plate, 8th International Conference on Integrated Power Electronics Systems, 2014.

2. **N. Terasaki**, Y. Nagatomo, T. Nagase, Y. Kuromitsu, Reliability and thermal resistance evaluation of Cu–Al composite insulating substrates for power modules, Conference on Mining and Smelting, 2014.
3. **N. Terasaki**, Y. Nagatomo, Y. Kuromitsu, Development of highly reliable power module substrates using new Cu/ceramics bonding technology, 109th Technical Commission on Solid Phase Welding and Brazing, 2018.

## Reviews and books

1. **N. Terasaki**, Development of a high reliability power-module substrate via metal/ceramic bonding technology, in Development and Mounting Technology of Printed Wiring Board Materials, Technical Information Institute Co., Ltd., Tokyo, 2020, 148–155.
2. **N. Terasaki**, New bonding technology for copper/nitride ceramics with silver-free bonding material, Control Factors and Optimization Techniques for Bonding and Joining, S&T Publishing Inc., Tokyo, 2021, 257–261.

## Commendation

1. **N. Terasaki**, Y. Nagatomo, Y. Kuromitsu, Development of highly reliable power module substrates using new Cu/ceramics bonding technology, JWS Interfacial Joining Award for Research Promotion, 2018.
2. S. Takakuwa, **N. Terasaki**, T. Ohashi, Development of a new bonding technique between Cu and $Si_3N_4$ by using Ag free bonding material, Mate 2020 Best Paper Award, 2020.

# Acknowledgements

First of all, I would like to express my sincere gratitude to my supervisor, Prof. Tohru Sekino, for his valuable advice and patient support throughout my Ph.D. program. His careful guidance has helped me greatly in this thesis and will continue to influence me in my future research. I would also like to thank the rest of my dissertation committee—Prof. Yuichiro Koizumi, Prof. Hidetoshi Fujii, and Assoc. Prof. Tomoyo Goto—for their insightful comments and professional suggestions, which encouraged me to expand my research from different perspectives.

I would like to express my deepest gratitude to Mr. Takeshi Isobe, Mr. Yutaka Hayashibe, Mr. Satoshi Okada, and Mr. Touyou Ohashi at Mitsubishi Materials Corporation for their understanding and support, and for giving me the opportunity to conduct my research in this doctoral program.

I would like to thank Dr. Yoshiro Kuromitsu, Dr. Yoshiyuki Nagatomo, Mr. Hajime Chiba, Mr. Hiroshi Okumura, Mr. Isao Arai, Mr. Naochika Kon, Ms. Moe Sakaguchi, Ms. Aoi Nii, and Mr. Kenta Arai at Mitsubishi Materials Corporation, and Dr. Kevin M. Knowles and Dr. Amir A. Shirzadi at the Department of Materials Science and Metallurgy, the University of Cambridge, for helpful discussions and cooperation during the course of this research.

Last but not least, I would like to express my sincere gratitude to my family for their constant support and warm encouragement throughout my Ph.D. program.